University of Southampton Research Repository

UNIVERSITY OF SOUTHAMPTON

FACULTY OF ENGINEERING AND PHYSICAL SCIENCES

Mechanical Engineering

Static and Dynamic Analysis of Repetitive Structures

by

Abdull Karim Ashari

Thesis for the degree of Doctor of Philosophy

January 2019

UNIVERSITY OF SOUTHAMPTON

<u>ABSTRACT</u>

FACULTY OF ENGINEERING AND PHYSICAL SCIENCES

<u>Mechanical Engineering</u>

Thesis for the degree of Doctor of Philosophy

STATIC AND DYNAMIC ANALYSIS OF REPETITIVE STRUCTURES

Abdull Karim Ashari

In this thesis, a one-dimensional (beam-like) repetitive pin-jointed structure with point masses located at nodal cross-sections is analysed with the aim to provide a simple physical explanation for the existence of frequency-propagation zones and decay zones.

Two forms of dynamic transfer matrix are derived for the model structure: the displacement-force transfer matrix $\mathbf{G}$, and the displacement-displacement transfer matrix $\mathbf{H}$; the focus is on the relationships between the two, including their respective (dis)advantages. Similarity matrices are introduced to relate $\mathbf{G}$ and $\mathbf{H}$, together with their respective metrics. Symplectic orthogonality relationships for the eigenvectors of both $\mathbf{G}$ and $\mathbf{H}$ are derived, together with relationships between their respective sets of eigenvectors. New expressions for the group velocity are derived. For repetitive structures of finite length, natural frequency equations are derived employing both $\mathbf{G}$ and $\mathbf{H}$, including phase-closure and the direct application of boundary (end) conditions.

The wave propagation and decay characteristics of the model structure are described in depth. The existence of propagation zones is explained in terms of phase-closure (implying a natural frequency) over the cross-section at the cut-on frequency, and phase-closure over the smallest axial unit – the repeating cell – at the cut-off frequency; these zones can therefore be regarded as extended resonances. Wave interaction between branches displaying normal and anomalous dispersion is explained in terms of the Krein signature, and leads to attenuating waves. At frequencies below cut-on, waves are generally monotonic evanescent, while above cut-off they are generally oscillatory evanescent.

Energetics of different wave types under the new taxonomy is investigated. Equations for energy and power are derived in terms of eigenvectors of $\mathbf{G}$ and $\mathbf{H}$. Numerical results for

axial phase velocity and group velocity of the different modes show some familiar and some peculiar phenomena. Condition for maximum group velocity is proposed. Numerical study on anomalous dispersion reveals that pin-jointed structure which allows negative eigenvalue to occur under static self-equilibrating load will presage anomalous dispersion under dynamic condition.

The solution of a two point boundary value problem is numerically stable when one employs the Riccati transfer matrix method. An alternative numerically stable transfer matrix method, which is more direct and transparent, is developed for a repetitive structure fixed at one end, and subject to point-wise distributed loading, with and without an intermediate support. This is achieved by constructing mixed column vectors of participation coefficients, so that spatial evolution involves multiplication by powers of the eigenvalues which are less than or equal to unity.

Table of Contents

List of Tables

List of Figures

DECLARATION OF AUTHORSHIP

I, Abdull Karim Ashari declare that this thesis entitled Static and Dynamic Analysis of Repetitive Structures and the work presented in it are my own and has been generated by me as the result of my own original research.

I confirm that:

1. This work was done wholly or mainly while in candidature for a research degree at this University;
2. Where any part of this thesis has previously been submitted for a degree or any other qualification at this University or any other institution, this has been clearly stated;
3. Where I have consulted the published work of others, this is always clearly attributed;
4. Where I have quoted from the work of others, the source is always given. With the exception of such quotations, this thesis is entirely my own work;
5. I have acknowledged all main sources of help;
6. Where the thesis is based on work done by myself jointly with others, I have made clear exactly what was done by others and what I have contributed myself;
7. Parts of this work have been published as:

A. K. Ashari, N. G. Stephen, On wave propagation in repetitive structures: Two forms of transfer matrix, *Journal of Sound and Vibration*, **439** (2019) 99-112.

Signed: ....

Date: ....

Acknowledgements

I wish to express my most sincere gratitude to Prof. Neil Stephen for his supervision, guidance and assistance. Throughout my long PhD journey, he has been very kind, patient and generous with his time, knowledge and experience. He has kindly offered countless valuable ideas, advice and support during my study and on my career development. I admired his commitment and dedication to the pursuit of academic excellence.

Prof. Atul Bhaskar has been kind enough to be my second thesis supervisor. He has given valuable assistance during my study at Southampton, and for that I am thankful to him.

I also would like to thank Dr. Suan Hui Pu for serving as the internal examiner in my thesis First Review and Upgrade Review. He has given me useful comments and suggestions on improving the thesis, and has contributed greatly to my work experience.

I wish to extend my thanks to the past and present Academics, Professional Services staffs and fellow PhD students at the University of Southampton Malaysia. They have assisted me immensely over the last seven years and I enjoyed working with them. I look forward to our continued rapport.

I would like to acknowledge the scholarship support I received over the many years from the Faculty of Engineering and Physical Sciences (formerly, Faculty of Engineering and the Environment), University of Southampton, and the University of Southampton Malaysia. This generous support is much appreciated.

Finally, and most importantly, I wish to thank my family for their love and encouragement. I am truly grateful to them.

Nomenclature

a, A, **A**	$1/(2\sqrt{2})$, cross-sectional area, arbitrary matrix
c_{p}, c_{g}	phase velocity, group velocity
C	column vector of participation coefficients
d, **D**, D, d	displacement vectors, components
DOF	degrees of freedom
E	Young's modulus, energy
ext	external
f, **F**, F, f	force vectors, components
FEA	finite element analysis
G	displacement-force transfer matrix
H	displacement-displacement transfer matrix
i, i, **I**	$\sqrt{-1}$, index, identity matrix
j, **J**	index, metric matrix
k, **K**, K	bar stiffness, stiffness matrix, kinetic
L, L, **L**	left, bar length, similarity matrix
m, **m**	mass, mass matrix
n, N, **N**	index, number of cells, similarity matrix
P	power
R, **R**	right, reflection matrix
S, S	singular value, strain
s, **S**	generic state vector, rectangular diagonal matrix whose diagonal entries are singular values of **A**

SVP	Saint-Venant's principle
$t, \mathbf{T}$	time, generic transfer matrix, transformation matrix
TMM	transfer matrix method
TPBVP	two-point boundary value problem
$\mathbf{U}$	unitary matrix whose columns are left-singular vectors of $\mathbf{A}$
$v, \mathbf{V}$	entries in matrix $\mathbf{V}$, (right) eigenvector of $\mathbf{G}$, matrix of eigenvectors, unitary matrix whose columns are right-singular vectors of $\mathbf{A}$
$\mathbf{w}, \mathbf{W}^{\mathrm{T}}, W$	wave amplitude vector, left eigenvector of $\mathbf{G}$, work done
$\mathbf{X}$	(right) eigenvector of $\mathbf{H}$
x, y	Cartesian coordinates
$\mathbf{Y}^{\mathrm{T}}$	left eigenvector of $\mathbf{H}$
α	scalar
δ	decay rate constant
κ	Krein signature
φ	phase constant, or wavenumber
$\lambda, \mathbf{\Lambda}$	eigenvalue, matrix of eigenvalues
μ	$\lambda + \lambda^{-1}$, propagation constant $(\delta + \mathrm{i}\varphi)$
$\omega, \mathbf{\Omega}$	radian frequency, generic metric matrix

Note that matrix and vector quantities are in bold. Subscripts D and F denotes displacement and force, respectively.

Chapter 1: Introduction

1.1   Repetitive structures

Repetitive, or periodic, structures are one with spatially repeating substructure connected together end-to-end and/or side-by-side in a regular pattern to form the entire structure which could be one-, two- or three-dimensional. Other terms have also been used such as modular, cellular, chain-like, lattice-like and reticulated [1]; 'cellular' is typically used to describe honeycomb-like structures but has also been used for other porous structures with irregular cell patterns such as foam. The substructure could be translationally or rotationally symmetric in at least one axial direction and may consist of beams, bars, flat plates, shells or point masses with various support conditions. The points or nodes where the structural members are connected are called couplings, joints or junctions—basically, they define the degrees of freedom that the substructure has. The locations of the coupling along the axial direction are called stations, or sections, and they are usually enumerated for analysis. Physical parameters, such as displacement and force, are usually defined at the couplings. In the case of a finite structure, the end conditions will also be specified.

In structural engineering, many structures have been, and can be, treated as repetitive. This includes railway track, oil pipeline, multi-storey building, elevated highways, bladed disk (blisk), aircraft fuselage, spacecraft boom, layered composite and stiffened plates in aerospace and ship structures. All these structures can be regarded as being constructed from a repeating substructure. For example, the railway track can be discretised into regular sections of steel rails supported by a sleeper that is resting on the ballast. Oil pipeline can be constructed from repeating units of hollow cylinders. Multi-storey building may be regarded as stacks of regular floor pattern while elevated highways may consist of many spans of railroad with supports from the ground. Unlike previous examples, a blisk is rotationally repetitive—consisting of a blade attached to a sector of the central disk. An aircraft fuselage can be built up of repeating rings that are constructed from the fuselage skin, longerons and stringers. A spacecraft boom usually takes a beam-like truss form with a regular pattern of bar members. A composite is formed from different layers and generally anisotropic, however its properties can be regarded as repetitive, at least in one direction. Large transport such as aircraft and ship employed stiffened plates construction which can be modelled as a repeating pattern of plate attached to stringers and a set of fasteners.

In the design of these structures, the static and dynamic loads that they may experience need to be considered. For example, railway track and elevated highways are exposed to the moving weight of the vehicles, pipe lines and buildings may be subjected to tremor and earthquakes, bladed disks are impacted by high pressure and turbulent air flow, and aircraft structures are impinged by the vibration and noise from the jet engines. Spacecraft boom tend to be long and light which means it is susceptible to long sustained vibrating motion, particularly in space environment.

The use of repetitive structures in engineering design offer many advantages. Analysis of such structure can be reduced to a single repeating substructure by taking its spatial periodicity into account. As its construction is also repetitive, it offers a cost effective design solution. Maintenance and repair of the structures could be reduced to a minimum number of concerned sections. In the case of pin-jointed structures, removal of members from such a structure can turn it to a mechanism, allowing it to collapse and take a compact form for ease of transportation; these attributes are favourable in aerospace application. Repetitive structures are also known to have frequency filtering property which can be exploited to control the vibrations that go through them. Furthermore, the structures portray aesthetically pleasing appearance.

In this chapter, a review of previous work on repetitive structures is presented in Section 1.2. Different methods which have been developed to analyse the structures are described briefly, particular emphasis is given on transfer matrix method which is employed in this thesis. Other aspects considered in this review are energetics and natural frequencies of the structures. In Section 1.3, motivation, aim, objectives, scopes and organisation of this thesis are presented.

1.2   Literature Review

1.2.1   Modelling and analysis of repetitive structures

The simplest model of repetitive structure is an infinite mass-spring chain as shown in Figure 1.1(a). The chain consists of point masses and massless springs (between the point masses). The substructure can take two symmetric[1] constructions—a cellular or a cross-sectional forms. The former consists of one-half of a point mass m each on its left- and right-hand

---

[1] A substructure which consists of a spring and a point mass m is asymmetric and leads to asymmetric stiffness matrix. For further details, see Brillouin [83], page 82.

sides and a spring connecting the two one-half masses in between, as shown in Figure 1.1(b). The latter consists of a point mass and two springs pin-jointed on either side of the mass, as shown in Figure 1.1(c).

(a)

(b)

(c)
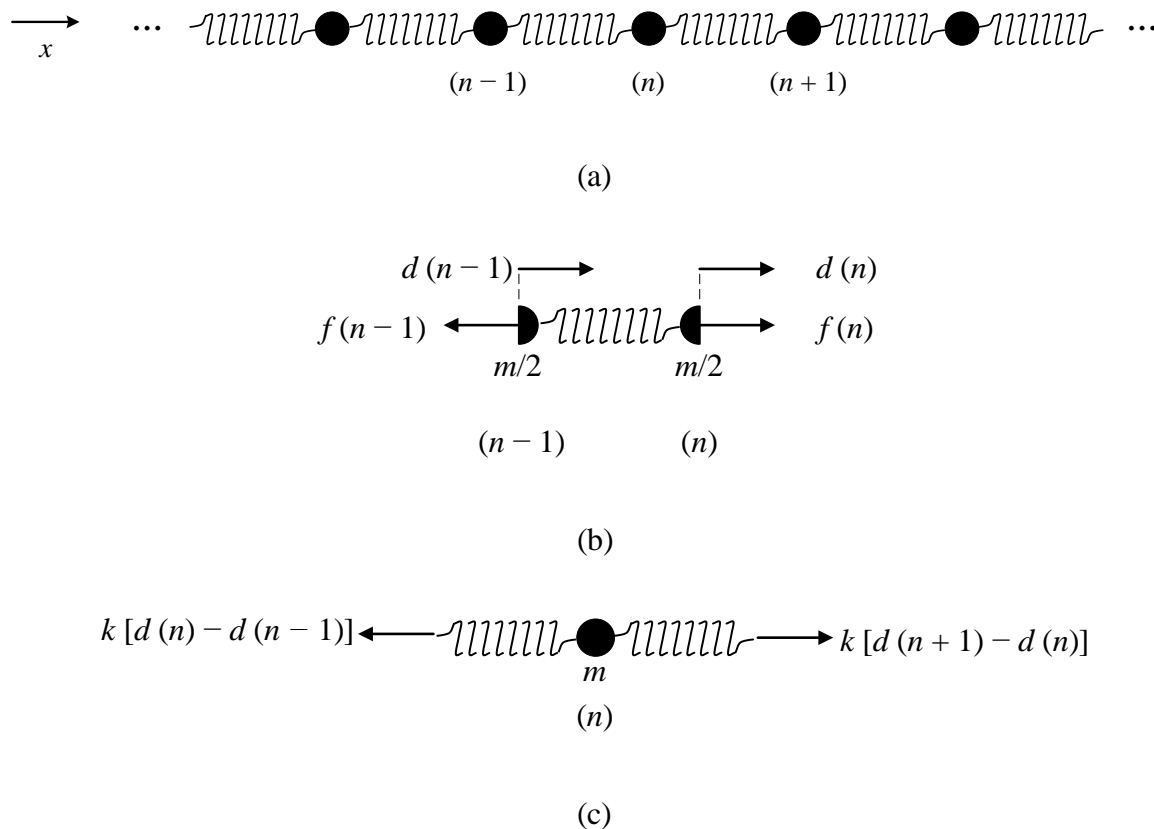
Figure 1.1 (a) A segment of infinite mass-spring chain. (b) nth cell. (c) nth cross-section.

Consider a dynamic problem whereby the chain is excited harmonically. The displacement of a point mass is given by $d \exp(i \omega t)$ where d is the peak displacement amplitude, $i = \sqrt{-1}$, ω is the angular frequency and t is time; hence its velocity and acceleration are $i \omega d \exp(i \omega t)$ and $-\omega^2 d \exp(i \omega t)$, respectively. First, consider the formulation for the cellular substructure. Assume the nth displacement is numerically larger than $(n-1)$th and positive forces are defined according to the normal conventions. Upon applying Newton's Second Law to the left- and right-hand sides of the cell, the resulting equations of motion are

3

$$k\left[d(n)-d(n-1)\right]-f(n-1)=-\frac{m\omega^2}{2}d(n-1) \tag{1.1}$$

$$f(n)-k\left[d(n)-d(n-1)\right]=-\frac{m\omega^2}{2}d(n) \tag{1.2}$$

where f is the traction force peak amplitude, k is the spring constant and m is the mass; the terms $\exp(i\omega t)$ have been cancelled out from the equations. Note that the indicial cross-section numbers are enclosed within the parentheses. The equations can be re-arranged in dynamic stiffness matrix form as

$$\begin{bmatrix} -f(n-1) \\ f(n) \end{bmatrix} = \begin{bmatrix} k-\dfrac{m\omega^2}{2} & -k \\ -k & k-\dfrac{m\omega^2}{2} \end{bmatrix} \begin{bmatrix} d(n-1) \\ d(n) \end{bmatrix} \tag{1.3}$$

or, in displacement-force transfer matrix form as

$$\begin{bmatrix} d(n) \\ f(n) \end{bmatrix} = \begin{bmatrix} 1-\dfrac{\omega^2}{2\omega_n^2} & \dfrac{1}{k} \\ k\left[\left(1-\dfrac{\omega^2}{2\omega_n^2}\right)^2-1\right] & 1-\dfrac{\omega^2}{2\omega_n^2} \end{bmatrix} \begin{bmatrix} d(n-1) \\ f(n-1) \end{bmatrix} \tag{1.4}$$

where $\omega_n^2 = k/m$.

Now, consider the formulation for a cross-sectional substructure. Following the same procedures and applying Newton's Second Law to the cross-section leads to the following equation of motion,

$$\left[kd(n+1)-kd(n)\right]-\left[kd(n)-kd(n-1)\right]=-m\omega^2 d(n) \tag{1.5}$$

which can be simplified to

$$d(n-1)-2\left(1-\frac{\omega^2}{2\omega_n^2}\right)d(n)+d(n+1)=0 \tag{1.6}$$

or, in the displacement-displacement transfer matrix (also known as recurrence matrix) form as

$$\begin{bmatrix} d(n) \\ d(n+1) \end{bmatrix} = \begin{bmatrix} 0 & 1 \\ -1 & 2\left(1-\dfrac{\omega^2}{2\omega_n^2}\right) \end{bmatrix} \begin{bmatrix} d(n-1) \\ d(n) \end{bmatrix}. \tag{1.7}$$

Again, note that the terms $\exp(i\omega t)$ have been cancelled out from the equations. The vectors $\begin{bmatrix} d(n-1) & f(n-1) \end{bmatrix}^T$ and $\begin{bmatrix} d(n-1) & d(n) \end{bmatrix}^T$ are called state vectors. Evidently, the two different sub-structural constructions lead to different forms of transfer matrix. While both forms of transfer matrix have been employed in previous work on repetitive structures, the displacement-force transfer is found to be more prevalent.

As equations (1.4) and (1.7) describe identical systems, they must be intimately related. In fact, equation (1.5) can be derived from equations (1.1) and (1.2) as follows: write

$$f(n) = -kd(n-1) + \left(k - \frac{m\omega^2}{2}\right)d(n),$$

$$-f(n) = \left(k - \frac{m\omega^2}{2}\right)d(n) - kd(n+1),$$

and then add the two equations. In the static problem of a finite structure, the boundary conditions are specified, that means either displacement or force at the ends is known. Therefore, it is desirable to employ displacement-force transfer matrix in the static case. However, in the dynamic problem, the harmonic response can be evaluated from the displacements, therefore the displacement-displacement transfer matrix is more appropriate.

Dimensionality of repetitive structures is defined according to the number of axial directions in which waves are allowed to propagate through the structures. For example, the mass-spring chain is considered to be mono-coupled one-dimensional structure because the wave can propagate in one axial direction only. For structures with multi-couplings at the cross-sections, multiple modes may propagate simultaneously. Figure 1.2 (a) shows a beam-like framework and can be regarded as a more complex version of the mass-spring chain; the springs are now represented by straight lines. The framework has two layers of point masses and two degrees of freedom at each joint, the diagonal springs are not connected where they intersect. Even though the framework has multiple couplings, it is considered to be one-dimensional because the normal wave modes can propagate only in the x-axial direction. The mass-spring system can also be extended in two dimensions to form a mass-spring net as shown in Figure 1.2 (b), and in three dimensions as a mass-spring lattice as shown in Figure 1.2 (c). (The three-dimensional lattice appears similar to the atomic structure of pure crystals.) Waves can travel in both x- and y-directions through the mass-spring net, and in all three axial directions through the mass-spring lattice.

All repetitive structures exhibit frequency filtering property, i.e. a particular wave mode is allowed to propagate through the structure over certain frequency band(s) only. Outside the propagation band, the wave decays[2] exponentially. This phenomenon has been attributed to complex interference pattern of transmitted and reflected waves at the boundaries of each cell [2]. However, one may argue that if a portion of the wave energy is reflected back to its source, then the wave should get attenuated. This implies that wave propagation is not possible, particularly through infinite repetitive structure wherein a portion of the wave energy is more likely to get reflected. Two-dimensional repetitive structures also have spatial filtering property, i.e. a particular wave is allowed to propagate over certain angular band at a given frequency. This property is called the beaming effect [3].
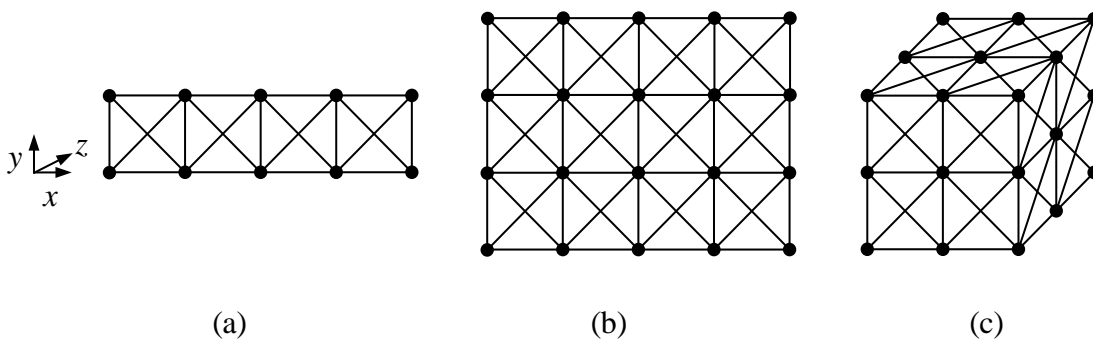
Figure 1.2 (a) A segment of beam-like framework. (b) A segment of mass-spring net. (c) A mass-spring lattice. The internal connections of spring are not shown.

There are many methods which have been developed to analyse repetitive structures. Reviews of the methods are provided by Noor and Mikulas [4], Mester and Benaroya [5] and Mead [6]. In Noor and Mikulas' review, the methods are grouped in four classes, namely:

(a) *Direct method* in which the structure is separated into discrete elements and solved using methods applicable to framework problem.

---

[2]There are three different types of decay—attenuating, monotonic evanescent and oscillatory evanescent. In Chapter 3, the three types of decaying wave are distinguished and described in detail.

(b) *Discrete field method* in which the displacements on either side of the repeating cell are related by finite difference equations, as described by Stephen and Ghosh [7] and Stephen and Zhang [8] but they inadvertently called the method as 'direct' field.

(c) *Periodic structure approach* which typically employs a transfer matrix relating a state vector consisting of nodal displacement and force components on either side of the repeating cell.

(d) *Substitute continuum*, or *homogenization*, *approach* in which original structure is replaced by a continuum model whose properties are in some sense equivalent to the original structure.

Method (a) is computationally inefficient for large structure as it does not exploit its periodicity. Method (b) does exploit periodicity of the structure; however, Noor and Mikulas [4] commented that the method will become involved for structures with complex geometry. Method (b) was employed by Karpov *et al.* [9] for pin-jointed beam lattice; according to them, the method was commonly used as an alternative to finite element method where saving in computational effort is possible, but recent advances in computer performance and the rise of other alternative methods have made this method less interesting. Approach (c) also exploits periodicity of the structure, for example, mass-spring chain and truss structure was studied by Engels and Meirovitch [10] using approach (c). When commenting on the approach, Noor and Mikulas [4] gave a restrictive remark by stating that the method is "efficient only for rotationally periodic structures and lattices with simple geometries". A more recent development has shown that the approach can be employed even for complex structures, especially when combined with other methods, such as finite element method. Approach (d) also exploits periodicity of the structure. According to Stephen and Zhang [8], this approach is suitable in the study of global, rather than local, behaviour of the structure and in areas where it is common for engineers to think in terms of continuum properties. Continuum modelling has been employed by Noor and Mikulas [4], and Tollenaere and Caillerie [11] on lattice structures. Approaches (c) and (d) can be combined to solve static and dynamic problems. For static problems, eigenanalysis and continuum modelling of pin-jointed straight, curved, asymmetric and pre-twisted beam-like repetitive structures have been considered by Stephen and his co-workers [7,12–14]. For dynamic problem, the approaches are employed by Stephen and Zhang [8] on structures that exhibit tension-torsion coupling.

Mester and Benaroya [5] also named four methods that are used in dynamic analysis of one-dimensional repetitive structure, they are *finite element method* (FEM), *transfer matrix analysis*, *wave propagation analysis* and *continuum modelling*. FEM involves modelling of the structure using commercial FE packages and element libraries; mass and stiffness matrices of the structure are found and post-processed by applying harmonic excitation through the structure [15]. This leads to eigenproblem whose solution yields the dispersion relations for free wave modes. Finite element analysis of periodic structures has been presented by Duhamel *et al.* [16]. For large structure, direct implementation of FEM may not be computationally efficient. Therefore, FEM can be used together with transfer matrix analysis; the repeated cell is analysed by FEM to obtain its properties and then transfer matrix method is used to evaluate the behaviour of overall structure. An example of combined finite element and transfer matrix method is presented by Bhutani and Loewy [17]. The wave propagation analysis is conceptually similar to the wave receptance analysis introduced by Mead in [18]. The method is based on receptance matrix which is the inverse of dynamic stiffness matrix. Translational symmetry allows one to write $d_R = \lambda d_L$ and $f_R = \lambda f_L$; applying the periodicity relations to the transfer matrix equation leads to quadratic eigenvalue problem for λ (for a given frequency ω). Continuum modelling is the same as substitute continuum approach described earlier. Note that the FEM is a numerical method while the other three methods are analytical.

An exposition of the methods developed at the University of Southampton since 1964 until 1995 to analyse repetitive structures are presented by Mead [6]. One of the many methods described in the exposition is the transfer matrix method. In this thesis, transfer matrix is the primary method used for both static and dynamic analysis; detailed review of the method is presented in Section 1.2.2. In the paper [6], Mead also reviewed some theorems relating to wave motion in periodic structures developed by Southampton researchers; one of the theorems is phase closure principle which states that natural frequency occurs when the total phase change of a wave circumnavigating a finite structure is an integer number of 2π. Detailed description of the principle is available in a separate paper by Mead [19]. At the end of the review, it is interesting to find out that Mead concluded the paper with the following statements: "Despite the numerous studies of wave motion in continuous periodic systems over the past 40 years, a simple physical explanation has yet to be presented for the very existence of frequency-propagation zones and attenuation zones. However, even if there is no simple answer to the question "Why does wave motion of one frequency

propagate freely while motion of another frequency is attenuated?", reliable prediction methods do exist for the properties of free motion and the magnitudes of forced motion."

In recent years, the research on repetitive structures has been reinvigorated by the discovery of unusual physical phenomena associated with phononic crystals and (acoustic or elastic) metamaterials [20]. A phononic[3] crystal is a composite with spatially regular construction that resemble a crystalline material. On the other hand, an acoustic or elastic metamaterial is a (phononic) material that exhibit properties beyond what is found in natural material such as negative refraction; its key feature is the presence of local resonance [21]. Unique properties of the phononic crystals and metamaterials can be exploited for numerous applications. For example, the phononic crystals have been developed for vibration filtering, noise control and defect detection while metamaterials have been employed in sound and vibration isolation, subwavelength focusing and cloaking—an effect observed when the acoustic or elastic wave is steered around an object within the metamaterials (see [20,22] and references therein). The similarity in analysis of wave motion through all forms of repetitive structures lies in the concept of a band diagram which is a plot relating frequency (or energy) to the wavenumber.

Wave modes in the repetitive structures can be modelled using Floquet-Bloch theorem [23]. According to the theorem, a solution is represented by a wave vector multiplied by a transfer function. Spatial periodicity of the structure implies similar periodicity for the wave vector, i.e. a pattern described by the wave vector components is unique to within a scalar multiplier. This leads to an eigenvalue problem whose solution relates the frequency to the wavenumber. In the asymptotic approach, the physical field components in the wave vector such as displacements are usually approximated by Fourier expansions [24].

The dynamic behaviour of repetitive structures can also be described by an asymptotic homogenisation approach, which is useful where finite element method is too computationally intensive, and has been demonstrated on numerous dynamic problems; for example, Boutin and Hans [25] employed the method to study vibrations of periodic multi-frame model that resembles an idealised building structure. Typically, asymptotic homogenisation is applied to cases where the wavelength of the propagating mode is considerably large in comparison to the size of a unit cell, therefore the classical approach of the asymptotic homogenisation theory is usually limited to low frequency. To overcome

---

[3] In analogy to the quantised light particle called photon, the discrete quantity of vibrational energy and sound that propagate through the crystal is known as phonon.

this limitation, Craster *et al.* [26,27] developed a high frequency asymptotic procedure by perturbing about the high cut-off frequency of the propagation mode. This approach is similar to the classical asymptotic homogenization; the difference is it involves perturbation away from the cell resonances rather than perturbing away from the static limit.

In the two-scale asymptotic homogenisation approach, the analysis performed provides the macroscopic equations that govern the structure behaviour at both low and high frequency. Spatial variables are scaled by a small parameter which characterises the size of the smallest unit cell [22]. Scaled and unscaled variables are then treated independently from each other. Asymptotic expansions of the unknown physical fields are introduced in ascending powers of the small parameter, this represents perturbations away from the leading approximation. Integration over the unit cell domain provides homogenised equations that describe the behaviour of the structure on a larger scale. In other words, the resulting equation is characterised by the integrated parameter that is valid over the short scale of the cell but does not affect the large scale substructure in the problem.

The high frequency homogenisation method is a powerful tool for the analysis of the dynamic response of repetitive structures, including phononic crystals and metamaterial. The method was demonstrated on a two-dimensional and a piecewise homogeneous string on a Winkler foundation by Craster *et al.* [26]. The method was also applied to a model of diatomic chain whereby each type of mass vary gradually with position, and to a square lattice with alternating masses [27]. Nolde *et al.* [28] illustrated the versatility of the method on nets created from elastic strings with point forcing. The results are compared with exact solutions; it is noted that the asymptotic techniques are able to capture the relationship between frequency and wavenumber where they become close or cross, including within the decay band. Craster *et al.* [29] also considered the asymptotic techniques on Bloch wave for a class of three-phase checkerboard media which are known to have unusual negative refraction property at high frequency. Interesting effects are revealed from the study such as lensing and cloaking.

More recently, Fossat *et al.* [30] derived asymptotic homogenised models for a ribbed plate with local resonances. The high frequency homogenisation method was extended to a mass-spring chain and framed reticulated beams by Rallu *et al.* [31] and further developed in [32]. In reference [33], the accuracy of the homogenisation method is compared with the condensed wave finite element on a model framed structure; it is noted that computational efficiency of the latter method can be improved by reducing the internal nodes of a unit cell.

Several state-of-the-art methods have also been developed to study cyclically repetitive structures. The nature of such structures imposes a cyclic structure on their mass and stiffness matrices whose properties are described by the theory of circulants; a detailed application of the theory to vibration analysis is presented by Olson *et al.* [34]. The special properties of cyclic symmetry are expressed quite naturally by the group representation theory. Therefore, one of the promising approaches combines the group representation theory with FEM [35]. A key step in the approach is selecting a local coordinate system that is symmetric with respect to each node. In [35], the approach is used to evaluate the dynamic characteristics of a defective planetary reduction gear. Another important approach is the transfer matrix method which is usually used in the evaluation of natural frequencies and normal modes [35]; the results can be verified against numerical and experimental findings. Mencik [36], proposed a wave finite element approach for computing wave modes and forced response of a single and an assembly of blades set with a ring connection, and the inner circumferential boundary is subjected to a distributed excitation. In this approach, a finite element model of a substructure is constructed and dynamic flexibility matrices are derived from it before further analyses are made. Numerical results show that the approach requires less computation time, is numerically more stable and more accurate than the FEM and the existing theory of cyclic symmetry, particularly at high frequency and as the number of periodic structures considered increases.

1.2.2 Transfer matrix method

Consider a beam-like framework as shown in Figure 1.3; the basic construction of the framework is similar to the mass-spring system shown in Figure 1.2(a) except for the missing point-masses and additional network of springs which add extra thickness to the structure. The framework has been employed extensively as a model structure by Stephen and his co-workers [1,12,37–39] for static analysis of repetitive structures and is used in this section to illustrate the implementation of the transfer matrix method.

(a)

(b)

(c)
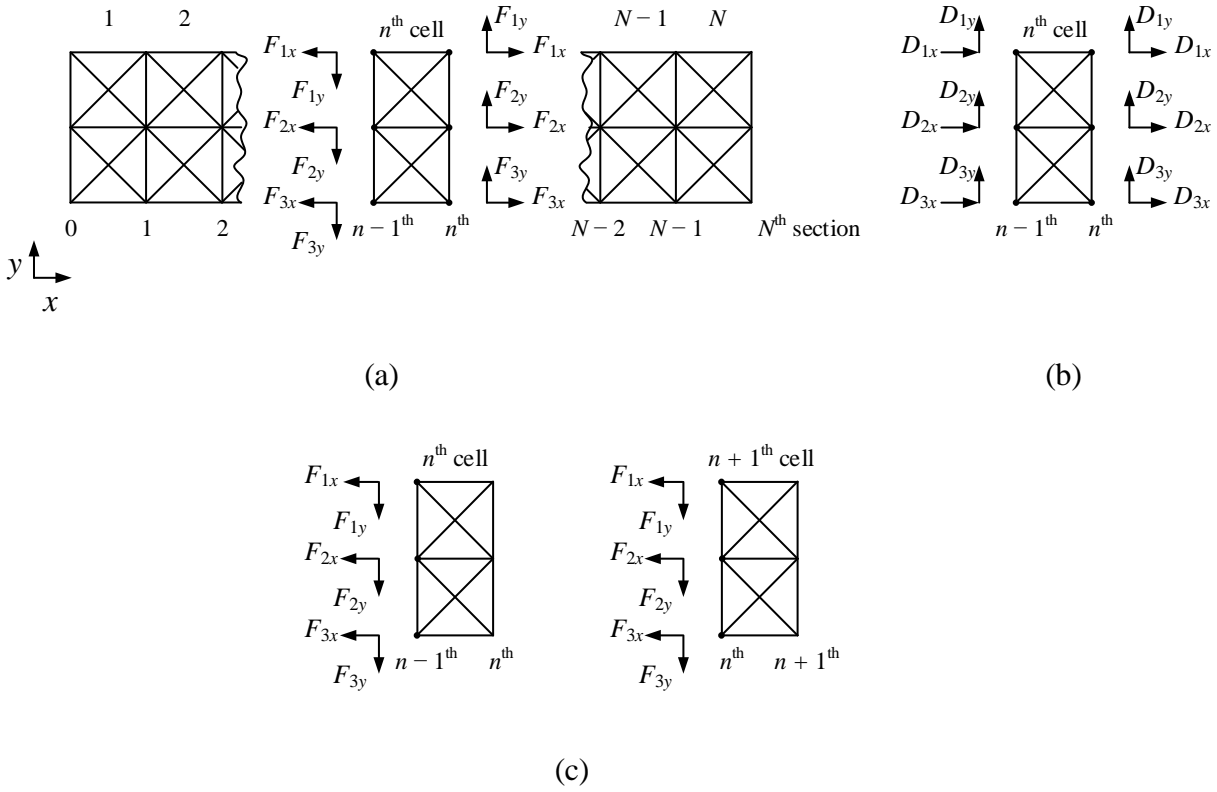
Figure 1.3 (a) *N* cells of repetitive framework. The force directions are shown according to the normal conventions, that is positive for tension and negative for compression. (b) Nodal displacements on the left- and right-hand side of *n*th cell. (c) Nodal forces on the left-hand side of *n*th and $(n+1)$ th cells.

The force and displacement vectors, $\mathbf{F}$ and $\mathbf{D}$, for the *n*th cell are related by stiffness equation $\mathbf{F} = \mathbf{KD}$, or in partitioned form

$$\begin{bmatrix} -\mathbf{F}(n-1) \\ \mathbf{F}(n) \end{bmatrix} = \begin{bmatrix} \mathbf{K}_{n-1,n-1} & \mathbf{K}_{n-1,n} \\ \mathbf{K}_{n,n-1} & \mathbf{K}_{n,n} \end{bmatrix} \begin{bmatrix} \mathbf{D}(n-1) \\ \mathbf{D}(n) \end{bmatrix}. \tag{1.8}$$

By convention, the force at section $(n-1)$ is positive when the components are parallel to the coordinate directions. Since all cells within the structure have identical stiffness matrix $\mathbf{K}$, the subscripts $(n-1)$ and (n) within $\mathbf{K}$ are replaced by subscripts L and R for left- and right-hand side, respectively; however, the subcripts $(n-1)$ and (n) are retained as indices for the state vector. One then has

$$\begin{bmatrix} -\mathbf{F}(n-1) \\ \mathbf{F}(n) \end{bmatrix} = \begin{bmatrix} \mathbf{K}_{LL} & \mathbf{K}_{LR} \\ \mathbf{K}_{RL} & \mathbf{K}_{RR} \end{bmatrix} \begin{bmatrix} \mathbf{D}(n-1) \\ \mathbf{D}(n) \end{bmatrix}. \tag{1.9}$$

In the transfer matrix method, the nodal displacements and forces at the left-hand side of the nth cell are combined into a single state vector of displacement and force, $\mathbf{s}_{\mathrm{L}}(n-1) = \begin{bmatrix} \mathbf{D}^{\mathrm{T}}(n-1) & \mathbf{F}^{\mathrm{T}}(n-1) \end{bmatrix}^{\mathrm{T}}$. The state vector at the left-hand side of the next cell is $\mathbf{s}_{\mathrm{L}}(n) = \begin{bmatrix} \mathbf{D}^{\mathrm{T}}(n) & \mathbf{F}^{\mathrm{T}}(n) \end{bmatrix}^{\mathrm{T}}$. The two state vectors are related by the transfer matrix $\mathbf{G}$ through the equation $\mathbf{s}_{\mathrm{L}}(n) = \mathbf{G}\mathbf{s}_{\mathrm{L}}(n-1)$, the subscript L can be omitted. The transfer matrix $\mathbf{G}$ for the nth cell is constructed by partitioning and re-arranging stiffness matrix $\mathbf{K}$, that is by expanding equation (1.9) and re-arranging in accordance with $\mathbf{s}(n) = \mathbf{G}\mathbf{s}(n-1)$ to get

$$\mathbf{G} = \begin{bmatrix} \mathbf{G}_{\mathrm{DD}} & \mathbf{G}_{\mathrm{DF}} \\ \mathbf{G}_{\mathrm{FD}} & \mathbf{G}_{\mathrm{FF}} \end{bmatrix} = \begin{bmatrix} -\mathbf{K}_{\mathrm{LR}}^{-1}\mathbf{K}_{\mathrm{LL}} & -\mathbf{K}_{\mathrm{LR}}^{-1} \\ \mathbf{K}_{\mathrm{RL}} - \mathbf{K}_{\mathrm{RR}}\mathbf{K}_{\mathrm{LR}}^{-1}\mathbf{K}_{\mathrm{LL}} & -\mathbf{K}_{\mathrm{RR}}\mathbf{K}_{\mathrm{LR}}^{-1} \end{bmatrix}. \tag{1.10}$$

The two blocks on the leading diagonal of $\mathbf{G}$, that is $\mathbf{G}_{\mathrm{DD}}$ and $\mathbf{G}_{\mathrm{FF}}$ are found to be independent of the Young's modulus E, while the blocks $\mathbf{G}_{\mathrm{DF}}$ and $\mathbf{G}_{\mathrm{FD}}$ are proportional to E^{-1} and E, respectively [39]. E is typically large, e.g. $E = 200$ GPa for steel; as a result, the blocks could have largely disparate values and this could lead to ill-conditioning. Further details on ill-conditioning and numerical instability are presented in Section 1.2.6.

In the static case, setting $\mathbf{s}(n) = \lambda\mathbf{s}(n-1)$ where λ is the (piecewise exponential) decay (or transmission) factor, leads to the eigenvalue problem $[\mathbf{G} - \lambda\mathbf{I}]\mathbf{s}(n) = \mathbf{0}$ in which $\mathbf{I}$ is the identity matrix. The eigenvalues and eigenvectors can be found numerically using MATLAB's eig command. Alternatively, a quadratic eigenvalue formulation involving the partitioned stiffness matrix can be found as follows: expand equation (1.9) as

$$-\mathbf{F}(n-1) = \mathbf{K}_{\mathrm{LL}}\mathbf{D}(n-1) + \mathbf{K}_{\mathrm{LR}}\mathbf{D}(n) \tag{1.11}$$

$$\mathbf{F}(n) = \mathbf{K}_{\mathrm{RL}}\mathbf{D}(n-1) + \mathbf{K}_{\mathrm{RR}}\mathbf{D}(n). \tag{1.12}$$

Multiply equation (1.11) by λ, substitute $\mathbf{D}(n) = \lambda\mathbf{D}(n-1)$ in equations (1.11) and (1.12) and add, to give

$$\left[\lambda^2\mathbf{K}_{\mathrm{LR}} + \lambda\left(\mathbf{K}_{\mathrm{LL}} + \mathbf{K}_{\mathrm{RR}} \right) + \mathbf{K}_{\mathrm{RL}} \right]\mathbf{D}(n-1) = 0, \tag{1.13}$$

which can be tackled as a "lambda" matrix[4] problem. Equation (1.13) can be re-cast back in matrix form as follows: note that the forces on the right-hand side of n th cell and left-hand

---

[4] A matrix whose elements are polynomials in the variable λ.

side of $(n+1)$th cell should be in static equilibrium, therefore $\mathbf{F}(n) - \lambda\mathbf{F}(n-1) = \mathbf{0}$ or in the matrix form,

$$\begin{bmatrix} \lambda\mathbf{I} & \mathbf{I} \end{bmatrix}\begin{bmatrix} -\mathbf{F}(n-1) \\ \mathbf{F}(n) \end{bmatrix} = \mathbf{0}. \tag{1.14}$$

Substitute the force vector with equation (1.9) and write

$$\begin{bmatrix} \mathbf{D}(n-1) \\ \mathbf{D}(n) \end{bmatrix} = \begin{bmatrix} \mathbf{I} \\ \lambda\mathbf{I} \end{bmatrix}\mathbf{D}(n-1), \tag{1.15}$$

gives

$$\begin{bmatrix} \lambda\mathbf{I} & \mathbf{I} \end{bmatrix}\begin{bmatrix} \mathbf{K}_{LL} & \mathbf{K}_{LR} \\ \mathbf{K}_{RL} & \mathbf{K}_{RR} \end{bmatrix}\begin{bmatrix} \mathbf{I} \\ \lambda\mathbf{I} \end{bmatrix}\mathbf{D}(n-1) = \mathbf{0}, \tag{1.16}$$

which upon expansion leads to equation (1.13). According to Stephen and Wang [38], this approach can reduce the problem size by half but has lost its standard eigenvalue form. Therefore, it is preferable to restore equation (1.16) back in the standard form; to do that, expand equation (1.16) and re-arrange the terms as

$$\lambda^2\mathbf{D}(n-1) = -\mathbf{K}_{LR}^{-1}\mathbf{K}_{RL}\mathbf{D}(n-1) - \lambda\mathbf{K}_{LR}^{-1}\begin{bmatrix} \mathbf{K}_{LL} + \mathbf{K}_{RR} \end{bmatrix}\mathbf{D}(n-1). \tag{1.17}$$

The equation can now take the following matrix form,

$$\begin{bmatrix} \mathbf{H} - \lambda\mathbf{I} \end{bmatrix}\begin{bmatrix} \mathbf{D}(n-1) \\ \lambda\mathbf{D}(n-1) \end{bmatrix} = \mathbf{0} \tag{1.18}$$

where

$$\mathbf{H} = \begin{bmatrix} \mathbf{0} & \mathbf{I} \\ -\mathbf{K}_{LR}^{-1}\mathbf{K}_{RL} & -\mathbf{K}_{LR}^{-1}\left(\mathbf{K}_{LL} + \mathbf{K}_{RR} \right) \end{bmatrix}. \tag{1.19}$$

Note that the top row of equation (1.19) is simply $\lambda\mathbf{D}(n-1) = \lambda\mathbf{D}(n-1)$ while the second row gives equation (1.17).

Another possible matrix form is presented by Zhong and Williams [40] whereby the equations of motion are first expressed as

$$\begin{bmatrix} \mathbf{D}(n-1) \\ \mathbf{F}(n-1) \end{bmatrix} = \begin{bmatrix} \mathbf{I} & \mathbf{0} \\ -\mathbf{K}_{LL} & -\mathbf{K}_{LR} \end{bmatrix}\begin{bmatrix} \mathbf{D}(n-1) \\ \mathbf{D}(n) \end{bmatrix} \tag{1.20}$$

and

$$\begin{bmatrix} \mathbf{D}(n) \\ \mathbf{F}(n) \end{bmatrix} = \begin{bmatrix} \mathbf{0} & \mathbf{I} \\ \mathbf{K}_{RL} & \mathbf{K}_{RR} \end{bmatrix}\begin{bmatrix} \mathbf{D}(n-1) \\ \mathbf{D}(n) \end{bmatrix}. \tag{1.21}$$

Immediately one can write

$$\begin{bmatrix} \mathbf{D}(n) \\ \mathbf{F}(n) \end{bmatrix} = \begin{bmatrix} \mathbf{0} & \mathbf{I} \\ \mathbf{K}_{RL} & \mathbf{K}_{RR} \end{bmatrix} \begin{bmatrix} \mathbf{I} & \mathbf{0} \\ -\mathbf{K}_{LL} & -\mathbf{K}_{LR} \end{bmatrix}^{-1} \begin{bmatrix} \mathbf{D}(n-1) \\ \mathbf{F}(n-1) \end{bmatrix}. \tag{1.22}$$

It can be verified that

$$\begin{bmatrix} \mathbf{I} & \mathbf{0} \\ -\mathbf{K}_{LL} & -\mathbf{K}_{LR} \end{bmatrix}^{T} \begin{bmatrix} \mathbf{0} & \mathbf{I} \\ -\mathbf{I} & \mathbf{0} \end{bmatrix} \begin{bmatrix} \mathbf{I} & \mathbf{0} \\ -\mathbf{K}_{LL} & -\mathbf{K}_{LR} \end{bmatrix} = \begin{bmatrix} \mathbf{0} & -\mathbf{K}_{LR} \\ \mathbf{K}_{RL} & \mathbf{0} \end{bmatrix}, \tag{1.23}$$

$$\begin{bmatrix} \mathbf{0} & \mathbf{I} \\ \mathbf{K}_{RL} & \mathbf{K}_{RR} \end{bmatrix}^{T} \begin{bmatrix} \mathbf{0} & \mathbf{I} \\ -\mathbf{I} & \mathbf{0} \end{bmatrix} \begin{bmatrix} \mathbf{0} & \mathbf{I} \\ \mathbf{K}_{RL} & \mathbf{K}_{RR} \end{bmatrix} = \begin{bmatrix} \mathbf{0} & -\mathbf{K}_{LR} \\ \mathbf{K}_{RL} & \mathbf{0} \end{bmatrix}. \tag{1.24}$$

By Bloch's theorem, the translational symmetry allows one to write

$$\begin{bmatrix} \mathbf{D}(n) \\ \mathbf{F}(n) \end{bmatrix} = \lambda \begin{bmatrix} \mathbf{D}(n-1) \\ \mathbf{F}(n-1) \end{bmatrix}, \tag{1.25}$$

where λ is a scalar multiplier. Substituting equations (1.20) and (1.21) into equation (1.25) gives

$$\begin{bmatrix} \mathbf{0} & \mathbf{I} \\ \mathbf{K}_{RL} & \mathbf{K}_{RR} \end{bmatrix} \begin{bmatrix} \mathbf{D}(n-1) \\ \mathbf{D}(n) \end{bmatrix} = \lambda \begin{bmatrix} \mathbf{I} & \mathbf{0} \\ -\mathbf{K}_{LL} & -\mathbf{K}_{LR} \end{bmatrix} \begin{bmatrix} \mathbf{D}(n-1) \\ \mathbf{D}(n) \end{bmatrix}. \tag{1.26}$$

Pre-multiply equation (1.26) by $\begin{bmatrix} \mathbf{I} & \mathbf{0} \\ -\mathbf{K}_{LL} & -\mathbf{K}_{LR} \end{bmatrix}^{T} \begin{bmatrix} \mathbf{0} & \mathbf{I} \\ -\mathbf{I} & \mathbf{0} \end{bmatrix}$ and $\begin{bmatrix} \mathbf{0} & \mathbf{I} \\ \mathbf{K}_{RL} & \mathbf{K}_{RR} \end{bmatrix}^{T} \begin{bmatrix} \mathbf{0} & \mathbf{I} \\ -\mathbf{I} & \mathbf{0} \end{bmatrix}$ in turn gives

$$\left. \begin{aligned} & \begin{bmatrix} \mathbf{I} & \mathbf{0} \\ -\mathbf{K}_{LL} & -\mathbf{K}_{LR} \end{bmatrix}^{T} \begin{bmatrix} \mathbf{0} & \mathbf{I} \\ -\mathbf{I} & \mathbf{0} \end{bmatrix} \begin{bmatrix} \mathbf{0} & \mathbf{I} \\ \mathbf{K}_{RL} & \mathbf{K}_{RR} \end{bmatrix} \begin{bmatrix} \mathbf{D}(n-1) \\ \mathbf{D}(n) \end{bmatrix} \\ & = \lambda \begin{bmatrix} \mathbf{I} & \mathbf{0} \\ -\mathbf{K}_{LL} & -\mathbf{K}_{LR} \end{bmatrix}^{T} \begin{bmatrix} \mathbf{0} & \mathbf{I} \\ -\mathbf{I} & \mathbf{0} \end{bmatrix} \begin{bmatrix} \mathbf{I} & \mathbf{0} \\ -\mathbf{K}_{LL} & -\mathbf{K}_{LR} \end{bmatrix} \begin{bmatrix} \mathbf{D}(n-1) \\ \mathbf{D}(n) \end{bmatrix}, \end{aligned} \right\} \tag{1.27}$$

$$\left. \begin{aligned} & \begin{bmatrix} \mathbf{0} & \mathbf{I} \\ \mathbf{K}_{RL} & \mathbf{K}_{RR} \end{bmatrix}^{T} \begin{bmatrix} \mathbf{0} & \mathbf{I} \\ -\mathbf{I} & \mathbf{0} \end{bmatrix} \begin{bmatrix} \mathbf{I} & \mathbf{0} \\ -\mathbf{K}_{LL} & -\mathbf{K}_{LR} \end{bmatrix} \begin{bmatrix} \mathbf{D}(n-1) \\ \mathbf{D}(n) \end{bmatrix} \\ & = \lambda^{-1} \begin{bmatrix} \mathbf{0} & \mathbf{I} \\ \mathbf{K}_{RL} & \mathbf{K}_{RR} \end{bmatrix}^{T} \begin{bmatrix} \mathbf{0} & \mathbf{I} \\ -\mathbf{I} & \mathbf{0} \end{bmatrix} \begin{bmatrix} \mathbf{0} & \mathbf{I} \\ \mathbf{K}_{RL} & \mathbf{K}_{RR} \end{bmatrix} \begin{bmatrix} \mathbf{D}(n-1) \\ \mathbf{D}(n) \end{bmatrix}. \end{aligned} \right\} \tag{1.28}$$

The product of the three matrices on the left-hand side of equations (1.27) and (1.28) are

$$\left. \begin{aligned} & \begin{bmatrix} \mathbf{I} & \mathbf{0} \\ -\mathbf{K}_{LL} & -\mathbf{K}_{LR} \end{bmatrix}^{T} \begin{bmatrix} \mathbf{0} & \mathbf{I} \\ -\mathbf{I} & \mathbf{0} \end{bmatrix} \begin{bmatrix} \mathbf{0} & \mathbf{I} \\ \mathbf{K}_{RL} & \mathbf{K}_{RR} \end{bmatrix} = \begin{bmatrix} \mathbf{I} & -\mathbf{K}_{LL} \\ \mathbf{0} & -\mathbf{K}_{LR} \end{bmatrix} \begin{bmatrix} \mathbf{K}_{RL} & \mathbf{K}_{RR} \\ \mathbf{0} & -\mathbf{I} \end{bmatrix} \\ & \qquad\qquad = \begin{bmatrix} \mathbf{K}_{RL} & (\mathbf{K}_{LL} + \mathbf{K}_{RR}) \\ \mathbf{0} & \mathbf{K}_{RL} \end{bmatrix}, \end{aligned} \right\} \tag{1.29}$$

$$\begin{bmatrix} \mathbf{0} & \mathbf{I} \\ \mathbf{K}_{RL} & \mathbf{K}_{RR} \end{bmatrix}^{T} \begin{bmatrix} \mathbf{0} & \mathbf{I} \\ -\mathbf{I} & \mathbf{0} \end{bmatrix} \begin{bmatrix} \mathbf{I} & \mathbf{0} \\ -\mathbf{K}_{LL} & -\mathbf{K}_{LR} \end{bmatrix} = \begin{bmatrix} \mathbf{0} & \mathbf{K}_{LR} \\ \mathbf{I} & \mathbf{K}_{RR} \end{bmatrix} \begin{bmatrix} -\mathbf{K}_{LL} & -\mathbf{K}_{LR} \\ -\mathbf{I} & \mathbf{0} \end{bmatrix}$$
$$= \begin{bmatrix} -\mathbf{K}_{LR} & \mathbf{0} \\ -(\mathbf{K}_{LL} + \mathbf{K}_{RR}) & -\mathbf{K}_{LR} \end{bmatrix}, \quad (1.30)$$

respectively. Add the two and note the equality of equations (1.23) and (1.24) yields

$$\begin{bmatrix} \mathbf{K}_{RL} - \mathbf{K}_{LR} & \mathbf{K}_{LL} + \mathbf{K}_{RR} \\ -(\mathbf{K}_{LL} + \mathbf{K}_{RR}) & \mathbf{K}_{RL} - \mathbf{K}_{LR} \end{bmatrix} \begin{bmatrix} \mathbf{D}(n-1) \\ \mathbf{D}(n) \end{bmatrix}$$
$$= (\lambda + \lambda^{-1}) \begin{bmatrix} \mathbf{0} & -\mathbf{K}_{LR} \\ \mathbf{K}_{RL} & \mathbf{0} \end{bmatrix} \begin{bmatrix} \mathbf{D}(n-1) \\ \mathbf{D}(n) \end{bmatrix} \quad (1.31)$$

where both matrices are skew-symmetric. Re-write equation (1.31) in the standard eigenvalue problem gives

$$\left\{ \begin{bmatrix} \mathbf{0} & -\mathbf{K}_{LR} \\ \mathbf{K}_{RL} & \mathbf{0} \end{bmatrix}^{-1} \begin{bmatrix} \mathbf{K}_{RL} - \mathbf{K}_{LR} & \mathbf{K}_{LL} + \mathbf{K}_{RR} \\ -(\mathbf{K}_{LL} + \mathbf{K}_{RR}) & \mathbf{K}_{RL} - \mathbf{K}_{LR} \end{bmatrix} - \mu \mathbf{I} \right\} \begin{bmatrix} \mathbf{D}(n-1) \\ \mathbf{D}(n) \end{bmatrix} = \mathbf{0}, \quad (1.32)$$

where $\mu = \lambda + \lambda^{-1}$ which occurs twice. The original eigenvalues, λ and $1/\lambda$, can then be determined by solving the quadratic equation $\mu = \lambda + 1/\lambda$. In the case of complex unity eigenvalues, $\lambda = e^{i\varphi}$, the quadratic equation can be expressed as a trigonometric function, i.e. $\mu = e^{i\varphi} + e^{-i\varphi} = 2\cos(\varphi)$. Let $\begin{bmatrix} \mathbf{D}^{T}(n-1) & \mathbf{D}^{T}(n) \end{bmatrix}_{1}^{T}$ and $\begin{bmatrix} \mathbf{D}^{T}(n-1) & \mathbf{D}^{T}(n) \end{bmatrix}_{2}^{T}$ be the eigenvectors associated with the repeated eigenvalues μ_{1} and μ_{2} where $\mu_{1} = \mu_{2}$. The original eigenvector $\begin{bmatrix} \mathbf{D}^{T}(n-1) & \mathbf{D}^{T}(n) \end{bmatrix}_{\lambda_{1}}^{T}$ associated with eigenvalue λ_{1} can be expressed as

$$\begin{bmatrix} \mathbf{D}(n-1) \\ \mathbf{D}(n) \end{bmatrix}_{\lambda_{1}} = \alpha_{1} \begin{bmatrix} \mathbf{D}(n-1) \\ \mathbf{D}(n) \end{bmatrix}_{1} + \alpha_{2} \begin{bmatrix} \mathbf{D}(n-1) \\ \mathbf{D}(n) \end{bmatrix}_{2}$$
$$= \begin{bmatrix} \begin{bmatrix} \mathbf{D}(n-1) \\ \mathbf{D}(n) \end{bmatrix}_{1} & \begin{bmatrix} \mathbf{D}(n-1) \\ \mathbf{D}(n) \end{bmatrix}_{2} \end{bmatrix} \begin{bmatrix} \alpha_{1} \\ \alpha_{2} \end{bmatrix}, \quad (1.33)$$

where α_{1} and α_{2} are scalars. Substitute equation (1.33) into equation (1.27) gives

$$\mathbf{A} \begin{bmatrix} \alpha_{1} \\ \alpha_{2} \end{bmatrix} = \mathbf{0} \quad (1.34)$$

where

$$\mathbf{A} = \begin{bmatrix} \mathbf{K}_{RL} & (\mathbf{K}_{LL} + \mathbf{K}_{RR}) + \lambda_{1} \mathbf{K}_{LR} \\ -\lambda_{1} \mathbf{K}_{RL} & \mathbf{K}_{RL} \end{bmatrix} \begin{bmatrix} \begin{bmatrix} \mathbf{D}(n-1) \\ \mathbf{D}(n) \end{bmatrix}_{1} & \begin{bmatrix} \mathbf{D}(n-1) \\ \mathbf{D}(n) \end{bmatrix}_{2} \end{bmatrix}. \quad (1.35)$$

Take singular value decomposition of $\mathbf{A}$, i.e. $\mathbf{A} = \mathbf{USV}^*$ where $\mathbf{U}$ is an $(n \times n)$ matrix, $\mathbf{S}$ is $(n \times 2)$ matrix of two singular values on its leading diagonal, one of these is almost zero, and $\mathbf{V} = \begin{bmatrix} v_{11} & v_{12} \\ v_{12} & -v_{11} \end{bmatrix}$. Note that $\mathbf{V}$ satisfies $\mathbf{V} = \mathbf{V}^* = \mathbf{V}^{-1}$. One can then write

$$\mathbf{A}\begin{bmatrix} v_{11} & v_{12} \\ v_{12} & -v_{11} \end{bmatrix} = \mathbf{U}\begin{bmatrix} S_1 & 0 \\ 0 & S_2 \approx 0 \\ \vdots & \vdots \\ 0 & 0 \end{bmatrix}. \tag{1.36}$$

Consider the second column of equation (1.36), one can write

$$\begin{bmatrix} \mathbf{K}_{RL} & (\mathbf{K}_{LL} + \mathbf{K}_{RR}) + \lambda_1 \mathbf{K}_{LR} \\ -\lambda_1 \mathbf{K}_{RL} & \mathbf{K}_{RL} \end{bmatrix} \begin{bmatrix} \begin{bmatrix} \mathbf{D}(n-1) \\ \mathbf{D}(n) \end{bmatrix}_1 & \begin{bmatrix} \mathbf{D}(n-1) \\ \mathbf{D}(n) \end{bmatrix}_2 \end{bmatrix} \begin{bmatrix} v_{12} \\ -v_{11} \end{bmatrix} \approx \mathbf{0} \tag{1.37}$$

which is (approximately) in the same form as equation (1.34). By comparison, one can deduce that

$$\frac{\alpha_2}{\alpha_1} = -\frac{v_{11}}{v_{12}}. \tag{1.38}$$

Zhong and Williams [40] re-cast $\mathbf{Gs}(n) = \lambda \mathbf{s}(n)$, where $\mathbf{G}$ is given by equation (1.10) and $\mathbf{s}(n) = \begin{bmatrix} \mathbf{D}^{\mathrm{T}}(n) & \mathbf{F}^{\mathrm{T}}(n) \end{bmatrix}^{\mathrm{T}}$, into equation (1.26), which is a transfer representation in terms of displacement vector alone, to avoid ill-conditioning. In this approach, the transfer matrix is decomposed into two matrices, each is found to have properties of a symplectic matrix. Further review on numerical stability and properties of symplectic matrix will be presented in Section 1.26 and Chapter 2, respectively.

To sum up, transfer matrix typically relates a state vector of displacement and force components on either side of the repeated cell; this matrix form is called displacement-force transfer matrix. A different form of transfer matrix relates a state vector of displacements at two consecutive cross-sections, $(n-1)$th and nth, with nth and $(n+1)$th cross-sections; this form is called displacement-displacement transfer matrix. An eigenvector of the transfer matrix describes a pattern of the state vector components which is unique to within a scalar multiplier λ. Application of the Bloch's theorem, which is a formalism of harmonic motion through translationally symmetric structure, demands that this (eigenvector) pattern is preserved as one moves from the left- to the right-hand sides of the cell or from $(n-1)$th to nth cross-sections. This leads to an eigenvalue problem for propagation constants λ. The

eigenvalues and eigenvectors can be evaluated numerically by employing MATLAB's eig function.

Analysis and treatment of Bloch's theorem for geometrically complex repetitive structures are presented in more recent publications. In [41], Farzbod and Leamy addressed the issues associated with elimination of internal forces when degrees of freedom in a unit cell are reduced. They showed that for two- and three-dimensional lattices, the internal forces are eliminated. Further analysis on the theorem shows that linearity of the system is also required for invoking the existence of a propagation constant; imposing the latter in a nonlinear system could lead to violation of energy conservation [42]. Application of Bloch wave expansion (BWE) method to complex geometry such as phononic crystals are presented by Kulpe *et al.* [43–46]. In [43], FEM is first used to formulate the dispersion relation of a two-dimensional phononic crystal before the BWE is implemented to study the wave transmission and reflection in the crystal. The method requires a selection of suitable Bloch waves (based on group velocity criterion) for the pressure (and velocity) field expansion at a prescribed frequency and incident angle. In [44], BWE are employed along with the Helmholtz-Kirchhoff integral theorem to determine external acoustic scattering from a two-dimensional finite phononic crystal. The Helmholtz-Kirchhoff integral theorem is applied to account for any loss in the field. The results obtained from the studies [43,44] are verified against FEM simulations. It is noted that the BWE method consumed less computation time than the FEM. The method developed in [44] is then extended to three dimensions: first on a cubic [45], and later on a spherical and a bean-shaped phononic crystals [46]. The results obtained in [45,46] are compared with an existing self-consistent scattering technique.

In the case of mass-spring chain described earlier in Section 1.2.1, application of Bloch's theorem gives

$$
\begin{bmatrix} d(n) \\ f(n) \end{bmatrix} = \lambda \begin{bmatrix} d(n-1) \\ f(n-1) \end{bmatrix}, \tag{1.39}
$$

$$
\begin{bmatrix} d(n) \\ d(n+1) \end{bmatrix} = \lambda \begin{bmatrix} d(n-1) \\ d(n) \end{bmatrix}. \tag{1.40}
$$

Substract equations (1.39) and (1.40) from equations (1.4) and (1.7), respectively, leads to the standard eigenvalue problems

$$\begin{bmatrix} 1 - \dfrac{\omega^2}{2\omega_n^2} - \lambda & \dfrac{1}{k} \\[2ex] k\left[\left(1 - \dfrac{\omega^2}{2\omega_n^2}\right)^2 - 1\right] & 1 - \dfrac{m\omega^2}{2\omega_n^2} - \lambda \end{bmatrix} \begin{bmatrix} d(n-1) \\ f(n-1) \end{bmatrix} = 0 \,, \tag{1.41}$$

$$\begin{bmatrix} -\lambda & 1 \\[1ex] -1 & 2k\left(1 - \dfrac{\omega^2}{2\omega_n^2}\right) - \lambda \end{bmatrix} \begin{bmatrix} d(n-1) \\ d(n) \end{bmatrix} = 0 \,. \tag{1.42}$$

It can be verified numerically using MATLAB's eig command that the two forms of transfer matrix share the same eigenvalues which implies that there is a possibility that the displacement-force and displacement-displacement transfer matrices are similar. The similarity relations between the two matrices are studied and presented in Chapter 2.

1.2.3 Participation coefficients

Displacement-force transfer matrix $\mathbf{G}$ relates the state-vectors at two-succeeding sections, n and $(n+1)$, as $\mathbf{s}(n+1) = \mathbf{G}\mathbf{s}(n)$. For the static problem, the state vectors $\mathbf{s}(n)$ and $\mathbf{s}(n+1)$ can be expressed as a linear combinations $\mathbf{s}(n) = \mathbf{T}\mathbf{C}_n$ and $\mathbf{s}(n+1) = \mathbf{T}\mathbf{C}_{n+1}$ where $\mathbf{T}$ is the transformation matrix of eigen- and principal vectors, $\mathbf{C}_n$ is the column vector of participation coefficients at section n [12,39]. The matrix $\mathbf{T}$ transforms $\mathbf{G}$ to its Jordan canonical form $\mathbf{J}$ according to $\mathbf{T}^{-1}\mathbf{G}\mathbf{T} = \mathbf{J}$, or $\mathbf{G} = \mathbf{T}\mathbf{J}\mathbf{T}^{-1}$; powers of $\mathbf{G}$ are then $\mathbf{G}^n = \mathbf{T}\mathbf{J}^n\mathbf{T}^{-1}$. Substituting into $\mathbf{s}(n+1) = \mathbf{G}\mathbf{s}(n)$ gives $\mathbf{T}\mathbf{C}_{n+1} = \left(\mathbf{T}\mathbf{J}\mathbf{T}^{-1}\right)\left(\mathbf{T}\mathbf{C}_n\right)$ which simplifies to $\mathbf{T}\mathbf{C}_{n+1} = \mathbf{T}\mathbf{J}\mathbf{C}_n$, and pre-multiplying by $\mathbf{T}^{-1}$ gives $\mathbf{C}_{n+1} = \mathbf{J}\mathbf{C}_n$. This represents the simplest possible description of spatial evolution as one move from one section to the other section.

Similarly, for the dynamic problem, the state vectors $\mathbf{s}(n)$ and $\mathbf{s}(n+1)$ can be expressed as a linear combinations $\mathbf{s}(n) = \mathbf{V}\mathbf{w}_n$ and $\mathbf{s}(n+1) = \mathbf{V}\mathbf{w}_{n+1}$ where $\mathbf{V}$ is the eigenvector matrix of transfer matrix $\mathbf{G}$, $\mathbf{w}_n$ is better known as wave (amplitudes) vector at section n [47,48]. The matrix $\mathbf{V}$ diagonalise matrix $\mathbf{G}$ according to $\mathbf{V}^{-1}\mathbf{G}\mathbf{V} = \boldsymbol{\Lambda}$, or $\mathbf{G} = \mathbf{V}\boldsymbol{\Lambda}\mathbf{V}^{-1}$; powers of $\mathbf{G}$ are then $\mathbf{G}^n = \mathbf{V}\boldsymbol{\Lambda}^n\mathbf{V}^{-1}$. Substituting into $\mathbf{s}(n+1) = \mathbf{G}\mathbf{s}(n)$ gives $\mathbf{V}\mathbf{w}_{n+1} = \left(\mathbf{V}\boldsymbol{\Lambda}\mathbf{V}^{-1}\right)\left(\mathbf{V}\mathbf{w}_n\right)$ which simplifies to $\mathbf{V}\mathbf{w}_{n+1} = \mathbf{V}\boldsymbol{\Lambda}\mathbf{w}_n$, and pre-multiplying by $\mathbf{V}^{-1}$ gives $\mathbf{w}_{n+1} = \boldsymbol{\Lambda}\mathbf{w}_n$. This also represents the simplest possible description of spatial evolution

as one move from one section to the other section. Equivalent expressions derived from displacement-displacement transfer matrix have not been found.

Clearly, the two formulations are closely related; the participation coefficient under static case is simply the wave amplitude under dynamic case. However, the two formulations are found to be employed differently: in the static case the formulation is used to solve two point boundary value problem (TPBVP), while in the dynamic case the formulation is used in the implementation of the phase closure principle to find the natural frequencies. Hence, it would be interesting to find out whether the phase closure principle is actually employable to solve the TPBVP.

1.2.4   Transfer matrix method and Saint-Venant's principle

The transfer matrix method is well developed for the dynamic problems but less so for static problems. And, within the scope of the dynamic problems, there are generally more reports on the propagating waves compared with the decaying waves. Therefore, this thesis intends to contribute in the research of static problem and decaying waves.

Stephen and his co-workers have contributed extensively on the static analysis of repetitive structures; these include transfer matrix analysis of one-dimensional pin-jointed frameworks [1,12], eigenanalysis and continuum modelling of beam-like structures [7,13,14,37] and Riccati transfer matrix method[5] for solving beam-like structures subjected to different static loads [49]. For one-dimensional static problems, they have shown that non-unity eigenvalues of the transfer matrix describe the decay of self-equilibrated end loading, as anticipated by Saint-Venant's principle (SVP). Multiple unity eigenvalues pertain to transmitting loads such as tension, bending moment and shear, together with rigid body displacements and rotations.

Extension of the SVP to the dynamic problems of repetitive structure has not been considered. This is not a surprise considering validity of the dynamic SVP is still debated [50]. The proponents of the idea have proposed different approaches to characterise dynamic SVP quantitatively. Berdichevsky and Foster [51] proposed a "probabilistic approach" whereby the unknown self-equilibrating load is assigned with probabilistic load model and probabilistic characteristic of the penetrating stress state is then determined. On the other

---

[5] Riccati transformation takes the form $\mathbf{F}(n) = \mathbf{R}(n)\mathbf{d}(n) + \mathbf{g}(n)$ where $\mathbf{R}$ is the Riccati matrix and $\mathbf{g}$ is a column vector of force components. Further details are given in Chapter 5.

hand, Karp [52] presented an analytical approach and consider SVP under symmetric dynamic fields for an elastic strip. Karp replaced the requirement of spatial decay due to application of self-equilibrated loads with the application of dynamic loads having zero average power. In this thesis, dynamic SVP is seen to manifest in the form of decaying waves. Therefore, the characteristic of decaying (and propagating) waves in one-dimensional repetitive structure are studied in detail.

Kaplunov and his co-workers [53,54] have proposed a rational approach in developing dynamic analogues of the SVP; they considered the plane problem for an elastic semi-infinite strip subjected to harmonic end stresses in the low and high frequency domains. The consideration is motivated by the derivation of refined boundary conditions in the dynamical problems of plates and shells [55]. In the low frequency domain, decay conditions for the end stresses are derived [53]. The conditions represent a perturbation in frequency of the well-known decay conditions of the classical SVP. The Laplace transform and residue theorem are employed in the formulation; the residues associated with small roots of the symmetric and antisymmetric Rayleigh-Lamb equations [56] are investigated and resulted in the asymptotic decay conditions which involve quadratic terms in frequency. In the high frequency domain, so-called radiation conditions on the end data are established [54]. The proposed conditions allow long wave modes near thickness resonance frequencies and are used to construct boundary conditions of high frequency long wave vibrations that represent an analogue to the classical low frequency plate theories.

1.2.5   Properties of the transfer matrix and the dispersion diagram

In dynamic analysis, the displacement-force transfer matrix is symplectic [57]; therefore, it has the properties of a symplectic matrix, one of which is its eigenvalues occur as reciprocal pairs. In turn, its determinant is equal to +1. The eigenvector associated with the reciprocal eigenvalue is called its adjoint eigenvector. Application of symplectic mathematics in the study of wave problems for repetitive structures is largely due to Zhong and Williams [40,57,58]. In [57], they stated that an eigenvector associated with an eigenvalue is symplectic orthogonal to all other eigenvectors including itself but not its adjoint. They further showed that symplectic orthogonality relation between eigenvectors of symplectic transfer matrix corresponds to a Betti reciprocal theorem [58]. Since an eigenvector and its adjoint is not symplectic orthogonal, they normalised the adjoint symplectic relation; this step could result in a loss of information in form of Krein signature. Stephen [1] extended the symplectic mathematics to static analysis of one-dimensional repetitive structures. In

[1] and [12], Stephen also derived a bi-orthogonality relation between right eigenvectors of the displacement-force transfer matrix and its transpose. It is noted that properties of displacement-displacement transfer matrix is not yet presented. Apart from that, the case of repeating eigenvalues in the symplectic analysis has not been considered.

The computed eigenvalues λ can be real and complex. Typically, λ is expressed as $\exp(\mu)$ where $\mu = \delta + i\varphi$ is known as propagation constant, while δ and φ is known as decay and phase (change) constants, respectively [18,59]. Decay constant, or decay rate, is a factor by which the amplitude is reduced (or amplified) as one move from one section to the next; positive and negative decay rate corresponds to leftward and rightward decay, respectively. Meanwhile, the phase constant is a factor by which the phase of the amplitude changes as one move from one section to the next. The phase constant is intimately related to the wavenumber whereby the latter is equal to the phase constant divided with the length of a unit cell, i.e.

$$\text{wavenumber} = \frac{2\pi}{\text{wavelength}} = \frac{\text{phase constant}}{\text{length of a unit cell}}. \tag{1.43}$$

If the length of a unit cell is one unit, then the phase constant is effectively equal in magnitude to the wavenumber.

Alternatively, complex wavenumber notation can be adopted [60], that is to express λ as $\exp(-i\mu)$ where $\mu = \varphi - i\delta$. In this notation, the real and imaginary parts of μ represent the phase constant φ and the decay rate δ, respectively. The directions of wave motion associated with the signs of φ and δ are also reversed: now, the positive and negative values of the parameters correspond to rightward and leftward motion, respectively.

For simple structures such as the mass-spring chain, the eigenvalues of the transfer matrix can be found analytically. For the chain, the eigenvalues are found by solving the determinantal equation

$$\begin{vmatrix} \left(1 - \dfrac{\omega^2}{2\omega_n^2}\right) - \lambda & \dfrac{1}{k} \\ k\left[\left(1 - \dfrac{\omega^2}{2\omega_n^2}\right) - 1\right] & \left(1 - \dfrac{\omega^2}{2\omega_n^2}\right) - \lambda \end{vmatrix} = 0, \tag{1.44}$$

which upon expansion and re-arrangement leads to

$$\lambda^2 - 2\left(1 - \frac{\omega^2}{2\omega_n^2}\right)\lambda + 1 = 0, \tag{1.45}$$

whose solutions are

$$\lambda = \left(1 - \frac{\omega^2}{2\omega_n^2}\right) \pm \sqrt{\left(1 - \frac{\omega^2}{2\omega_n^2}\right)^2 - 1} \; . \tag{1.46}$$

For $0 < \omega/\omega_n < 2$, μ is purely imaginary, i.e. $\lambda = e^{\pm i\varphi}$. For $\omega/\omega_n > 2$, λ is real (and negative). Alternatively, the dispersion relation can be found from equation (1.5), i.e.

$$\left[2k - m\omega^2\right]d(n) - kd(n+1) - kd(n-1) = 0 \; . \tag{1.47}$$

Divide all terms by k and noting that $\omega_n^2 = k/m$, equation (1.47) becomes

$$\left[2 - \omega^2/\omega_n^2\right]d(n) - d(n+1) - d(n-1) = 0 \; . \tag{1.48}$$

But we can write $d(n+1) = \lambda d(n)$ and $d(n-1) = \lambda^{-1} d(n)$, which upon substitution into equation (1.48) gives

$$\left\{2 - \omega^2/\omega_n^2 - \left[\lambda + \lambda^{-1}\right]\right\}d(n) = 0 \; .$$

Write $\lambda = e^{\mu}$ (where $\mu = \delta + i\varphi$) and note that $2\cosh\mu = e^{\mu} + e^{-\mu}$, we get

$$\left\{2 - \omega^2/\omega_n^2 - 2\cosh\mu\right\}d(n) = 0 \; . \tag{1.49}$$

For a non-trivial solution,

$$2 - \omega^2/\omega_n^2 - 2\cosh\mu = 0 \; , \tag{1.50}$$

which gives

$$\mu = \cosh^{-1}\left(1 - \frac{\omega^2}{2\omega_n^2}\right) \; . \tag{1.51}$$

It is possible to relate back equation (1.51) with equation (1.46) using the inverse hyperbolic function formula $\cosh^{-1} x = \ln\left(x + \sqrt{x^2 - 1}\right)$ for $x \geq 1$.

The plot of frequency against decay and phase constants is known as dispersion diagram, or frequency spectra. Despite the fact that three variables are involved in the plot, the diagram is typically drawn in two dimensions with two y-axes, each for the decay and phase constants, against frequency on the x-axis [59,61,62]. For example, the dispersion diagram for the mass-spring chain is shown in Figure 1.4(a) where all the δ and φ values are plotted against the normalised frequency within the frequency range $0 < \omega/\omega_n < 4$. Wave propagation occurs from $\omega/\omega_n = 0$ up to the cut-off frequency $\omega/\omega_n = 2$, after which the wave decays rapidly. Note that for $2 < \omega/\omega_n < 4$, the eigenvalues take the form $+\delta + i\pi$

and $-\delta - i\pi$, hence the imaginary part appears as straight vertical lines. Alternatively, the dispersion diagram can be represented compactly as in Figure 1.4(b) whereby the *x*- and *y*-axes are exchanged and only the positive half of Figure 1.4(a) is shown in order to exploit its symmetry; we find that the layout in Figure 1.4(b) is more commonly adopted. The phase constant is usually normalised with respect to π; the vertical straight line ($\varphi = \pi$) shown bold in Figure 1.4(a) now becomes the bold horizontal line $\varphi/\pi = 1$ in Figure 1.4(b) and would be plotted on the border of the diagram and would not be apparent. Evidently, the two-dimensional plotting layouts are unable to represent the dispersion diagram accurately and succinctly. It is foreseeable that more inaccuracies will occur when this layout is used to represent the dispersion curves of more complex structures. Therefore, in this thesis, we seek to find a better representation for the dispersion diagram.

In the analysis of two-dimensional (plate-like) repetitive structures, the phase constants in two axial directions are plotted against the frequency; therefore, the plots form dispersion surfaces (rather than curves) [59] and the dispersion diagram is presented in three-dimensions. It is noted that in the field of dynamic system stability, both two- and three-dimensional plot of dispersion relation is widely used [63] (chapter 1, page 4). We believe that the three-dimensional layout could also be used to represent dispersion curves of one-dimensional system.

We expect that one-dimensional repetitive structures with multiple couplings will give multiple eigencurves on the dispersion diagram; each is identifiable to a particular wave mode. The next issue is on how to label them properly. In [64], Miklowitz presented the dispersion diagram of axially symmetric waves in an infinite circular rod in three dimensions; each curve is labelled sequentially based on which mode propagates through the structure first, as the frequency is increased. When two dispersion curves merge, the combined segment of the curves is labelled using two figures, each correspond to the original curves. Individual and merged curves are plotted with continuous and dashed line, respectively. The notation used in the diagram is adopted in this thesis, and modified accordingly to clearly represent the dispersion diagram of our model structure.
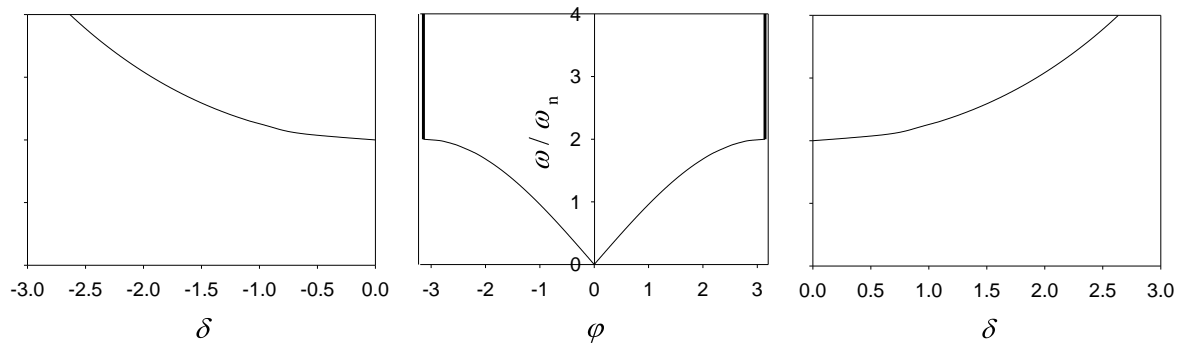
(a)
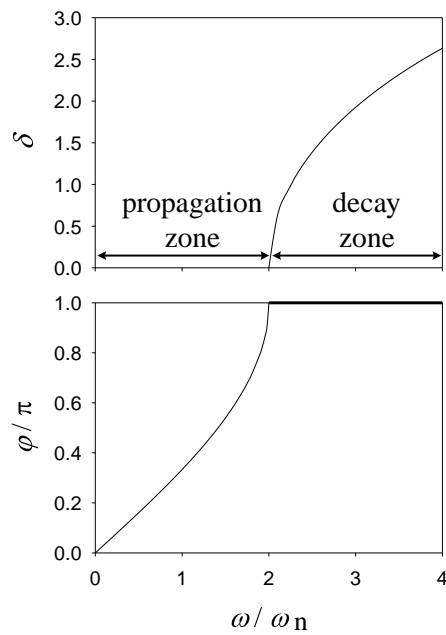
(b)

Figure 1.4 Dispersion diagram of an infinite mass-spring chain. (a) Normalised frequency is plotted against phase and decay constants, φ and δ , respectively.   (b) Normalised phase and decay constants against normalised frequency. Only the positive half of the dispersion relation is shown.

The frequencies at which a mode starts and stops propagating through the structure are usually called cut-off frequencies; some authors refer to them as low and high cut-off frequencies, respectively, in order to distinguish the two based on their relative magnitudes [65]. However, we found that two propagating modes could interact and stop propagating over a certain frequency range before begin to propagate again; the frequencies at which

these happen are again called cut-off frequencies. It appears that there is a need to provide clear definition for the term cut-off and cut-on frequencies so that the different phenomena can be properly described.

1.2.6   Numerical issues

Implementation of transfer matrix method is susceptible to numerical instabilities. One of the early numerical issues encountered is in computing the chain product of the transfer matrix. According to Mester and Benaroya [5], multiplication of many matrices can lead to significant roundoff errors.

Also, the eigenvector of the transfer matrix is usually ill-conditioned because the eigenvectors are expressed in terms of displacement and force components, whose values can largely differ in magnitude [66]. Zhong and Williams [40] regarded the ill-conditioning problem is embedded in the construction of the transfer matrix itself through the inversion of $\mathbf{K}_{LR}$ partition of the stiffness matrix of a single cell, see equation (1.10). Detail inspection of the transfer matrix reveals that the ill-conditioning problem arises because a typical element of the stiffness matrix (of a pin-jointed structure) is proportional to EA/L where E is the Young's modulus, A is the cross-sectional area and L is the length. The Young's modulus is typically large, e.g. $E = 200 \times 10^3$ N/mm^2; in turn, inversion of a partition of the matrix leads to ill-conditioning with the transfer matrix reportedly having a large condition number [39].

In order to avoid such numerical ill-conditioning, Zhong and Williams [40] decomposed the transfer matrix so that the matrix is expressed in terms of displacement components only. The decompositions employ equations (1.20) and (1.21) as follows: the displacement and force on the left- and right-hand side of a cell are

$$\begin{bmatrix} \mathbf{D}_L \\ \mathbf{F}_L \end{bmatrix} = \begin{bmatrix} \mathbf{I} & \mathbf{0} \\ -\mathbf{K}_{LL} & -\mathbf{K}_{LR} \end{bmatrix} \begin{bmatrix} \mathbf{D}_L \\ \mathbf{D}_R \end{bmatrix} = \mathbf{L} \begin{bmatrix} \mathbf{D}_L \\ \mathbf{D}_R \end{bmatrix}, \tag{1.52}$$

$$\begin{bmatrix} \mathbf{D}_R \\ \mathbf{F}_R \end{bmatrix} = \begin{bmatrix} \mathbf{0} & \mathbf{I} \\ \mathbf{K}_{RL} & \mathbf{K}_{RR} \end{bmatrix} \begin{bmatrix} \mathbf{D}_L \\ \mathbf{D}_R \end{bmatrix} = \mathbf{N} \begin{bmatrix} \mathbf{D}_L \\ \mathbf{D}_R \end{bmatrix}. \tag{1.53}$$

Clearly, one can write

$$\begin{bmatrix} \mathbf{D}_R \\ \mathbf{F}_R \end{bmatrix} = \mathbf{N}\mathbf{L}^{-1} \begin{bmatrix} \mathbf{D}_L \\ \mathbf{F}_L \end{bmatrix}, \tag{1.54}$$

and employing Bloch's theorem, gives

$$\begin{bmatrix} \mathbf{D}_R \\ \mathbf{F}_R \end{bmatrix} = \lambda \begin{bmatrix} \mathbf{D}_L \\ \mathbf{F}_L \end{bmatrix}. \tag{1.55}$$

Using such decomposition, one can also write equation (1.26) as

$$\mathbf{N} \begin{bmatrix} \mathbf{D}_L \\ \mathbf{D}_R \end{bmatrix} = \lambda \mathbf{L} \begin{bmatrix} \mathbf{D}_L \\ \mathbf{D}_R \end{bmatrix}. \tag{1.56}$$

Similar decomposition scheme is employed by Mencik [66].

On the other hand, Stephen [39] easily resolved the ill-conditioning problem by reducing the order of Young's modulus E in the computation; for example, instead of setting $E = 200 \times 10^3$ N/mm^2, E is set to 2 N/mm^2. This effectively reduces the transfer matrix condition number. Consequently, the displacement components of the normalised eigenvector as computed by MATLAB need to be scaled accordingly.

Another form of numerical difficulties is exponentiation of the transfer matrix or eigenvalues greater than unity which will magnify any error and render the method wholly inaccurate. For example, when a tip-loaded cantilever is to be analysed, one has a two-point boundary value problem [49]. The force at the tip and the displacement at the fixed root will be known, while the displacement at the tip and the reaction force at the root are unknowns. Such problems are typically ill-conditioned [67]. In [39], the analysis of cantilevered ten-cell repetitive pin-jointed structure subjected to tip-loading, and to distributed loading with an intermediate support, was described. The need to construct powers of the transfer matrix is observed to be the source of the ill-conditioning. This becomes abundantly clear when the state-vector of displacement and force components is expressed in terms of the participation coefficients of the eigen- and principal vectors, and spatial evolution is expressed in terms of powers of the Jordan canonical form, as described in Section 1.2.3. It is reported in [39] that a participation coefficient can increase by a factor of the order 10^{12} for the largest eigenvalue over ten cells of the framework. If the number of cells is increased to 50, the factor is increased to the order 10^{61}. Metaphorically, while SVP is physically applicable, it is not numerically stable in such formulation.

One possible approach to the problem is to employ equivalent continuum properties derived from the eigen- and principal vectors of a single cell [37]. Alternatively, one can employ Riccati transformation to produce a numerically reliable formulation [49]. Xue [68–70] has combined the finite element-transfer matrix method and Riccati transform to analyse transient dynamic response and to determine the natural frequencies of trusses. The Riccati transfer matrix method is numerically reliable because the eigenvalues of particular terms in

the recursive relationships are equal to or less than unity [49]. Again, metaphorically, SVP is now both physically and numerically applicable. Despite its evident numerical stability, its use is by no means widespread. A disadvantage of this method is it requires recursive computation of unknown vectors which can be a programming issue for very long structures.

The wave vector approach [48] is another formulation that can overcome numerical difficulties arising from exponentiation of the transfer matrix. The approach describes right-going and left-going spatial evolution of state vector in terms of wave amplitudes and eigenvalues equal to or less than unity. The approach has two advantages: first, it is inherently stable because eigenvalues greater than unity are avoided in its formulation; second, the size of the problem is reduced to half of the transfer matrix. In [47], Signorelli and von Flotow employed the approach and applied phase closure principle to find the natural frequencies of a cantilever truss. However, they reported numerical difficulty when solving the resulting characteristic determinantal equation. The absolute value of the complex determinant is plotted against frequency and the natural frequencies of the truss are identified whenever the absolute value vanishes. The numerical difficulties lie on the failure of the approach to identify closely spaced natural frequencies, even with smaller frequency step. They attributed the failure to error introduced during eigenvalue/eigenvector calculation. In addition, another plot of power flow against frequency shows 'noisy' power within the stop bands, with complex[6] modes appearing to transmit power many orders of magnitude greater than the pure stop[7] bands. They suspected that the erroneous apparent power flow in the stop bands is an artifact of finite-precision arithmetic, indicating possible numerical round-off errors in the eigenvector computation.

Luongo and Romeo [71] identified that the numerical difficulties in the wave vector approach are due to the ill-posed formulation of the problem—natural frequencies are found as real solutions to complex characteristic equations. They proposed a modified version of the traditional wave vector computational scheme; the modified version retains the advantages of wave transfer matrix and deals with real quantities only. Unlike the traditional scheme which requires transformation of frequency-dependent real transfer matrix for state vectors to complex transfer matrix for wave vectors, their modified version provides for transformation to real matrices. In a private communication, Romeo pointed out that the scheme has not been implemented on repetitive structures with multiple couplings.

---

[6] Wave modes associated with complex non-unity eigenvalues.
[7] Wave modes associated with real non-unity eigenvalues.

Numerical issues concerning the wave and finite element (WFE) method for vibrations of waveguides are presented by Waki *et al.* [15]. The WFE method starts from FE model of the repeating substructure, typically by using existing element libraries and commercial FE packages. Once the dynamic stiffness matrix is obtained, the matrix is partitioned and re-arranged into the transfer matrix form; then, the Bloch's theorem is applied to get the eigenvalue problem whose solution gives the dispersion relation (i.e. eigenvalues against frequency) and wave mode shapes (i.e. eigenvectors). In [15], three major issues concerning the method are presented, namely,

(a) *Discretisation errors* which occur if the modelled substructure (or cell) is too large compared to the wavelength.

(b) *Round-off errors* which occur if the modelled cell is too small. When $\mathbf{K} - \omega^2 \mathbf{m}$ is calculated numerically, particular element in $\mathbf{K}$, say $\mathbf{K}_{ij}$, becomes very large compared to $\omega^2 \mathbf{m}_{ij}$, so some digits associated with the inertia term in $\mathbf{K}_{ij} - \omega^2 \mathbf{m}_{ij}$ are truncated after the substraction leading to round-off errors.

(c) *Ill-conditioning* which arise because the eigenproblem may have both very large and very small eigenvalues. As explained earlier, $\mathbf{K}_{LR}$ can be poorly conditioned, so determining its inverse is prone to ill-conditioning.

Issue (a) can be overcomed by re-meshing the structure using a shorter cell; the rule-of-thumb is there should be at least six cells per wavelength. Issue (b) can be reduced by re-meshing the structure with a longer cell, or by concatenating a number of original cells to form a super-cell, the internal DOFs are then condensed. Since the resolution to issues (a) and (b) are conflicting, a compromised must be reached, i.e. the cell length should be carefully determined when the structure is modelled. Solutions to issue (c) have been addressed earlier.

1.2.7   Transfer matrix analysis of wave energetics in undamped one-dimensional repetitive structures

Analysis of the work done by static load on one-dimensional undamped repetitive structure is presented by Stephen [1] who showed that eigenvectors associated with $\lambda = \pm 1$ do no work by considering the total work done W on the left- and right-hand boundaries of a unit cell, i.e.

$$W = -\frac{1}{2}\mathbf{D}_{\mathrm{L}}^{\mathrm{T}}\mathbf{F}_{\mathrm{L}} + \frac{1}{2}\mathbf{D}_{\mathrm{R}}^{\mathrm{T}}\mathbf{F}_{\mathrm{R}} = \frac{1}{2}\mathbf{D}_{\mathrm{L}}^{\mathrm{T}}\mathbf{F}_{\mathrm{L}}\left(\lambda^2 - 1\right),\qquad(1.57)$$

where $\mathbf{D}_{\mathrm{L}}$ and $\mathbf{F}_{\mathrm{L}}$ are displacement and force vectors, respectively, on the left-hand side of the cell. This agrees with the fact that eigenvectors associated with $\lambda = 1$ are rigid body translations and rotation. Stephen [1] also showed that the principal vector $\mathbf{F}_{\mathrm{L}}^{\mathrm{P}}$ (e.g. tension) does work, which is stored in the structure as strain energy. The work done by the principal vector is simply $W = \frac{1}{2}\mathbf{D}_{\mathrm{L}}^{\mathrm{T}}\mathbf{F}_{\mathrm{L}}^{\mathrm{P}}$.

The energetics of the different wave types under dynamic case are discussed by Mead [18] using the energy and power equations which are derived in terms of (partitions of) the receptance matrix. It is shown that the energy is propagated through the structure by the propagating waves. As the nodal force and displacement are always perpendicular, there is no work done. The time-averaged kinetic and strain energies are known to be equal. On the other hand, Langley [72] expressed the time-averaged kinetic energy as

$$E_{\mathrm{K}} = -\frac{1}{8}\omega\mathbf{V}_{\mathrm{L}}^{*}\left[\mathbf{G}^{*}\mathbf{J}\frac{\partial\mathbf{G}}{\partial\omega}\right]\mathbf{V}_{\mathrm{L}}\qquad(1.58)$$

where $\mathbf{G}$ is the transfer matrix, $\partial\mathbf{G}/\partial\omega$ is the rate of change of the transfer matrix with respect to frequency, $\mathbf{V}_{\mathrm{L}}$ is the eigenvector of $\mathbf{G}$ pertaining to the left-hand side of the cell and $\mathbf{V}_{\mathrm{L}}^{*}$ is the transposed conjugate of $\mathbf{V}_{\mathrm{L}}$. The expression shows that the mean kinetic energy stored at the frequency ω depends on the transfer matrix and on the rate of change of the transfer matrix with respect to frequency. Langley [72] also showed that the time-averaged kinetic energy of a conservative system can be expressed as

$$E_{\mathrm{K}} = \frac{1}{8}\omega\mathbf{D}^{*}\frac{\partial\left(\mathbf{K} - \omega^2\mathbf{m}\right)}{\partial\omega}\mathbf{D}\qquad(1.59)$$

where $\mathbf{D} = \begin{bmatrix}\mathbf{D}_{\mathrm{L}}^{\mathrm{T}} & \mathbf{D}_{\mathrm{R}}^{\mathrm{T}}\end{bmatrix}^{\mathrm{T}}$ and $\partial\left(\mathbf{K} - \omega^2\mathbf{m}\right)/\partial\omega$ is the rate of change of the dynamic stiffness matrix with frequency. Meanwhile, the time-averaged strain energy for a cell is given by Zhong and Williams [57] as

$$E_{\mathrm{S}} = \frac{1}{2}\mathbf{X}^{\mathrm{T}}\mathbf{K}\mathbf{X}\qquad(1.60)$$

where $\mathbf{X} = \begin{bmatrix}\mathbf{D}^{\mathrm{T}}(n-1) & \mathbf{D}^{\mathrm{T}}(n)\end{bmatrix}^{\mathrm{T}}$ and $\mathbf{K} = \begin{bmatrix}\mathbf{K}_{\mathrm{LL}} & \mathbf{K}_{\mathrm{LR}} \\ \mathbf{K}_{\mathrm{RL}} & \mathbf{K}_{\mathrm{RR}}\end{bmatrix}$. It appears that equation (1.60) is more succint compared with equations (1.58) and (1.59).

Unlike propagating waves, solitary evanescent and attenuating waves do not propagate energy through the structure, as shown by Mead [18]. Instead, in each cycle, the energy is used to do work on the boundaries of each cell. Nonetheless, two attenuating waves which spatially decay in amplitude interact to transport energy [73]. Langley [72] argued that this effect can only occur over a finite length given that the amplitude of individual wave decays as the wave travels away from the point of excitation.

The power flow associated with the energy that is transported by the propagating wave through the structure can be expressed as the product of velocity and force. Langley [72] showed that the time-averaged power flow associated with a propagating wave into the left-hand side of a cell is given by

$$P_{\mathrm{L}} = \frac{1}{2}\mathrm{Re}\left(-\mathrm{i}\,\omega\mathbf{D}_{\mathrm{L}}^{*}\mathbf{F}_{\mathrm{L}}\right) = -\frac{1}{4}\mathrm{i}\,\omega\left[\mathbf{D}_{\mathrm{L}}^{*}\mathbf{F}_{\mathrm{L}} - \mathbf{F}_{\mathrm{L}}^{*}\mathbf{D}_{\mathrm{L}}\right] = -\frac{1}{4}\mathrm{i}\,\omega\mathbf{V}_{\mathrm{L}}^{*}\mathbf{J}\mathbf{V}_{\mathrm{L}}, \qquad (1.61)$$

where $\mathrm{i} = \sqrt{-1}$, ω is the angular frequency of the wave motion, $\mathbf{D}_{\mathrm{L}}^{*}$ is the transposed conjugate of the displacement vector $\mathbf{D}_{\mathrm{L}}$, $\mathbf{F}_{\mathrm{L}}$ is the force vector, $\mathbf{V}_{\mathrm{L}} = \begin{bmatrix} \mathbf{D}_{\mathrm{L}}^{\mathrm{T}} & \mathbf{F}_{\mathrm{L}}^{\mathrm{T}} \end{bmatrix}^{\mathrm{T}}$, $\mathbf{J} = \begin{bmatrix} \mathbf{0} & \mathbf{I} \\ -\mathbf{I} & \mathbf{0} \end{bmatrix}$ and superscript $*$ denotes transpose conjugation[8].

Substitute $-\mathbf{F}_{\mathrm{L}} = \mathbf{K}_{\mathrm{LL}}\mathbf{D}_{\mathrm{L}} + \mathbf{K}_{\mathrm{LR}}\mathbf{D}_{\mathrm{R}}$ into equation (1.61) gives [57]

$$P_{\mathrm{L}} = -\frac{1}{4}\mathrm{i}\,\omega\left(\mathbf{D}_{\mathrm{R}}^{*}\mathbf{K}_{\mathrm{RL}}\mathbf{D}_{\mathrm{L}} - \mathbf{D}_{\mathrm{L}}^{*}\mathbf{K}_{\mathrm{LR}}\mathbf{D}_{\mathrm{R}}\right). \qquad (1.62)$$

The time-averaged power that flows out of the right hand side of the cell is

$$P_{\mathrm{R}} = \frac{1}{2}\mathrm{Re}\left(-\mathrm{i}\,\omega\mathbf{D}_{\mathrm{R}}^{*}\mathbf{F}_{\mathrm{R}}\right) = -\frac{1}{4}\mathrm{i}\,\omega\mathbf{V}_{\mathrm{R}}^{*}\mathbf{J}\mathbf{V}_{\mathrm{R}}, \qquad (1.63)$$

where $\mathbf{V}_{\mathrm{R}} = \begin{bmatrix} \mathbf{D}_{\mathrm{R}}^{\mathrm{T}} & \mathbf{F}_{\mathrm{R}}^{\mathrm{T}} \end{bmatrix}^{\mathrm{T}}$. For a conservative (i.e. undamped) system, it can be easily verified that $P_{\mathrm{L}} = P_{\mathrm{R}}$, which means that the rate at which energy enters and exits each cell is equal as the wave propagates through the structure [57,72]. The imaginary part of the product between instantaneous velocity and force is the reactive power which is temporally cyclic and remains across the boundaries, i.e. not transmitted through the system. As such, over one time cycle, the reactive power is zero.

Let $\mathbf{V}$ be a matrix whose columns are composed of eigenvectors of transfer matrix $\mathbf{G}$, i.e.

---

[8] The minus sign is mistakenly omitted from the equation in [72].

$$\mathbf{V} = \begin{bmatrix} \mathbf{V}_{R,D} & \mathbf{V}_{L,D} \\ \mathbf{V}_{R,F} & \mathbf{V}_{L,F} \end{bmatrix}, \qquad (1.64)$$

where the subscripts R and L denote right-going and left-going waves, respectively, and D and F denote displacement and force components of the eigenvectors, respectively. Matrix $\mathbf{V}$ is symplectic as it satisfies $\mathbf{V}^T \mathbf{JV} = \mathbf{J}$ ([57], equation (18)). We found numerically that $\mathbf{V}^* \mathbf{JV} \neq \mathbf{J}$.

Zhong and Williams [57] also analysed the power orthogonality relations between rightward and leftward waves and concluded that:

a) for real eigenvalues, only adjoint evanescent waves can interact to produce power;

b) for complex unity eigenvalues, the propagating waves cannot interact to produce power;

c) for complex non-unity eigenvalues, only the complex conjugate of the symplectic adjoint eigenvectors can interact to produce power and can only exist for finite length.

Conclusion (a) is particularly odd considering that equation (1.61) [now takes the form $P = -i\omega \mathbf{V}_1^T \mathbf{JV}_2 / 4$] gives imaginary power for eigenvectors, $\mathbf{V}_1$ and $\mathbf{V}_2$, that are associated with real adjoint eigenvalues, λ_1 and $\lambda_2 = 1/\lambda_1$, respectively; while conclusion (c) appears to be in agreement with the result obtained by Bobrovnitskii [73] and Langley [72].

The velocity at which a phase of a wave travels is called phase velocity and can be found by dividing the angular frequency ω with the wavenumber φ, i.e. ω/φ. Meanwhile, the velocity at which the energy is transported by the wave is called group velocity and is given by the derivative of the angular frequency with respect to the wavenumber, i.e. $\partial\omega/\partial\varphi$. On the dispersion diagram, the derivative represents the gradient of dispersion curves (that are associated with propagating waves) with respect to the wavenumber axis. Lighthill [74] remarked that this result "appears distinctly odd" considering that "in a perfectly periodic motion of fixed wavenumber, energy is propagated at a velocity which can be expressed as a ratio of changes of frequency and wavenumber in going to a neighbouring wave solution". The two velocities for a particular wave could be different in magnitude and direction; when their directions of travel are the same, the wave dispersion is regarded as normal, otherwise when their directions of travel are opposite, the dispersion is regarded as anomalous.

Langley [72] showed that the equation for group velocity satisfies the following equation,

$$c_{\mathrm{g}} = \frac{\partial \omega}{\partial \varphi} = \frac{P}{\left(E_{\mathrm{K}} + E_{\mathrm{S}} \right)} \tag{1.65}$$

where E_{K}, E_{S} and P are given by equations (1.59), (1.60) and (1.61), respectively. This means that the group velocity is equal to the time-averaged power flux divided with the total time-averaged energy density through an arbitrary cross-section. On the other hand, Finnveden [75] showed that the group velocity can be evaluated through numerical differentiation. This is done by first differentiating the eigenvalue problem with respect to the wavenumber. In [75], the eigenvalue problem is given as

$$\left[\mathbf{K} - \omega^2 \mathbf{M} \right] \mathbf{D} = \mathbf{0} \tag{1.66}$$

where $\mathbf{K}$ is the 'stiffness' matrix, ω is the angular frequency, $\mathbf{M}$ is the mass matrix and $\mathbf{D}$ is the displacement eigenvector; upon differentiation, the equation becomes

$$\left[\frac{\mathrm{d}\mathbf{K}}{\mathrm{d}\varphi} - 2\omega \frac{\mathrm{d}\omega}{\mathrm{d}\varphi} \mathbf{M} \right] \mathbf{D} + \left[\mathbf{K} - \omega^2 \mathbf{M} \right] \frac{\mathrm{d}\mathbf{D}}{\mathrm{d}\varphi} = \mathbf{0}. \tag{1.67}$$

Then, pre-multiply equation (1.67) with the left eigenvector $\bar{\mathbf{D}}^{\mathrm{T}}$ and note that $\bar{\mathbf{D}}^{\mathrm{T}} \left[\mathbf{K} - \omega^2 \mathbf{M} \right] = \mathbf{0}$. Finally, the remaining terms are re-arranged to get the equation for the group velocity as

$$c_{\mathrm{g}} = \frac{\bar{\mathbf{D}}^{\mathrm{T}} \dfrac{\mathrm{d}\mathbf{K}}{\mathrm{d}\varphi} \mathbf{D}}{2\omega \bar{\mathbf{D}}^{\mathrm{T}} \mathbf{M} \mathbf{D}}. \tag{1.68}$$

Waki *et al.* [76] proposed a slight modification to the approach and that is to express the group velocity as

$$c_{\mathrm{g}} = \frac{\mathrm{d}\omega}{\mathrm{d}\varphi} = \frac{1}{2\omega} \frac{\mathrm{d}\omega^2}{\mathrm{d}\varphi}, \tag{1.69}$$

and the term $\mathrm{d}\varphi / \mathrm{d}\omega^2$ is obtained by differentiating the associated eigenvalue problem with respect to ω^2; the subsequent steps are the same as outlined by Finnveden [75]. In Chapter 2, new expressions for the group velocity are determined from the transfer matrices; the expression derived from the displacement-displacement transfer matrix is found to be simpler than the expressions given in [72,75,76].

The direction of energy travel can be determined from the direction of progression of the dispersion curve in the canonical plane which is given by the Krein signature [77]. As frequency is increased, if the eigenvalue 'moves' from 0 to π (or 0 to $-\pi$), then the

signature is positive; otherwise, if the eigenvalue 'moves' from π to 0 (or $-\pi$ to 0), then the signature is negative. Positive and negative signatures are associated with normal and anomalous dispersions, respectively. Two dispersion curves that have the same signature may cross one another - the point of intersection is known as Krein crossing. Two dispersions curves that have different signatures may collide – the point of collision is known as Krein collision. When this happen, the eigenvalues come out of and eventually return to the plane (at a different point) forming a closed loop. This graphical feature basically represents the collision between normal and anomalous dispersion curves which leads to the formation of attenuating waves (which is represented by the loop). Existence of anomalous dispersion has been attributed to symmetry breaking [78] but this idea is not explored in this thesis.

1.2.8 Natural frequency

The natural frequencies of finite repetitive structures have been studied for many decades. One of the earliest reports was by Williams [79]. Wittrick and Williams [80] also presented an algorithm for computing the natural frequencies of such structures but the method adopted was not transfer matrix. In a review paper [6], Mead stated that Mercer and Seavey [81] at Southampton had used transfer matrices to compute natural frequencies of stiffened plates but they did not take the advantage of structural periodicity.

Mead has contributed significantly in the study of natural frequencies through a number of publications. In [61], Mead proved that the relationship between the bounding frequencies of propagation zones and the natural frequencies of a single repeating cell. According to Mead, if the mono-coupled periodic element are symmetric about their spanwise centres, the bounding frequencies are the same as the natural frequencies of an isolated element with its end either fixed or free. If the periodic element is asymmetric, its natural frequency must occur outside the propagation zones of the periodic system. In general, most of the natural frequencies will still fall in the propagation zones. Mead [62] also showed that the phase closure principle can be applied to a multi-coupled repetitive structures and leads to an equation for the phase constants at which the natural frequencies occur. Consideration must be given to the reflection matrices at the extreme ends of the structure which account for the changes of phase of the characteristic waves as they get reflected. An evanescent wave which is generated from the reflection process can make its own complete circuit of the finite system. Detailed description of the phase closure principle was presented by Mead in a later publication [19].

Signorelli and von Flotow [47] applied the phase closure principle using the transfer matrix to determine the natural frequencies of truss structures. The method involves transformation of the state vector into wave amplitude vector, and spatial evolution of the amplitude from one cell to the next is achieved by multiplying the wave vector with the diagonal eigenvalue matrix whose elements have magnitude less than or equal to unity [48]. The complete formulation includes the reflection matrices at the extreme ends of the structure, i.e. whether they are free-fixed, fixed-free, free-free or fixed-fixed. The natural frequencies are then determined from the characteristic determinantal equation, that is whenever both the real and imaginary parts of the complex determinant tend to vanish.

Luongo and Romeo [71] found that the wave vector approach presented by Signorelli and von Flotow [47] can be modified such that the determinantal equation yields real values only. The modification requires that the elements in the transformation matrix and the eigenvalue matrix to be re-arranged and the real and imaginary parts of complex numbers are placed in separate columns. The proposed computational scheme is implemented on mono- and bi-coupled periodic structures and showed to be more stable than the complex wave vector approach. In a private communication, Romeo stated that the method has not been extended on multi-coupled periodic structure but foreseeably possible.

1.2.9 Static analysis

When a complete structure is to be analysed, one usually have a two-point boundary value problem. For example, in a case of tip-loaded cantilever, the load vector at the tip and the zero displacement at the fixed root will be known; the displacement vector at the tip and the reaction vector at the root are unknowns. According to Mufti *et al.* [67], such problems are usually ill-conditioned. In [39], Stephen analysed a cantilevered ten-cell repetitive pin-jointed structure subjected to tip-loading, and to distributed loading with an intermediate support and pointed out that the source of ill-conditioning was the exponentiation of the transfer matrix, not the inversion of one partition of the stiffness matrix as claimed by Zhong and Williams [40]. The claim was based on the fact that a typical element of the stiffness matrix of a pin-jointed structure is proportional to EA/L; inversion of the large Young's modulus value, e.g. 200×10^3 N/mm^2, can lead to ill-conditioning. However, Stephen [39] offered a simple solution to the problem; that is to set a lower value for the Young's modulus, e.g. $E = 2$ N/mm^2 with displacement predictions scaled accordingly. In the present problem, when the spatial evolution is expressed in terms of powers of Jordan canonical form; any

elements of the matrix whose magnitude is much greater than unity will become dominant and magnify any errors.

In a later publication, Stephen [49] employed Riccati transformation to produce a numerically stable formulation. The transformation is numerically reliable because the eigenvalues of particular terms in the recursive relationship have magnitudes less than or equal to unity—powers of those terms will be diminishing. In this sense, the Riccati transformation is similar to the phase closure principle and wave vector approach in the way that only eigenvalues whose magnitude less than or equal to unity are employed.

Despite its numerical stability, the Riccati transfer matrix formulation is not transparent, i.e. it is not obvious that the recursive relationship would yield a reliable result as one moves backward and forward along the structure. Also, the formulation requires recursive computation as one move from one end of the structure to the other end; such computation is unappealing to very long structural problem. It is to no surprise that the method is not widespread.

1.3 Motivation, Aim, Objectives, Scopes and Organisation of the Thesis

Matrix eigenanalysis allows computation of the equivalent properties and the Saint-Venant decay characteristics from the knowledge of the stiffness matrix of a single repeating cell. This technique has been applied extensively to one-dimensional beam-like structures under static load. This thesis wishes to extend the techniques to the dynamic case.

The aim of this thesis is to answer a question posed by Mead 23 years ago [6], and that is to present a simple physical explanation for the existence of frequency-propagation zones and attenuation zones. In doing so, we hope to achieve the following objectives:

(i) to analyse different forms of transfer matrix and their relationships;

(ii) to present the dispersion diagram in the best possible form so that the propagation and decay zones are well-defined;

(iii) to analyse the energetics of different wave types;

(iv) to formulate a numerically stable technique to solve two-point boundary value problem (TPBVP); and

(v) to analyse dynamic Saint-Venant's principle through elementary observations of the phenomena in the propagation and decay zones.

The fourth objectives evolved naturally as an attempt to apply phase closure principle to the static case failed because the force vectors associated with rigid body translations and rotation reduced to become columns of zero vector, hence the reflection matrix cannot be computed. Also, the diagonal matrix of eigenvalues under dynamic case becomes Jordan block matrix under static case; the latter cannot be simply partitioned into blocks of 'eigenvalues' that represent rightward and leftward decay of self-equilibrating loads or transmission of the coupled principal vectors. Even though the phase closure principle is failed to be implemented in the static case, a new simple method to solve TPBVP (for a multi-coupled repetitive structure) has been developed; the approach is to switch the unknown participation factors with the known participation factors such that the known and unknown factors are grouped on the same side of the equation, this requires the transformation matrix and the Jordan canonical form to be partitioned and re-arranged accordingly.

Throughout this thesis, a pin-jointed framework is used as the example structure. This choice is made because the finite element analyses (FEA) of such structures involve a rod in tension or compression only, whose finite element is *exact*; therefore, the computational process alone limits the accuracy of the FEA. This means that the results obtained from the transfer matrix approach can be verified by comparison with the finite element method which may be regarded as exact.

In the study of repetitive structure, the use of framework as the model is not new [47,48,82]; however, the bar members are usually considered to have inertia. As a result, the dispersion curves diagram appears to have many more branches than the model employed in this thesis, in which the bar members are considered to be massless and inertia are lumped at point masses. We believe that it is in our interest to have a reasonably simple model and dispersion curve diagram to allow for detailed analyses, and hopefully, this would lead to better understanding of the underlying physical phenomena.

The scope of this thesis is primarily on the steady-state harmonic vibration of undamped multi-coupled one-dimensional repetitive structures; where applicable, the study is extended to the static case, i.e. when $\omega = 0$. The main methodology employed to solve the problems is transfer matrix method; and together with Bloch's theorem [83], they lead to the eigenanalysis technique aforementioned (see Section 1.2.2).

This thesis presents six chapters. The first chapter is the Introduction which includes a section of the literature review on one-dimensional repetitive structures. The next four chapters present each of the objectives aforementioned. Chapter 2 presents the two most commonly employed forms of transfer matrices, their properties and relations. Chapter 3 presents the dispersion curves of the model structure and describes their characteristic waves under propagation and decay frequency-bands in detail. Chapter 4 presents the energetics of the different wave types. In Chapter 5, a simple and stable numerical formulation to solve TPBVP is presented; we believe that the formulation is an alternative to Riccati transformation which are adopted by many to solve such problem. The final chapter is the concluding remarks where a summary for this thesis is presented as well as some suggestions on future work.

Chapter 2: Wave Propagation in Repetitive Structures: Two Forms of Transfer Matrix

2.1 Introduction

Repetitive or periodic structures consist of a cell which spatially repeats in one-, two- or three-dimensions. Each cell is connected to another in a regular pattern to form the complete structure. Such construction are widely employed in engineering, and include rail track, turbine blade assemblies (bladed discs), building frameworks, cranes, aircraft fuselages, trusses and honeycomb panels. Since the manufacture and construction of such structures can also be a repetitive process, they represent a cost effective design solution for many engineering applications. Early contributions are described in references [6,61,62,79,84–86]. The joints between the structural members can be designed so that they allow additional degrees of freedom, providing the possibility of a change in structural shape [87], or to become a deployable mechanism/structure [88]. Furthermore, repetitive structures portray symmetrical features and often have an aesthetically pleasing appearance.

The present chapter is concerned with one-dimensional (beam-like) repetitive structures. When periodicity is taken into account, the static and dynamic analysis of an entire structure can be reduced to the analysis of a single repeating cell, together with boundary (end) conditions if the structure is not of infinite extent; equivalent continuum properties can be determined for segmented structures such as trusses [12]. The primary approach is through the use of a transfer matrix $\mathbf{T}$, which relates state vector components on the right-hand side to those on the left-hand side of the cell, i.e. $\mathbf{s}_R = \mathbf{T}\mathbf{s}_L$. (Alternative analytical approaches, including the receptance method, are described in Mead's 1996 review paper [6].) An eigenvector of the transfer matrix describes a pattern of state vector components which is unique to within a scalar multiplier, λ. Translational symmetry demands that this pattern is preserved as one moves from the left-hand to the right-hand side of the cell, allowing one to write $\mathbf{s}_R = \lambda \mathbf{s}_L$; this immediately leads to the standard eigenvalue problem $\mathbf{T}\mathbf{s}_L = \lambda \mathbf{s}_L$, or $(\mathbf{T} - \lambda)\mathbf{s}_L = \mathbf{0}$. There are two forms of the transfer matrix $\mathbf{T}$ in frequent use: the first and more common [1,12,16,22,24–26,30,44,56,60–62] relates a state vector $\mathbf{s}$ of displacement and force components on either side of the cell, here presented as transfer matrix $\mathbf{G}$; the

second and less common form [9,15,40,87,92] relates state vectors $\mathbf{s}$ of displacements at three consecutive nodal cross-sections of the complete structure, here presented as $\mathbf{H}$.

Both $\mathbf{G}$ and $\mathbf{H}$ can be determined from the (dynamic) stiffness matrix $\mathbf{K}$; the latter is symmetric for linear elastic displacements and, in turn, both transfer matrices are symplectic, that is they satisfy a relationship of the form $\mathbf{T}^T \mathbf{\Omega} \mathbf{T} = \mathbf{\Omega}$ where $\mathbf{T}^T$ denotes the transpose of $\mathbf{T}$, and $\mathbf{\Omega}$ is a skew-symmetric matrix, known as the *metric*. For transfer matrix $\mathbf{G}$, the metric takes its simplest, canonical, form, and is written as $\mathbf{J} = \begin{bmatrix} \mathbf{0} & \mathbf{I} \\ -\mathbf{I} & \mathbf{0} \end{bmatrix}$. The significance of the metric is rooted in Hamiltonian mechanics. The metric in a Euclidean vector space is the *length* of a vector, calculated as the square root of the dot product of the vector with itself, an inner product. However, in a symplectic vector space, where the state vector consists of both displacement and force components, such an inner product has no physical meaning. Instead, a symplectic inner product, employing $\mathbf{J}$ as the metric, multiplies displacement with force which is work or energy; rather than *length*, it is an *area*, which is preserved during (here spatial) evolution. Ultimately, it implies conservation of energy.

For the static problem, the *force-displacement* transfer matrix $\mathbf{G}$ is perhaps the more appropriate, as one can readily identify force resultants; thus the decay modes associated with self-equilibrated loading (as anticipated by Saint-Venant's principle), the rigid body modes associated with zero force components, and the transmission modes associated with the force resultants of tension, bending moment and shearing force can be easily recognised. This static problem is characterised by multiple unity eigenvalues for the rigid body and transmission modes. In turn the transfer matrix cannot be diagonalised, but can only be reduced to a Jordan canonical block form; e.g. the principal vector describing tension is coupled with the eigenvector for a rigid-body displacement in the axial *x*-direction within a (2×2) block [12].

For wave propagation, the *displacement-displacement* transfer matrix $\mathbf{H}$ is perhaps the more appropriate, as waves are naturally described in terms of their displacement characteristics, e.g. extensional, flexural, thickness-shear, rather than force resultants.

For the dynamic problem considered here, irrespective of whether one employs $\mathbf{G}$ or $\mathbf{H}$, repeating eigenvalues are unusual for a given frequency; it generally implies a crossing of branches on a dispersion diagram, when the eigenvectors are distinct. The exception is a so-called Krein *collision* [63], which occurs when one has equal eigenvalues at the same

frequency, and one of the propagation modes displays anomalous dispersion, the other normal; this is considered in detail in Chapter 4.

Each formulation has advantages and disadvantages: for example, symplectic orthogonality of the eigenvectors of $\mathbf{G}$ is seen to be a special case of the reciprocal theorem of Betti-Maxwell [58], whereas the weighted symplectic orthogonality of the eigenvectors of $\mathbf{H}$ is not so obviously related. On the other hand, a new expression for the group velocity [47,72,75,93] is much more succinct when one employs $\mathbf{H}$. For a repetitive structure having finite length, boundary conditions are generally expressed in terms of zero force or zero displacement so transfer matrix $\mathbf{G}$ is the more appropriate. If the number of repeating cells N is small, then the natural frequencies can be determined from a zero value determinant of a partition of $\mathbf{G}^N$; if one employs transfer matrix $\mathbf{H}$, then since the force vector does not naturally feature it has to be introduced at a free end, which leads to a frequency equation which involves $\mathbf{H}^{N-1}$. However, both of these methods become inaccurate when the number of cells is large, and natural frequencies are then most accurately found using phase closure for $\mathbf{G}$.

This chapter presents relationships between the two forms of transfer matrix, $\mathbf{G}$ and $\mathbf{H}$, between their respective eigenvectors and also orthogonality relationships. Some of the results are not new but re-derived in a concise formulation and provided here as a convenient resource for comparison with new results. The results are formulated for the dynamic problem, but apply equally for the static case, $\omega = 0$.

The example structure consists of an (in)finite planar framework of pin-jointed members with a point mass m located at each pin-joint, as shown in Figure 2.1(a). The indices $(n-1)$, n and $(n+1)$ denote three consecutive nodal cross-sections of the framework, and numbers 1, 2 and 3 denote tiers of the masses. Horizontal and vertical rods, assumed massless, have stiffness $k = EA/L$ where E is the Young's modulus, A is the cross-sectional area and L is the rod's length. The cross-sectional area of the diagonal members, also assumed massless, is taken to be one-half of the horizontal and vertical members, so their stiffness is $k/(2\sqrt{2})$. The diagonal members are not pinned where they cross. The structure is, in fact, identical to that which has been subject to extensive elastostatic eigenanalysis by Stephen and co-workers [1,12,39,49], but with the addition of point masses at the nodal cross-sections.

The complete structure can be regarded as a repetition of two possible entities, as shown in Figure 2.1(b) and 2.1(c). In Figure 2.1(b), the vertical members and the cross-sectional masses are regarded as being shared between adjacent cells, therefore their stiffness and mass must be halved; for a pin-jointed rod, this is accomplished by taking the cross-sectional area as $A/2$. Similarly, the masses are drawn as semi-circles, to denote the fact that each has mass $m/2$. This repeating cell is the more appropriate for the construction of transfer matrix $\mathbf{G}$. On the other hand, the structure can be regarded as a repetition of nodal cross-sections, Figure 2.1(c), and this is the more appropriate for the construction of transfer matrix $\mathbf{H}$; the vertical members are no longer shared, so the full stiffness (cross-sectional area) is now employed.
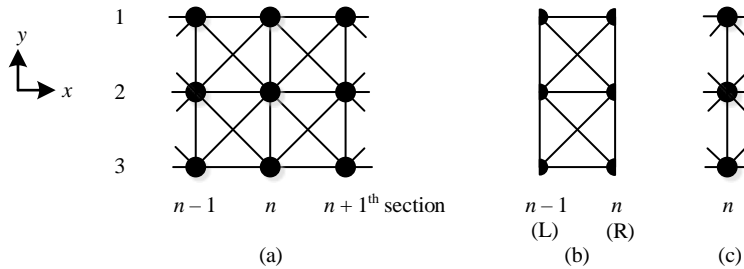
Figure 2.1 Segment of the example framework, (a), and two possible repeating entities; (b) shows the complete nth repeating cell, whereas (c) shows a repeating nodal cross-section with attached pin-jointed rods. For (b), the sections $(n-1)$ and n can also be represented by left (L) and right (R), respectively.

2.2 Formulation of the dynamic transfer matrices

2.2.1 Displacement-force transfer matrix, $\mathbf{G}$

First consider the repeating cell shown in Figure 2.1(b); the governing equations of motion for the half-masses on sections $(n-1)$ and (n) are

$$-\mathbf{f}(n-1) = \frac{\mathbf{m}}{2}\ddot{\mathbf{d}}(n-1) + \mathbf{K}_{\mathrm{LL}}\mathbf{d}(n-1) + \mathbf{K}_{\mathrm{LR}}\mathbf{d}(n),\tag{2.1}$$

$$\mathbf{f}(n) = \frac{\mathbf{m}}{2}\ddot{\mathbf{d}}(n) + \mathbf{K}_{\mathrm{RL}}\mathbf{d}(n-1) + \mathbf{K}_{\mathrm{RR}}\mathbf{d}(n),\tag{2.2}$$

respectively, where $\mathbf{f}$ is the nodal force vector, $\mathbf{m}$ is the mass matrix, $\mathbf{d}$ is the displacement vector, and dot denotes differentiation with respect to time. The matrices $\mathbf{K}_{LL}$, $\mathbf{K}_{LR}$, $\mathbf{K}_{RL}$ and $\mathbf{K}_{RR}$ are presented explicitly in Appendix A.1. The mass matrix $\mathbf{m}$ is equal to m times a (6×6) identity matrix. Following transfer matrix sign convention, the negative sign before $\mathbf{f}(n-1)$ is introduced to indicate that it acts in the opposite direction to $\mathbf{f}(n)$, that is, it acts in the negative x-direction. A factor of one-half for the mass matrix takes into account the halved point masses on both sides of the cell. For harmonic motion, one can write $\mathbf{f}(n) = \mathbf{F}(n)\exp(\mathrm{i}\omega t)$ and $\mathbf{d}(n) = \mathbf{D}(n)\exp(\mathrm{i}\omega t)$ where $\mathbf{F}$ and $\mathbf{D}$ are force and displacement amplitudes, respectively, $\mathrm{i} = \sqrt{-1}$, ω is frequency and t is time. The acceleration vector can then be expressed as $\ddot{\mathbf{d}}(n) = -\omega^2 \mathbf{D}(n)\exp(\mathrm{i}\omega t)$ which upon substitution into equations (2.1) and (2.2) yields the dynamic stiffness matrix in partitioned form

$$\begin{bmatrix} -\mathbf{F}(n-1) \\ \mathbf{F}(n) \end{bmatrix} = \begin{bmatrix} \left[\mathbf{K}_{LL} - \dfrac{\omega^2 \mathbf{m}}{2} \right] & \mathbf{K}_{LR} \\ \mathbf{K}_{RL} & \left[\mathbf{K}_{RR} - \dfrac{\omega^2 \mathbf{m}}{2} \right] \end{bmatrix} \begin{bmatrix} \mathbf{D}(n-1) \\ \mathbf{D}(n) \end{bmatrix}. \tag{2.3}$$

Equation (2.3) can be rearranged into transfer matrix form as

$$\begin{bmatrix} \mathbf{D}(n) \\ \mathbf{F}(n) \end{bmatrix} = \mathbf{G} \begin{bmatrix} \mathbf{D}(n-1) \\ \mathbf{F}(n-1) \end{bmatrix}, \tag{2.4}$$

where

$$\mathbf{G} = \begin{bmatrix} -\mathbf{K}_{LR}^{-1} \left[\mathbf{K}_{LL} - \dfrac{\omega^2 \mathbf{m}}{2} \right] & -\mathbf{K}_{LR}^{-1} \\ \mathbf{K}_{RL} - \left[\mathbf{K}_{RR} - \dfrac{\omega^2 \mathbf{m}}{2} \right] \mathbf{K}_{LR}^{-1} \left[\mathbf{K}_{LL} - \dfrac{\omega^2 \mathbf{m}}{2} \right] & -\left[\mathbf{K}_{RR} - \dfrac{\omega^2 \mathbf{m}}{2} \right] \mathbf{K}_{LR}^{-1} \end{bmatrix}$$

or more compactly $\mathbf{V}(n) = \mathbf{G}\mathbf{V}(n-1)$, with $\mathbf{V}(n) = \begin{bmatrix} \mathbf{D}^{\mathrm{T}}(n) & \mathbf{F}^{\mathrm{T}}(n) \end{bmatrix}^{\mathrm{T}}$ and $\mathbf{V}(n-1) = \begin{bmatrix} \mathbf{D}^{\mathrm{T}}(n-1) & \mathbf{F}^{\mathrm{T}}(n-1) \end{bmatrix}^{\mathrm{T}}$.

The matrix $\mathbf{G}$ is symplectic, that is it satisfies the relationship

$$\mathbf{G}^{\mathrm{T}} \mathbf{J} \mathbf{G} = \mathbf{J} \tag{2.5}$$

where $\mathbf{J} = \begin{bmatrix} \mathbf{0} & \mathbf{I} \\ -\mathbf{I} & \mathbf{0} \end{bmatrix}$ is the *metric* for $\mathbf{G}$ and has the properties $\mathbf{J}^{\mathrm{T}} = \mathbf{J}^{-1} = -\mathbf{J}$. The

determinant of $\mathbf{G}$ is $+1$ for all values of ω. The inverse of $\mathbf{G}$ is given by

$\mathbf{G}^{-1} = \mathbf{J}^{-1}\mathbf{G}^{\mathrm{T}}\mathbf{J} = -\mathbf{J}\mathbf{G}^{\mathrm{T}}\mathbf{J}$. Writing $\mathbf{V}(n) = \lambda\mathbf{V}(n-1)$, leads to the frequency-dependent

eigenvalue problem

$$\begin{bmatrix} -\mathbf{K}_{LR}^{-1}\left[\mathbf{K}_{LL} - \dfrac{\omega^2\mathbf{m}}{2}\right] - \lambda\mathbf{I} & -\mathbf{K}_{LR}^{-1} \\ \mathbf{K}_{RL} - \left[\mathbf{K}_{RR} - \dfrac{\omega^2\mathbf{m}}{2}\right]\mathbf{K}_{LR}^{-1}\left[\mathbf{K}_{LL} - \dfrac{\omega^2\mathbf{m}}{2}\right] & -\left[\mathbf{K}_{RR} - \dfrac{\omega^2\mathbf{m}}{2}\right]\mathbf{K}_{LR}^{-1} - \lambda\mathbf{I} \end{bmatrix}\begin{bmatrix} \mathbf{D}(n-1) \\ \mathbf{F}(n-1) \end{bmatrix} = \mathbf{0} , \quad (2.6)$$

or more compactly, $(\mathbf{G} - \lambda\mathbf{I})\mathbf{V}(n-1) = \mathbf{0}$.

2.2.2   Displacement-displacement transfer matrix, $\mathbf{H}$

Now consider the repeating nodal cross-section at an arbitrary station n, as shown in Figure 2.1(c). The governing equation of motion now takes the form

$$\mathbf{m}\ddot{\mathbf{d}}(n) + \mathbf{K}_{RL}\mathbf{d}(n-1) + \left[\mathbf{K}_{LL} + \mathbf{K}_{RR}\right]\mathbf{d}(n) + \mathbf{K}_{LR}\mathbf{d}(n+1) = \mathbf{0}. \quad (2.7)$$

(Referring to Appendix A.1, one sees that the term $k/2$, pertaining to the one-half stiffness of the vertical members for Figure 2.1(b), only appears in the partitions $\mathbf{K}_{LL}$ and $\mathbf{K}_{RR}$; since these partitions are added in equation (2.7), this leads to the full stiffness of the vertical members in Figure 2.1(c).)

Writing $\mathbf{d}(n) = \mathbf{D}(n)\exp(i\omega t)$ leads to

$$\mathbf{K}_{RL}\mathbf{D}(n-1) + \left[\mathbf{K}_{LL} + \mathbf{K}_{RR} - \omega^2\mathbf{m}\right]\mathbf{D}(n) + \mathbf{K}_{LR}\mathbf{D}(n+1) = \mathbf{0}. \quad (2.8)$$

Pre-multiplying by $\mathbf{K}_{LR}^{-1}$ gives

$$\mathbf{D}(n+1) = -\mathbf{K}_{LR}^{-1}\mathbf{K}_{RL}\mathbf{D}(n-1) - \mathbf{K}_{LR}^{-1}\left[\mathbf{K}_{LL} + \mathbf{K}_{RR} - \omega^2\mathbf{m}\right]\mathbf{D}(n). \quad (2.9)$$

Introducing state vectors

$$\mathbf{X}(n-1) = \begin{bmatrix} \mathbf{D}^{\mathrm{T}}(n-1) & \mathbf{D}^{\mathrm{T}}(n) \end{bmatrix}^{\mathrm{T}} \text{ and } \mathbf{X}(n) = \begin{bmatrix} \mathbf{D}^{\mathrm{T}}(n) & \mathbf{D}^{\mathrm{T}}(n+1) \end{bmatrix}^{\mathrm{T}} \quad (2.10\text{a,b})$$

allows one to reconstruct equation (2.9) in the difference equation form

$$\begin{bmatrix} \mathbf{D}(n) \\ \mathbf{D}(n+1) \end{bmatrix} = \begin{bmatrix} \mathbf{0} & \mathbf{I} \\ -\mathbf{K}_{LR}^{-1}\mathbf{K}_{RL} & -\mathbf{K}_{LR}^{-1}\left[\mathbf{K}_{LL} + \mathbf{K}_{RR} - \omega^2\mathbf{m}\right] \end{bmatrix}\begin{bmatrix} \mathbf{D}(n-1) \\ \mathbf{D}(n) \end{bmatrix}, \quad (2.11)$$

or more compactly $\mathbf{X}(n) = \mathbf{H}\mathbf{X}(n-1)$. Finally, writing $\mathbf{X}(n) = \lambda \mathbf{X}(n-1)$ leads to the frequency-dependent eigenvalue problem

$$\begin{bmatrix} -\lambda \mathbf{I} & \mathbf{I} \\ -\mathbf{K}_{LR}^{-1}\mathbf{K}_{RL} & -\mathbf{K}_{LR}^{-1}\left[\mathbf{K}_{LL} + \mathbf{K}_{RR} - \omega^2 \mathbf{m}\right] - \lambda \mathbf{I} \end{bmatrix} \mathbf{X}(n-1) = \mathbf{0}, \qquad (2.12)$$

or more compactly, $(\mathbf{H} - \lambda \mathbf{I})\mathbf{X}(n-1) = \mathbf{0}$. Note that matrix $\mathbf{H}$ is still symplectic, but does not satisfy equation (2.5), that is $\mathbf{H}^T\mathbf{J}\mathbf{H} \neq \mathbf{J}$; however, the equivalent relationship, together with a new metric, is developed in the following section.

2.3 Relationships between transfer matrices $\mathbf{G}$ and $\mathbf{H}$

The relationships between the dynamic transfer matrices $\mathbf{G}$ and $\mathbf{H}$ can be established as follows: let $\mathbf{L}$ and $\mathbf{N}$ be the matrices

$$\mathbf{L} = \begin{bmatrix} \mathbf{I} & \mathbf{0} \\ -\left[\mathbf{K}_{LL} - \dfrac{\omega^2 \mathbf{m}}{2}\right] & -\mathbf{K}_{LR} \end{bmatrix} \text{ and } \mathbf{N} = \begin{bmatrix} \mathbf{0} & \mathbf{I} \\ \mathbf{K}_{RL} & \left[\mathbf{K}_{RR} - \dfrac{\omega^2 \mathbf{m}}{2}\right] \end{bmatrix} \qquad (2.13\text{a,b})$$

then it is straightforward to show that

$$\mathbf{G} = \mathbf{N}\mathbf{L}^{-1} \text{ and } \mathbf{H} = \mathbf{L}^{-1}\mathbf{N}. \qquad (2.14\text{a,b})$$

The inverse of matrix $\mathbf{L}$ is found using the block-wise matrix inversion formula, Appendix A.2, as

$$\mathbf{L}^{-1} = \begin{bmatrix} \mathbf{I} & \mathbf{0} \\ -\mathbf{K}_{LR}^{-1}\left(\mathbf{K}_{LL} - \omega^2 \dfrac{\mathbf{m}}{2}\right) & -\mathbf{K}_{LR}^{-1} \end{bmatrix}.$$

Matrices $\mathbf{L}$ and $\mathbf{N}$ were first introduced by Zhong and Williams [40] as a means to avoid numerical ill-conditioning. Now, from equations (2.14a,b) $\mathbf{G}^T = \mathbf{L}^{-T}\mathbf{N}^T$ and $\mathbf{H}^T = \mathbf{N}^T\mathbf{L}^{-T}$, so equation (2.5) becomes

$$\left(\mathbf{L}^{-T}\mathbf{N}^T\right)\mathbf{J}\left(\mathbf{N}\mathbf{L}^{-1}\right) = \mathbf{J}; \qquad (2.15)$$

now pre-multiply by $\mathbf{N}^T$ and post-multiply by $\mathbf{N}$ to give $\left(\mathbf{N}^T\mathbf{L}^{-T}\right)\mathbf{N}^T\mathbf{J}\mathbf{N}\left(\mathbf{L}^{-1}\mathbf{N}\right) = \mathbf{N}^T\mathbf{J}\mathbf{N}$ or $\mathbf{H}^T\left(\mathbf{N}^T\mathbf{J}\mathbf{N}\right)\mathbf{H} = \mathbf{N}^T\mathbf{J}\mathbf{N}$. Write $\tilde{\mathbf{J}} = \mathbf{N}^T\mathbf{J}\mathbf{N}$, then we have $\mathbf{H}^T\tilde{\mathbf{J}}\mathbf{H} = \tilde{\mathbf{J}}$ as the expression equivalent to equation (2.5) for matrix $\mathbf{H}$. The *metric* is $\tilde{\mathbf{J}} = \begin{bmatrix} \mathbf{0} & -\mathbf{K}_{LR} \\ \mathbf{K}_{RL} & \mathbf{0} \end{bmatrix}$, and has the skew-symmetric property $\tilde{\mathbf{J}}^T = -\tilde{\mathbf{J}}$ since $\mathbf{K}_{RL} = \mathbf{K}_{LR}^T$; this allows one to write

$\mathbf{H}^{-1} = \tilde{\mathbf{J}}^{-1}\mathbf{H}^{\mathrm{T}}\tilde{\mathbf{J}}$. The metric can also be expressed in terms of $\mathbf{L}$: pre-multiply equation (2.15) by $\mathbf{L}^{\mathrm{T}}$ and post-multiply by $\mathbf{L}$ gives $\mathbf{N}^{\mathrm{T}}\mathbf{J}\mathbf{N} = \mathbf{L}^{\mathrm{T}}\mathbf{J}\mathbf{L} = \tilde{\mathbf{J}}$. The formula to find the inverse of $\mathbf{H}$ as given by Gry and Gontier [92] is wrong because the result showed that $\mathbf{H}^{-1}\mathbf{H} \neq \mathbf{I}$ and $\mathbf{H}\mathbf{H}^{-1} \neq \mathbf{I}$.

Matrices $\mathbf{G}$ and $\mathbf{H}$ are related as follows: from equation (2.14a), pre-multiply by $\mathbf{L}^{-1}$ to give $\mathbf{L}^{-1}\mathbf{G} = \left(\mathbf{L}^{-1}\mathbf{N}\right)\mathbf{L}^{-1} = \mathbf{H}\mathbf{L}^{-1}$ and hence $\mathbf{G} = \mathbf{L}\mathbf{H}\mathbf{L}^{-1}$, or equally $\mathbf{H} = \mathbf{L}^{-1}\mathbf{G}\mathbf{L}$. Pre-multiply equation (2.14b) by $\mathbf{N}$ to give $\mathbf{N}\mathbf{H} = \left(\mathbf{N}\mathbf{L}^{-1}\right)\mathbf{N} = \mathbf{G}\mathbf{N}$ and hence $\mathbf{H} = \mathbf{N}^{-1}\mathbf{G}\mathbf{N}$, or equally $\mathbf{G} = \mathbf{N}\mathbf{H}\mathbf{N}^{-1}$. Thus both $\mathbf{L}$ and $\mathbf{N}$ serve as similarity matrices for $\mathbf{G}$ and $\mathbf{H}$. Since $\mathbf{G}$ and $\mathbf{H}$ are similar, they must have the same eigenvalues, as one would expect, although the eigenvectors are quite different as will be noted below; however the eigenvectors are related, again through matrices $\mathbf{L}$ and $\mathbf{N}$. In the above, the inverse of $\mathbf{N}$ may be found by means of the Schur complement, Appendix A.2, as

$$\mathbf{N}^{-1} = \begin{bmatrix} -\mathbf{K}_{\mathrm{RL}}^{-1}\left(\mathbf{K}_{\mathrm{RR}} - \omega^2\dfrac{\mathbf{m}}{2}\right) & \mathbf{K}_{\mathrm{RL}}^{-1} \\ \mathbf{I} & \mathbf{0} \end{bmatrix}.$$

Similarly, $\tilde{\mathbf{J}}^{-1} = \begin{bmatrix} \mathbf{0} & \mathbf{K}_{\mathrm{RL}}^{-1} \\ -\mathbf{K}_{\mathrm{LR}}^{-1} & \mathbf{0} \end{bmatrix}.$

2.4 Eigenvalues and eigenvectors of transfer matrices $\mathbf{G}$ and $\mathbf{H}$

The frequency-dependent eigenproblems, equations (2.6) and (2.12), can be solved computationally using the eig function of MATLAB. For a specified ω, or ω^2, MATLAB returns the eigenvalues λ in a diagonal matrix and the corresponding normalised right eigenvectors $\mathbf{V}$ arranged accordingly in the eigenvector matrix, that is the eigenvector associated with the first eigenvalue will be in the first column of the eigenvector matrix, and so on.

For a cell with $2N$ degrees of freedom, there are N reciprocal pairs of eigenvalues: if the eigenvalue λ_i is associated with a propagating or decaying wave from sections $(n-1)$ to n, that is from left-to-right, then its reciprocal pair λ_j where $\lambda_j = 1/\lambda_i$ represents the same wave propagating or decaying from n to $(n-1)$, that is from right-to-left. Usually, λ is expressed in exponential form, i.e. $\lambda = \exp(\delta + \mathrm{i}\varphi)$ where δ and φ represent decay rate

and phase change of amplitudes from one section to the next, respectively. The eigenvalues take five possible forms [1]:

(i)   The positive real unity eigenvalue $\lambda = 1 = \exp(0)$ must occur an even number of times since its inverse will also be 1.

(ii)   The negative real unity eigenvalue $\lambda = -1 = \exp(i\pi)$ must also occur an even number of times since its inverse will be -1.

(iii)   The real non-unity eigenvalues occur as a pair λ and λ^{-1}. If $\lambda > 0$, then $\lambda = \exp(\delta)$, but if $\lambda < 0$, then $\lambda = \exp(\delta + i\pi)$.

(iv)   The complex unity eigenvalues $|\lambda| = 1$ occur as a unitary pair, that is $\lambda = a + ib$ and $\lambda = a - ib$. If $\lambda = \exp(i\varphi)$, then $\lambda^{-1} = \exp(-i\varphi)$; the inverse is also the complex conjugate.

(v)   The complex non-unity eigenvalues occur as a quartet of reciprocals and complex conjugates, that is $\lambda = a + ib$, $\lambda = a - ib$, $\lambda = (a + ib)^{-1}$, $\lambda = (a - ib)^{-1}$; in exponential form, $\lambda = \exp(\pm\delta \pm i\varphi)$ where $\delta > 0$ and $\varphi > 0$. For example, if $|\lambda_i| < 1$, then $\lambda_i = \exp(-\delta - i\varphi)$, the complex conjugate is $\bar{\lambda}_i = \exp(-\delta + i\varphi)$, the inverses are $\lambda_i^{-1} = \exp(+\delta + i\varphi)$ and $\bar{\lambda}_i^{-1} = \exp(+\delta - i\varphi)$. The minimum size of transfer matrix for complex non-unity eigenvalues to occur is (8×8), because the quartet of eigenvalues can multiply both a minimum four degrees of cross-sectional displacement freedom, and four force components in the case of $\mathbf{G}$ or an additional four displacements in the case of $\mathbf{H}$; in turn the state vector of both $\mathbf{G}$ or $\mathbf{H}$ will be (8×1).

For the model framework, the first six rows and the last six rows of the right eigenvector $\mathbf{V}$ of matrix $\mathbf{G}$ represent displacement and force components, respectively, at an arbitrary station $(n-1)$, i.e.

$$\mathbf{V}^{\mathrm{T}}(n-1) = \begin{bmatrix} D_{1x}^{n-1} & D_{1y}^{n-1} & D_{2x}^{n-1} & D_{2y}^{n-1} & D_{3x}^{n-1} & D_{3y}^{n-1} & F_{1x}^{n-1} & F_{1y}^{n-1} & F_{2x}^{n-1} & F_{2y}^{n-1} & F_{3x}^{n-1} & F_{3y}^{n-1} \end{bmatrix}^{\mathrm{T}}.$$

The first six rows and the last six rows of the right eigenvector $\mathbf{X}$ of matrix $\mathbf{H}$ represent displacement components at adjacent arbitrary stations $(n-1)$ and n, respectively, i.e.

$$\mathbf{X}^{\mathrm{T}}(n-1) = \begin{bmatrix} D_{1x}^{n-1} & D_{1y}^{n-1} & D_{2x}^{n-1} & D_{2y}^{n-1} & D_{3x}^{n-1} & D_{3y}^{n-1} & D_{1x}^{n} & D_{1y}^{n} & D_{2x}^{n} & D_{2y}^{n} & D_{3x}^{n} & D_{3y}^{n} \end{bmatrix}^{\mathrm{T}}.$$

These components of the eigenvectors associated with both transfer matrices are shown in Figure 2.2.

Despite the obvious difference between eigenvectors $\mathbf{V}$ and $\mathbf{X}$, they are related as follows: $\mathbf{V}$ is an eigenvector of $\mathbf{G}$, that is it satisfies $\mathbf{GV} = \lambda\mathbf{V}$; $\mathbf{X}$ is an eigenvector of $\mathbf{H}$, that is it satisfies $\mathbf{HX} = \lambda\mathbf{X}$. But $\mathbf{G} = \mathbf{LHL}^{-1}$, or equally $\mathbf{H} = \mathbf{L}^{-1}\mathbf{GL}$; employing the former, one has $\left(\mathbf{LHL}^{-1}\right)\mathbf{V} = \lambda\mathbf{V}$ and pre-multiplying by $\mathbf{L}^{-1}$ gives $\mathbf{H}\left(\mathbf{L}^{-1}\mathbf{V}\right) = \lambda\left(\mathbf{L}^{-1}\mathbf{V}\right)$ and hence $\mathbf{X} = \mathbf{L}^{-1}\mathbf{V}$, or $\mathbf{V} = \mathbf{LX}$.
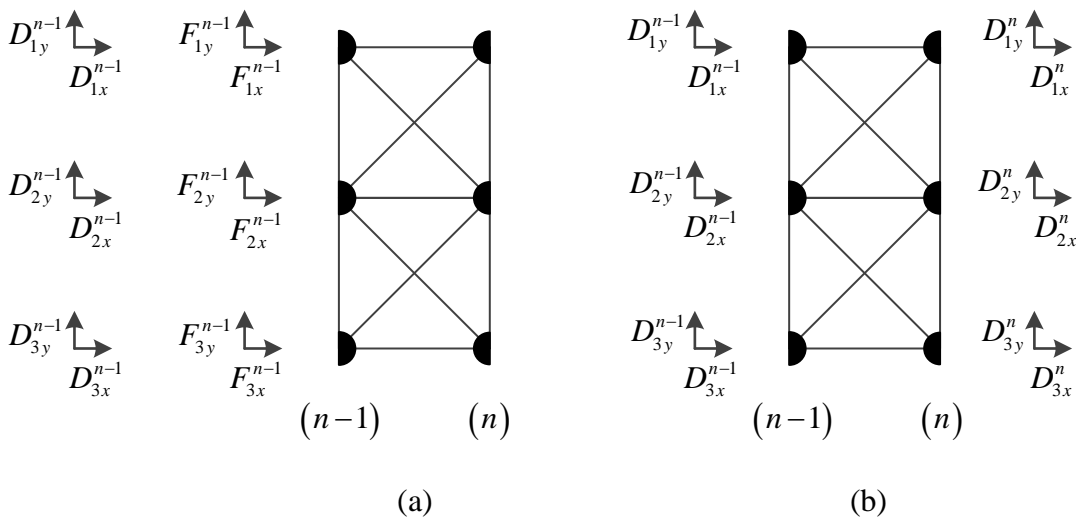
Figure 2.2 (a) Nodal displacements and forces pertaining to eigenvector $\mathbf{V}$ of transfer matrix $\mathbf{G}$; (b) nodal displacements pertaining to eigenvector $\mathbf{X}$ of transfer matrix $\mathbf{H}$.

But we also have $\mathbf{H} = \mathbf{N}^{-1}\mathbf{GN}$, or equally $\mathbf{G} = \mathbf{NHN}^{-1}$; employing the former, one has $\left(\mathbf{N}^{-1}\mathbf{GN}\right)\mathbf{X} = \lambda\mathbf{X}$ and pre-multiplying by $\mathbf{N}$ gives $\mathbf{G}\left(\mathbf{NX}\right) = \lambda\left(\mathbf{NX}\right)$ and hence $\mathbf{V} = \mathbf{NX}$. Employing the latter provides the equivalent $\mathbf{X} = \mathbf{N}^{-1}\mathbf{V}$, or $\mathbf{V} = \mathbf{NX}$.

From the above, it has been found that $\mathbf{V} = \mathbf{NX}$ and $\mathbf{V} = \mathbf{LX}$, that is both $\mathbf{L}$ and $\mathbf{N}$ serve equally to relate $\mathbf{X}$ to $\mathbf{V}$. However there is a subtlety that only becomes apparent when one expands these expressions: write $\mathbf{X}(n-1) = \left[\mathbf{D}^{\mathrm{T}}(n-1) \quad \mathbf{D}^{\mathrm{T}}(n)\right]^{\mathrm{T}}$, then the former becomes

$$\mathbf{V} = \mathbf{NX}(n-1) = \begin{bmatrix} \mathbf{D}(n) \\ \mathbf{K}_{RL}\mathbf{D}(n-1) + \left[\mathbf{K}_{RR} - \dfrac{\omega^2\mathbf{m}}{2}\right]\mathbf{D}(n) \end{bmatrix} = \begin{bmatrix} \mathbf{D}(n) \\ \mathbf{F}(n) \end{bmatrix} = \mathbf{V}(n) \quad (2.16)$$

where the second row of equation (2.3) has been employed. Thus strictly, we have $\mathbf{V}(n) = \mathbf{NX}(n-1)$. For the latter,

$$\mathbf{V} = \mathbf{LX}(n-1) = \begin{bmatrix} \mathbf{D}(n-1) \\ -\left[\mathbf{K}_{LL} - \dfrac{\omega^2\mathbf{m}}{2}\right]\mathbf{D}(n-1) - \mathbf{K}_{LR}\mathbf{D}(n) \end{bmatrix} = \begin{bmatrix} \mathbf{D}(n-1) \\ \mathbf{F}(n-1) \end{bmatrix} = \mathbf{V}(n-1) \quad (2.17)$$

where the first row of equation (2.3) has been employed. Thus strictly, we have $\mathbf{V}(n-1) = \mathbf{LX}(n-1)$.

Finally, we derive expressions for the left eigenvectors of $\mathbf{G}$ and $\mathbf{H}$, as these are required in subsequent analysis to obtain the group velocity. The left eigenvector of matrix $\mathbf{G}$ can be evaluated as follows: let $\overline{\mathbf{V}}$ be the eigenvector associated with the eigenvalue λ^{-1}, i.e. $\mathbf{G}\overline{\mathbf{V}} = \lambda^{-1}\overline{\mathbf{V}}$ or $\mathbf{G}^{-1}\overline{\mathbf{V}} = \lambda\overline{\mathbf{V}}$; but $\mathbf{G}^{-1} = \mathbf{J}^{-1}\mathbf{G}^{T}\mathbf{J}$, so we have $\mathbf{J}^{-1}\mathbf{G}^{T}\mathbf{J}\overline{\mathbf{V}} = \lambda\overline{\mathbf{V}}$ or $\mathbf{G}^{T}\left(\mathbf{J}\overline{\mathbf{V}}\right) = \lambda\left(\mathbf{J}\overline{\mathbf{V}}\right)$ which upon transposition gives $\left(\mathbf{J}\overline{\mathbf{V}}\right)^{T}\mathbf{G} = \lambda\left(\mathbf{J}\overline{\mathbf{V}}\right)^{T}$ or simply $\mathbf{W}^{T}\mathbf{G} = \lambda\mathbf{W}^{T}$ where $\mathbf{W}^{T} = \left(\mathbf{J}\overline{\mathbf{V}}\right)^{T}$ is the left eigenvector of $\mathbf{G}$.

The left eigenvector of matrix $\mathbf{H}$ can be obtained by following a similar procedure: let $\overline{\mathbf{X}}$ be the eigenvector associated with the eigenvalue λ^{-1}, i.e. $\mathbf{H}\overline{\mathbf{X}} = \lambda^{-1}\overline{\mathbf{X}}$ or $\mathbf{H}^{-1}\overline{\mathbf{X}} = \lambda\overline{\mathbf{X}}$; but we know that $\mathbf{H}^{-1} = \tilde{\mathbf{J}}^{-1}\mathbf{H}^{T}\tilde{\mathbf{J}}$, hence $\tilde{\mathbf{J}}^{-1}\mathbf{H}^{T}\tilde{\mathbf{J}}\overline{\mathbf{X}} = \lambda\overline{\mathbf{X}}$ or $\mathbf{H}^{T}\left(\tilde{\mathbf{J}}\overline{\mathbf{X}}\right) = \lambda\left(\tilde{\mathbf{J}}\overline{\mathbf{X}}\right)$ which upon transposition, gives $\left(\tilde{\mathbf{J}}\overline{\mathbf{X}}\right)^{T}\mathbf{H} = \lambda\left(\tilde{\mathbf{J}}\overline{\mathbf{X}}\right)^{T}$ or $\mathbf{Y}^{T}\mathbf{H} = \lambda\mathbf{Y}^{T}$ where $\mathbf{Y}^{T} = \left(\tilde{\mathbf{J}}\overline{\mathbf{X}}\right)^{T}$ is the left eigenvector of $\mathbf{H}$.

2.5 Symplectic orthogonality for transfer matrices G and H

Let $\mathbf{V}_i$ and $\mathbf{V}_j$ be eigenvectors of $\mathbf{G}$ associated with eigenvalues λ_i and λ_j, respectively. Then one has $\mathbf{GV}_i = \lambda_i\mathbf{V}_i$ and $\mathbf{GV}_j = \lambda_j\mathbf{V}_j$. Transpose the former to give $\mathbf{V}_i^{T}\mathbf{G}^{T} = \lambda_i\mathbf{V}_i^{T}$ and then post-multiply by $\mathbf{JGV}_j$ to give $\mathbf{V}_i^{T}\left(\mathbf{G}^{T}\mathbf{JG}\right)\mathbf{V}_j = \lambda_i\mathbf{V}_i^{T}\mathbf{JGV}_j$ which reduces to $\mathbf{V}_i^{T}\mathbf{JV}_j = \lambda_i\lambda_j\mathbf{V}_i^{T}\mathbf{JV}_j$. Finally, rearrange as $\left(1 - \lambda_i\lambda_j\right)\mathbf{V}_i^{T}\mathbf{JV}_j = 0$ which implies that $\mathbf{V}_i^{T}\mathbf{JV}_j = 0$ for $\lambda_i \neq 1/\lambda_j$. This result shows that an eigenvector associated with an

eigenvalue of the transfer matrix $\mathbf{G}$ is symplectic orthogonal to all other eigenvectors including itself with the exception of the eigenvector(s) associated with its reciprocal eigenvalue; the possible plurality of eigenvectors noted above can occur when one has a crossing of branches on a dispersion diagram, with a repeated eigenvalue and distinct eigenvectors. The symplectic orthogonality is a special case of the Betti-Maxwell reciprocal theorem as shown by Zhong and Williams [57,58] and later by Stephen [1]. For completeness, an implementation of the reciprocal theorem to obtain this expression is given in Appendix A.3. Zhong and Williams [57] have also shown that if $\mathbf{V}_i$ and $\mathbf{V}_j$ correspond to a reciprocal eigenpair, that is $\lambda_i = 1/\lambda_j$, then one can scale the eigenvector lengths such that $\mathbf{V}_i^{\mathrm{T}} \mathbf{J} \mathbf{V}_j = 1$ and $\mathbf{V}_j^{\mathrm{T}} \mathbf{J} \mathbf{V}_i = -1$; however, as will be seen in Chapter 3 (Section 3.10), this procedure loses information in the form of the Krein signature [63].

A similar procedure can be followed for matrix $\mathbf{H}$. Let $\mathbf{X}_i$ and $\mathbf{X}_j$ be the eigenvectors of $\mathbf{H}$ associated with eigenvalues λ_i and λ_j, respectively. Then one has $\mathbf{H}\mathbf{X}_i = \lambda_i \mathbf{X}_i$ and $\mathbf{H}\mathbf{X}_j = \lambda_j \mathbf{X}_j$. Transpose the former to give $\mathbf{X}_i^{\mathrm{T}} \mathbf{H}^{\mathrm{T}} = \lambda_i \mathbf{X}_i^{\mathrm{T}}$ and then post-multiply by $\tilde{\mathbf{J}} \mathbf{H} \mathbf{X}_j$ to give $\mathbf{X}_i^{\mathrm{T}} \left(\mathbf{H}^{\mathrm{T}} \tilde{\mathbf{J}} \mathbf{H} \right) \mathbf{X}_j = \lambda_i \mathbf{X}_i^{\mathrm{T}} \tilde{\mathbf{J}} \mathbf{H} \mathbf{X}_j$ which reduces to $\mathbf{X}_i^{\mathrm{T}} \tilde{\mathbf{J}} \mathbf{X}_j = \lambda_i \lambda_j \mathbf{X}_i^{\mathrm{T}} \tilde{\mathbf{J}} \mathbf{X}_j$. Finally, rearrange as $\left(1 - \lambda_i \lambda_j \right) \mathbf{X}_i^{\mathrm{T}} \tilde{\mathbf{J}} \mathbf{X}_j = 0$ which implies that $\mathbf{X}_i^{\mathrm{T}} \tilde{\mathbf{J}} \mathbf{X}_j = 0$ for $\lambda_i \neq 1/\lambda_j$; again, for $\mathbf{X}_i$ and $\mathbf{X}_j$ which corresponds to a reciprocal eigenpair, the eigenvector lengths can be scaled such that $\mathbf{X}_i^{\mathrm{T}} \tilde{\mathbf{J}} \mathbf{X}_j = 1$ and $\mathbf{X}_j^{\mathrm{T}} \tilde{\mathbf{J}} \mathbf{X}_i = -1$. In terms of the metric $\mathbf{J}$, this can be expressed as $\left(1 - \lambda_i \lambda_j \right) \left(\mathbf{N} \mathbf{X}_i \right)^{\mathrm{T}} \mathbf{J} \left(\mathbf{N} \mathbf{X}_j \right) = 0$ or equivalently $\left(1 - \lambda_i \lambda_j \right) \left(\mathbf{L} \mathbf{X}_i \right)^{\mathrm{T}} \mathbf{J} \left(\mathbf{L} \mathbf{X}_j \right) = 0$. This is referred to as weighted symplectic orthogonality.

2.6   Group velocity

The velocity at which energy flows through a dispersive structure or medium is known as the group velocity [47,72,75,93] and is defined as the derivative of frequency with respect to wavenumber, i.e. $c_{\mathrm{g}} = \dfrac{\mathrm{d}\omega}{\mathrm{d}\varphi}$. Using the chain rule $c_{\mathrm{g}} = \dfrac{\mathrm{d}\omega}{\mathrm{d}\varphi} = \dfrac{\mathrm{d}\omega}{\mathrm{d}\lambda} \dfrac{\mathrm{d}\lambda}{\mathrm{d}\varphi}$, and since $\lambda = \exp(\mathrm{i}\varphi)$, then $\dfrac{\mathrm{d}\lambda}{\mathrm{d}\varphi} = \mathrm{i}\exp(\mathrm{i}\varphi) = \mathrm{i}\lambda$; and one finds $c_{\mathrm{g}} = \mathrm{i}\lambda \dfrac{\mathrm{d}\omega}{\mathrm{d}\lambda}$. We now write matrix $\mathbf{H}$ in the form

$$\mathbf{H} = \begin{bmatrix} \mathbf{0} & \mathbf{I} \\ -\mathbf{K}_{LR}^{-1}\mathbf{K}_{RL} & -\mathbf{K}_{LR}^{-1}\left[\mathbf{K}_{LL} + \mathbf{K}_{RR}\right] \end{bmatrix} + \omega^2 \begin{bmatrix} \mathbf{0} & \mathbf{0} \\ \mathbf{0} & \mathbf{K}_{LR}^{-1}\mathbf{m} \end{bmatrix} \quad (2.18)$$

or more compactly, $\mathbf{H} = \mathbf{H}_0 + \omega^2\mathbf{H}_2$. The eigenvalue problem $[\mathbf{H} - \lambda\mathbf{I}]\mathbf{X}(n-1) = \mathbf{0}$, where

$\mathbf{X}(n-1) = \left[\mathbf{D}^{\mathrm{T}}(n-1) \quad \mathbf{D}^{\mathrm{T}}(n)\right]^{\mathrm{T}}$, can then be written as $\left[\mathbf{H}_0 + \omega^2\mathbf{H}_2 - \lambda\mathbf{I}\right]\mathbf{X}(n-1) = \mathbf{0}$.

Differentiating with respect to λ gives

$$\left[2\omega\frac{\mathrm{d}\omega}{\mathrm{d}\lambda}\mathbf{H}_2 - \mathbf{I}\right]\mathbf{X} + \left[\mathbf{H}_0 + \omega^2\mathbf{H}_2 - \lambda\mathbf{I}\right]\frac{\mathrm{d}\mathbf{X}}{\mathrm{d}\lambda} = \mathbf{0} \quad (2.19)$$

where the index $(n-1)$ has been omitted. Let $\mathbf{Y}^{\mathrm{T}}$ be the left eigenvector of matrix $\mathbf{H}$,

pertaining to the same eigenvalue λ, then $\mathbf{Y}$ satisfies $\left[\mathbf{H}_0 + \omega^2\mathbf{H}_2 - \lambda\mathbf{I}\right]^{\mathrm{T}}\mathbf{Y} = \mathbf{0}$ or by

transposing $\mathbf{Y}^{\mathrm{T}}\left[\mathbf{H}_0 + \omega^2\mathbf{H}_2 - \lambda\mathbf{I}\right] = \mathbf{0}$. So if we pre-multiply equation (2.19) by $\mathbf{Y}^{\mathrm{T}}$, the

second term will disappear to give $\mathbf{Y}^{\mathrm{T}}\left[2\omega\frac{\mathrm{d}\omega}{\mathrm{d}\lambda}\mathbf{H}_2 - \mathbf{I}\right]\mathbf{X} = 0$ or $\frac{\mathrm{d}\omega}{\mathrm{d}\lambda} = \frac{\mathbf{Y}^{\mathrm{T}}\mathbf{X}}{2\omega\mathbf{Y}^{\mathrm{T}}\mathbf{H}_2\mathbf{X}}$. The

group velocity is then

$$c_{\mathrm{g}} = \mathrm{i}\lambda\frac{\mathbf{Y}^{\mathrm{T}}\mathbf{X}}{2\omega\mathbf{Y}^{\mathrm{T}}\mathbf{H}_2\mathbf{X}}. \quad (2.20)$$

A similar approach can be adopted for the matrix $\mathbf{G}$, which may be decomposed as $\mathbf{G} = \mathbf{G}_0 + \omega^2\mathbf{G}_2 + \omega^4\mathbf{G}_4$ where

$$\mathbf{G}_0 = \begin{bmatrix} -\mathbf{K}_{LR}^{-1}\mathbf{K}_{LL} & -\mathbf{K}_{LR}^{-1} \\ \mathbf{K}_{RL} - \mathbf{K}_{RR}\mathbf{K}_{LR}^{-1}\mathbf{K}_{LL} & -\mathbf{K}_{RR}\mathbf{K}_{LR}^{-1} \end{bmatrix}, \quad \mathbf{G}_2 = \begin{bmatrix} \dfrac{\mathbf{m}}{2}\mathbf{K}_{LR}^{-1} & \mathbf{0} \\ \dfrac{\mathbf{m}}{2}\left[\mathbf{K}_{LR}^{-1}\mathbf{K}_{LL} + \mathbf{K}_{RR}\mathbf{K}_{LR}^{-1}\right] & \dfrac{\mathbf{m}}{2}\mathbf{K}_{LR}^{-1} \end{bmatrix} \text{ and }$$

$\mathbf{G}_4 = \begin{bmatrix} \mathbf{0} & \mathbf{0} \\ -\dfrac{\mathbf{m}^2}{4}\mathbf{K}_{LR}^{-1} & \mathbf{0} \end{bmatrix}$; proceeding as above for the eigenvalue problem $[\mathbf{G} - \lambda\mathbf{I}]\mathbf{V} = \mathbf{0}$ one

finds $\dfrac{\mathrm{d}\omega}{\mathrm{d}\lambda} = \dfrac{\mathbf{W}^{\mathrm{T}}\mathbf{V}}{2\omega\mathbf{W}^{\mathrm{T}}\mathbf{G}_2\mathbf{V} + 4\omega^3\mathbf{W}^{\mathrm{T}}\mathbf{G}_4\mathbf{V}}$ and hence group velocity

$$c_{\mathrm{g}} = \mathrm{i}\lambda\frac{\mathbf{W}^{\mathrm{T}}\mathbf{V}}{2\omega\mathbf{W}^{\mathrm{T}}\mathbf{G}_2\mathbf{V} + 4\omega^3\mathbf{W}^{\mathrm{T}}\mathbf{G}_4\mathbf{V}}, \quad (2.21)$$

where $\mathbf{W}^{\mathrm{T}}$ is the left eigenvector of matrix $\mathbf{G}$. For both equations (2.20) and (2.21), we

note that c_{g} is real because the product of λ and $\mathrm{d}\omega/\mathrm{d}\lambda$ is purely imaginary.

Clearly, the expression for group velocity involving transfer matrix $\mathbf{H}$ is the more succinct,

and since the (12×12) matrix $\mathbf{H}_2$ contains three (6×6) zero partitions, the structure of

expression (2.20) can be revealed, as follows: since $\mathbf{X}(n-1)=\begin{bmatrix}\mathbf{D}^{\mathrm{T}}(n-1) & \mathbf{D}^{\mathrm{T}}(n)\end{bmatrix}^{\mathrm{T}}$, the

product in the denominator $\mathbf{H}_2\mathbf{X}=\begin{bmatrix}\mathbf{0} & m\mathbf{K}_{\mathrm{LR}}^{-1}\mathbf{D}^{\mathrm{T}}(n)\end{bmatrix}^{\mathrm{T}}$ is a column vector, while from

Section 2.4 one has $\mathbf{Y}^{\mathrm{T}}=\left(\tilde{\mathbf{J}}\overline{\mathbf{X}}\right)^{\mathrm{T}}$, or written in full

$\mathbf{Y}^{\mathrm{T}}=\begin{bmatrix}-\overline{\mathbf{D}}^{\mathrm{T}}(n)\mathbf{K}_{\mathrm{LR}}^{\mathrm{T}} & \overline{\mathbf{D}}^{\mathrm{T}}(n-1)\mathbf{K}_{\mathrm{RL}}^{\mathrm{T}}\end{bmatrix}=\begin{bmatrix}-\overline{\mathbf{D}}^{\mathrm{T}}(n)\mathbf{K}_{\mathrm{RL}} & \overline{\mathbf{D}}^{\mathrm{T}}(n-1)\mathbf{K}_{\mathrm{LR}}\end{bmatrix}$ since $\mathbf{K}_{\mathrm{RL}}=\mathbf{K}_{\mathrm{LR}}^{\mathrm{T}}$.

In turn, the denominator reduces to the scalar $\mathbf{Y}^{\mathrm{T}}\mathbf{H}_2\mathbf{X}=m\overline{\mathbf{D}}^{\mathrm{T}}(n-1)\mathbf{D}(n)$. The numerator

is the scalar $\mathbf{Y}^{\mathrm{T}}\mathbf{X}=\overline{\mathbf{D}}^{\mathrm{T}}(n-1)\mathbf{K}_{\mathrm{LR}}\mathbf{D}(n)-\overline{\mathbf{D}}^{\mathrm{T}}(n)\mathbf{K}_{\mathrm{RL}}\mathbf{D}(n-1)$. If we now express all of the

displacement vectors in term of cross-section index $(n-1)$, that is $\mathbf{D}(n)=\lambda\mathbf{D}(n-1)$ and

$\overline{\mathbf{D}}(n)=\lambda^{-1}\mathbf{D}(n-1)$, the expression for the group velocity becomes

$$c_{\mathrm{g}}=\frac{\mathrm{i}\,\overline{\mathbf{D}}^{\mathrm{T}}\left(\lambda\mathbf{K}_{\mathrm{LR}}-\lambda^{-1}\mathbf{K}_{\mathrm{RL}}\right)\mathbf{D}}{2m\omega\overline{\mathbf{D}}^{\mathrm{T}}\mathbf{D}},\qquad(2.22)$$

where the $(n-1)$ index has been omitted. While not as succinct as equation (2.20), this form

is suggestive of possible opposing contributions which could lead to both positive and

negative group velocity, this signifying normal and anomalous dispersion, respectively. For

the example structure, such anomalous dispersion does indeed occur as will be seen in

Chapter 3 where it is explored in detail.

2.7   Natural frequencies of finite length structures

Finite length repetitive structures inevitably have boundary conditions, typically of zero

displacement (fixed) or zero force (free), and for this reason the formulation employing

transfer matrix $\mathbf{G}$ seems the more appropriate. For example, for a structure having N cells,

at a fixed left-hand end one immediately has $\mathbf{V}(0)=\begin{bmatrix}\mathbf{D}^{\mathrm{T}}(0) & \mathbf{F}^{\mathrm{T}}(0)\end{bmatrix}^{\mathrm{T}}=\begin{bmatrix}\mathbf{0} & \mathbf{F}^{\mathrm{T}}(0)\end{bmatrix}^{\mathrm{T}}$,

whilst for a free right-hand end one has $\mathbf{V}(N)=\begin{bmatrix}\mathbf{D}^{\mathrm{T}}(N) & \mathbf{F}^{\mathrm{T}}(N)\end{bmatrix}^{\mathrm{T}}=\begin{bmatrix}\mathbf{D}^{\mathrm{T}}(N) & \mathbf{0}\end{bmatrix}^{\mathrm{T}}$. It is

also possible to have *mixed* end conditions, for example some but not all of the nodal masses

at either end could be fixed, the remaining free; for such cases, one can always re-cast the

state vector column so that the first six elements are zero and the following six are unknown,

and re-order the rows of the transfer matrix $\mathbf{G}$ accordingly. We now present three approaches

to derive the frequency equation.

2.7.1 Phase closure

Phase closure [19,94] is based upon the idea that for a standing wave, the total phase change for a complete circumnavigation of the structure is an integer multiple of 2π. The state vector $\begin{bmatrix} \mathbf{D}^{\mathrm{T}}(n) & \mathbf{F}^{\mathrm{T}}(n) \end{bmatrix}^{\mathrm{T}}$ at any given cross-section n can only consist of the eigenvectors; how much of each is defined by *participation coefficients*, also known as the wave amplitudes $\mathbf{w}(n)$, and since some waves are propagating while others are decaying, the amount of each will be different at each cross-section. Thus we may write $\begin{bmatrix} \mathbf{D}^{\mathrm{T}}(n) & \mathbf{F}^{\mathrm{T}}(n) \end{bmatrix}^{\mathrm{T}} = \mathbf{V}\mathbf{w}(n)$ where $\mathbf{V}$ is now an ordered (12×12) matrix containing the twelve eigenvectors of $\mathbf{G}$; in partitioned form

$$\begin{bmatrix} \mathbf{D}(n) \\ \mathbf{F}(n) \end{bmatrix} = \begin{bmatrix} \mathbf{V}_{\mathrm{R}} & \mathbf{V}_{\mathrm{L}} \end{bmatrix} \begin{bmatrix} \mathbf{w}_{\mathrm{R}}(n) \\ \mathbf{w}_{\mathrm{L}}(n) \end{bmatrix} = \begin{bmatrix} \mathbf{V}_{\mathrm{R,D}} & \mathbf{V}_{\mathrm{L,D}} \\ \mathbf{V}_{\mathrm{R,F}} & \mathbf{V}_{\mathrm{L,F}} \end{bmatrix} \begin{bmatrix} \mathbf{w}_{\mathrm{R}}(n) \\ \mathbf{w}_{\mathrm{L}}(n) \end{bmatrix} \tag{2.23}$$

where the subscripts R and L refer to right- and left-going waves, respectively, while subscripts D and F refer to the displacement and force vectors, respectively. The order of columns of $\mathbf{V}_{\mathrm{R}}$ and $\mathbf{V}_{\mathrm{L}}$ must correspond to their eigenvalue pairs.

Now introduce reflection matrices $\mathbf{R}$ which describe the effect of the end-condition on each of the impinging wave amplitudes. Consider a finite length structure of N cells. For a free left-hand end, the force vector is $\mathbf{F}(0) = \mathbf{0}$; from the second row of equation (2.23) one has $\mathbf{V}_{\mathrm{R,F}}\mathbf{w}_{\mathrm{R}}(0) + \mathbf{V}_{\mathrm{L,F}}\mathbf{w}_{\mathrm{L}}(0) = \mathbf{0}$, which may be arranged in the form $\mathbf{w}_{\mathrm{R}}(0) = \mathbf{R}(0)\mathbf{w}_{\mathrm{L}}(0)$, where $\mathbf{R}(0) = -\mathbf{V}_{\mathrm{R,F}}^{-1}\mathbf{V}_{\mathrm{L,F}}$ is the reflection matrix at the free left-hand end. Similarly, for a free right-hand end, the force vector is $\mathbf{F}(N) = \mathbf{0}$. Following the same procedure gives $\mathbf{w}_{\mathrm{L}}(N) = \mathbf{R}(N)\mathbf{w}_{\mathrm{R}}(N)$, where $\mathbf{R}(N) = -\mathbf{V}_{\mathrm{L,F}}^{-1}\mathbf{V}_{\mathrm{R,F}}$ is the reflection matrix at the free right-hand end. Note that $\mathbf{R}(N) = \mathbf{R}^{-1}(0)$, which can be attributed to symmetry.

To apply the phase closure principle, consider right-going waves impinging upon the right-hand end, station N, $\mathbf{w}_{\mathrm{R}}(N)$ which can be written in terms of $\mathbf{w}_{\mathrm{R}}(0)$ as $\mathbf{w}_{\mathrm{R}}(N) = \mathbf{\Lambda}_{\mathrm{R}}^{N}\mathbf{w}_{\mathrm{R}}(0)$ where $\mathbf{\Lambda}_{\mathrm{R}}$ is a diagonal eigenvalue matrix associated with right-going waves. By repeated substitution,

$$\begin{aligned}
\mathbf{w}_R(N) &= \mathbf{\Lambda}_R^N \mathbf{w}_R(0) \\
&= \mathbf{\Lambda}_R^N \mathbf{R}(0) \mathbf{w}_L(0) \\
&= \mathbf{\Lambda}_R^N \mathbf{R}(0) \mathbf{\Lambda}_R^N \mathbf{w}_L(N) \\
&= \mathbf{\Lambda}_R^N \mathbf{R}(0) \mathbf{\Lambda}_R^N \mathbf{R}(N) \mathbf{w}_R(N),
\end{aligned}$$

(2.24)

or $\left[\mathbf{\Lambda}_R^N \mathbf{R}(0) \mathbf{\Lambda}_R^N \mathbf{R}(N) - \mathbf{I} \right] \mathbf{w}_R(N) = \mathbf{0}$. For a standing wave to occur, one must have

$$\det\left[\mathbf{\Lambda}_R^N \mathbf{R}(0) \mathbf{\Lambda}_R^N \mathbf{R}(N) - \mathbf{I} \right] = 0 . \tag{2.25}$$

Note that the determinant is complex, and the natural frequencies are found when the real and imaginary parts vanish simultaneously.

The formulation, equation (2.25), is unchanged for structures with different end conditions; what do change are the reflection matrices. These are summarised as follows:

Free left-hand end $\quad \mathbf{w}_R(0) = \mathbf{R}(0) \mathbf{w}_L(0)$ where $\mathbf{R}(0) = -\mathbf{V}_{R,F}^{-1} \mathbf{V}_{L,F}$

Fixed left-hand end $\quad \mathbf{w}_R(0) = \mathbf{R}(0) \mathbf{w}_L(0)$ where $\mathbf{R}(0) = -\mathbf{V}_{R,D}^{-1} \mathbf{V}_{L,D}$

Free right-hand end $\quad \mathbf{w}_L(N) = \mathbf{R}(N) \mathbf{w}_R(N)$ where $\mathbf{R}(N) = -\mathbf{V}_{L,F}^{-1} \mathbf{V}_{R,F}$

Fixed right-hand end $\quad \mathbf{w}_L(N) = \mathbf{R}(N) \mathbf{w}_R(N)$ where $\mathbf{R}(N) = -\mathbf{V}_{L,D}^{-1} \mathbf{V}_{R,D}$

Two comments should be made: first, the $\mathbf{w}_R(N)$ on the left-hand side of equation (2.24) is the same as that on the right-hand side only by virtue of a spatial phase change of an integer multiple of 2π. For the fundamental natural frequency, this phase change will be 2π, for the second 4π, and so on. Second, for a free vibration, right-going waves can only propagate, $|\lambda| = 1$, or decay, $|\lambda| < 1$, as one moves from left to right along the structure; thus each of the eigenvalues within matrix $\mathbf{\Lambda}_R$ has modulus equal to or less than unity, and powers of $\mathbf{\Lambda}_R$ will in turn only lead to terms whose modulus is equal to or less than unity. Similarly, left-going waves after reflection from the right-hand end can only propagate or decay as one moves from right to left along the structure, so one must still employ those eigenvalues whose modulus is equal to or less than unity, that is $\mathbf{\Lambda}_R$, which is why one has employed $\mathbf{w}_L(0) = \mathbf{\Lambda}_R^N \mathbf{w}_L(N)$ in the development of equation (2.24). The reciprocal eigenvalue matrix, $\mathbf{\Lambda}_L$, which contains eigenvalues with modulus equal to or greater than unity, does not therefore feature in the formulation, and this exclusion ensures numerical

stability however large the value of N. The Riccati transfer matrix method, previously employed for the static analysis of the present structure [49], also excludes eigenvalues greater than unity, again ensuring numerical stability.

2.7.2 Direct application of boundary conditions for matrix $\mathbf{G}$

Again for a finite length structure of N cells, the state vector at station N is related to that at station 0 by

$$\begin{bmatrix} \mathbf{D}(N) \\ \mathbf{F}(N) \end{bmatrix} = \mathbf{G}^N \begin{bmatrix} \mathbf{D}(0) \\ \mathbf{F}(0) \end{bmatrix}; \tag{2.26}$$

powers of $\mathbf{G}$ are computed most efficiently by noting that $\mathbf{G} = \mathbf{V}\mathbf{\Lambda}\mathbf{V}^{-1}$, so that $\mathbf{G}^N = \mathbf{V}\mathbf{\Lambda}^N\mathbf{V}^{-1}$. However, since the diagonal $\mathbf{\Lambda}$ contains both $\mathbf{\Lambda}_\mathrm{L}$ and $\mathbf{\Lambda}_\mathrm{R}$, powers of the former will become large for large N, leading to numerical instability. Introduce the notation

$$\mathbf{G}^N = \hat{\mathbf{G}} = \begin{bmatrix} \hat{\mathbf{G}}_{\mathrm{DD}} & \hat{\mathbf{G}}_{\mathrm{DF}} \\ \hat{\mathbf{G}}_{\mathrm{FD}} & \hat{\mathbf{G}}_{\mathrm{FF}} \end{bmatrix}.$$

For free-free ends, $\mathbf{F}(0) = \mathbf{F}(N) = \mathbf{0}$, and from the second row of equation (2.26) one has $\hat{\mathbf{G}}_{\mathrm{FD}}\mathbf{D}(0) = \mathbf{0}$ and hence the frequency equation $\det\left(\hat{\mathbf{G}}_{\mathrm{FD}}\right) = 0$. For fixed-fixed ends, $\mathbf{D}(0) = \mathbf{D}(N) = \mathbf{0}$ and from the first row of equation (2.26), one has $\hat{\mathbf{G}}_{\mathrm{DF}}\mathbf{F}(0) = \mathbf{0}$ and hence the frequency equation $\det\left(\hat{\mathbf{G}}_{\mathrm{DF}}\right) = 0$. Finally, for fixed-free and free-fixed ends, the frequency equations are $\det\left(\hat{\mathbf{G}}_{\mathrm{FF}}\right) = 0$ and $\det\left(\hat{\mathbf{G}}_{\mathrm{DD}}\right) = 0$, respectively. Unlike phase closure, these determinantal frequency equations employing transfer matrix $\mathbf{G}$ are real.

2.7.3 Direct application of boundary conditions for matrix $\mathbf{H}$

Consider, again, a free-free structure of N cells. Since the force vector does not naturally feature within this formulation, it has to be introduced at either end. For a free vibration, the equations of motion at the left- and right-hand ends are, respectively

$$-\mathbf{F}(0) = \left[\mathbf{K}_{\mathrm{LL}} - \frac{\omega^2\mathbf{m}}{2}\right]\mathbf{D}(0) + \mathbf{K}_{\mathrm{LR}}\mathbf{D}(1), \text{ and } \mathbf{F}(N) = \mathbf{K}_{\mathrm{RL}}\mathbf{D}(N-1) + \left[\mathbf{K}_{\mathrm{RR}} - \frac{\omega^2\mathbf{m}}{2}\right]\mathbf{D}(N).$$

From the boundary condition $\mathbf{F}(0) = \mathbf{0}$ one has $\mathbf{D}(1) = -\mathbf{K}_{\mathrm{LR}}^{-1}\left[\mathbf{K}_{\mathrm{LL}} - \frac{\omega^2\mathbf{m}}{2}\right]\mathbf{D}(0)$, and

hence for the first cell,

$$\mathbf{X}(0) = \begin{bmatrix} \mathbf{D}(0) \\ \mathbf{D}(1) \end{bmatrix} = \begin{bmatrix} \mathbf{I} \\ -\mathbf{K}_{\text{LR}}^{-1} \left[\mathbf{K}_{\text{LL}} - \dfrac{\omega^2 \mathbf{m}}{2} \right] \end{bmatrix} \mathbf{D}(0). \tag{2.27}$$

From the boundary condition $\mathbf{F}(N) = \mathbf{0}$ one has for the Nth cell

$$\left[\mathbf{K}_{\text{RL}} \quad \left[\mathbf{K}_{\text{RR}} - \dfrac{\omega^2 \mathbf{m}}{2} \right] \right] \mathbf{X}(N-1) = \mathbf{0}, \tag{2.28}$$

where $\mathbf{X}(N-1) = \begin{bmatrix} \mathbf{D}^{\text{T}}(N-1) & \mathbf{D}^{\text{T}}(N) \end{bmatrix}^{\text{T}}$. Since

$$\mathbf{X}(N-1) = \mathbf{H}^{N-1} \mathbf{X}(0), \tag{2.29}$$

one immediately has

$$\left[\mathbf{K}_{\text{RL}} \quad \left[\mathbf{K}_{\text{RR}} - \dfrac{\omega^2 \mathbf{m}}{2} \right] \right] \mathbf{H}^{N-1} \begin{bmatrix} \mathbf{I} \\ -\mathbf{K}_{\text{LR}}^{-1} \left[\mathbf{K}_{\text{LL}} - \dfrac{\omega^2 \mathbf{m}}{2} \right] \end{bmatrix} \mathbf{D}(0) = \mathbf{0}, \tag{2.30}$$

and for a natural frequency

$$\det\left(\left[\mathbf{K}_{\text{RL}} \quad \left[\mathbf{K}_{\text{RR}} - \dfrac{\omega^2 \mathbf{m}}{2} \right] \right] \mathbf{H}^{N-1} \begin{bmatrix} \mathbf{I} \\ -\mathbf{K}_{\text{LR}}^{-1} \left[\mathbf{K}_{\text{LL}} - \dfrac{\omega^2 \mathbf{m}}{2} \right] \end{bmatrix} \right) = 0, \tag{2.31}$$

where $N \geq 1$ must be satisfied.

For fixed-fixed ends, the left- and right-hand boundary conditions are $\mathbf{D}(0) = \mathbf{D}(N) = \mathbf{0}$, or in state vector form

$$\mathbf{X}(0) = \begin{bmatrix} \mathbf{D}(0) \\ \mathbf{D}(1) \end{bmatrix} = \begin{bmatrix} \mathbf{0} \\ \mathbf{I} \end{bmatrix} \mathbf{D}(1) \text{ and} \tag{2.32}$$

$$\begin{bmatrix} \mathbf{0} & \mathbf{I} \end{bmatrix} \mathbf{X}(N-1) = \mathbf{0}, \tag{2.33}$$

where $\mathbf{X}(N-1) = \begin{bmatrix} \mathbf{D}^{\text{T}}(N-1) & \mathbf{D}^{\text{T}}(N) \end{bmatrix}^{\text{T}}$, respectively. Substitute equation (2.32) into equation (2.29) and the resulting expression into equation (2.33) gives $\begin{bmatrix} \mathbf{0} & \mathbf{I} \end{bmatrix} \mathbf{H}^{N-1} \begin{bmatrix} \mathbf{0} & \mathbf{I} \end{bmatrix}^{\text{T}} \mathbf{D}(1) = \mathbf{0}$, where $N > 1$ must be satisfied (if $N = 1$, then all the point masses are fixed, and vibration is impossible as the bars themselves are considered massless). For a natural frequency, one must have $\det\left(\begin{bmatrix} \mathbf{0} & \mathbf{I} \end{bmatrix} \mathbf{H}^{N-1} \begin{bmatrix} \mathbf{0} & \mathbf{I} \end{bmatrix}^{\text{T}} \right) = 0$. If we mimic the notation employed in the previous section, that is write $\mathbf{H}^{N-1} = \hat{\mathbf{H}} = \begin{bmatrix} \hat{\mathbf{H}}_{11} & \hat{\mathbf{H}}_{12} \\ \hat{\mathbf{H}}_{21} & \hat{\mathbf{H}}_{22} \end{bmatrix}$,

then the determinantal frequency equation above reduces to the more succinct form $\det\left(\hat{\mathbf{H}}_{22}\right)=0$.

For fixed-free ends, the fixed left-hand end satisfies equation (2.32), while the free right-hand end satisfies equation (2.28); following the same procedures leads to

$$\left[\mathbf{K}_{RL}\quad\left[\mathbf{K}_{RR}-\frac{\omega^2\mathbf{m}}{2}\right]\right]\mathbf{H}^{N-1}\begin{bmatrix}\mathbf{0}\\\mathbf{I}\end{bmatrix}\mathbf{D}(1)=\mathbf{0},\tag{2.34}$$

and for a natural frequency one has

$$\det\left(\left[\mathbf{K}_{RL}\quad\left[\mathbf{K}_{RR}-\frac{\omega^2\mathbf{m}}{2}\right]\right]\mathbf{H}^{N-1}\begin{bmatrix}\mathbf{0}\\\mathbf{I}\end{bmatrix}\right)=0.\tag{2.35}$$

For free-fixed ends, the free left-hand end satisfies equation (2.27) while the fixed right-hand end satisfies equation (2.33). Again, following the same procedures gives

$$\begin{bmatrix}\mathbf{0}&\mathbf{I}\end{bmatrix}\mathbf{H}^{N-1}\begin{bmatrix}\mathbf{I}\\-\mathbf{K}_{LR}^{-1}\left[\mathbf{K}_{LL}-\frac{\omega^2\mathbf{m}}{2}\right]\end{bmatrix}\mathbf{D}(0)=\mathbf{0},\tag{2.36}$$

and for a natural frequency one has

$$\det\left(\begin{bmatrix}\mathbf{0}&\mathbf{I}\end{bmatrix}\mathbf{H}^{N-1}\begin{bmatrix}\mathbf{I}\\-\mathbf{K}_{LR}^{-1}\left[\mathbf{K}_{LL}-\frac{\omega^2\mathbf{m}}{2}\right]\end{bmatrix}\right)=0.\tag{2.37}$$

Again, these determinantal equations employing transfer matrix $\mathbf{H}$ are real.

As with $\mathbf{G}$, powers of $\mathbf{H}$ are computed most efficiently by noting that $\mathbf{H}=\mathbf{X}\boldsymbol{\Lambda}\mathbf{X}^{-1}$, so that $\mathbf{H}^{N-1}=\mathbf{X}\boldsymbol{\Lambda}^{N-1}\mathbf{X}^{-1}$, but again one can expect numerical instability as N becomes large.

2.7.4 Numerical example

Natural frequencies of finite length (repetitive) structures can be found by using phase closure principle or by direct application of boundary conditions on state space relations involving transfer matrices $\mathbf{G}$ or $\mathbf{H}$. In this section, both methods are implemented on a five cells free-free framework and the results are compared with those obtained from the finite element method where exact solutions can be achieved for the model framework. Figure 2.3 is a plot of complex determinant against frequency squared obtained using the phase closure method, computed with frequency (squared) step change of 0.01 rad^2/s^2. The

natural frequencies are identified when both the real and imaginary parts vanish. Alternatively, one can plot the absolute values of the determinant against the frequency.

We found numerically that the force eigenvectors associated with the right-going wave $\mathbf{V}_{R,F}$ and/or left-going wave $\mathbf{V}_{L,F}$ degenerate when two columns of the matrix appear identical, as happens when the dispersion branches cross each other, or one of its columns becomes zero as happens when $\omega^2 = 4$. As a result, the natural frequency determinantal equation becomes singular and gives a large determinant; these appear as spikes on Figure 2.3. The gaps on Figure 2.3 appear because extreme determinants are removed from the plot since the values affect the *y*-axis scaling. Clearly, phase closure method is affected by matrix degeneracy at certain frequencies. Nonetheless, all of the natural frequencies (except at $\omega^2 = 4$) can be identified because a sufficiently small frequency step is taken in the computation. Accuracy of the method can be improved (over certain frequency interval) by taking a smaller frequency step.
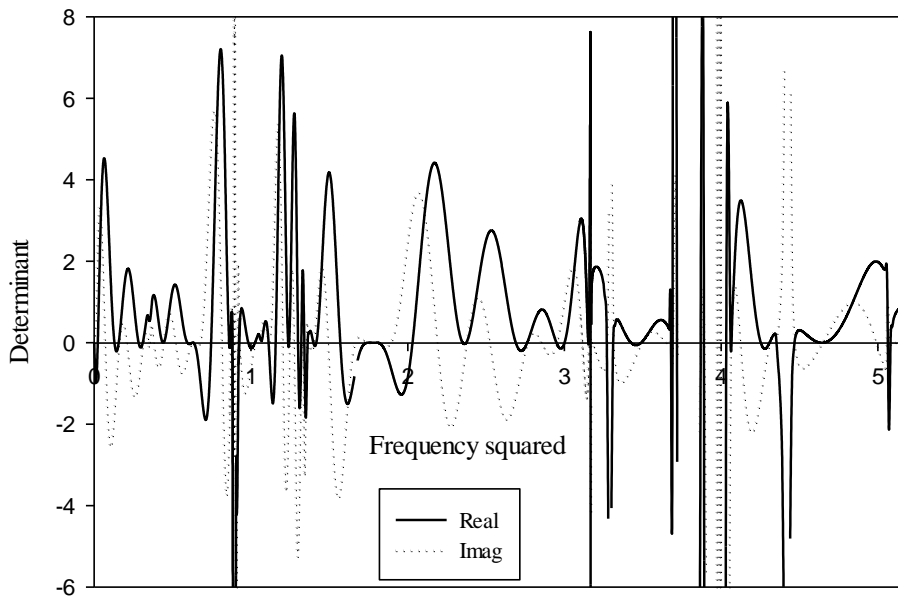
Figure 2.3 Real and imaginary parts of determinant against frequency squared, ω^2, ($\mathrm{rad}^2\ \mathrm{s}^{-2}$) for a free-free five cells framework evaluated using phase closure method.

Figure 2.4 shows a plot of determinant against frequency squared evaluated using direct application of boundary conditions on state space relation involving transfer matrix $\mathbf{H}$. The determinant becomes very large at high frequencies; since the natural frequencies are

identified when the determinants vanish, the determinants above 1 and below −1 are ignored. Since the vertical axis is bounded to values close to zero, the curve appears as vertical straight lines as it crosses the horizontal axis.

Natural frequencies of the finite model framework can also be computed using the finite element method where exact results (accurate to the accuracy of the computer) is achieved. The results obtained using the two methods described above are in good agreement with the results obtained using the finite element method; the biggest percentage difference is 0.0064 %.

The disadvantage of the direct method is that the determinant grows quickly with frequency, and with number of cells because eigenvalues greater than unity are raised to the power of $(N-1)$ for matrix $\mathbf{H}$. For very long structure, the determinants can get extremely large, that is larger than the order of computational error, leading to false results. For the example framework, number of cells greater than eight is found to give incorrect results. However, for the phase closure method, eigenvalues greater than unity do not appear in the determinantal equation, hence the determinants are numerically stable.
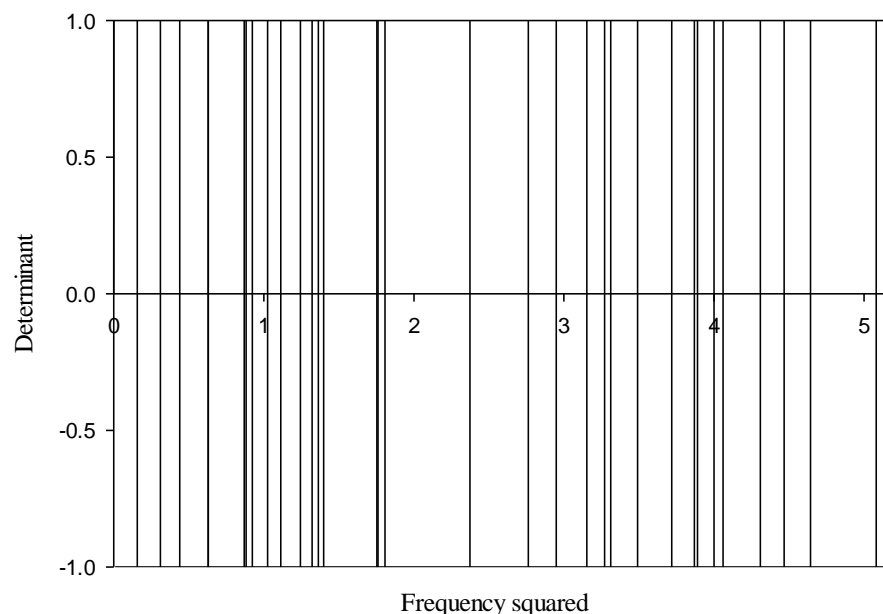
Figure 2.4 Determinant against frequency squared, ω^2, (rad^2 s^{-2}) for a free-free five cells framework evaluated using direct application of boundary conditions on transfer matrix $\mathbf{H}$.

2.8   Conclusions

Two forms of dynamic transfer matrix have been derived for a one-dimensional (beam-like) repetitive pin-jointed structure with point masses located at nodal cross-sections, the displacement-force transfer matrix $\mathbf{G}$, and the displacement-displacement transfer matrix, $\mathbf{H}$. Wave propagation through the structure is described by the eigenvalues of either transfer matrix, expressed as $\lambda = \exp(\delta + i\varphi)$, where the real part δ is the decay constant, and φ is the phase constant as one moves from one cross-section to the next. The emphasis of the present chapter has been the relationship between $\mathbf{G}$ and $\mathbf{H}$, and their respective properties, and also between their respective eigenvectors. Orthogonality relationships are derived for both sets of eigenvectors, allowing an arbitrary disturbance to be resolved into propagating and decaying waves. Both $\mathbf{G}$ and $\mathbf{H}$ can be employed to determine new expressions for the group velocity, but that which employs $\mathbf{H}$ is the more succinct.

For structures of finite length, the determination of natural frequencies of standing waves requires the application of boundary conditions, normally in terms of zero force (free-end), and/or zero displacement (fixed-end); accordingly, the displacement-force transfer matrix $\mathbf{G}$ is the more natural choice. Direct application of boundary conditions leads to very succinct frequency determinants based on partitions of $\mathbf{G}^N$. This approach is suitable for short beam-like structures, where the number of cells N is small; however, since some of the eigenvalues are greater than unity, it becomes numerically unstable when N is large. The displacement-displacement transfer matrix $\mathbf{H}$ approach does not feature a force vector, so this needs to be introduced into the formulation, leading to less succinct frequency determinants; the exception is for the fixed-fixed beam. Again, this approach is numerically unstable when N is large. Instead, phase closure – the idea that for a standing wave, the total phase change for a complete circumnavigation of the structure is an integer multiple of 2π – has been developed in terms of reflection matrices, and features only those eigenvalues less than, or equal to unity; this ensures numerical stability whatever the magnitude of N. Both these approaches require the search for zero-values of a determinant; this can be done by evaluating and plotting the determinant over a frequency range, and noting where the value changes sign. For the direct method, the determinant is real, whereas for phase closure, the determinant is complex, so both real and imaginary parts must be zero simultaneously.

Dispersion diagrams and numerical results on the group velocity for the example structure are considered in Chapters 3 and 4, respectively.

Chapter 3: Wave Propagation in Repetitive Structures: Dispersion Diagram

3.1 Introduction

The present chapter describes in detail the wave propagation and decay characteristics: while such studies are not new, indeed there is a wealth of literature in this area [2,6,18,40,47,59,91,95,96], the sample structure reveals a variety of behaviour, not all of which is familiar within the mechanical vibration literature. Besides, the emphasis is on developing an understanding of why the structure behaves dynamically as it does.

A general theory on wave propagation in one-dimensional repetitive structures was presented by Mead [18]. It is known that under harmonic steady state excitation, free waves can propagate through such structures over certain frequency bands only, known as propagation bands, and are attenuated outside the propagation bands. Mead [6] later wrote "Despite the numerous studies of wave motion in continuous periodic systems over the past 40 years, a simple physical explanation has yet to be presented for the very existence of frequency-propagation zones and attenuation zones. However, even if there is no simple answer to the question "Why does wave motion of one frequency propagate freely while motion of another frequency is attenuated?", reliable prediction methods do exist for the properties of free motion and the magnitudes of forced motion." We note that the decay of self-equilibrated static loading, as anticipated by Saint-Venant's principle (SVP), is represented by those points of the dispersion diagram where branches pierce the plane $\omega = 0$; accordingly, the formulation of a possible *dynamic* SVP [50,52] appears to be intimately related to Mead's question. It is found that the criterion for propagation, or attenuation, is not determined by the frequency *per se*, rather by the associated wavelength, so the present work goes some way towards answering Mead's question and the formulation of a dynamic SVP. A propagation zone can be seen as an "extended resonance": cut-on generally occurs when one has phase closure (implying a natural frequency) over the cross-sectional depth of the structure; cut-off generally occurs when one has phase closure (again implying a natural frequency) over the shortest axial unit – the repeating cell.

Unlike an isotropic continuum structure, the present discrete structure has both *cut-on* and *cut-off* frequencies, as the frequency is increased. In contrast, a continuum structure typically only has cut-on frequencies – although the term cut-off is often (incorrectly) employed. The present work makes clear the need to distinguish between the two (some authors have referred to them as low- and high-frequency cut-offs). Those frequencies at which waves start and stop propagating are associated with real unity eigenvalues, i.e. either $\lambda = 1$ or $\lambda = -1$. According to Zhong [97], "The boundaries between the pass- and stop-bands are of great concern and are given by solving to find ω for $\lambda = 1$ and $\lambda = -1$." Zhong implies that $\lambda = -1$ coincides with a cut-off frequency, and this is generally true for the present example, with the exception of one branch which displays anomalous dispersion, for which $\lambda = -1$ coincides with cut-on. These cut-off frequencies can be found using a Rayleigh quotient.

For the example structure, one can distinguish three decay forms for non-propagating waves; these are monotonic evanescent, oscillatory evanescent and attenuating. The first two of these are typically associated with decay below cut-on and above cut-off frequencies, respectively; the last is associated with the interference of (otherwise) propagating waves over particular frequency ranges, and the interference of oscillatory evanescent waves which changes their decay characteristics, and give rise to loops in the dispersion diagram. For propagating waves, the loop originates when two branches having different Krein signatures meet on the unit circle [77,98], and is known as a Krein collision. The Krein signature is also related to whether dispersion is normal or anomalous. Since a loop also originates when two oscillatory evanescent waves collide, we propose a new expression for the signature applicable to such evanescent waves.

Dispersion diagrams associated with one-dimensional structures are usually plotted in a two-dimensional plane with plots of decay rate and phase change against frequency shown separately; this is seen as rather disjointed. Three-dimensional dispersion diagrams are usually given for two-dimensional structures with a plot of frequency against phase constants giving phase constant surfaces because there are two directions of propagation [59]. Here, a novel form of dispersion diagram is presented where frequency (squared) is plotted against decay rate and phase change in a three-dimensional form; this provides a better qualitative understanding of the dynamic behavior of the structure, in particular how the various modes evolve and interact as frequency is increased. Discussion of the dispersion diagram, and study of the displacement vectors at various critical points, and in terms of cross-sectional

and axial wavelengths at cut-on and cut-off frequencies, forms the major part of this chapter. Finally, some preliminary comments on the cause of anomalous dispersion are made.

3.2   The example framework

A segment of an infinite planar framework of pin-jointed members with a point mass at each joint, is shown in Figure 3.1(a); $(n-1)$, n and $(n+1)$ are consecutive cross-sections of the framework while top, middle and bottom layer of masses are indicated by numbers 1, 2 and 3, respectively. Horizontal and vertical rods have length L and stiffness $k = EA/L$ where E is the Young's modulus and A is the cross-sectional area. The diagonal members are not connected where they cross and have length $\sqrt{2}L$; their cross-sectional area is taken to be one-half that of the horizontal and vertical members, so the diagonal members have stiffness $k/(2\sqrt{2})$. The geometric and material properties are identical to those employed by Stephen and Wang [12] but with a point mass added at each pin-joint of the framework: $E = 200 \times 10^9$ N m^{-2}, $L = 1$ m and $A = 1$ cm^2, hence $k = 20$ MN m^{-1}. For numerical stability, we set $k = 1$ N/m and $m = 1$ kg; for any other values, frequency (squared) can be multiplied by k/m. This helps avoid numerical instability, but also reveals the influence of the diagonal members: the frequency (squared) at cut-on and cut-off, and other critical points, often feature the quantity $0.3536 \cdots = 1/(2\sqrt{2})$. Finally, bars are assumed massless.

The framework can be constructed by two possible repeating entities: a cell and a cross-section, as shown in Figure 3.1(b) and Figure 3.1(c), respectively, connected end-to-end. In Figure 3.1(b), the vertical members and point masses are regarded as being shared between adjacent cells, therefore their stiffness and mass must be halved; for a pin-jointed structure, this requires that the cross-sectional area be $A/2$. Newton's Second Law applied to each point mass of the cell gives the equations of motion which can be re-arranged to give the displacement-force transfer matrix $\mathbf{G}$. On the other hand, Newton's Second Law applied to the nth cross-section shown in Figure 3.1(c) leads to the displacement-displacement transfer matrix $\mathbf{H}$ (see Chapter 2). This model framework is employed for three reasons; first, it has been analysed previously by Stephen and Wang [12] for the static case, which is the zero-frequency limit of the present dynamic case; second, it can be modelled in finite element software which would give exact results (should massless rods actually exist, correct to the accuracy of the computer); and third, the structure has three layer of masses with double thickness and features multi-coupled connections between adjacent cells, this represents a

more general case of a one-dimensional beam-like structure and provides a greater degree of complexity of behaviour than the single thickness truss models which have been more commonly considered previously, for example see reference [47].

Assume that the framework is harmonically excited at some arbitrary section n then, in steady state, waves travel along the framework from that section to the right and to the left. The excitation can be applied directly to any of the three masses at the input section, but in order to drive a particular mode, the forces applied or the displacements imposed must be in accordance with the eigenvector associated with the particular mode *at that frequency*. For example, if the second thickness shear mode is to be driven, then all three masses need to be driven harmonically in the x-direction in a particular pattern, with the middle mass m_2 in opposition to the upper m_1 and lower m_3. If only m_1 and m_3 are being driven, then m_2 will be displaced (harmonically) by the action of deforming members attached to it, and its displacement is determined by the resultant of the elastic forces acting upon it; however, other modes of propagation would also be excited.
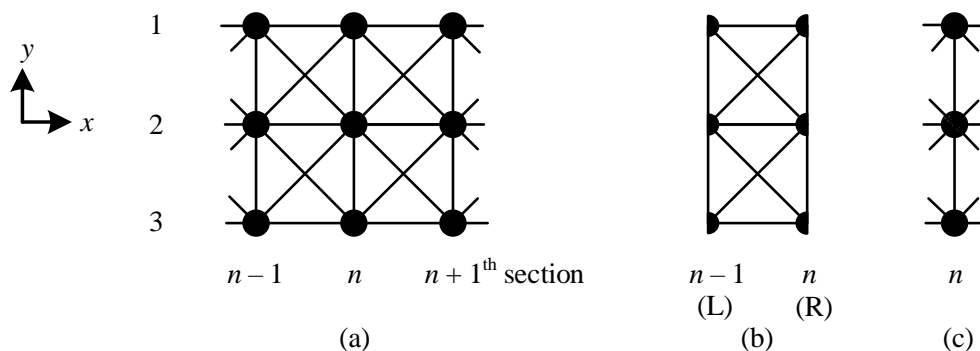
Figure 3.1 (a) A segment of the model framework. (b) The nth cell. L for left-hand
side, R for right-hand side. (c) The nth cross-section.

3.3   Properties of the eigenvalues

For both transfer matrices $\mathbf{G}$ and $\mathbf{H}$, Bloch's theorem leads to a frequency-dependent eigenvalue problem which can be solved numerically by employing the MATLAB eig function. The eigenequations are derived in Chapter 2. Typically, one specifies the frequency and then determine the eigenvalues and eigenvectors at that frequency. The number of eigensolutions is equal to the dimension of the (square) transfer matrix, and that must be twice the number of degrees of freedom at a cross-section, Figure 3.1(c), which is six; in turn there are twelve eigenvalues which exist as reciprocal pairs. Each eigenvalue

pair corresponds to identical free waves which travel in opposite directions. For the static problem ($\omega = 0$), the eigenvalues are six unities and 0.2829, 0.0596 and -0.0702 together with their respective inverses 3.5346, 16.7798 and -14.2435.

For dynamic problems ($\omega > 0$), the eigenvalues falls into five possible classes as given in Chapter 2. The wave type and direction of travel associated with each class are shown in Table 3.1, based upon Hinke *et al.* [95], and is most clearly seen when one writes $\lambda = \exp(\delta + i\varphi)$, where δ and φ are known as the decay rate and phase constant or wavenumber, respectively. The direction of travel of a propagating wave is defined in accordance with the direction of the phase velocity: a right-going wave is one that travels in the positive x-direction, while a left-going wave is one that travels in the negative x-direction. Propagating waves are associated with complex eigenvalues with a magnitude of unity, $|\lambda| = 1$; the direction of travel depends upon the sign of the phase constant φ, with right-going waves having $\varphi < 0$, and left-going waves having $\varphi > 0$; the decay rate parameter δ is obviously zero.

Decaying waves can take three general forms, according to the real and imaginary part of the eigenvalue λ, or equivalently according to the sign of the phase angle, and the sign of the decay rate. The simplest is described as *monotonic* evanescent, for which the phase angle φ is zero; the sign of the decay rate δ then determines whether it is leftward ($\delta > 0$) or rightward ($\delta < 0$) decay. The next simplest, *oscillatory* evanescent, has a phase angle φ equal to π; the wavelength of the decaying wave is then equal to twice the length of the repeating cell. Again, the sign of the decay rate δ determines whether it is leftward ($\delta > 0$) or rightward ($\delta < 0$) decay. Finally, one has *attenuating* decay, for which δ and φ are non-zero and φ lies between zero and $\pm\pi$. The sign of δ reflects the direction of decay, that is $\delta < 0$ for a right decaying wave and $\delta > 0$ for a left decaying wave. The sign of φ reflects the direction of wave travel, that is $-\pi < \varphi < 0$ for a rightward wave and $0 < \varphi < \pi$ for a leftward wave. The magnitude of φ determines the wavelength. These properties for the three cases are summarised in Table 3.1, and depicted in Figure 3.2 where, for simplicity, each nodal cross-section is shown as a single point mass, and it is assumed that displacements are in the transverse y-direction only.

λ	$|\lambda|$	δ	φ	type of wave	direction of travel/decay
positive real non-unity	< 1	< 0	0	monotonic evanescent	rightward
positive real non-unity	> 1	> 0	0	monotonic evanescent	leftward
negative real non-unity	< 1	< 0	π	oscillatory evanescent	rightward
negative real non-unity	> 1	> 0	π	oscillatory evanescent	leftward
complex unity	1	0	< 0	propagating	right-going
complex unity	1	0	> 0	propagating	left-going
complex non-unity	< 1	< 0	$-\pi < \varphi < 0$	attenuating	rightward/ rightward
complex non-unity	> 1	> 0	$-\pi < \varphi < 0$	attenuating	rightward/ leftward
complex non-unity	< 1	< 0	$0 < \varphi < \pi$	attenuating	leftward/ rightward
complex non-unity	> 1	> 0	$0 < \varphi < \pi$	attenuating	leftward/ leftward

Table 3.1   Properties of eigenvalues and associated wave type and direction.

(a)

(b)

(c)

(d)
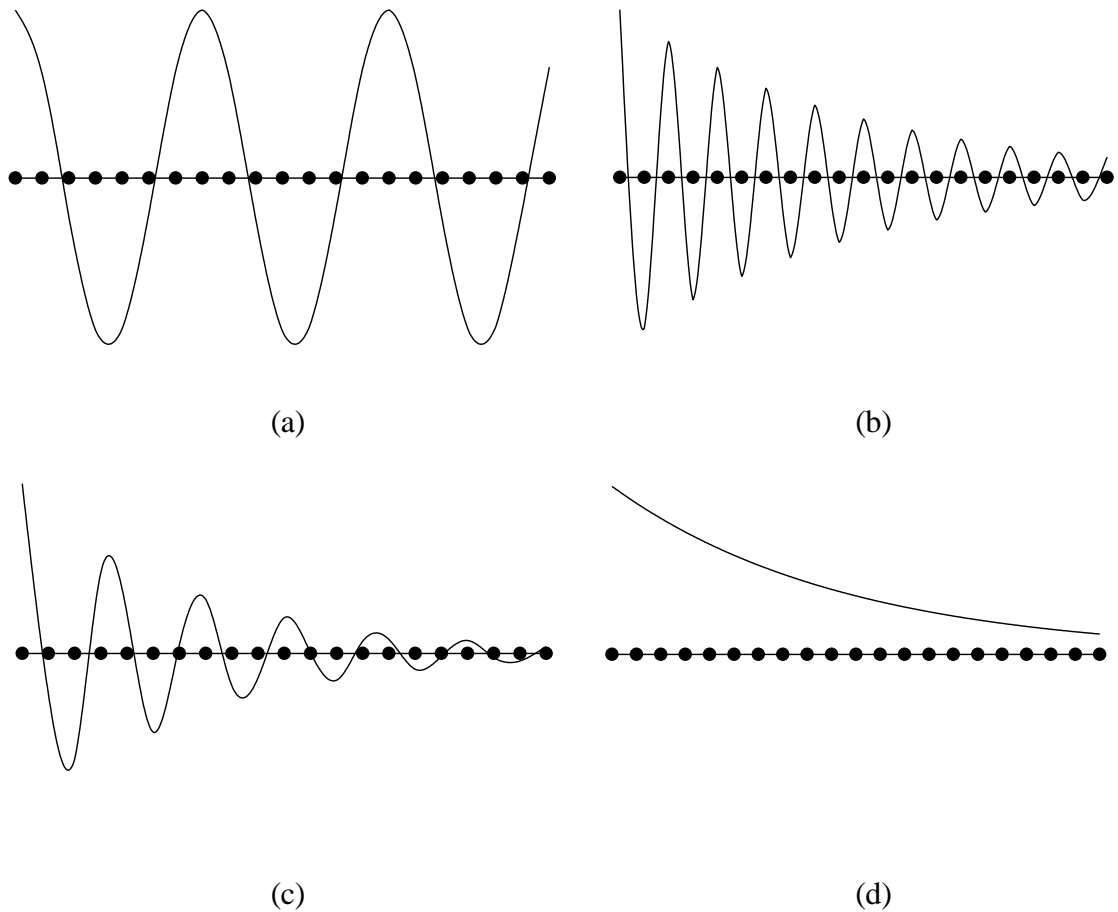
Figure 3.2 Representation of wave types for right-going travel and/or rightward decay. (a) Propagating ($\delta = 0$, $\varphi < 0$). (b) Oscillatory evanescent ($\delta < 0$, $\varphi = \pi$). (c) Attenuating ($\delta < 0$, $-\pi < \varphi < 0$). (d) Monotonic evanescent ($\delta < 0$, $\varphi = 0$).

Next we consider relationships between different forms of eigenvalues with partitions of the dynamic stiffness matrix and displacement vectors. The work is prompted by Mead [18], who considered time-averaged energy flow in terms of the partitions of the receptance matrix and force vectors. Different eigenvalue forms and energy flow can be determined from the relative magnitude of two expressions constructed from partitions of the dynamic stiffness matrix and the displacement vectors.

For three consecutive repeating cross-sections, centred at an arbitrary section n, Figure 3.1(c), the equation of motion is

$$\mathbf{K}_{RL}\mathbf{D}(n-1) + \left[\mathbf{K}_{LL} + \mathbf{K}_{RR} - \omega^2\mathbf{m}\right]\mathbf{D}(n) + \mathbf{K}_{LR}\mathbf{D}(n+1) = \mathbf{0} \tag{3.1}$$

where ω is frequency, $\mathbf{m}$ is the mass matrix and $\mathbf{D}$ is the displacement vector, and the partitions of the stiffness matrix $\mathbf{K}_{LL}$, $\mathbf{K}_{LR}$, $\mathbf{K}_{RL}$ and $\mathbf{K}_{RR}$ are shown explicitly in Appendix A.1. Write $\mathbf{D}(n) = \lambda \mathbf{D}(n-1)$ and $\mathbf{D}(n+1) = \lambda^2 \mathbf{D}(n-1)$, where λ is an eigenvalue, and substitute into equation (3.1); then pre-multiply each term with the transposed conjugate of $\mathbf{D}(n-1)$ to give

$$\mathbf{D}^* \mathbf{K}_{RL} \mathbf{D} + \lambda \mathbf{D}^* \left[\mathbf{K}_{LL} + \mathbf{K}_{RR} - \omega^2 \mathbf{m} \right] \mathbf{D} + \lambda^2 \mathbf{D}^* \mathbf{K}_{LR} \mathbf{D} = 0 \tag{3.2}$$

where the arbitrary section $(n-1)$ is implied, and the coefficients of λ are scalar. Express λ as the quadratic roots of equation (3.2) as

$$\left. \begin{aligned} \lambda = &-\frac{\mathbf{D}^* \left[\mathbf{K}_{LL} + \mathbf{K}_{RR} - \omega^2 \mathbf{m} \right] \mathbf{D}}{2 \left[\mathbf{D}^* \mathbf{K}_{LR} \mathbf{D} \right]} \\ &\pm \frac{\sqrt{\left\{ \mathbf{D}^* \left[\mathbf{K}_{LL} + \mathbf{K}_{RR} - \omega^2 \mathbf{m} \right] \mathbf{D} \right\}^2 - 4 \mathbf{D}^* \mathbf{K}_{LR} \mathbf{D} \left[\mathbf{D}^* \mathbf{K}_{RL} \mathbf{D} \right]}}{2 \left[\mathbf{D}^* \mathbf{K}_{LR} \mathbf{D} \right]} \cdot \end{aligned} \right\} \tag{3.3}$$

Now, for real and complex non-unity eigenvalues, the plus-minus sign corresponds to the reciprocal eigenvalue pair. However, for complex unity eigenvalues, we find numerically that both the plus and the minus signs give the correct eigenvalues, but they are not reciprocal; no explanation has been found for this. Matrices $\mathbf{K}_{LL}$, $\mathbf{K}_{RR}$ and $\mathbf{m}$ are real and symmetric, hence the scalar product $\mathbf{D}^* \left[\mathbf{K}_{LL} + \mathbf{K}_{RR} - \omega^2 \mathbf{m} \right] \mathbf{D}$ is real, as shown by Mead [18]. Matrix $\mathbf{K}_{LR}$ is real and non-symmetric, therefore the scalar product $\mathbf{D}^* \mathbf{K}_{LR} \mathbf{D}$ is real if $\mathbf{D}$ is real and complex if $\mathbf{D}$ is complex. Since $\mathbf{K}_{LR} = \mathbf{K}_{RL}^T$, then $\mathbf{D}^* \mathbf{K}_{RL} \mathbf{D} = \overline{\mathbf{D}^* \mathbf{K}_{LR} \mathbf{D}}$. Post-multiply the numerator and the denominator of equation (3.3) by $\overline{\mathbf{D}^* \mathbf{K}_{LR} \mathbf{D}}$ and using the result $\left[\mathbf{D}^* \mathbf{K}_{LR} \mathbf{D} \right] \left[\overline{\mathbf{D}^* \mathbf{K}_{LR} \mathbf{D}} \right] = \left| \mathbf{D}^* \mathbf{K}_{LR} \mathbf{D} \right|^2$ leads to the form

$$\lambda = \left(A \pm \sqrt{A^2 - 1} \right) B, \tag{3.4}$$

where $A = \dfrac{-\mathbf{D}^* \left[\mathbf{K}_{LL} + \mathbf{K}_{RR} - \omega^2 \mathbf{m} \right] \mathbf{D}}{2 \left| \mathbf{D}^* \mathbf{K}_{LR} \mathbf{D} \right|}$ and $B = \dfrac{\overline{\mathbf{D}^* \mathbf{K}_{LR} \mathbf{D}}}{\left| \mathbf{D}^* \mathbf{K}_{LR} \mathbf{D} \right|}$; an overbar denotes the conjugate, while an asterisk denotes the conjugate transpose.

The parameters A and B are introduced as alternative propagation parameters; since A is always real, one can define the conditions for complex unity, complex non-unity, real non-unity, and real unity eigenvalues in terms of the different values of A and B.

i. Condition for complex unity eigenvalues, $\lambda = \exp(\pm i\varphi)$ (propagating).

If $-1 < A < 1$, then $A^2 - 1$ is negative, and we may write $\left(A \pm \sqrt{A^2-1}\right)$ as $\left(A \pm i\sqrt{1-A^2}\right)$ which is clearly a complex unity. It is found numerically that B is also a complex unity. Let $\left(A \pm \sqrt{A^2-1}\right) = \exp(\pm i\varphi_1)$ and $B = \exp(\pm i\varphi_2)$, therefore one can write $\varphi = \varphi_1 + \varphi_2$; the plus and minus signs in the above must correspond. Numerically it is found that $\mathbf{D}^*\mathbf{K}_{RR}\mathbf{D} = \mathbf{D}^*\mathbf{K}_{LL}\mathbf{D}$, so the inequality can be simplified to

$$-1 < \frac{\mathbf{D}^*\mathbf{K}_{LL}\mathbf{D} - \dfrac{1}{2}\omega^2\mathbf{D}^*\mathbf{m}\mathbf{D}}{\left|\mathbf{D}^*\mathbf{K}_{LR}\mathbf{D}\right|} < 1$$

as the condition for a complex unity travelling waves.

ii. Condition for complex non-unity eigenvalues, $\lambda = \exp(\delta \pm i\varphi)$ (attenuating loop).

If $A < -1$ or $A > 1$, then $\left(A \pm \sqrt{A^2-1}\right)$ are purely real and can be expressed as $\exp(\delta + i\pi)$ or $\exp(\delta)$, respectively. It is found numerically that B is a complex unity, and provides the phase constant φ, which can be positive or negative according to the chosen displacement vector $\mathbf{D}$.

iii. Condition for real non-unity eigenvalues (evanescent decay).

Again, if $A < -1$ or $A > 1$, then $\left(A \pm \sqrt{A^2-1}\right)$ can take the form $\exp(\delta + i\pi)$ or $\exp(\delta)$, respectively; numerically it is found that B takes the values $+1$, or -1; $B = 1$ is associated with branch 6 which displays anomalous dispersion when propagating.

iv. Conditions for real unity eigenvalues, $\lambda = \pm 1$ (cut-on and cut-off).

There are two conditions pertaining to real unity eigenvalues. First, if $A = \pm 1$, then $\left(A \pm \sqrt{A^2-1}\right) = \pm 1$ and $B = \pm 1$. Second, if $A = 0$, then $\left(A \pm \sqrt{A^2-1}\right) = \pm i$ and $B = \pm i$. The latter condition is found numerically to be satisfied by the real unity eigenvalues when $\omega^2 = 1.3536$, which is the cut-off frequency for extensional waves ($\lambda = -1$) and the cut-on for the first breathing mode ($\lambda = 1$). The former condition is satisfied for all remaining branches at cut-on and cut-off.

These observations on the values of parameter B are developed in Section 3.11 to complement the Krein signature.

3.4 Dispersion diagram

The dispersion diagram is a three dimensional plot of δ and φ as a function of ω^2, as shown in Figure 3.3. Only the positive quadrant of the entire plot need be shown, as the dispersion diagram is symmetric about the planes $\varphi = 0$ and $\delta = 0$. Note that the quadrant shown corresponds to left-going waves, and leftward decay, as the notion of positive and negative slopes is more intuitive within this sector; the φ-axis is scaled by a factor of π. The curved segments are referred to as branches and each of them is numbered from 1 to 6, according to their order of appearance on the (propagating) plane $\delta = 0$ as frequency is increased. The frequency (squared) range considered, $0 \le \omega^2 \le 6$ rad^2 s^{-2}, encompasses the propagation of all six branches including cut-on for four of the branches, and cut-off for all. Two out-of-plane half loops emerge where two branches meet and interact (the other halves are within the omitted quadrants); these loops are designated by two numbers associated with the meeting branches, a notation adapted from that employed by Miklowitz [64]. A third loop starts at the origin and evolves into branch 3, and is designated loop 3.

The group velocity, $c_g = \mathrm{d}\omega/\mathrm{d}\varphi$, was determined in Chapter 2 as $c_g = \mathrm{i}\,\lambda\,\dfrac{\mathbf{Y}^{\mathrm{T}}\mathbf{X}}{2\omega\mathbf{Y}^{\mathrm{T}}\mathbf{H}_2\mathbf{X}}$. For the present dispersion diagram, one should employ partial differentiation, that is $c_g = \partial\omega/\partial\varphi$, and note that $\partial\left(\omega^2\right)/\partial\varphi = 2\omega\,\partial\omega/\partial\varphi$; accordingly, a zero gradient with respect to the φ-axis implies zero group velocity, except at the origin. However, branches can also vary with δ and, following the result in Chapter 2, we find that $\dfrac{\partial\omega}{\partial\delta} = \lambda\,\dfrac{\mathbf{Y}^{\mathrm{T}}\mathbf{X}}{2\omega\mathbf{Y}^{\mathrm{T}}\mathbf{H}_2\mathbf{X}} = \dfrac{c_g}{\mathrm{i}}$, and also $\partial\left(\omega^2\right)/\partial\delta = 2\omega\,\partial\omega/\partial\delta$. Thus we may determine that the evanescent branches have zero gradient with respect to both the φ and δ-axes at cut-on and cut-off.

There are five features to first note about Figure 3.3:

i. The plane $\omega^2 = 0$ (strictly, the δ-φ plane) corresponds to the static behaviour of the structure, and the origin ($\varphi = 0$, $\omega^2 = 0$) pertains to the six-fold unity eigenvalue $\lambda = 1$ for the static case. Associated with these six unity eigenvalues are two eigenvectors describing

rigid body displacements in the x- and y-directions, and four principal vectors describing tension, rigid body displacement, bending moment and shearing force; the three branches which emerge from the plane correspond to the decay of self-equilibrated load, as anticipated by Saint-Venant's principle [12]. As frequency increases from zero, extensional and bending waves immediately start propagating both left-going and right-going, and this accounts for four of the six (previously) unity eigenvalues; Figure 3.3 shows only the two left-going waves. Of the remaining two, loop 3 shows a monotonic evanescent decaying leftward wave, while the rightward wave would appear in a separate quadrant. The six static decay modes (the leftward three are shown in Figure 3.3) emerge from the plane $\omega^2 = 0$ with $\partial \omega / \partial \delta = \infty$; that is they would emerge perpendicular to this plane if the ordinate was ω rather than ω^2, but $\partial \left(\omega^2 \right) / \partial \delta = \infty$ at these locations.

ii. Branches 3 and 4 cross each other twice, at $\omega^2 = 1.3536$ and $\omega^2 \approx 1.6702$. Branch 3 crosses branch 5 when $\omega^2 \approx 3.7151$. It is noted that these crossings do not lead to formation of loops because there is no interaction of one mode with the other. This can be attributed to the fact that branch 3 is asymmetric about the x-axis, while branches 4 and 5 are symmetric; this is explored more fully in Section 3.10, in terms of the Krein signature.

iii. The gradient (with respect to the φ-axis) at points where the branches intersect the vertical axes of the graph, i.e, where $\varphi = 0$ and $\varphi = \pi$, are zero. Zero-gradient corresponds to a start (cut-on) or the finish (cut-off) of branches on the plane $\delta = 0$. No correlation is found to exist between the inflection points of any particular branch with any of the zero-gradient points of the other branches.

iv. The half loops which pertain to the complex non-unity eigenvalues are the result of an interaction of two modes. Loop 1,6 starts at $\omega^2 = 1.3536$ and ends at $\omega^2 \approx 3.0217$ while loop 3,6 starts at $\omega^2 \approx 3.1707$ and ends at $\omega^2 \approx 3.6951$. The points at which loop 3,6 emerges from the plane $\delta = 0$ and returns, have zero gradient with respect to the δ-axis. The points at which loop 1,6 emerges from the plane $\varphi = \pi$ and returns, have zero gradient with respect to both the φ- and δ-axes. Loop 3 emerges from the origin into the plane $\varphi = 0$ and returns to the plane $\delta = 0$ at $\omega^2 = 0.3536$ with zero gradient with respect to the δ-axis; a close up view is shown in Figure 3.4.

v. All branches on the plane $\delta = 0$ have positive gradient with respect to the φ-axis, except branch 6. Positive gradient is associated with normal dispersion which means that the

71

wave's energy is flowing in the direction of wave travel; negative gradient is associated with anomalous dispersion which implies that the wave's energy is flowing in the opposite direction to the wave travel.
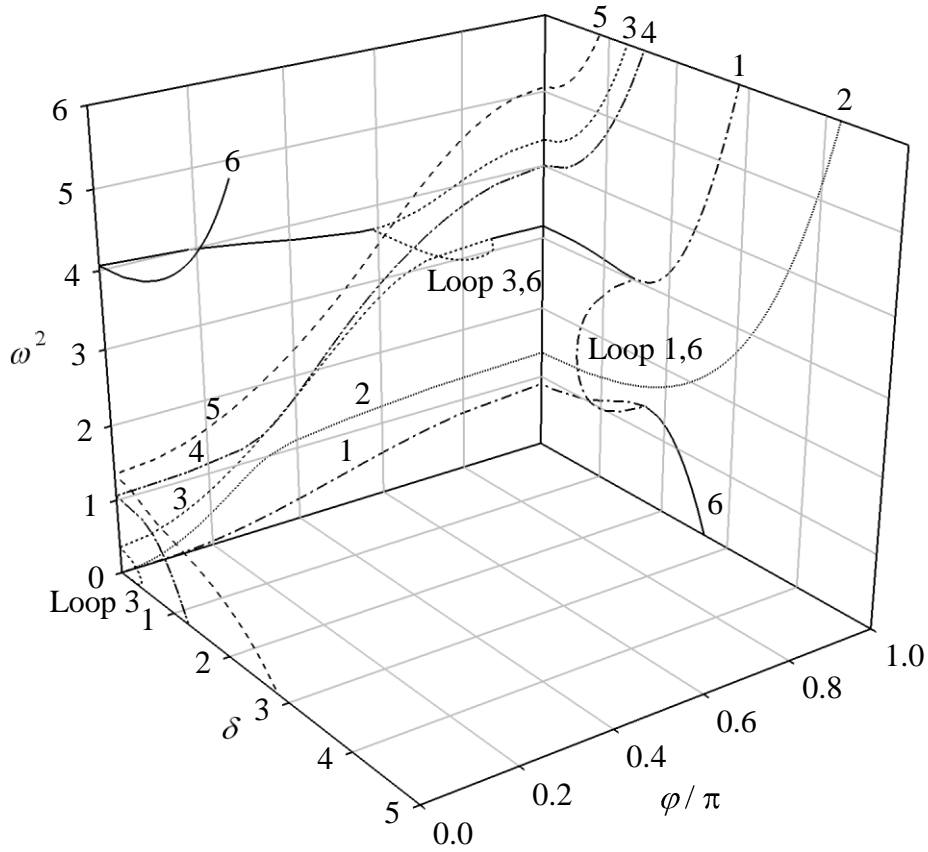
Figure 3.3 Dispersion diagram for the example framework.

—·—·—·	1 Bending,	··········	2 Extensional,
— — — — —	3 First thickness shear,	—··—··—	4 Second thickness shear,
— — — —	5 First breathing,	————	6 Second breathing.
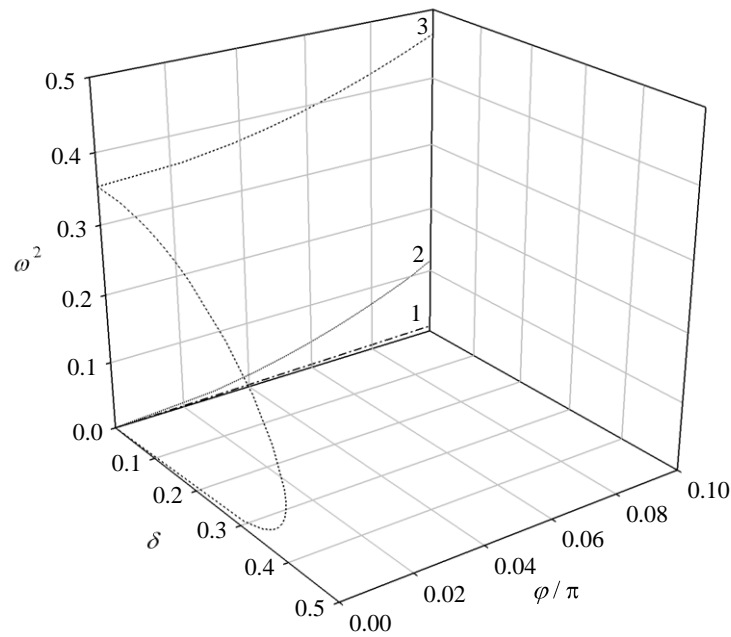
Figure 3.4 Close up view of Loop 3.

3.5   Displacement vectors

The displacement vector $\mathbf{D}(n)$ at an arbitrary section n can be taken from the eigenvector of either transfer matrix $\mathbf{G}$ or $\mathbf{H}$ (see Chapter 1); displacement at adjacent sections are found by multiplying $\mathbf{D}(n)$ with the corresponding eigenvalue λ, i.e. $\mathbf{D}(n+1) = \lambda \mathbf{D}(n)$. To visualize the waveform, only the real part of the complex displacement vector is considered. Figure 3.5 shows ten cells of the un-deformed infinite framework. A mode of vibration for which the dominant characteristic displacement is symmetric about the framework's longitudinal axis of symmetry is regarded as a symmetric wave, otherwise the wave is regarded as asymmetric. For the model framework, $D_{2y} = 0$ for all symmetric modes and $D_{2x} = 0$ for all asymmetric modes.
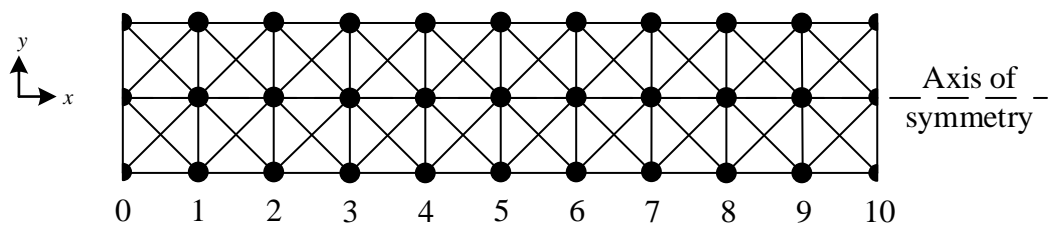
Figure 3.5 A ten-cell segment of the infinite framework and its longitudinal axis of symmetry.

73

At any cross-section of the framework, there are six degrees of freedom. Excitation at the nth cross-section, Figure 3.6, can lead to six different modes of free wave motion that travel rightward, and a further six of the same modes that can travel leftward, giving a total of twelve modes of vibration. A bending or flexural wave is a vibration as a result of harmonic excitation in the y-direction; it is characterised by equal displacements D_{1y} and D_{3y}, both generally in-phase with displacement D_{2y} (at higher frequencies, D_{2y} becomes out-of-phase with D_{1y} and D_{3y}). An extensional or compressional wave is a vibration in the x-direction; displacements D_{1x} and D_{3x} are equal, and generally in-phase with D_{2x}. The first thickness shear wave is a shearing wave across the overall framework depth; it is characterised by displacements D_{1x} and D_{3x} which are equal in magnitude but opposite in direction. The second thickness shear wave is a symmetric shearing wave across half the depth of the framework; it is characterised by equal displacements of D_{1x} and D_{3x}, but D_{2x} is opposite in direction. The first breathing wave is a symmetric expansion and contraction across the framework depth; it is a wave pattern one would expect to arise from harmonic 'pinching' excitation and hence characterised by opposing displacements of D_{1y} and D_{3y}, with D_{2y} equal to zero. The second breathing wave is also a transverse expansion/contraction but across half of the depth of the framework; when the top half is under contraction, the bottom half would be under expansion, and *vice versa*; therefore the displacements are characterised by in-phase displacements of D_{1y} and D_{3y}, both out-of-phase with D_{2y}. Of course, the displacements mentioned above are those which are dominant at low frequencies; for example, an extensional mode has *primary* cross-sectional displacements in the x-direction, but there are *secondary* displacements of the upper and lower masses consistent with a Poisson's ratio-like contraction, and reminiscent of the first breathing mode. Indeed, one may regard the cut-off of the extensional mode and the cut-on of the first breathing mode, which occurs at the same frequency $\omega^2 = 1.3536$, as the point at which a secondary displacement becomes primary.

n − 1   n   n + 1   n − 1   n   n + 1   n − 1   n   n + 1

Bending   Extensional   First thickness shear

n − 1   n   n + 1   n − 1   n   n + 1   n − 1   n   n + 1

Second thickness shear   First breathing   Second breathing
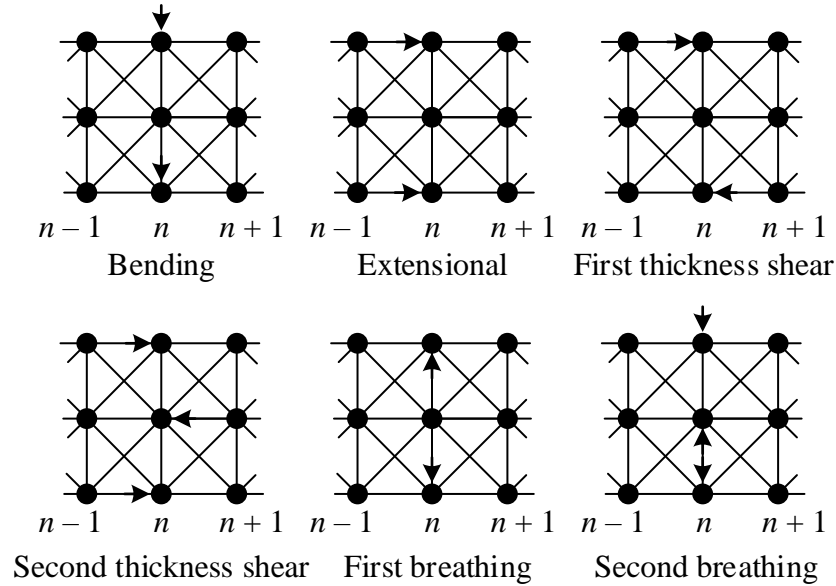
Figure 3.6 Possible free waves. Arrows show the principal displacement of masses at the driven input section.

3.6   Cut-on and cut-off frequencies

The eigenvalues $\lambda = 1$ and $\lambda = -1$ are of particular significance as they are repeating eigenvalues, and indicate that a mode is starting to propagate (cut-on) or is ceasing (cut-off) in relation to *increasing* frequency. The cut-on and cut-off frequencies for the example framework are shown in Tables 3.2 and 3.3 together with their associated modes and corresponding displacement vectors.

The cut-on frequencies are typically characterised by displacements which do not vary in the axial x-direction, that is $\lambda = 1$, which implies that $\mathbf{D}(n-1) = \mathbf{D}(n) = \mathbf{D}(n+1)$, and equation (3.1) becomes $\left[\mathbf{K}_{LL} + \mathbf{K}_{RR} + \mathbf{K}_{LR} + \mathbf{K}_{RL} - \omega^2\mathbf{m}\right]\mathbf{D}(n) = \mathbf{0}$. Pre-multiply by $\mathbf{m}^{-1}$ gives $\left[\mathbf{m}^{-1}(\mathbf{K}_{LL} + \mathbf{K}_{RR} + \mathbf{K}_{LR} + \mathbf{K}_{RL}) - \omega^2\mathbf{I}\right]\mathbf{D}(n) = \mathbf{0}$, so the non-zero eigenvalues of the matrix $\mathbf{m}^{-1}(\mathbf{K}_{LL} + \mathbf{K}_{RR} + \mathbf{K}_{LR} + \mathbf{K}_{RL})$ are the squares of the supposed cut-on frequencies; zero frequencies pertain to rigid body displacements. Since each of the displacement vectors could have been anticipated, the frequencies could have been found using a Rayleigh quotient as

$$\omega^2 = \frac{\mathbf{D}^{T}\mathbf{m}^{-1}(\mathbf{K}_{LL} + \mathbf{K}_{RR} + \mathbf{K}_{LR} + \mathbf{K}_{RL})\mathbf{D}}{\mathbf{D}^{T}\mathbf{D}} . \tag{3.5}$$

In each case, the averaged nodal displacements in the x- and y-directions are zero, with the exception of the rigid body modes. Note that the eigenvalue $\lambda = 1$ is actually a cut-off rather

than a cut-on frequency for the second breathing mode, as this branch exhibits anomalous dispersion. Also note the presence of the term $1/\left(2\sqrt{2}\right)$ in each of the frequencies (squared), indicating that the diagonal bars always deform when $\lambda = 1$; however, the horizontal and vertical members can remain at the same length (note the absence of the integer terms for the two thickness shear modes).

ω^2	Description	Displacement vector $\mathbf{D}(n)$
0	Rigid body displacement in the x-direction	$\begin{bmatrix} 1 & 0 & 1 & 0 & 1 & 0 \end{bmatrix}^{\mathrm{T}}$
0	Rigid body displacement in the y-direction	$\begin{bmatrix} 0 & 1 & 0 & 1 & 0 & 1 \end{bmatrix}^{\mathrm{T}}$
$1/\left(2\sqrt{2}\right) = 0.3536$	First thickness shear (cut-on)	$\begin{bmatrix} 1 & 0 & 0 & 0 & -1 & 0 \end{bmatrix}^{\mathrm{T}}$
$3/\left(2\sqrt{2}\right) = 1.0607$	Second thickness shear (cut-on)	$\begin{bmatrix} 1 & 0 & -2 & 0 & 1 & 0 \end{bmatrix}^{\mathrm{T}}$
$1+1/\left(2\sqrt{2}\right) = 1.3536$	First breathing (cut-on)	$\begin{bmatrix} 0 & 1 & 0 & 0 & 0 & -1 \end{bmatrix}^{\mathrm{T}}$
$3+3/\left(2\sqrt{2}\right) = 4.0607$	Second breathing (cut-off)	$\begin{bmatrix} 0 & 1 & 0 & -2 & 0 & 1 \end{bmatrix}^{\mathrm{T}}$

Table 3.2   Squares of cut-on and cut-off frequencies $\lambda = 1$.

Next consider $\lambda = -1$, presumed to pertain to a cut-off frequency; this implies that $-\mathbf{D}(n-1) = \mathbf{D}(n) = -\mathbf{D}(n+1)$, and equation (3.1) becomes $\left[\mathbf{K}_{\mathrm{LL}} + \mathbf{K}_{\mathrm{RR}} - \mathbf{K}_{\mathrm{LR}} - \mathbf{K}_{\mathrm{RL}} - \omega^2 \mathbf{m}\right]\mathbf{D}(n) = \mathbf{0}$. Pre-multiplication by $\mathbf{m}^{-1}$ now gives $\left[\mathbf{m}^{-1}\left(\mathbf{K}_{\mathrm{LL}} + \mathbf{K}_{\mathrm{RR}} - \mathbf{K}_{\mathrm{LR}} - \mathbf{K}_{\mathrm{RL}}\right) - \omega^2 \mathbf{I}\right]\mathbf{D}(n) = \mathbf{0}$, so the eigenvalues of the matrix $\mathbf{m}^{-1}\left(\mathbf{K}_{\mathrm{LL}} + \mathbf{K}_{\mathrm{RR}} - \mathbf{K}_{\mathrm{LR}} - \mathbf{K}_{\mathrm{RL}}\right)$ are the squares of the supposed cut-off frequencies. The

eigenvalues may be found numerically using the MATLAB command $[\mathrm{v,d}]=\mathrm{eig}\left[\mathbf{m}^{-1}\left(\mathbf{K}_{LL}+\mathbf{K}_{RR}-\mathbf{K}_{LR}-\mathbf{K}_{RL}\right)\right]$ where v and d represent eigenvectors and eigenvalues, respectively. Alternatively, one may use MATLAB to perform symbolic computation as follows: the elements of matrix $\mathbf{m}^{-1}\left(\mathbf{K}_{LL}+\mathbf{K}_{RR}-\mathbf{K}_{LR}-\mathbf{K}_{RL}\right)$ are expressed in terms of symbolic variable a which represents $1/\left(2\sqrt{2}\right)\approx0.3536$. The characteristic determinant factorises as

$$\left(\omega^4-3(1+a)\omega^2+8a\right)\left(\omega^2-(1+a)\right)\left(\omega^2-4\right)\left(\omega^2-(4+a)\right)\left(\omega^2-(4+3a)\right)=0. \quad (3.6)$$

ω^2	Description	Displacement vector $\mathbf{D}(n)$
0.8929*	Bending (cut-off)	$[0 \quad 1 \quad 0 \quad 0.7126 \quad 0 \quad 1]^{\mathrm{T}}$
$1+1/\left(2\sqrt{2}\right)=1.3536$	Extensional (cut-off)	$[0 \quad 1 \quad 0 \quad 0 \quad 0 \quad -1]^{\mathrm{T}}$
3.1678*	Second breathing (cut-on)	$[0 \quad 1 \quad 0 \quad -2.8065 \quad 0 \quad 1]^{\mathrm{T}}$
4.0000	Second thickness shear (cut-off)	$[1 \quad 0 \quad -1 \quad 0 \quad 1 \quad 0]^{\mathrm{T}}$
$4+1/\left(2\sqrt{2}\right)=4.3536$	First thickness shear (cut-off)	$[1 \quad 0 \quad 0 \quad 0 \quad -1 \quad 0]^{\mathrm{T}}$
$4+3/\left(2\sqrt{2}\right)=5.0607$	First breathing (cut-off)	$[1 \quad 0 \quad 2 \quad 0 \quad 1 \quad 0]^{\mathrm{T}}$

Table 3.3   Squares of cut-on and cut-off frequencies for $\lambda=-1$.

Referring to Tables 3.2 and 3.3, first note that the displacement vector $[0 \quad 1 \quad 0 \quad 0 \quad 0 \quad -1]^{\mathrm{T}}$ pertains to the cut-on of the first breathing mode, and to the cut-off of the extensional mode, both at the same frequency $\omega^2=1.3536$, which is the second factor in equation (3.6). One might regard the first breathing mode as a reincarnation of the extensional mode; the secondary displacement of the latter become the primary displacement of the former.

Second, note that the first thickness shear mode has the same displacement vector, $\begin{bmatrix} 1 & 0 & 0 & 0 & -1 & 0 \end{bmatrix}^{\mathrm{T}}$, at both the cut-on frequency $\omega^2 = 0.3536$ and at the cut-off, $\omega^2 = 4.3536$ which is the fourth factor of equation (3.6).

Again, note the term $1/\left(2\sqrt{2}\right)$ features explicitly in three of the frequencies (squared), indicating diagonal bars deformation. The two frequencies marked with an asterisk are the roots of the quadratic equation $\omega^4 - 3(1+a)\omega^2 + 8a = 0$, which is the factor of equation (3.6), or $\omega_{1,2}^{*2} = \left(3(1+a) \mp \sqrt{9a^2 - 14a + 9}\right)/2$, so again diagonal bar deformation is implicit. The corresponding displacement vectors also involve the same discriminant, that is $-2.8065 = \left(1 + a + \sqrt{9a^2 - 14a + 9}\right)/(2a - 2)$, and

$0.7126 = \left(1 + a - \sqrt{9a^2 - 14a + 9}\right)/(2a - 2)$. These two displacements components can be regarded as a ratio of D_{2y} to D_{1y} such that the magnitude of the restoring force per unit displacement per unit mass (represented by ω^2) subjected to each point mass, are equal. This can be shown as follows: for bending and second breathing modes, the displacement of the top and bottom masses at an arbitrary station n will be the same at all frequencies, i.e. $D_{3y} = D_{1y}$; thus $\mathbf{D}(n) = \begin{bmatrix} 0 & D_{1y} & 0 & D_{2y} & 0 & D_{1y} \end{bmatrix}^{\mathrm{T}}$ and $-\mathbf{D}(n-1) = \mathbf{D}(n) = -\mathbf{D}(n+1)$. Substitute this displacement vector $\mathbf{D}(n)$ into equation (3.1) and upon expansion and re-arrangement, it can be expressed as

$$
\begin{bmatrix}
0 \\
ak\left(D_{1y} + D_{2y}\right) + k\left(D_{1y} - D_{2y}\right) - \omega^2 m D_{1y} \\
0 \\
2ak\left(D_{1y} + D_{2y}\right) - 2k\left(D_{1y} - D_{2y}\right) - \omega^2 m D_{2y} \\
0 \\
ak\left(D_{1y} + D_{2y}\right) + k\left(D_{1y} - D_{2y}\right) - \omega^2 m D_{1y}
\end{bmatrix} = \mathbf{0} ,
\qquad (3.7)
$$

where again $a = 1/\left(2\sqrt{2}\right)$. Express the second and fourth rows for ω^2 in terms of D_{1y} and D_{2y}, then equate them and re-arrange as a quadratic equation in terms of $\left(D_{2y}/D_{1y}\right)$ to give

$$
(k/m)\left\{(a-1)\left(D_{2y}/D_{1y}\right)^2 - (a+1)\left(D_{2y}/D_{1y}\right) - 2(a-1)\right\} = 0 ,
\qquad (3.8)
$$

with roots -2.8065 and 0.7126; these numbers appear in the displacement vector column of Table 3.3.

Last, note that the cut-off frequency (squared) for the second thickness shear mode is the exception, in that it does not feature the term $1/(2\sqrt{2})$ either explicitly or implicitly; this is because the diagonal bars do not undergo a change in length.

Again, these cut-off frequencies can be found using a Rayleigh quotient as

$$\omega^2 = \frac{\mathbf{D}^{\mathrm{T}}\mathbf{m}^{-1}(\mathbf{K}_{\mathrm{LL}} + \mathbf{K}_{\mathrm{RR}} - \mathbf{K}_{\mathrm{LR}} - \mathbf{K}_{\mathrm{RL}})\mathbf{D}}{\mathbf{D}^{\mathrm{T}}\mathbf{D}}, \qquad (3.9)$$

although the displacement vectors could not have been anticipated. Comparing Table 3.3 with Table 3.2 only in two cases, the extensional and first thickness shear cut-off, are the averaged nodal displacements equal to zero; these displacement vectors are common with two of the cut-on frequencies, and give the same frequency in one case.

Figure 3.7 shows the characteristic displacements of the six different modes at their cut-on and cut-off frequencies; bending and extensional waves do not exhibit cut-on. We note that either the x-component displacements are all zero (cases a, b, g, i and j), or the y-component displacements are all zero (cases c, d, e, f and h).

The cut-on and cut-off frequencies can also be defined based on periodicity and anti-periodicity of the wave modes. When the neighbouring point masses in the axial direction move in phase, the mode is considered to be periodic in that direction; otherwise, if they move perfectly out of phase, the mode is called anti-periodic. At the cut-on frequencies, the normally dispersive first thickness shear, second thickness shear and first breathing modes are periodic but the anomalously dispersive second breathing mode is anti-periodic. At the cut-off frequencies, the normally dispersive bending, extensional, first thickness shear, second thickness shear and first breathing modes are anti-periodic but the anomalously dispersive second breathing mode is periodic. In Figure 3.7, the arrows may also represent the anti-periodicity conditions. Colquitt *et al.* [22] and Andrianov *et al.* [24] noted that the anti-periodicity modes appear as standing waves and can be considered as 'hidden' or 'trapped' modes in the sense that no energy is transmitted through the framework but each unit cell exhibits oscillatory motion.

Long-wave behavior near the cut-on/off frequency in waveguides is described by Craster [99] using the asymptotic method. Application of long-wavelength asymptotic theories to repetitive structure are presented by Craster *et al.* [100]. One of the key features in the theory

is the introduction of separate scales for the short unit cell and the long wavelength. The method is then developed to establish so-called composite wave models for elastic plates [100] and periodically heterogeneous media [22,24] where the periodicity condition is considered in detail. It is noted in [22] that if the wavelength is larger than the length of a unit cell, the obtained homogenised model is able to describe asymptotically the propagation of both periodic and anti-periodic modes. For two-dimensional cases, it is shown in [24] that combined periodicity and anti-periodicity conditions in different directions of the translational symmetry reveals different types of modes that do not arise in the one-dimensional periodic case.

Application of the homogenisation method to repetitive reticulated beams made of symmetric unbraced framed cells is presented by Boutin and Hans [25]. The framed structure is akin to the framework considered in Figure 3.7 but its stiffness and mass are continuously distributed in the beam elements, thus opening the possibility of enriched local kinematics. The dynamics of the structure may represent an idealised building under seismic loading and the structural response can be used for vulnerability studies. Through the homogenisation method and systematic use of spatial scaling, the transverse modes of the structure are studied in detail by Hans and Boutin [101] while the existence of atypical gyration modes is established theoretically by Chesnais *et al.* [102]. The accuracy of the analytical homogenisation method is compared to the numerical condensed wave finite element method by Changwei *et al.* [33]; the latter method allows reduction of the model order for efficient computation of the problem particularly when a unit cell contains large number of internal nodes. The homogenisation method is found to provide better prediction of the dispersion relation and the natural frequencies calculated by the method correlate well with the results reported in [101]. However, the valid frequency range of the homogenisation method is more restricted presumably because the natural modes are determined by both propagating and evanescent waves, but the latter wave is predicted poorly when approaching higher frequencies. Recently, the homogenisation method is adapted to high frequency range associated with modulation phenomena [31,32]. The high-frequency modulation provide dispersion relations in limited frequency ranges but the approach can describe large scale evolutions of rapidly oscillating motions, i.e. their envelope, explicitly.

(a) Bending at cut-off

(b) Extensional at cut-off

(c) First thickness shear at cut-on

(d) First thickness shear at cut-off

(e) Second thickness shear at cut-on

(f) Second thickness shear at cut-off

(g) First breathing at cut-on

(h) First breathing at cut-off

(i) Second breathing at cut-on

(j) Second breathing at cut-off
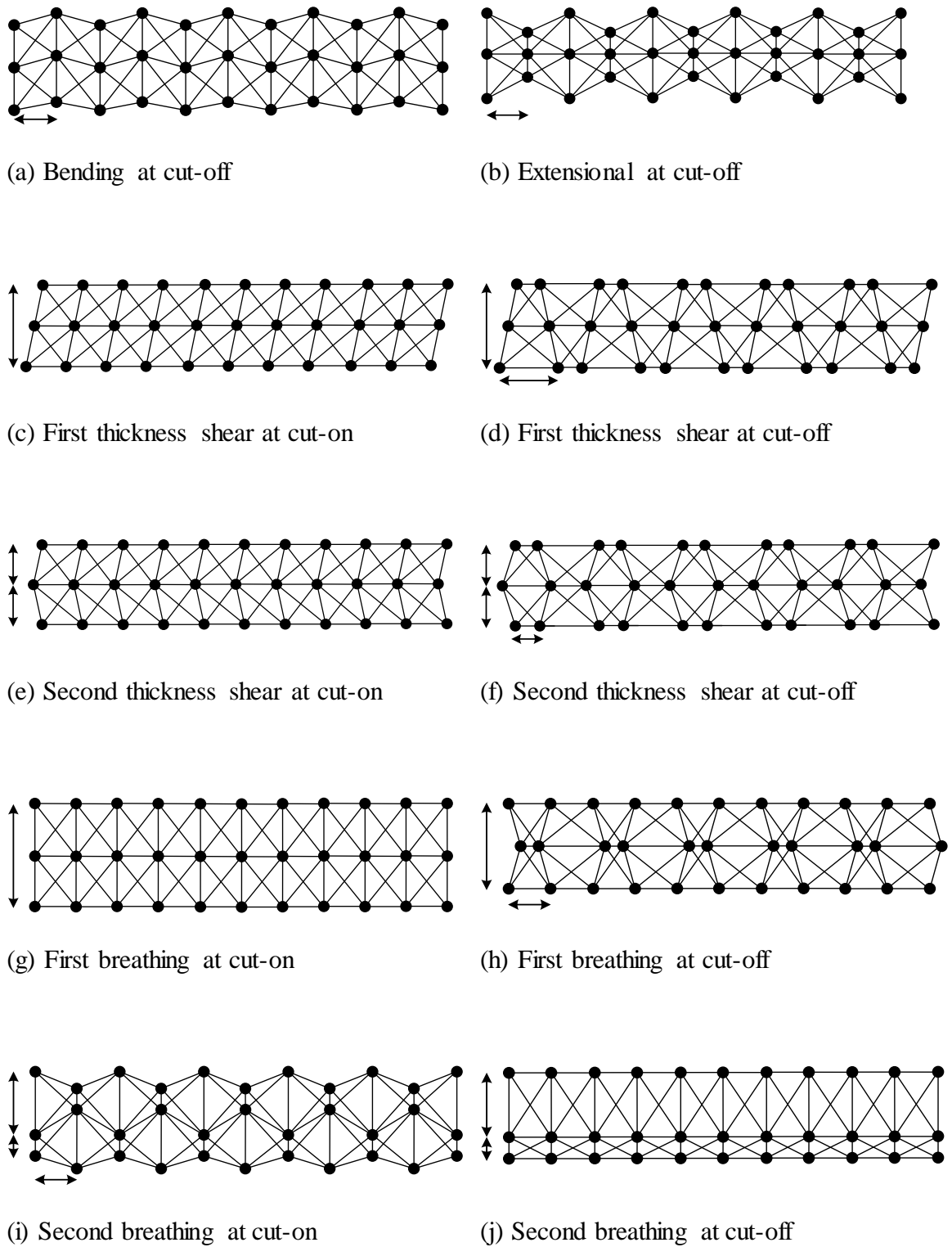
Figure 3.7 Modes at cut-on and cut-off frequencies. The arrows indicate the occupation of one half-wavelength within the structure.

3.7   Propagating waves

We now describe in detail the behaviour of each of the branches, including at frequencies below cut-on, and above cut-off. Referring to Figure 3.3, as frequency is increased from zero, branches 1 and 2, and loop 3 emanate from the origin. Branch 1 is the asymmetric bending mode which propagates immediately when the framework is excited harmonically in the y-direction at an arbitrary station n and at a frequency above zero; waves propagate immediately because one half-wavelength can be accommodated within the infinite span of the framework. As frequency increases, the wavenumber increases, or equivalently the wavelength decreases. The propagation ceases (cuts-off, $\lambda = -1$) at $\omega^2 = 0.8929$ where one wavelength occupies exactly two cells (one half-wavelength over one cell length). Above the cut-off frequency, the wave becomes *oscillatory* evanescent, decaying more rapidly (in a spatial sense) as frequency continues to increase. However, at $\omega^2 = 1.3536$, this oscillatory evanescent bending wave interacts with the oscillatory evanescent second breathing wave, branch 6, resulting in the formation of two *attenuating* waves travelling in both directions (one of the leftward attenuating waves is represented by loop 1,6). The two attenuating waves revert to their previous character at $\omega^2 \approx 3.021$ where oscillatory evanescent bending and second breathing waves reappear; the former continues to decay at an increasing rate while the latter decays at a decreasing rate until it reaches its cut-on frequency ($\lambda = -1$) at $\omega^2 = 3.1678$.

Branch 2 exhibits symmetric extensional displacements with symmetric Poisson's ratio-like contraction in the transverse direction. Again, propagation starts immediately when the frequency is above zero because one half-wavelength can be accommodated within the infinite span of the framework. As frequency increases, the wavelength decreases until one half-wavelength occupies one cell length where the mode reaches its cut-off frequency $\left(\lambda = -1 \right)$ at $\omega^2 = 1.3536$; above that frequency the wave becomes oscillatory evanescent, and decays at an increasing rate as the frequency is increased.

Loop 3, shown in detail in Figure 3.4, commences at the origin and initially remains in the plane $\varphi = 0$ ($\lambda = 1$) as frequency increases from zero. At zero frequency, the eigenvector is a rigid body displacement in the y-direction, coupled with cross-sectional rotation as a principal vector, as noted in Section 3.4; as frequency is increased from zero, loop 3 initially has relatively large displacements in the y-direction with some cross-sectional rotation, and waves show monotonic evanescent decay. Waves decay at an increasing rate up to a turning

point at $\omega^2 \approx 0.0808$ with increasing cross-sectional rotation. Decay rate then decreases as frequency approaches cut-on at $\omega^2 = 0.3536$; displacements in the y-direction approach zero and the mode exhibits first thickness shear, pure cross-sectional rotation, still with $\lambda = 1$. Displacement vectors for the loop below, at and above the turning point are shown in Table 3.4. At the cut-on frequency, where loop 3 becomes branch 3, the top and bottom masses oscillate in opposition with equal amplitude, which suggests that one half-wavelength occupies the framework depth. As frequency increases, wavenumber increases and wavelength decreases. At $\omega^2 \approx 3.1707$, branch 3 meets branch 6, forming loop 3,6 which represents one of the two leftward *attenuating* waves. At $\omega^2 \approx 3.695$, loop 3,6 rejoins the plane $\delta = 0$ and reverts back to the two propagating branches 3 and 6. Branch 3 continues as first thickness shear until it reaches its cut-off frequency at $\omega^2 = 4.3536$, when the wavelength occupies two cells, i.e. one half-wavelength over one cell length. Above that frequency, the wave shows oscillatory evanescent decay, with more rapid decay as the frequency increases.

Branch 4 exhibits symmetric second thickness shear. The initial frequency stop band is from $\omega^2 = 0$ to $\omega^2 = 1.0607$, where the wave shows monotonic evanescent decay. The branch commences at $\omega^2 = 0$ and $\delta = 1.2626$, which is equivalent to the static leftward decay of a self-equilibrating load with eigenvalue $\lambda = 3.5346$ ($\ln 3.5346 = 1.2626$). As frequency increases, the rate of decay reduces; eventually the wave starts to propagate when it reaches its cut-on frequency at $\omega^2 = 1.0607$, with $\lambda = 1$, where the top and bottom masses oscillate in-phase with equal amplitude, but out-of-phase with the middle mass which has double the amplitude; this suggests that there is one half-wavelength between the top and middle masses and a second half-wavelength between the bottom and middle masses. As frequency increases, wavelength decreases; the cut-off frequency ($\lambda = -1$) is reached when $\omega^2 = 4$ and one half-wavelength occupies exactly one cell length. Even though branches 3 and 4 cross each other twice, no interaction is observed between the two branches and this is attributed to the fact that the latter is symmetric while the former is not; again this is considered in more depth in Section 3.10. The components of the displacement vector show only subtle changes where the branches cross, and generally maintain their character. For the first crossing, the displacement vectors are shown in Table 3.5, where one sees that the (imaginary) y-direction component of the middle mass goes through zero for mode 3 while the other components are nearly unchanged, to the accuracy shown. However at the point of crossing ($\omega^2 = 1.3536$) the y-direction component of the top mass and both components

of the bottom masses (shown in bold) show a significant change compared to those just below and just above; this is regarded as a numerical instability of the QR algorithm employed by MATLAB. Similar subtle changes occur for mode 4, where now it is the (real) x-direction component of the middle mass that goes through zero, and the imaginary components show very small changes; again there appears to be a numerical instability. Note that the imaginary part of the displacement components are shown with $\pm$ and $\mp$ conjugates: the lower sign pertains to left-going waves, as in Figure 3.3, while the upper sign pertains to right-going.

ω^2	0.0100	0.0600	0.0608	0.0700	0.0808
λ	0.7350	0.6735	0.6734	0.6718	0.6712
δ	−0.3079	−0.3952	−0.3954	−0.3978	−0.3987
D	$\begin{bmatrix} 0.4373 \\ 1 \\ 0 \\ 0.9804 \\ -0.4373 \\ 1 \end{bmatrix}$	$\begin{bmatrix} 0.9921 \\ 1 \\ 0 \\ 0.9363 \\ -0.9921 \\ 1 \end{bmatrix}$	$\begin{bmatrix} 1 \\ 1 \\ 0 \\ 0.9357 \\ -1 \\ 1 \end{bmatrix}$	$\begin{bmatrix} 1 \\ 0.9186 \\ 0 \\ 0.8532 \\ -1 \\ 0.9186 \end{bmatrix}$	$\begin{bmatrix} 1 \\ 0.8380 \\ 0 \\ 0.7717 \\ -1 \\ 0.8380 \end{bmatrix}$

ω^2	0.0900	0.1000	0.3000	0.3500
λ	0.6716	0.6727	0.8118	0.9469
δ	−0.3981	−0.3964	−0.2085	−0.0546
D	$\begin{bmatrix} 1 \\ 0.7790 \\ 0 \\ 0.7123 \\ -1 \\ 0.7790 \end{bmatrix}$	$\begin{bmatrix} 1 \\ 0.7227 \\ 0 \\ 0.6557 \\ -1 \\ 0.7227 \end{bmatrix}$	$\begin{bmatrix} 1 \\ 0.1728 \\ 0 \\ 0.1337 \\ -1 \\ 0.1728 \end{bmatrix}$	$\begin{bmatrix} 1 \\ 0.0402 \\ 0 \\ 0.0298 \\ -1 \\ 0.0402 \end{bmatrix}$

Table 3.4   Displacement vectors associated with Loop 3 of the dispersion diagram, close to its turning point $\omega^2 \approx 0.0808$.

ω^2	Mode 3 First thickness shear
1.35	$\begin{bmatrix} 1 & \pm0.2602i & 0 & \pm0.0008i & -1 & \pm0.2602i \end{bmatrix}^T$
1.352	$\begin{bmatrix} 1 & \pm0.2602i & 0 & \pm0.0003i & -1 & \pm0.2602i \end{bmatrix}^T$
1.3536	$\begin{bmatrix} 1 & \mathbf{0.8351\pm2.1339i} & 0 & 0 & \mathbf{-5.4743\pm1.9941i} & \mathbf{-0.3162\mp0.4493i} \end{bmatrix}^T$
1.354	$\begin{bmatrix} 1 & \pm0.2602i & 0 & \mp0.0001i & -1 & \pm0.2602i \end{bmatrix}^T$
1.36	$\begin{bmatrix} 1 & \pm0.2602i & 0 & \mp0.0014i & -1 & \pm0.2602i \end{bmatrix}^T$

ω^2	Mode 4 Second thickness shear
1.35	$\begin{bmatrix} 1 & \mp0.5849i & -0.0068 & 0 & 1 & \pm0.5849i \end{bmatrix}^T$
1.352	$\begin{bmatrix} 1 & \mp0.5807i & -0.0029 & 0 & 1 & \pm0.5807i \end{bmatrix}^T$
1.3536	$\begin{bmatrix} 1 & \mathbf{-0.0172\mp0.1638i} & 0 & 0 & \mathbf{0.0125\mp0.0410i} & \mathbf{0.0065\pm0.4208i} \end{bmatrix}^T$
1.354	$\begin{bmatrix} 1 & \mp0.5764i & 0.0008 & 0 & 1 & \pm0.5764i \end{bmatrix}^T$
1.36	$\begin{bmatrix} 1 & \mp0.5640i & 0.0118 & 0 & 1 & \pm0.5640i \end{bmatrix}^T$

Table 3.5 Displacement vectors below, at, and above the crossing frequency $\omega^2 = 1.3536$ for modes 3 and 4.

Similar subtle changes occur at the second crossing of branches 3 and 4 ($\omega^2 \approx 1.6702$), and also for the crossings of branches 3 and 5 ($\omega^2 \approx 3.7151$), and again there is numerical instability at the point of crossing. These displacement vectors are shown in Appendix B.

Branch 5, which is the symmetric first breathing wave, exhibits monotonic evanescent decay from $\omega^2 = 0$ to $\omega^2 = 1.3536$. The branch commences at $\omega^2 = 0$ and $\delta = 2.8202$, which is equivalent to the static leftward decay of a self-equilibrating load with eigenvalue $\lambda = 16.7798$ ($\ln 16.7798 = 2.8202$). As frequency increases, the decay rate decreases gradually and the mode propagates when the cut-on frequency $\omega^2 = 1.3536$ is reached,

where the masses at the top and bottom of the framework oscillate in the y-direction with equal amplitude, but 180 degrees out-of-phase with each other. This suggests that one half-wavelength occupies the depth, despite the wavelength in the axial x-direction being infinite. As frequency increases, so wavelength decreases. The mode ceases to propagate when it reaches its cut-off frequency ($\lambda = -1$) at $\omega^2 = 5.0607$, where one half-wavelength occupies one cell length, in the x-direction. Above the cut-off frequency, the decay is oscillatory evanescent.

Branch 6 is the asymmetric second breathing wave, and unlike other branches, it starts in the $\varphi = \pi$ plane because the eigenvalue $\lambda = -14.2435$ ($\delta = 2.6563$) is negative when $\omega^2 = 0$. From $\omega^2 = 0$ to $\omega^2 = 1.3536$, the wave is oscillatory evanescent and decays rapidly but at a decreasing decay rate as frequency is increased. At $\omega^2 = 1.3536$ the branch collides with the oscillatory evanescent bending mode; the two waves interact to form two attenuating waves, with the leftward decay represented by the loop 1,6. The oscillatory evanescent second breathing wave reappears at $\omega^2 \approx 3.021$ and continues to decay at a decreasing rate until it reaches its cut-on frequency ($\lambda = -1$) at $\omega^2 = 3.1678$ where one half-wavelength can be accommodated across one cell length; also note from Figure 3.7(i) that one full wavelength occupies the depth of the framework. As frequency increases, wavenumber (phase) decreases and wavelength increases. The gradient of branch 6 is negative, implying that energy is propagated in a direction opposite to the direction of wave propagation; this phenomenon is known as anomalous dispersion. This anomalous second breathing mode (branch 6) meets the normal first thickness shear mode (branch 3) at $\omega^2 \approx 3.1707$, where the two modes interact to form attenuating waves. One of the two leftward attenuating waves is represented by loop 3,6 in Figure 3.3, and represents leftward decay because δ is positive in the quadrant shown; not shown is the image where δ is negative, which would represent rightward decay. The group velocity of the two modes are in opposite directions: the loop arises as a result of their energy interaction when one has zero-energy resultant which does not travel along the structure. The branch start to propagate again at $\omega^2 \approx 3.695$ where the interaction ceases, and reaches its cut-off frequency ($\lambda = 1$) at $\omega^2 = 4.0607$. Above the cut-off frequency, the branch is monotonic evanescent which decays increasingly rapidly.

We now make some general observations regarding Figure 3:

i.   The framework is dispersive for all propagating branches – waves of different wavenumber travel at different phase velocity $c_\mathrm{p} = \omega/\varphi$. All waves decay above $\omega^2 = 5.0607$.

ii. Attenuating waves (loops) occur when a wave associated with a normal dispersion branch interacts with a wave associated with an anomalous dispersion branch. For the example framework, it is seen that such interactions only occur when the normal and anomalous waves are both asymmetric, but they can be initially propagating (loop 3,6) or oscillatory evanescent (loop 1,6).

iii.   There is no branch crossing of symmetric waves, but symmetric and asymmetric branches can cross without interaction and the consequent formation of attenuating waves.

iv. For normal dispersion branches, the axial wavelength at the cut-on frequency is infinite. Tension and bending moment transmit along the structure in the static case, and such waves propagate immediately: the branches emanate from the origin. Branches 3, 4 and 5 start to propagate at a cut-on frequency, when one-half wavelength occupies the depth of the structure (branches 3 and 5), or one-half of the depth (branch 4). This can be likened to phase closure *over the cross-section*. In Chapter 2, phase closure is used to determine the natural frequencies of a finite length structure, and is based on the idea that the phase change for a complete circumnavigation of the structure *in the axial direction*, is an integer multiple of 2π. At a cut-on frequency we have phase closure over the cross-sectional depth. For branches 3 and 5, the phase changes is 2π, while for branch 4, it is 4π; these branches also have phase closure over the cross-section at their cut-off frequencies.

v.   Again, for all normal dispersion branches, cut-off occurs when one-half wavelength occupies the length of the repeating cell; that is one has phase closure over a single cell in the axial direction.

vi. The anomalous branch 6 also displays phase closure at cut-on and cut-off, but now phase closure over a single cell in the axial direction coincides with cut-on, and over the cross-section with cut-off.

3.8 Evanescent waves, and a dynamic Saint-Venant's principle

The term *evanescent* is generally used to describe wave amplitude decaying over distance with or without phase change. In the present work, we describe a wave that decays without phase change (from section to section) as monotonic evanescent, and one with a phase change of π radians over each cell as oscillatory evanescent.

Monotonic evanescent waves occur when a normally dispersive wave is driven at a frequency below its cut-on frequency and when the anomalously dispersive wave is driven at a frequency above its cut-off frequency. Oscillatory evanescent waves occur when a normally dispersive wave is driven at a frequency above its cut-off frequency and when the anomalously dispersive wave is driven at a frequency below its cut-on frequency. Examples of both are shown in Figures 3.8 and 3.9.

When the framework is driven at a given frequency ω at a particular cross-section then, in steady-state, each mass at that section will vibrate at that driving frequency. If the cross-section was isolated, either as part of a single cell or a single cross-section, that is not part of an infinite repetitive structure, then the amplitude of vibration vector **D** would depend on the magnitude of the force and the dynamic stiffness: in the absence of damping, one could write a matrix equation of the form $\mathbf{D} = \left(\mathbf{K} - \omega^2 \mathbf{m} \right)^{-1} \mathbf{F}$. For a driving frequency below the first natural frequency, the net work done per cycle would be zero, and the amplitude is proportional to the magnitude of the force, and constant at a given frequency. (If damping was present, the work done per cycle would be equal to the energy dissipated per cycle, and the amplitude would remain constant.) If the forcing frequency coincided with a natural frequency one would have resonance, work would be done, and the amplitude would build up linearly with time. In the absence of damping and non-linearity, the mathematical model would predict infinite amplitude, although it would take infinite time to achieve that infinite amplitude. However, the driven cross-section is not isolated but is attached to adjacent cross-sections on either side by means of the elastic pin-jointed bars. The net force applied to the driven section is equal to the exciting force, less the force transmitted to adjacent cross-sections by virtue of elastic deformation of the bars, at the same frequency. Also, the restoring force at the driven section is provided in part by the exciting force, in part by virtue of deformation of the bars. However, adjacent cross-sections are driven by virtue of elastic deformation alone; in turn their amplitudes must be smaller. Cross-sections further from the driven section will in turn be excited by the lesser amplitudes of the adjacent cross-sections, leading to the decay.

For normal dispersion, at driving frequencies below cut-on, the exciting force still does no work, and no energy is propagated along the structure. Cut-on is the equivalent of resonance: the exciting frequency is equal to the cross-sectional natural frequency as determined by phase closure *over the cross-section*. The exciting force now does work; however, unlike the isolated cross-section considered above, the amplitude does not increase with time, rather that energy is transmitted along the structure, and the amplitude remains constant – infinite structure replaces infinite time. The mode at cut-on corresponds to a configuration in which adjacent masses on the same tier oscillate at the same amplitude and in the same direction ($\lambda = 1$). The anomalous branch 6 also displays phase closure over the cross-section at cut-on; the difference is that one also has phase closure over the length of a single cell.

Again for normal dispersion, cut-off ($\lambda = -1$) occurs when one has a resonance over a single cell length: one has phase closure over that single cell in the axial direction. If the driving frequency is greater than the cut-off, then the wave becomes oscillatory evanescent. Again, the net (including restoring) force at the driven section is equal to the exciting force, less the force transmitted to adjacent cross-sections by virtue of elastic deformation of the bars; adjacent sections are excited by the latter alone. Now, masses at adjacent sections have a phase difference of π radians; this can be attributed to the fact that the masses at any section have insufficient time to accelerate in one direction before the force at the preceding section changes direction.

(a)   (b)
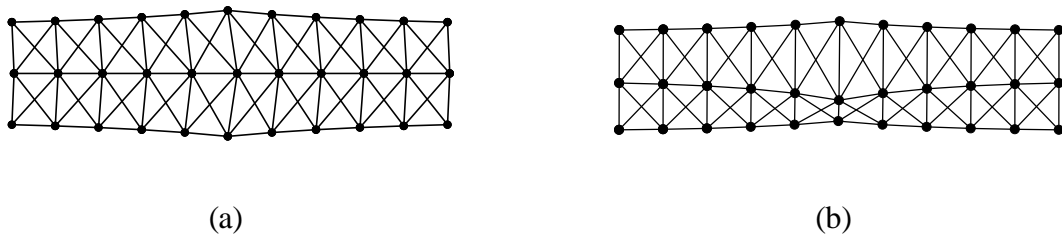
Figure 3.8 (a) Monotonic evanescent first breathing wave at $\omega^2 = 1.3$ with eigenvalue $\lambda = 0.7449$. (b) Monotonic evanescent second breathing wave at $\omega^2 = 4.1$ with eigenvalue $\lambda = 0.6384$.

(a)   (b)
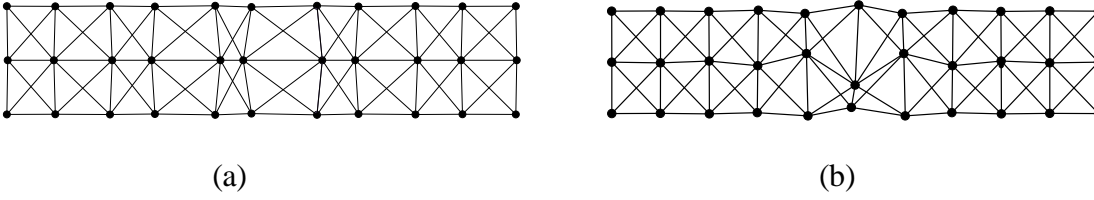
Figure 3.9 (a) Oscillatory evanescent first breathing wave at $\omega^2 = 5.3$ with eigenvalue $\lambda = -0.6414$. (b) Oscillatory evanescent second breathing wave at $\omega^2 = 3.1$ with eigenvalue $\lambda = -0.3852$.

3.9   Attenuating waves

The amplitude of an attenuating wave decreases by a decay rate constant and its phase changes by a constant value φ (not equal to π radians) from one section to the next in the direction of wave travel. In Figure 3.3, such waves are represented by loops 1,6 and 3,6. Loop 1,6 occurs from $\omega^2 = 1.3536$ to $\omega^2 \approx 3.0216864$, which corresponds to eigenvalues $\lambda = \exp(\pm 1.7 \pm i\pi)$ and $\lambda = \exp(\pm 1.4832 \pm i\pi)$, respectively, see Table 3.6. Loop 3,6 starts at $\omega^2 \approx 3.1707$ and stops at $\omega^2 \approx 3.6951$ which corresponds to $\lambda = \exp(\pm i0.8705\pi)$ and $\lambda = \exp(\pm i0.5861\pi)$, respectively, see Table 3.7. The loops are not perfect semi-circles. The end points of the loops are behind their respective starting points, as frequency increases – that is, loop 3,6 finishes at a smaller value of $\varphi = 0.5861\pi$ than the value where it starts, $\varphi = 0.8705\pi$. Likewise, loop 1,6 finishes at a smaller value of $\delta = 1.4832$ than the value where it starts, $\delta = 1.7000$, see Table 3.6.

It is noted that extreme values of the decay rate and the wavenumber (phase) occur at different frequencies: for loop 1,6, the decay rate maximum occurs at $\omega^2 \approx 2.022$, while the wavenumber minimum occurs at $\omega^2 \approx 2.3$, see Table 3.6. For loop 3,6, the decay rate maximum occurs at $\omega^2 = 3.35$; however, there is no extreme value for the wavenumber as it continues a decreasing trend as frequency increases, see Table 3.7.

Loop 1,6 occurs as a result of interaction between the oscillatory evanescent bending wave and oscillatory evanescent second breathing wave; the former has increasing decay rate while the latter has decreasing decay rate as a function of increasing ω^2. The bending wave is characterised by in-phase displacements of $D_{1y}(n)$, $D_{2y}(n)$ and $D_{3y}(n)$. However, as frequency increases above the bending mode cut-off frequency, $D_{2y}(n)$ diminishes and then

starts to become out-of-phase with $D_{1y}(n)$ and $D_{3y}(n)$; hence this bending wave displacement vector starts to resemble the second breathing wave displacement vector. The collision occurs at $\omega^2 = 1.3536$ where $D_{2y} = 0$ and the two oscillatory evanescent waves have the same displacement vector; the evolution of the displacement vectors at frequencies close to this frequency is shown in Table 3.8.

Loop 3,6 occurs as a result of interaction between the propagating first thickness shear wave and propagating second breathing wave; the wavenumber of the former increases with respect to frequency while the latter decreases. The displacement vectors associated with loop 3,6 at different frequencies are shown in Table 3.9. Close to the collision frequency, the first thickness shear wave eigenvector already resembles that of the second breathing wave. At the collision point, $\omega^2 \approx 3.1707$, the displacement vector of each branch become equal and remain so along the loop, albeit as complex conjugates, resembling the second breathing mode shape. It is only towards the end of branch 3 at $\omega^2 \approx 3.8004$ that the character of the first thickness shear mode once again becomes apparent.

We further noted that attenuating waves always occur as a result of interaction between normal and anomalous dispersions. The details on this observation are as follows.

i. Attenuating waves arise in two ways: for propagating waves, as a result of the interaction between two asymmetric waves of the same wavelength each having power flow in opposite directions, loop 3,6; for oscillatory evanescent waves, through the interaction of two asymmetric waves having opposite decay rate gradients, that is one with increasing rate, the other decreasing (with increasing frequency), loop 1,6. The common features are the asymmetry, and the involvement of the anomalous branch 6.

ii. Loop 1,6 represents the interaction between the bending and second breathing modes, initially both leftward oscillatory evanescent. Their collision results in leftward and rightward attenuating waves that decay in leftward direction; the leftward decay is shown in Figure 3.3 as the sign of δ is positive. However, the eigenvalue plotted is but one of a quartet: the rightward decay would be in the positive φ but negative δ quadrant. The reciprocal complex conjugate branch segments of loop 1,6, with negative φ, lie within omitted quadrants. For loop 3,6, the interaction between left-going first thickness and left-going second breathing waves results in two leftward attenuating waves that decay in both directions; again, the leftward decay is shown in Figure 3.3 as the sign of δ is positive, and

the rightward decay has negative δ. Again, the reciprocal conjugate branch segments of loop 3,6 lie within omitted quadrants.

iii. Loops 1,6 and 3,6 present the notion of an attenuating wave that travels in a direction opposite to its direction of decay. It is suspected that this arises from the relative difference, or opposing contributions, in 'decay rate' or 'energy flow speed' between the two interacting modes.

iv. The gradient at the collision and bifurcation points of the interacting branches is zero; with reference to Figure 3.3, the slope of the propagating branches is taken with respect to the φ-axis while the slope of the oscillatory evanescent branches is taken with respect to δ-axis. At these points, zero gradient implies that the group velocity is zero.

ω^2	λ	$\delta \pm \mathrm{i}\varphi$
1.3536	−0.1827	$1.7000 \pm \pi\mathrm{i}$
1.36	$-0.1817 \pm 0.0140\mathrm{i}$	$1.7026 \pm 3.0647\mathrm{i}$
……	……	……
1.9	$-0.1398 \pm 0.0851\mathrm{i}$	$1.8099 \pm 2.5951\mathrm{i}$
2.0	$-0.1375 \pm 0.0878\mathrm{i}$	$1.8131 \pm 2.5735\mathrm{i}$
2.1	$-0.1364 \pm 0.0899\mathrm{i}$	$1.8119 \pm 2.5589\mathrm{i}$
2.2	$-0.1364 \pm 0.0915\mathrm{i}$	$1.8062 \pm 2.5505\mathrm{i}$
2.3	$-0.1376 \pm 0.0928\mathrm{i}$	$1.7959 \pm 2.5484\mathrm{i}$
2.4	$-0.1402 \pm 0.0936\mathrm{i}$	$1.7806 \pm 2.5529\mathrm{i}$
……	……	……
3.0	$-0.2180 \pm 0.0399\mathrm{i}$	$1.5069 \pm 2.9604\mathrm{i}$
3.022	−0.2269	$1.4832 \pm \pi\mathrm{i}$

Table 3.6 The evolution of eigenvalues, decay rates and wavenumbers at different frequencies for loop 1,6.

ω^2	λ	$\delta \pm \mathrm{i}\varphi$
3.1707	$-0.9184 \pm 0.3956\mathrm{i}$	$\pm 2.7349\mathrm{i} = \pm 0.8705\pi\mathrm{i}$
3.18	$-0.6632 \pm 0.3756\mathrm{i}$	$-0.2716 \pm 2.6263\mathrm{i}$
……	……	……
3.34	$-0.3492 \pm 0.4798\mathrm{i}$	$-0.5219 \pm 2.2000\mathrm{i}$
3.35	$-0.3424 \pm 0.4844\mathrm{i}$	$-0.5222 \pm 2.1860\mathrm{i}$
3.36	$-0.3359 \pm 0.4891\mathrm{i}$	$-0.5220 \pm 2.1725\mathrm{i}$
……	……	……
3.69	$-0.2484 \pm 0.8810\mathrm{i}$	$-0.0885 \pm 1.8456\mathrm{i}$
3.6951	$-0.2671 \pm 0.9637\mathrm{i}$	$\pm 1.8412\mathrm{i} = \pm 0.5861\pi\mathrm{i}$

Table 3.7   Evolution of eigenvalues, decay rates and wavenumbers at different frequencies for loop 3,6. The maximum decay rate occurs at $\omega^2 \approx 3.35$.

ω^2	Bending	Second breathing
1.2	$\begin{bmatrix} -0.0488 & 1 & 0 & 0.4342 & 0.0488 & 1 \end{bmatrix}^T$	$\begin{bmatrix} 0.0598 & 1 & 0 & -0.4015 & -0.0598 & 1 \end{bmatrix}^T$
1.3	$\begin{bmatrix} -0.0333 & 1 & 0 & 0.2596 & 0.0333 & 1 \end{bmatrix}^T$	$\begin{bmatrix} 0.0363 & 1 & 0 & -0.2475 & -0.0363 & 1 \end{bmatrix}^T$
1.3536	$\begin{bmatrix} 0 & 1 & 0 & 0 & 0 & 1 \end{bmatrix}^T$	
1.4	$\begin{bmatrix} -0.0010 \pm 0.0348i & 1 & 0 & -0.0056 \mp 0.2430i & 0.0010 \mp 0.0348i & 1 \end{bmatrix}^T$	
1.5	$\begin{bmatrix} -0.0024 \pm 0.0659i & 1 & 0 & -0.0188 \mp 0.4447i & 0.0024 \mp 0.0659i & 1 \end{bmatrix}^T$	
……	……	
3.0	$\begin{bmatrix} 1.0788 \pm 0.8497i & 1 & 0 & -5.8284 \mp 4.5071i & -1.0788 \mp 0.8497i & 1 \end{bmatrix}^T$	
3.0217	$\begin{bmatrix} 1.7192 & 1 & 0 & -9.2266 & -1.7192 & 1 \end{bmatrix}^T$	
3.03	$\begin{bmatrix} 3.2567 & 1 & 0 & -17.37 & -3.2567 & 1 \end{bmatrix}^T$	$\begin{bmatrix} 1.1564 & 1 & 0 & -6.2507 & -1.1564 & 1 \end{bmatrix}^T$

Table 3.8 Evolution of the displacement vectors of the bending and second breathing waves during transition from distinct oscillatory evanescent to conjugate attenuating waves, loop 1,6.

ω^2	First thickness shear	Second breathing
3.17	$\begin{bmatrix}\mp 0.46i & 1 & 0 & -2.641 & \pm 0.46i & 1\end{bmatrix}^T$	$\begin{bmatrix}\mp 0.26i & 1 & 0 & -2.7439 & \pm 0.26i & 1\end{bmatrix}^T$
3.1707	$\begin{bmatrix}\mp 0.3691i & 1 & 0 & -2.6909 & \pm 0.3691i & 1\end{bmatrix}^T$	
3.18	$\begin{bmatrix}0.3130\pm 0.4224i & 1 & 0 & -2.6690\mp 0.1877i & -0.3130\mp 0.4224i & 1\end{bmatrix}^T$	
……	……	
3.6951	$\begin{bmatrix}\pm 1.0912i & 1 & 0 & -2.5857 & \mp 1.0912i & 1\end{bmatrix}^T$	
3.7	$\begin{bmatrix}\pm 1.36i & 1 & 0 & -2.6737 & \mp 1.36i & 1\end{bmatrix}^T$	$\begin{bmatrix}\pm 0.88i & 1 & 0 & -2.5038 & \mp 0.88i & 1\end{bmatrix}^T$
3.8	$\begin{bmatrix}\pm 3.07i & 1 & 0 & -3.076 & \mp 3.07i & 1\end{bmatrix}^T$	$\begin{bmatrix}\pm 0.39i & 1 & 0 & -2.2411 & \mp 0.39i & 1\end{bmatrix}^T$
3.9	$\begin{bmatrix}1 & \mp 0.208i & 0 & 0.7i & -1 & \mp 0.208i\end{bmatrix}^T$	$\begin{bmatrix}\pm 0.23i & 1 & 0 & -2.124 & \mp 0.23i & 1\end{bmatrix}^T$

Table 3.9   Evolution of the displacement vectors of the first thickness shear and second breathing waves during transition from distinct propagating to conjugate attenuating waves, and *vice versa*, loop 3,6.

3.10   Krein signature

In the two-dimensional complex plane, propagating complex unity eigenvalues lie on the unit circle; the Krein signature is associated with the direction of rotation of the eigenvalue loci on that circle [77,98]. As the frequency is increased, eigenvalues with positive signature move anti-clockwise while those with negative signature move clockwise [98]. In the three-dimensional Cartesian plane, as in Figure 3.3, the complex unity eigenvalues lie on distinct curves, or branches, on the plane $\delta = 0$; branches with positive signature move in the direction of increasing φ (that is, eigenvalues rotate anti-clockwise on the unit circle) while eigenvalues with negative signature move in the direction of decreasing φ, as frequency is increased. Along the positive φ-axis, branches and eigenvalues with positive and negative signatures are associated with normal and anomalous dispersions, respectively. Conversely, along the negative φ-axis, branches and eigenvalues with positive and negative signatures are associated with anomalous and normal dispersions, respectively. When branches with the same signature intersect, or cross, they remain on the plane and with the same signature; likewise, their eigenvalues remain on the unit circle. However, when branches with opposite signs collide, they move out of the plane $\delta = 0$ (and their eigenvalues move off the unit circle) forming a closed loop before returning to the plane and splitting into separate branches again with opposite signs. The signature is not defined on the loop.

The Krein signature κ associated with a complex unity eigenvalue λ_i can be expressed as $\kappa = \text{sgn}\left(-i\,\mathbf{V}_i^*\mathbf{J}\mathbf{V}_i\right)$ where $\mathbf{V}_i$ is the corresponding eigenvector of transfer matrix $\mathbf{G}$, $\mathbf{V}_i^*$ is its transposed conjugate, $\mathbf{J} = \begin{bmatrix} \mathbf{0} & \mathbf{I} \\ -\mathbf{I} & \mathbf{0} \end{bmatrix}$ and $\mathbf{I}$ is the (6×6) identity matrix, [98]. A similar expression can be obtained in terms of the eigenvectors of transfer matrix $\mathbf{H}$ as $\kappa = \text{sgn}\left(-i\,\mathbf{X}_i^*\tilde{\mathbf{J}}\mathbf{X}_i\right)$ where $\mathbf{X}_i$ is the eigenvector corresponding to eigenvalue λ_i, $\mathbf{X}_i^*$ is the transposed conjugate of $\mathbf{X}_i$ and $\tilde{\mathbf{J}} = \begin{bmatrix} \mathbf{0} & -\mathbf{K}_{\text{LR}} \\ \mathbf{K}_{\text{RL}} & \mathbf{0} \end{bmatrix}$. In either form, the signature is not affected by any scaling of the eigenvector length. For example, suppose $\mathbf{V}_i$ is scaled by $\alpha = a + ib$; then $\kappa = \text{sgn}\left(-i\left(\alpha\mathbf{V}_i\right)^*\mathbf{J}\left(\alpha\mathbf{V}_i\right)\right) = \text{sgn}\left(-i\,\alpha^*\alpha\mathbf{V}_i^*\mathbf{J}\mathbf{V}_i\right)$; but $\alpha^*\alpha = \left(a - ib\right)\left(a + ib\right) = a^2 + b^2$, which must be positive, so the sign is unchanged.

The expressions for κ are intimately related to the power flow, which can be expressed as $P = -\mathrm{i}\,\omega \mathbf{V}_i^* \mathbf{J} \mathbf{V}_i / 4$ or $P = -\mathrm{i}\,\omega \mathbf{X}_i^* \tilde{\mathbf{J}} \mathbf{X}_i / 4$. If the power P and wavenumber φ have the same sign, the dispersion is normal, otherwise it is anomalous. Accordingly, in such a form, the signature can only be defined for propagating branches since there is no power flow for evanescent and attenuating branches. This can be shown as follows: the ith eigenvector of transfer matrix $\mathbf{G}$ satisfies $\mathbf{G}\mathbf{V}_i = \lambda_i \mathbf{V}_i$; taking the transposed conjugate, one has $\mathbf{V}_i^* \mathbf{G}^{\mathrm{T}} = \lambda_i^* \mathbf{V}_i$ where $\mathbf{G}^* = \mathbf{G}^{\mathrm{T}}$ since $\mathbf{G}$ is real. Now post-multiply the latter by $\mathbf{J}\mathbf{G}\mathbf{V}_i$ to give $\mathbf{V}_i^* \left(\mathbf{G}^{\mathrm{T}} \mathbf{J} \mathbf{G} \right) \mathbf{V}_i = \lambda_i^* \mathbf{V}_i^* \mathbf{J} \mathbf{G} \mathbf{V}_i$ which reduces to $\mathbf{V}_i^* \mathbf{J} \mathbf{V}_i = \lambda_i^* \lambda_i \mathbf{V}_i^* \mathbf{J} \mathbf{V}_i$ since $\mathbf{G}^{\mathrm{T}} \mathbf{J} \mathbf{G} = \mathbf{J}$, and finally rearrange as $\left(1 - \lambda_i^* \lambda_i \right) \mathbf{V}_i^* \mathbf{J} \mathbf{V}_i = 0$; this implies that $\mathbf{V}_i^* \mathbf{J} \mathbf{V}_i = 0$ unless $\lambda_i^* \lambda_i = 1$, which is the case for a complex unity eigenvalue.

In the case of repeated complex unity eigenvalues but with distinct eigenvectors, that is a branch crossing, $\mathbf{V}_i^* \mathbf{J} \mathbf{V}_i$ are also distinct, nonzero and purely imaginary; in turn, the Krein signature is positive if the associated wavenumber is positive, and *vice versa*. Evidently, the eigenvalues cross each other at a point and, as aforementioned, their signatures remain unchanged after the crossing. With reference to Figure 3.3, eigenvalue crossing occurs twice between branches 3 and 4, and once between branches 3 and 5. In the case of repeated complex unity eigenvalues associated with normal and anomalous eigenvectors, that is at a collision, $\mathbf{V}_i^* \mathbf{J} \mathbf{V}_i = 0$, so $\kappa = 0$. This case is associated with the beginning and the end of loop 3,6 in Figure 3.3. Following similar procedures for an eigenvector $\mathbf{X}_i$ of transfer matrix $\mathbf{H}$ leads to $\left(1 - \lambda_i^* \lambda_i \right) \mathbf{X}_i^* \tilde{\mathbf{J}} \mathbf{X} = 0$ and similar results.

The expression of Krein signature associated with complex unity eigenvalue is readily extendable to the case of real unity eigenvalues ($\lambda = \pm 1$). The signature takes the form $\kappa = \mathrm{sgn}\left(-\mathbf{V}_i^{\mathrm{T}} \mathbf{J} \mathbf{V}_i \right)$ where $\mathbf{V}_i^{\mathrm{T}}$ is the transpose of $\mathbf{V}_i$, or $\kappa = \mathrm{sgn}\left(-\mathbf{X}_i^{\mathrm{T}} \tilde{\mathbf{J}} \mathbf{X}_i \right)$ where $\mathbf{X}_i^{\mathrm{T}}$ is the transpose of $\mathbf{X}_i$; the factor i is now omitted because the vectors are real. Similar to the case of repeated complex unity eigenvalues with repeated eigenvector, the real unity eigenvalues signature is zero in the plane $\delta = 0$.

In order to extend the signature to the evanescent branches which lie on the planes $\varphi = 0$ and $\varphi = \pi$, and for the latter extend the concept of a Krein collision to loop 1,6, we employ the power flow equation. Since there is no power flow transported by an evanescent wave

and the eigenvector $\mathbf{X}$ is real for real non-unity eigenvalues, the equation becomes $i\,\omega\mathbf{X}_i^{\mathrm{T}}\tilde{\mathbf{J}}\mathbf{X}_i = 0$; expanding this gives

$$i\,\omega\left[-\mathbf{D}_{\mathrm{L}}^{\mathrm{T}}\mathbf{K}_{\mathrm{LR}}\mathbf{D}_{\mathrm{R}} + \mathbf{D}_{\mathrm{R}}^{\mathrm{T}}\mathbf{K}_{\mathrm{RL}}\mathbf{D}_{\mathrm{L}}\right] = i\,\omega\lambda\left[-\mathbf{D}_{\mathrm{L}}^{\mathrm{T}}\mathbf{K}_{\mathrm{LR}}\mathbf{D}_{\mathrm{L}} + \mathbf{D}_{\mathrm{L}}^{\mathrm{T}}\mathbf{K}_{\mathrm{RL}}\mathbf{D}_{\mathrm{L}}\right] = 0,$$

which reduces to $\mathbf{D}_{\mathrm{L}}^{\mathrm{T}}\mathbf{K}_{\mathrm{LR}}\mathbf{D}_{\mathrm{L}} \equiv \mathbf{D}_{\mathrm{L}}^{\mathrm{T}}\mathbf{K}_{\mathrm{RL}}\mathbf{D}_{\mathrm{L}}$. Either term represents part of the strain energy that is stored across a cell as a result of the work done on the left-hand side of the cell. We find numerically (prompted by the work of Mead [18], see Section 3.3) that the sign of $\mathbf{D}_{\mathrm{L}}^{\mathrm{T}}\mathbf{K}_{\mathrm{LR}}\mathbf{D}_{\mathrm{L}}$ is an invariant, unique to normal and anomalous evanescent branches. In order to keep the sign consistent with the convention for propagating waves, we introduce a minus sign and define a new signature for evanescent waves as $\kappa' = \mathrm{sgn}\left(-\mathbf{D}_{\mathrm{L}}^{\mathrm{T}}\mathbf{K}_{\mathrm{LR}}\mathbf{D}_{\mathrm{L}}\right)$, so the eigenvalue loci of normal and anomalous evanescent branches are associated with positive and negative signs, respectively, irrespective of the direction of eigenvalue loci in planes $\varphi = 0$ and $\varphi = \pi$.

This signature arises as a property of the $\mathbf{K}_{\mathrm{LR}}$ matrix as can be shown as follows. First, express $\mathbf{K}_{\mathrm{LR}}$ as a sum of symmetric and skew-symmetric matrices, i.e. $\mathbf{K}_{\mathrm{LR}} = \mathbf{K}_{\mathrm{LR,\,sym}} + \mathbf{K}_{\mathrm{LR,\,skew}}$ where $\mathbf{K}_{\mathrm{LR,\,sym}} = \frac{1}{2}\left[\mathbf{K}_{\mathrm{LR}} + \mathbf{K}_{\mathrm{LR}}^{\mathrm{T}}\right]$ and $\mathbf{K}_{\mathrm{LR,\,skew}} = \frac{1}{2}\left[\mathbf{K}_{\mathrm{LR}} - \mathbf{K}_{\mathrm{LR}}^{\mathrm{T}}\right]$. We find numerically that $\mathbf{D}_{\mathrm{L}}^{\mathrm{T}}\mathbf{K}_{\mathrm{LR,\,skew}}\mathbf{D}_{\mathrm{L}} = 0$, which is generally true for any skew-symmetric matrix. Therefore, $\kappa' = \mathrm{sgn}\left(-\mathbf{D}_{\mathrm{L}}^{\mathrm{T}}\mathbf{K}_{\mathrm{LR}}\mathbf{D}_{\mathrm{L}}\right)$ reduces to $\kappa' = \mathrm{sgn}\left(-\mathbf{D}_{\mathrm{L}}^{\mathrm{T}}\mathbf{K}_{\mathrm{LR,\,sym}}\mathbf{D}_{\mathrm{L}}\right)$. Expanding the term within parentheses, one has

$$-k\begin{bmatrix} D_{1x} \\ D_{1y} \\ D_{2x} \\ D_{2y} \\ D_{3x} \\ D_{3y} \end{bmatrix}^{\mathrm{T}} \begin{bmatrix} -1 & 0 & -a/2 & 0 & 0 & 0 \\ 0 & 0 & 0 & -a/2 & 0 & 0 \\ -a/2 & 0 & -1 & 0 & -a/2 & 0 \\ 0 & -a/2 & 0 & 0 & 0 & -a/2 \\ 0 & 0 & -a/2 & 0 & -1 & 0 \\ 0 & 0 & 0 & -a/2 & 0 & 0 \end{bmatrix} \begin{bmatrix} D_{1x} \\ D_{1y} \\ D_{2x} \\ D_{2y} \\ D_{3x} \\ D_{3y} \end{bmatrix},$$

where again $a = 1/\left(2\sqrt{2}\right)$. Since k is positive, it may be omitted to give

$$\kappa' = \mathrm{sgn}\left[D_{1x}^2 + D_{2x}^2 + D_{3x}^2 + \frac{1}{2\sqrt{2}}D_{2x}\left(D_{1x} + D_{3x}\right) + \frac{1}{2\sqrt{2}}D_{2y}\left(D_{1y} + D_{3y}\right)\right].$$

We know that in each mode, either D_{2x} or D_{2y} is zero. For the former, one has

$$\kappa' = \mathrm{sgn}\left[D_{1x}^2 + D_{3x}^2 + \frac{1}{2\sqrt{2}}D_{2y}\left(D_{1y} + D_{3y}\right)\right].$$

For the latter, one has

$$\kappa' = \mathrm{sgn}\left[D_{1x}^2 + D_{2x}^2 + D_{3x}^2 + \frac{1}{2\sqrt{2}} D_{2x}\left(D_{1x} + D_{3x} \right) \right].$$

In the case where $D_{2x} = 0$, we find numerically that $D_{3x} = -D_{1x}$ and $D_{3y} = D_{1y}$; the signature can then be further simplified to

$$\kappa' = \mathrm{sgn}\left(2D_{1x}^2 + \frac{1}{\sqrt{2}} D_{1y} D_{2y} \right).$$

Based on this expression, we can say that:

i. if D_{1y} and D_{2y} have the same sign, i.e. displaced in the same direction, then κ' is positive. This is found numerically to be the case for bending.

ii. if D_{1y} and D_{2y} have different signs and $\left| 2D_{1x}^2 \right| > \left| \frac{1}{\sqrt{2}} D_{1y} D_{2y} \right|$, then κ' is positive. This is found numerically to be the case for the first thickness shear mode because $\left| D_{1x} \right| > \left| D_{1y} \right|$ and $\left| D_{1x} \right| > \left| D_{2y} \right|$.

iii. if D_{1y} and D_{2y} have different signs and $\left| 2D_{1x}^2 \right| < \left| \frac{1}{\sqrt{2}} D_{1y} D_{2y} \right|$, then κ' is negative. This is found numerically to be the case for the second breathing mode because $\left| D_{1x} \right| < \left| D_{1y} \right|$ and $\left| D_{1x} \right| < \left| D_{2y} \right|$.

In the case where $D_{2y} = 0$, we find numerically that $D_{3x} = D_{1x}$ and $D_{3y} = -D_{1y}$; the signature can then be further simplified to

$$\kappa' = \mathrm{sgn}\left(2D_{1x}^2 + D_{2x}^2 + \frac{1}{\sqrt{2}} D_{1x} D_{2x} \right).$$

Complete the squares of the term in parentheses to get

$$\kappa' = \mathrm{sgn}\left(2\left(D_{1x} + \frac{1}{4\sqrt{2}} D_{2x} \right)^2 + \frac{15}{16} D_{2x}^2 \right).$$

Clearly, the sign of all the evanescent modes which have $D_{2y} = 0$ must be positive; this includes extensional, second thickness shear and first breathing evanescent waves.

The expression $\kappa' = \mathrm{sgn}\left(-\mathbf{D}_L^\mathrm{T} \mathbf{K}_{\mathrm{LR,\,sym}} \mathbf{D}_L \right)$ is also applicable to the real unity eigenvalues

$(\lambda = \pm 1)$; κ' is positive at the cut-on and cut-off of all normal modes and is negative at the cut-on and cut-off of the anomalous mode, except at the cut-on of the first breathing mode and cut-off of the extensional mode which occur at $\omega^2 = 1.3536$ where κ' is zero. κ' is also found to be zero at the beginning of loop 1,6 and approximately zero at the end of the loop.

The term $-\mathbf{D}_L^T\mathbf{K}_{LR,sym}\mathbf{D}_L$ within this new signature is complex for the attenuating loops 3,6 and 1,6, so the signum function is not defined. This is perhaps inevitable, as these loops only exist by virtue of the interaction of branches having different Krein signature: the attenuating loops should not share a characteristic with either.

3.11   Discussion

The dispersion curves diagram are usually two-dimensional and shown in two separate plots, each represents variation of phase constant and decay rate against (normalised) frequency. As such, an attenuating wave which has both phase constant and decay rate will be represented by a curve in both plots. Figure 3.10 shows how the three-dimensional dispersion curves for the example framework (Figure 3.3) would appear in the two-dimensional form.

The advantage of two-dimensional plot is it is relatively easier to plot, visually simpler and allows one to accurately read data from the graph in the sense that abscissa and ordinate are clearly shown with respect to each curve. However, there are two main disadvantages. First, some branches appear disjointed at the cut-on and cut-off frequencies, particularly those branches which are associated with attenuating waves. This is evident from the description given by Signorelli and von Flotow [47], "After the first appearance of the complex modes, the dispersion curves cross over each other and become intertwined. At this point it becomes difficult, if not impossible, to identify which mode is which". Second, one cannot distinguish the branches that are associated with monotonic and oscillatory evanescent wave. The latter are represented by $\delta + i\pi$, but the straight lines representing $\varphi = \pi$ would be overlapping and lie on the graph's borderline ($\varphi/\pi = 1$) if they are to be plotted.
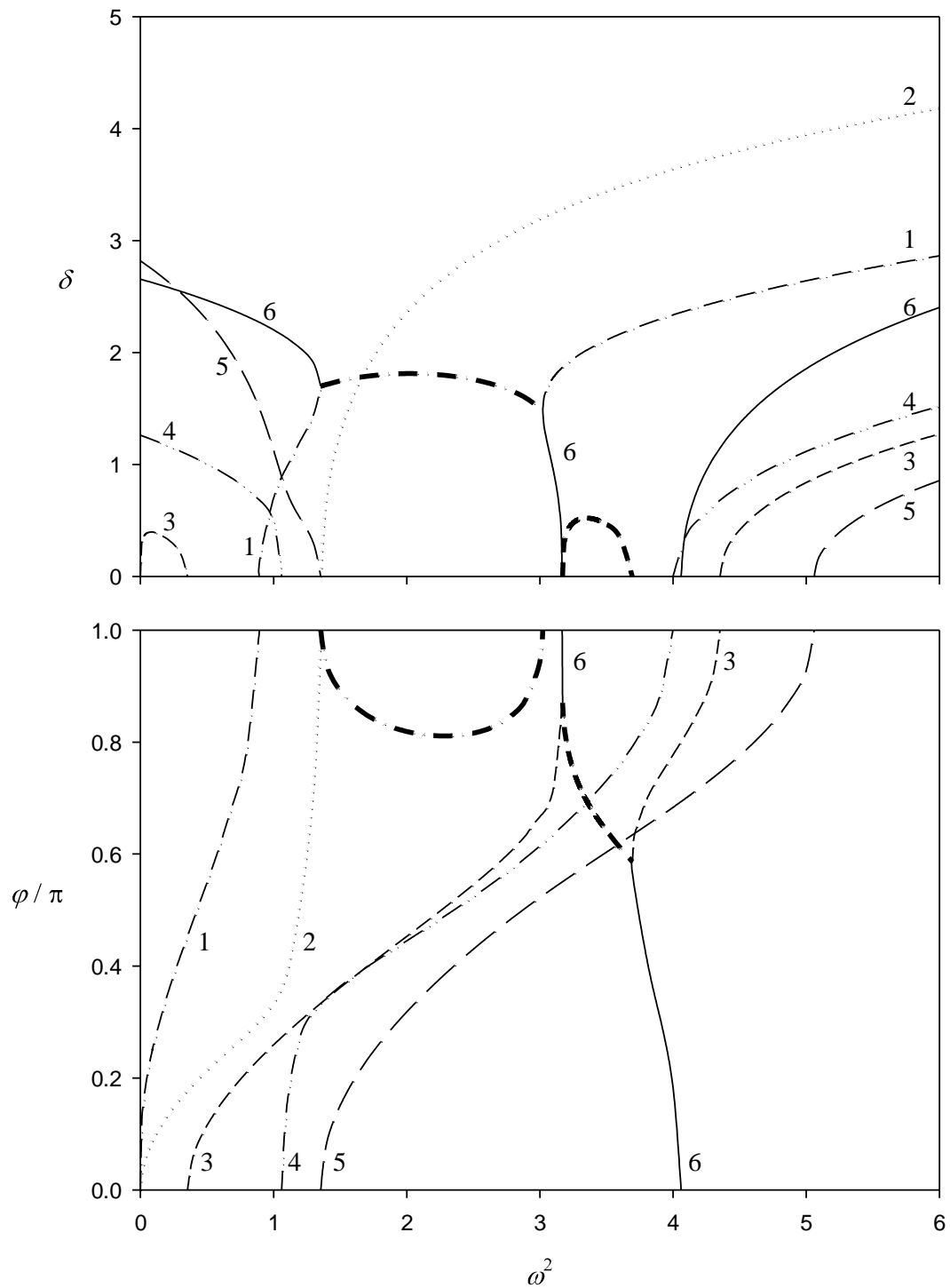
Figure 3.10   Two-dimensional plot of the dispersion curves for the example

framework. The branches associated with complex non-unity

eigenvalues are shown in bold.

— · — · —	1 Bending,	············	2 Extensional,
— — — —	3 First thickness shear,	— · — · · —	4 Second thickness shear,
— — —	5 First breathing,	———————	6 Second breathing.

Availability of graphing software such as Sigmaplot has enabled three-dimensional graph to be plotted relatively easily, and allows one to combine all features of the dispersion diagram into a single plot. The loops which appear as two separate curves in two-dimensional plot now can appear as a single curve. A disadvantage of the three-dimensional plot is it can be difficult to read off data accurately for a point on the loop because its position relative to the axes is not so clear in comparison to the two-dimensional plot.

There are four specific features that deserve further discussion with regard to the dispersion diagram (Figure 3.3):

i. $\omega^2 = 1.3536$ appears as a special frequency at which the middle masses remain stationary, see Table 3.10 which shows the displacement vectors for all branches; it is evident that the middle masses are not displaced under longitudinal, transverse or shear deformation. This is consistent with the 'effective' axial, transverse and shear stiffness of a single square fragment of a cell which is $1 + 1/(2\sqrt{2}) = 1.3536$, and hence the same frequency (squared) when $k = m = 1$.

Branch	Displacement vector	Remarks
Loop 1,6	$\begin{bmatrix} 0 & 1 & 0 & 0 & 0 & 1 \end{bmatrix}^{\mathrm{T}}$	Krein collision on the plane $\varphi = \pi$, $\delta = 1.7$, $\lambda = -5.4735$.
2	$\begin{bmatrix} 0 & 1 & 0 & 0 & 0 & -1 \end{bmatrix}^{\mathrm{T}}$	Extensional cut-off, $\lambda = -1$.
3	$\begin{bmatrix} 1 & \pm 0.2602\mathrm{i} & 0 & 0 & -1 & \pm 0.2602\mathrm{i} \end{bmatrix}^{\mathrm{T}}$	First crossing of branches 3 and 4 on the plane $\delta = 0$, at $\varphi = \pi/3$, $\lambda = 1/2 + (\sqrt{3}/2)\mathrm{i}$.
4	$\begin{bmatrix} 1 & \mp 0.5773\mathrm{i} & 0 & 0 & 1 & \pm 0.5773\mathrm{i} \end{bmatrix}^{\mathrm{T}}$	
5	$\begin{bmatrix} 0 & 1 & 0 & 0 & 0 & -1 \end{bmatrix}^{\mathrm{T}}$	First breathing mode cut-on, $\lambda = 1$.

Table 3.10 Displacement vectors for all branches at $\omega^2 = 1.3536$.

ii. Loop 3 is notable as an example of monotonic evanescent decay at low frequency wherein the decay rate initially increases before decreasing at higher frequencies. This contrasts with branches 4 and 5 which always decay with decreasing rate below cut-on.

iii. Branches associated with symmetric waves never cross each other while branches associated with asymmetric waves collide (leading to the formation of loops); branches associated with asymmetric and symmetric waves do cross each other, but without the formation of loops. Waki *et al*. [91] claim that symmetric wave branches do not cross each other due to curve veering – a condition of converging/diverging eigenvalue loci – which occurs "when two wave modes are not orthogonal in the wave domain"; however the dispersion diagram, Figure 3.3, shows no obvious evidence of eigenvalue veering – rather crossings and collisions. However, a rotationally symmetric tyre model is used in [91], while the present structure is translationally symmetric, which may explain this difference.

iv. The very existence of a static decay mode having a negative eigenvalue would appear to presage a propagation branch which exhibits anomalous dispersion. Branch 6 originates with an eigenvalue of $\lambda = -14.2435$, or equivalently $\delta = 2.6563$ and $\varphi = \pi$, when $\omega^2 = 0$. As frequency increases, this branch does not leave the plane $\varphi = \pi$ except where it interacts with branch 1 to form loop 1,6. As soon as it cuts-on at $\omega^2 = 3.1678$, with $\lambda = -1$ ($\delta = 0$ and $\varphi = \pi$), a negative slope with increasing frequency is inevitable: the branch can only move towards the plane $\varphi = 0$ as frequency increases, as there is nowhere else for it to go within the quadrant shown in Figure 3.3. Accordingly, any attempt to explain the fundamental mechanics underpinning anomalous dispersion should probably start with an explanation for the negative decay eigenvalue for the static decay: the self-equilibrating force vector at the n th cross-section is $\mathbf{F}(n) = \begin{bmatrix} 0 & 1 & 0 & -2 & 0 & 1 \end{bmatrix}^{\mathrm{T}}$, so the upper vertical member (between masses 1 and 2) is in tension. In turn, both diagonals are in tension, which puts the equivalent vertical in the adjacent $(n+1)$ th cross-section into compression, so it shortens. Likewise, the lower vertical member (between masses 2 and 3) is in compression, which puts both diagonals into compression and the equivalent lower vertical in the adjacent section into tension, so it lengthens; hence the negative eigenvalue. The skew-symmetry of this mode together with the concerted effect of the diagonal members may be of importance for this particular structure, but the existence of two or more layers is probably more germane – particularly as anomalous dispersion is present over the entirety of the branch, unlike continuum waveguides such as the circular cylinder or plane strain strip, for which anomalous dispersion occurs only over particular frequency ranges for any

given mode [103]. The implications of a negative group velocity remain unclear; at first sight it would suggest that energy is flowing towards, rather than away from, the source of excitation, which rather defies logic. Mace *et al.* [91] have described anomalous dispersion as resembling "a Michael Jackson "Moonwalk"; it goes forward but moves backward". In the physics literature, particularly optics, it is variously associated with negative refractive index, superluminal velocity and, indeed, time reversal. We consider this conundrum in more detail in Chapter 4.

It is instructive to compare the present discrete beam-like framework with a one-dimensional beam-like continuum waveguide. In the continuum, cut-on occurs when one half-wavelength can be accommodated within some characteristic transverse dimension of the waveguide in the case of normal dispersion; this is also found to be the case for the discrete framework. The (axial) wavenumber is zero and the wavelength is infinite, but so is the waveguide or framework, so this axial one half-wavelength can also be accommodated in the longitudinal direction; this occurs when $\lambda = 1$ for normal dispersion. In the continuum model, as the wavenumber becomes larger the wavelength becomes shorter, and there is no limit to the number of (half) wavelengths that can fit into a unit length L of the waveguide, and in turn there is no cut-off frequency. Typically, waves approach the Rayleigh surface wave velocity, with displacement concentrated at the surface. However in the discrete model, the maximum number of wavelengths that can be accommodated over a unit length L (one cell) is one half, which coincides with $\lambda = -1$. Thus, one concludes that the existence of a cut-off frequency is a consequence of the discrete nature of the model in the axial direction, and that any discrete model can and will exhibit such behavior, including finite element models of continuum structures.

For our model structure, we noted that D_{2y} of symmetric waves and D_{2x} of asymmetric waves are always zero. Also, the forces in the *y*-direction are always self-equilibrating for symmetric modes, and the forces in the *x*-direction are always self-equilibrating for asymmetric modes. At the cut-on frequencies, at least three of the following vector component sums, $\sum D_x, \sum D_y, \sum F_x, \sum F_y$, are observed to be zero: for the first thickness shear, $\sum D_x$, $\sum D_y$ and $\sum F_x$ are zero; for the second thickness shear, all the sums are zero; for the first breathing, $\sum D_x$, $\sum D_y$ and $\sum F_y$ are zero; for the second breathing, $\sum D_x$, $\sum F_x$ and $\sum F_y$ are zero. At the cut-off frequencies, $\sum F_x$ and $\sum F_y$ are zero for all modes, and either one or both of $\sum D_x$ and $\sum D_y$ are zero: in the case of bending,

$\sum D_x$ is zero; for second thickness shear and first breathing, $\sum D_y$ is zero; for extensional, first thickness shear and second breathing, both are zero.

3.12   Conclusions

The present chapter describes an in-depth study of the dispersion diagram, in novel form, for a model repetitive structure featuring pin-jointed members with point masses located at nodal cross-sections, concentrating on wave propagation and decay characteristics. The need to be specific in the description of cut-on and cut-off frequencies, marking the start and finish of propagation zones with increasing frequency, is emphasised. Explanations for the existence of these zones are provided in terms of cross-section and axial natural frequencies, as defined by phase closure; this goes some way towards the establishment of a dynamic Saint-Venant's principle. Three distinct types of decaying waves have been identified: monotonic evanescent and oscillatory evanescent generally occur at frequencies below cut-on and above cut-off, respectively; the exception is for the single anomalous branch, for which the situation is reversed. Attenuating decay occurs as a result of interaction between branches which display normal and anomalous dispersions, and results in the formation of loops on the dispersion diagram. The latter can be explained in terms of a Krein collision. Finally, some preliminary comments on the cause of anomalous dispersion are made.

Chapter 4:   Wave Propagation in Repetitive Structures: Energetics

4.1   Introduction

Energy flow of free waves in undamped repetitive structures has been studied by Mead [18] and Langley [72]; both of them employed transfer matrix approach in their analyses. Among the many results, they have shown that (i) only free waves with complex unity eigenvalue can transmit energy, (ii) the energy is transmitted at a rate given by the group velocity, (iii) when energy is transmitted, no work is done at the cell boundaries and the time-averaged kinetic and potential energies are equal at every section along the structure, and (iv) energy in a propagating wave can be expressed in the form of Rayleigh quotient. We notice that equations (2.4), (2.5), (2.11) and (2.12) of reference [72] by Langley are missing a factor of -1.

The velocity at which the energy flows through the structure is known as the group velocity and is defined as the derivative of frequency with respect to the wavenumber, i.e. $c_{\mathrm{g}} = \partial\omega/\partial\varphi$. Commenting on the definition, Lighthill [74] stated, "… the fact that, in a perfectly periodic motion of fixed wavenumber, energy is propagated at a velocity which can be expressed as a ratio of changes of frequency and wavenumber in going to a neighbouring wave solution, appears distinctly odd." Indeed, it is difficult to conceive an idea that a harmonic traveling wave of a single frequency could carry energy or information, apart from the fact that it is exists. Possible ways for the wave to transmit information are to change its amplitude, frequency or phase so that the change can be interpreted by the receiver as information.

Some expressions for the group velocity have previously been reported. Langley [72] expressed the velocity in terms of the transfer matrix and its frequency derivative. Finnveden [75] evaluated the group velocity by numerically differentiating the eigenequation with respect to wavenumber. In Chapter 2, expressions for the group velocity in terms of the eigenvectors of $\mathbf{G}$ and $\mathbf{H}$, are presented; the latter appears more succinct. In Section 4.4, the group velocity of each mode for the example structure is presented and explored in more detail.

If the group velocity travels in the same direction as the phase velocity, the dispersion is regarded as normal; otherwise, if the two velocities are in opposite directions, the dispersion is called anomalous. Mace *et al.* [91] described the anomalous dispersion metaphorically as "… a wave carrying energy in the negative x-direction, but with a positive wavenumber. The motion thus somewhat resembles a Michael Jackson "Moonwalk:" it goes forward but moves backwards." It is an interest of the present work to explore this special case and understand the mechanism by which such phenomenon could occur because the description given thus far is not satisfying.

As stated earlier, Mead [18] has shown that a single spatially decaying wave, i.e. evanescent or attenuating, does not transfer energy. However, two interacting attenuating waves can transfer energy, as raised by Bobrovnitskii [73] who stated that, "When the displacements in the two opposite evanescent waves are not in phase, and are not in counter-phase, the work done by the stresses in one wave through the displacements in the other wave is not zero, and that leads to a uniform flow of energy along the structure." Langley [72] argued that the energy flow is "not a physical quantity" and not fully analogous to the real power flow based on the fact that individually the waves decay which implies that they exist only over a finite number of cells; this suggest that energy does not propagate to infinite extent and evaluation of group velocity for the case is irrelevant. We could further argue that the decay is exponential, metaphorically, which implies that it would take infinitely long structure for the wave amplitude to completely vanish, therefore it is possible for the two waves to interact and transfer (decreasing amount of) energy over an infinite extent.

It is worth pointing out that in the present work, the concerned decaying waves are called *attenuating* instead of *evanescent* (the term used by Bobrovnitskii, Langley and many authors) to distinguish one from the other. In Chapter 3, we define evanescent wave as one with rapidly decreasing amplitude, and if the phase change $\varphi = 0$ the wave is called *monotonic evanescent*, and if the phase change $\varphi = \pi$ the wave is called *oscillatory evanescent*. On the other hand, *attenuating* wave has rapidly decreasing amplitude with non-zero phase constant but $\varphi \neq \pi$. This terminology follows the work of Hinke *et al.* [95] but with the word monotonic and oscillatory added to evanescent in order to distinguish between the two.

The present chapter investigates the energetics of the different wave types under the new taxonomy. In the next section, equations for energy and power are derived in terms of eigenvectors associated with transfer matrices $\mathbf{G}$ and $\mathbf{H}$. Axial phase velocity and group

velocity associated with each mode are discussed in Sections 4.3 and 4.4, respectively. In Section 4.5, energy flow associated with two interacting attenuating waves is considered. Finally, in Section 4.6, some further observations are presented on the numerical study of the anomalous dispersion.

4.2   Energy and power

Consider the example framework as shown in Figure 4.1; the geometrical and material properties of the framework are identical to those employed in Chapters 2 and 3. The framework is harmonically excited at an angular frequency ω and free modes of vibration are set up. The three forms of energy that exist in the system, namely, work done, kinetic energy and strain energy, are conserved in the absence of damping.
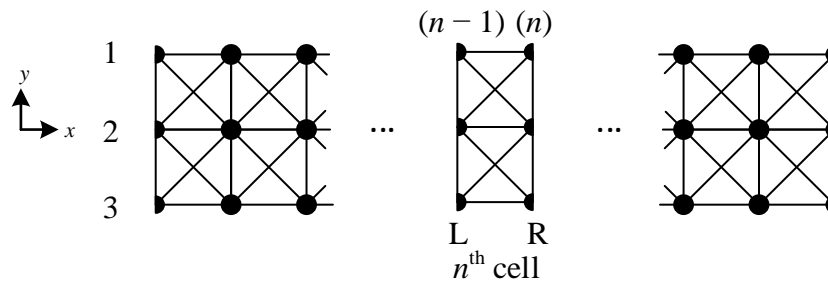

Figure 4.1 An infinite framework. L and R indicate left- and right-hand side of the
nth cell, respectively. The top, middle and bottom tiers of masses are
denoted by numbers 1, 2 and 3, respectively. n refers to the cross-
sectional numbering along the framework.

Now, consider the single cell of the framework as shown in Figure 4.1. The governing equations of motion for the half-masses on the left- and right-hand sides of the cell are given by

$$-\mathbf{F}_{\mathrm{L}} = \left[\mathbf{K}_{\mathrm{LL}} - \frac{\omega^2 \mathbf{m}}{2} \right] \mathbf{D}_{\mathrm{L}} + \mathbf{K}_{\mathrm{LR}} \mathbf{D}_{\mathrm{R}} , \qquad (4.1)$$

and

$$\mathbf{F}_{\mathrm{R}} = \mathbf{K}_{\mathrm{RL}} \mathbf{D}_{\mathrm{L}} + \left[\mathbf{K}_{\mathrm{RR}} - \frac{\omega^2 \mathbf{m}}{2} \right] \mathbf{D}_{\mathrm{R}} , \qquad (4.2)$$

respectively, where $\mathbf{D}$ is the displacement vector, $\mathbf{F}$ is the force vector, $\mathbf{m}$ is the mass matrix, ω is the angular frequency and the matrices $\mathbf{K}_{LL}, \mathbf{K}_{LR}, \mathbf{K}_{RL}$ and $\mathbf{K}_{RR}$ are presented explicitly in Appendix A.1. The time-averaged work done by the nodal forces on the left-hand side of the cell through the corresponding displacements on the same side is given by

$$W_L = -\frac{1}{2} \mathrm{Re}\left(\mathbf{D}_L^* \mathbf{F}_L\right), \qquad (4.3)$$

where $\mathbf{D}_L^*$ is the transposed conjugate of the displacement vector; the negative sign appears in the equation due to the fact that the force on the left-hand side acts in opposite direction to the force on the right hand side.

The time-averaged strain energy stored in the cell due to the displacement field caused by the force on the left-hand side is given by

$$E_{S,L} = \frac{1}{2} \mathrm{Re}\left[\mathbf{D}_L^* \left(\mathbf{K}_{LL}\mathbf{D}_L + \mathbf{K}_{LR}\mathbf{D}_R\right)\right]. \qquad (4.4)$$

Equation (4.4) is actually equal to equation (4.3) but without the kinetic energy term; this is evident in equation (4.1).

The time-averaged kinetic energy of the left-hand side is given by

$$E_{K,L} = \frac{1}{2}\omega^2 \mathrm{Re}\left(\mathbf{D}_L^* \frac{\mathbf{m}}{2}\mathbf{D}_L\right) = \frac{1}{4}\omega^2 \mathrm{Re}\left(\mathbf{D}_L^* \mathbf{m}\mathbf{D}_L\right). \qquad (4.5)$$

Complete derivation for equations (4.3), (4.4) and (4.5) is presented in Appendix C.1. The time-averaged energy equations for the right-hand side are as follow:

$$W_R = \frac{1}{2} \mathrm{Re}\left(\mathbf{D}_R^* \mathbf{F}_R\right), \qquad (4.6)$$

$$E_{S,R} = \frac{1}{2} \mathrm{Re}\left[\mathbf{D}_R^* \left(\mathbf{K}_{RL}\mathbf{D}_L + \mathbf{K}_{RR}\mathbf{D}_R\right)\right], \qquad (4.7)$$

$$E_{K,R} = \frac{1}{4}\omega^2 \mathrm{Re}\left(\mathbf{D}_R^* \mathbf{m}\mathbf{D}_R\right), \qquad (4.8)$$

where W_R, $E_{S,R}$ and $E_{K,R}$ are work done, strain energy and kinetic energy, respectively; note that there is no negative sign in equation (4.6). The three forms of energy are related by the energy balance equation which is given by

$$W_L = E_{S,L} - E_{K,L}. \qquad (4.9)$$

Based on equation (4.9), we now consider the energetics of the different wave types. For the rightward monotonic and rightward oscillatory evanescent waves before cut-off (note that the former and the latter are associated with normal and anomalous branches,

respectively), the displacement and force vectors are real and the time-averaged work done W_L is found to be positive because the time-averaged strain energy $E_{S,L}$ is larger than the time-averaged kinetic energy $E_{K,L}$. As frequency increases towards the cut-on frequency, the magnitude of W_L reduces. On the other hand, after cut-off, W_L is found to be negative because $E_{S,L}$ is now smaller than $E_{K,L}$. As the frequency is further increased, W_L becomes more negative because $E_{S,L}$ continue to decrease while $E_{K,L}$ increases. It is noted that, for the example framework, no time-averaged work is done by the oscillatory evanescent bending and second breathing waves at the particular frequency $\omega^2 = 1.3536$, $\lambda = \exp(\pm 1.7 \pm i\pi)$ because the corresponding displacement and force vectors satisfy the following:

$$W_L = -\frac{1}{2}\mathrm{Re}\left(\begin{bmatrix} 0 & 1 & 0 & 0 & 0 & 1 \end{bmatrix}\begin{bmatrix} 0.1768 & 0 & 0 & -0.9354 & -0.1768 & 0 \end{bmatrix}^T\right) = 0.$$

For both the rightward monotonic and rightward oscillatory evanescent waves below the cut-off frequency, the time-averaged work done by the forces on the right-hand side of a cell through the corresponding displacements on the right W_R is negative. The negative value implies that the work done is in opposite direction to the work done on the left-hand side. This is evident from the fact that the work done on the right-hand side of a cell and the work done on the left-hand side of the succeeding cell are equal in magnitude but opposite in sign, that is $W_R(n)$ of the nth cell is equal to $-W_L(n)$ of the $(n+1)$th cell.

In a steady state, total time-averaged work done by an evanescent wave, monotonic or oscillatory, decaying simultaneously in both right and left directions over the infinite framework can be evaluated as

$$\sum_{n=-\infty}^{n=\infty} W(n) = 2\sum_{n=0}^{n=\infty} W(n) = 2\left[W_L(0) + \sum_{n=1}^{n=\infty} W_L(n) + \sum_{n=1}^{n=\infty} W_R(n)\right].\qquad(4.10)$$

Considering the magnitude of each term and noting that $W_R(n)$ is equal in magnitude to $W_L(n)$, then equation (4.10) can be further simplified as

$$\begin{aligned}\sum_{n=-\infty}^{n=\infty} W(n) &= 2\left[W_L(0) + 2\sum_{n=1}^{n=\infty} W_L(n)\right]\\ &= 2W_L(0)\left[1 + 2\sum_{n=1}^{n=\infty} \lambda^{2n}\right]\\ &= 2\mathbf{D}_L^T(0)\mathbf{F}_L(0)\left[1 + 2\frac{\lambda^2}{1-\lambda^2}\right],\end{aligned}\qquad(4.11)$$

where $W_L(0) = \mathbf{D}_L^T(0)\mathbf{F}_L(0)$ and $\sum_{n=1}^{\infty} \lambda^{2n} = \frac{\lambda^2}{1-\lambda^2}$ for $|\lambda| < 1$. The displacement vector is transposed (not conjugate transposed) to account for the fact that the vector is real. For the case where $\lambda = \pm 1$, $\mathbf{D}_L^T(0)\mathbf{F}_L(0) = 0$ but $\sum_{n=-\infty}^{n=\infty} W(n)$ is undefined because $\lambda^2/(1-\lambda^2)$ is indeterminate; employing L'Hôpital's rule leads to a determinate form and $\sum_{n=-\infty}^{n=\infty} W(n) = 0$.

For the propagating waves, the displacement and force vectors are complex and perpendicular to each other, therefore there is no time-averaged work done. The equations for $E_{S,L}$ and $E_{K,L}$ can be written succinctly in terms of the eigenvector of transfer matrix $\mathbf{H}$, that is $\mathbf{X}$, as follows: combine the expressions for $E_{S,L}$ with $E_{S,R}$, and $E_{K,L}$ with $E_{K,R}$ noting that $E_{S,R} = E_{S,L}$ and $E_{K,R} = E_{K,L}$ leads to

$$E_{S,L} = \frac{1}{4}\mathbf{X}^*\mathbf{K}\mathbf{X} \tag{4.12}$$

and

$$E_{K,L} = \frac{1}{8}\omega^2\mathbf{X}^*\mathbf{m}\mathbf{X}, \tag{4.13}$$

where $\mathbf{K} = \begin{bmatrix} \mathbf{K}_{LL} & \mathbf{K}_{LR} \\ \mathbf{K}_{RL} & \mathbf{K}_{RR} \end{bmatrix}$.

The time-averaged strain energy stored in a cell and the time-averaged kinetic energy at the boundary of each cell are equal, and the time-averaged total energy in a cell is simply the sum of the two.

For the attenuating waves, the displacement and force vectors are complex but not perpendicular to each other, therefore, the time-averaged work done at the boundary of a cell is not zero. Expanding the expression for the time-averaged work done on the left boundary of a cell by a rightward attenuating wave in terms of the nodal components of displacement and force reveals that the work is purely real; this is shown as follows,

$$\begin{aligned} W_L &= -\frac{1}{2}\mathrm{Re}\left[\mathbf{D}_L^*\mathbf{F}_L\right] \\ &= -\frac{1}{2}\mathrm{Re}\left[\left(D_{1x}^*F_{1x} + D_{2x}^*F_{2x} + D_{3x}^*F_{3x}\right) + \left(D_{1y}^*F_{1y} + D_{2y}^*F_{2y} + D_{3y}^*F_{3y}\right)\right] \\ &= -\frac{1}{2}\mathrm{Re}\left[(a+b\mathrm{i}) + (a-b\mathrm{i})\right], \end{aligned} \tag{4.14}$$

where a and b are real values. In reference to the dispersion diagram, Figure 3.3 in Chapter 3, it is noted that the sign of W_L for the attenuating wave associated with the eigenvalues along loop 1,6 does not changes as frequency increases, but along loop 3,6, the sign changes from negative to positive at $\omega^2 \approx 3.22637$. The sign change cannot be associated with the turning of the decay rate δ because that happens when $\omega^2 \approx 3.35$. It is worth pointing out that loop 1,6 occurs when oscillatory evanescent bending branch collides with oscillatory evanescent second breathing branch; the former is associated with negative work while the latter is associated with positive work.

The power associated with a propagating wave is defined as the rate at which the energy of the wave flows across a boundary of a cell. Mathematically, that is given by the product of the force acting on the masses at the boundary and velocity at which the masses are moving. The velocity can be obtained by simply taking the time-derivative of the corresponding displacement. Power flow is associated with propagating waves only and there is no power flow associated with the solitary monotonic evanescent, oscillatory evanescent, attenuating waves and the modes at the cut-on and cut-off frequencies. The time-averaged power flow into the left-hand side of a cell is given by

$$P_L = -\frac{1}{2}\mathrm{Re}\left(\mathrm{i}\,\omega \mathbf{D}_L^* \mathbf{F}_L\right). \tag{4.15}$$

Equation (4.15) can be expressed in terms of the eigenvector of transfer matrix $\mathbf{G}$, that is $\mathbf{V}$, as follows:

$$
\begin{aligned}
P_L &= -\frac{1}{2}\mathrm{Re}\left(\mathrm{i}\,\omega \mathbf{D}_L^* \mathbf{F}_L\right) \\
&= -\frac{1}{2}\left(\frac{\mathrm{i}\,\omega \mathbf{D}_L^* \mathbf{F}_L + \overline{\mathrm{i}\,\omega \mathbf{D}_L^* \mathbf{F}_L}}{2}\right) \\
&= -\frac{1}{4}\left(\mathrm{i}\,\omega \mathbf{D}_L^* \mathbf{F}_L - \mathrm{i}\,\omega \mathbf{F}_L^* \mathbf{D}_L\right) \\
&= -\frac{1}{4}\mathrm{i}\,\omega \begin{bmatrix} \mathbf{D}_L^* & \mathbf{F}_L^* \end{bmatrix} \begin{bmatrix} \mathbf{0} & \mathbf{I} \\ -\mathbf{I} & \mathbf{0} \end{bmatrix} \begin{bmatrix} \mathbf{D}_L \\ \mathbf{F}_L \end{bmatrix} \\
&= -\frac{1}{4}\mathrm{i}\,\omega \mathbf{V}^* \mathbf{J} \mathbf{V},
\end{aligned}
\tag{4.16}
$$

where $\mathbf{J} = \begin{bmatrix} \mathbf{0} & \mathbf{I} \\ -\mathbf{I} & \mathbf{0} \end{bmatrix}$ and the overbar implies complex conjugate. Similar equation can be written in terms of the eigenvector of transfer matrix $\mathbf{H}$, that is $\mathbf{X}$, as

$$P_L = -\frac{1}{4}\mathrm{i}\,\omega \mathbf{X}^* \tilde{\mathbf{J}} \mathbf{X} \tag{4.17}$$

where $\tilde{\mathbf{J}} = \begin{bmatrix} \mathbf{0} & -\mathbf{K}_{LR} \\ \mathbf{K}_{RL} & \mathbf{0} \end{bmatrix}$. The metric $\tilde{\mathbf{J}}$ was introduced in Chapter 2 to determine the symplectic relationship for transfer matrix $\mathbf{H}$. Detailed derivations of equations (4.15) and (4.17) are given in Appendix C.2. Even though the mass matrix does not explicitly appear in equation (4.17), it is implied through the dependence of eigenvector $\mathbf{X}$ on transfer matrix $\mathbf{H}$ which includes the mass matrix. This suggests that, in a course of one period, the strain energy is propagated through the system by the elastic members and the masses act as intermediary storage.

Time-averaged power that flows out of the right boundary of a cell (and into the left boundary of the succeeding cell) is equal to the time-averaged power that flows into the left boundary of the cell; this can be shown as follows:

$$
\begin{aligned}
P_R &= -\frac{1}{2}\operatorname{Re}\left\{ i\,\omega\mathbf{D}_R^*\mathbf{F}_R \right\} \\
&= -\frac{1}{2}\operatorname{Re}\left\{ i\,\omega\left[\lambda\mathbf{D}_L\right]^*\left[\lambda\mathbf{F}_L\right] \right\} \\
&= -\frac{1}{2}\operatorname{Re}\left\{ i\,\omega\lambda^*\lambda\mathbf{D}_L^*\mathbf{F}_L \right\} \\
&= P_L,
\end{aligned}
\tag{4.18}
$$

since $\lambda^*\lambda = 1$. This equation however does not show the amount of energy that is stored in the cell.

If the power flows in the same direction as the wave, that is the signs of power and wavenumber are the same, then the dispersion is termed normal, otherwise the dispersion is termed anomalous. The phenomena of anomalous dispersion is discussed in further detail in Section 4.6.

4.3   Axial phase velocity

The axial phase velocity associated with a propagating wave is defined as the velocity in the x-axis at which a particular phase of a wave cycle travels and that is given by $c_p = \omega/\varphi$ where ω is angular frequency and φ is phase constant (or wavenumber). Uniqueness is imposed on φ by taking $-\pi \le \varphi \le \pi$. The term 'axial' is used to distinguish the phase velocity in the axial direction from the phase velocity in the transverse direction. Figure 4.2 shows the variation of the axial phase velocity against wavenumber for the six propagating modes of the example structure shown in Figure 4.1. Note that there are two segments for each of the first thickness shear (mode 3) and the second breathing (mode 6); the two

segments meet at $\varphi \approx 0.5861\pi$ and $\varphi \approx 0.8705\pi$—these points are indicated by the solid circles. The segments arise due to the formation of Krein bubble which extends between the two solid circles, shown as loop 3,6 on Figure 3.3. Also, mode 3 crosses mode 4 twice at points $\varphi/\pi = 1/3$, $c_p = 1.1110$ and $\varphi/\pi \approx 0.3932$, $c_p \approx 1.0461$; and mode 3 intersects mode 5 at point $\varphi/\pi \approx 0.6375$, $c_p \approx 0.9624$.

The phase velocity of the bending wave (mode 1) increases steadily from zero up to a maximum, $c_p \approx 0.4174$, for wavenumber $\varphi = 0.4379\pi$ which occurs when $\omega^2 \approx 0.3295$ before decreases gradually up to the cut-off frequency. Compared with the other wave modes, the bending wave always has the lowest phase velocity for any wavenumber.

The extensional wave (mode 2) has a finite and maximum velocity of 1.0836 cells per second close to $\varphi = 0$. This is interesting as one would expect that the phase velocity is zero for the static case. Based on the earlier work by Stephen and Zhang [37], for a unit axial displacement, the strain energy per unit cell of the framework under tension is found to be 1.7612 J. If the energy is transformed into kinetic energy, one can write $mc_p^2/2 = 1.7612$ where total mass per unit cell is $m = 3$ kg (for six one-half masses); therefore the phase velocity is $c_p = 1.0836$ cells per second and this agrees with the observation. As the wavenumber increases, its phase velocity decreases slowly at the beginning, before decreases at a faster rate and then approaching the bending wave phase velocity towards the cut-off. It is expected that the phase velocity of the bending and extensional modes would coincide were it not for the cut-off; indeed for a continuum structure, this would be the Rayleigh surface wave velocity [104].

At the cut-on frequencies of the normal dispersions, that is when $\varphi = 0$ ($\lambda = 1$), the phase velocity of the first thickness shear (mode 3), the second thickness shear (mode 4) and the first breathing (mode 5) waves are infinite. However, the phase velocity decreases exponentially, metaphorically, with increasing wavenumber. As stated earlier, the phase velocity of mode 3 stops at the point $\varphi/\pi \approx 0.8705$, $c_p \approx 0.6511$ (indicated by a solid circle) and appears again at the point $\varphi/\pi \approx 0.5861$, $c_p \approx 1.0440$ (indicated by the other circle) and continue to decrease with increasing wavenumber. On the contrary, at the cut-on frequency of the anomalous dispersion, that is when $\varphi = \pi$ ($\lambda = -1$), the phase velocity of the second breathing wave increases from a finite value to infinity as the wavenumber decreases from π to zero. The phase velocity of mode 6 stops and re-appears at the same points as mode 3.

The phase velocities for each mode at $\varphi = \pi$ can be calculated by taking the corresponding frequency and divide with π; for modes 1, 2, 6, 4, 3 and 5, the phase velocities are 0.3008, 0.3703, 0.5665, 0.6366, 0.6642 and 0.7161, respectively.
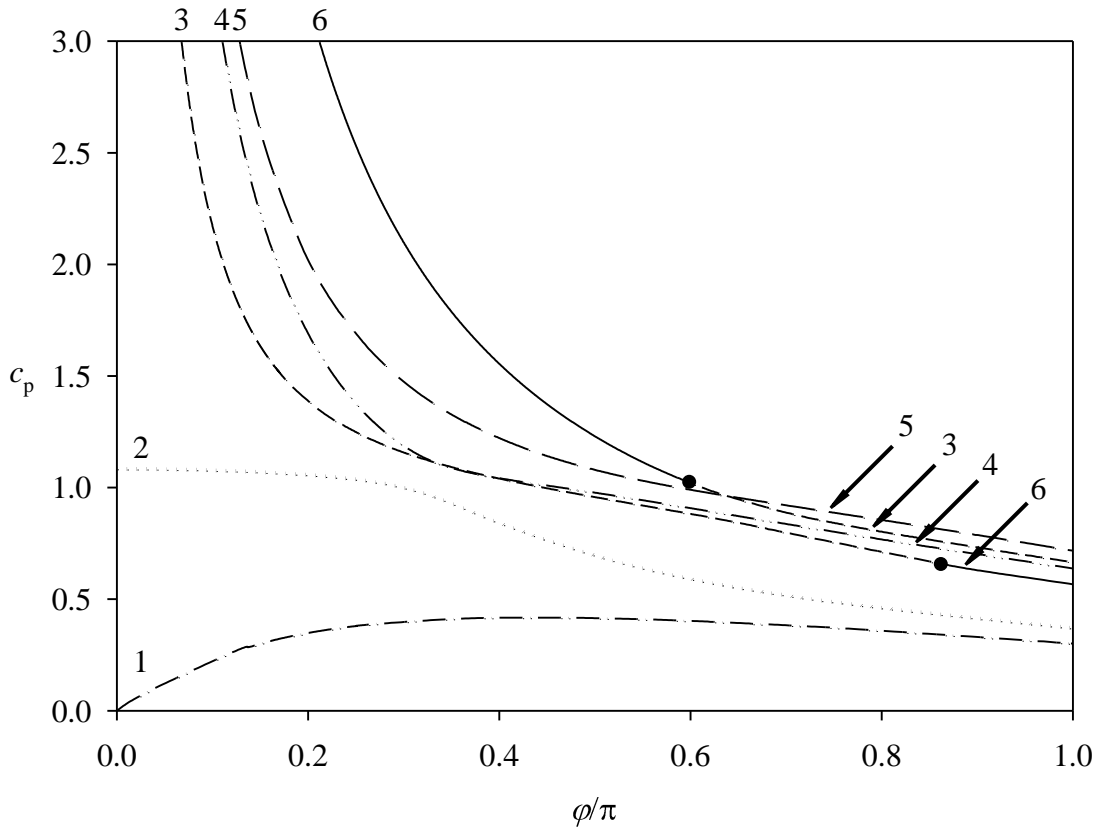

Figure 4.2 Axial phase velocity c_p, in cells per second, against normalised wavenumber φ/π.

—·—·— 1 Bending,   ··········· 2 Extensional,

— — — — 3 First thickness shear,   —··—··— 4 Second thickness shear,

— — — 5 First breathing,   ———— 6 Second breathing.

4.4   Axial group velocity

The group velocity associated with a propagating wave is the velocity at which the energy of the wave flows and is different from the phase velocity.   The group velocity can be expressed as

$$c_{\mathrm{g}} = \frac{P}{E_{\mathrm{S}} + E_{\mathrm{K}}} \, , \qquad (4.19)$$

where P is the time-averaged power that flows across a boundary of a cell, E_{S} and E_{K} are time-averaged strain and kinetic energies, respectively, at the boundary.   In Chapter 2, the equation for the group velocity is derived based on the derivative of frequency with respect to wavenumber, and is expressed succinctly in terms of the left and right eigenvectors of the transfer matrix $\mathbf{H}$.

In this section, the group velocity equation is implemented for all propagating modes of the example framework.   Equation (4.19) is used to check that the results are correct.   Figure 4.3 shows the group velocity as a function of the wavenumber.   Note that there are two separate curve segments for each of modes 3 and 6; the segments meet where the group velocity is zero which are the start ($\varphi/\pi \approx 0.8705$) and the end ($\varphi/\pi \approx 0.5861$) of a Krein bubble, as increasing frequency.

From Figure 4.3, five observations can be made.   First, the group velocity at the cut-on and cut-off frequencies is zero for all modes except for the cut-on of mode 2 where the group velocity is found to be finite.   In comparison to Figure 4.2, it is found that $\lim_{\omega \to 0+} c_{\mathrm{g}} = \lim_{\omega \to 0+} c_{\mathrm{p}} = 1.0836$.   In Section 4.3, a description is given for why phase velocity of the extensional wave is finite for $\varphi \to 0$.   We believe that the same description holds for the case of extensional wave group velocity.   Figure 4.4 shows a plot of frequency against wavenumber for branches 1 and 2 close to the origin of the dispersion diagram.   The plot confirms that the gradient of branch 2 is indeed finite for $\varphi \to 0$.
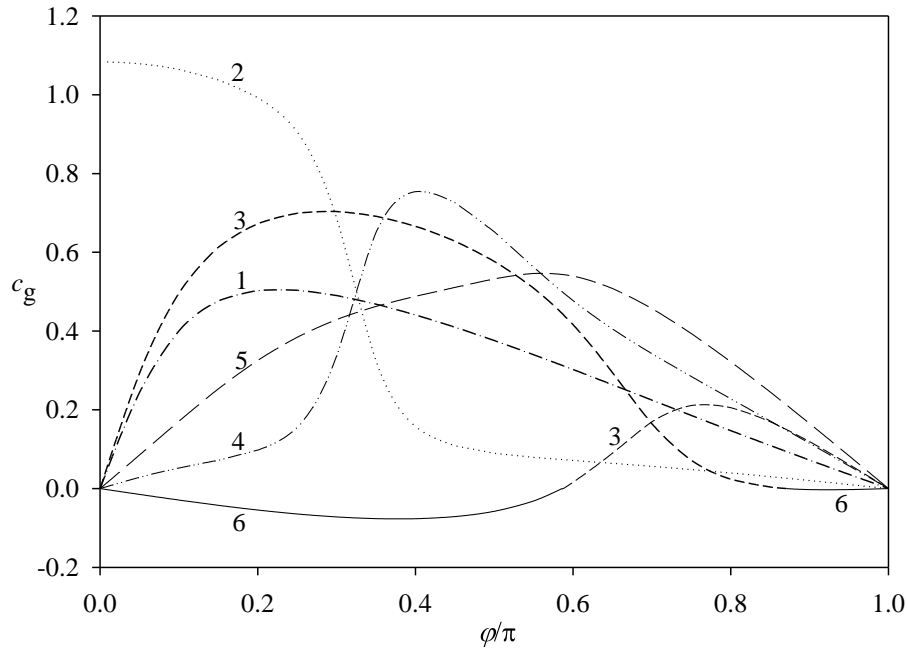
Figure 4.3 Group velocity, in cells per second, as a function of normalised
wavenumber associated with the propagating branches of the dispersion
curve for the example framework.

—·—·—·—   1 Bending,   ············ 2 Extensional,

— — — —   3 First thickness shear, —··—··— 4 Second thickness shear,

——— ——— 5 First breathing,   —————— 6 Second breathing.
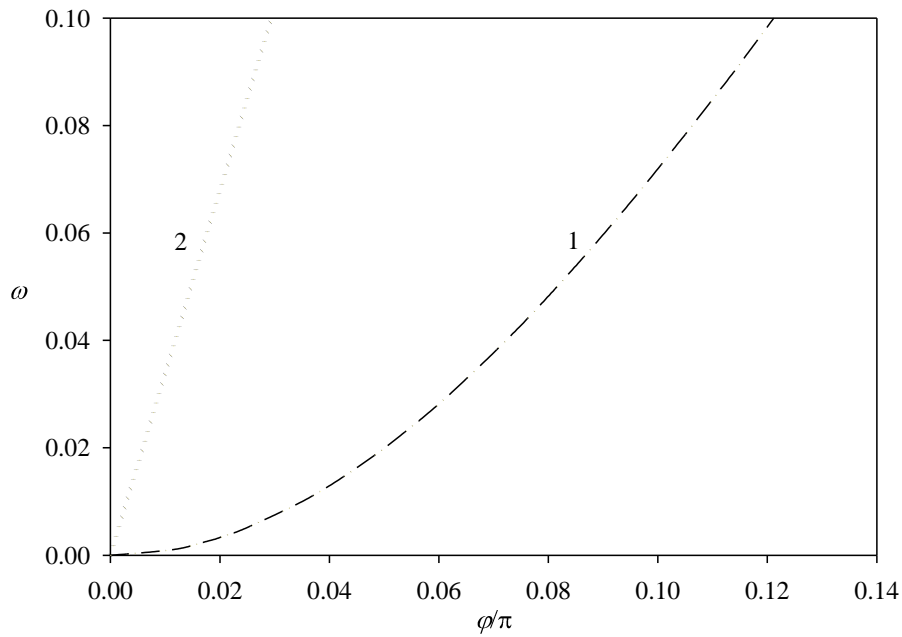
Figure 4.4 Frequency against normalised wavenumber for propagating branches 1
and 2 of the dispersion curves close to zero frequency.

—·—·—·—   1 Bending,   ············ 2 Extensional.

118

Second, in comparison with the dispersion curve diagram, Figure 3.3 in Chapter 3, no correlation has been found between the inflection points of the dispersion branches with any of the maximum and minimum points on the group velocity diagram. The maximum group velocity for each mode appears at different wavenumbers. The extensional mode (mode 2) at cut-on has the highest group velocity, followed by second thickness shear (mode 4), first thickness shear (mode 3), first breathing (mode 5), bending (mode 1) and second breathing (mode 6).

Third, at the points where branches 3 and 6 meet which are the start and the end of a Krein bubble, the combined modes continue to propagate but do not transport energy; this appears like a standing wave. Fourth, all branches are associated with normal dispersion except branch 6 which is associated with anomalous dispersion. Fifth, the group velocity cannot be determined exactly at those locations where the displacement vectors cannot be determined exactly; this occurs due to numerical instability at the beginning and end of loop 3,6 (the Krein bubble).

The condition for the maximum group velocity can be found as follows: from Chapter 2, the eigenvalue problem in terms of transfer matrix $\mathbf{H}$ is $\left[\mathbf{H}_0 + \omega^2 \mathbf{H}_2 - \lambda \mathbf{I} \right] \mathbf{X} = \mathbf{0}$ where the matrices $\mathbf{H}_0$ and $\mathbf{H}_2$ are expressed explicitly in equation (2.18). Differentiate the eigenequation with respect to λ gives

$$\left[2\omega \frac{\mathrm{d}\omega}{\mathrm{d}\lambda} \mathbf{H}_2 - \mathbf{I} \right] \mathbf{X} + \left[\mathbf{H}_0 + \omega^2 \mathbf{H}_2 - \lambda \mathbf{I} \right] \frac{\mathrm{d}\mathbf{X}}{\mathrm{d}\lambda} = \mathbf{0} , \tag{4.20}$$

which can be re-arranged for $\mathrm{d}\mathbf{X}/\mathrm{d}\lambda$ as

$$\frac{\mathrm{d}\mathbf{X}}{\mathrm{d}\lambda} = -\left[\mathbf{H}_0 + \omega^2 \mathbf{H}_2 - \lambda \mathbf{I} \right]^{+} \left[2\omega \frac{\mathrm{d}\omega}{\mathrm{d}\lambda} \mathbf{H}_2 - \mathbf{I} \right] \mathbf{X} , \tag{4.21}$$

where $\left[\mathbf{H}_0 + \omega^2 \mathbf{H}_2 - \lambda \mathbf{I} \right]^{+}$ is the Moore-Penrose pseudo-inverse of $\left[\mathbf{H}_0 + \omega^2 \mathbf{H}_2 - \lambda \mathbf{I} \right]$. Differentiate equation (4.20) with respect to λ again gives

$$2\left[\left(\frac{\mathrm{d}\omega}{\mathrm{d}\lambda} \right)^2 + \omega \frac{\mathrm{d}^2\omega}{\mathrm{d}\lambda^2} \right] \mathbf{H}_2 \mathbf{X} + 2\left[2\omega \frac{\mathrm{d}\omega}{\mathrm{d}\lambda} \mathbf{H}_2 - \mathbf{I} \right] \frac{\mathrm{d}\mathbf{X}}{\mathrm{d}\lambda} + \left[\mathbf{H}_0 + \omega^2 \mathbf{H}_2 - \lambda \mathbf{I} \right] \frac{\mathrm{d}^2\mathbf{X}}{\mathrm{d}\lambda^2} = \mathbf{0} . \tag{4.22}$$

Pre-multiply equation (4.22) with the left eigenvector of $\mathbf{H}$, that is $\mathbf{Y}^{\mathrm{T}}$. Note that $\mathbf{Y}^{\mathrm{T}} \left[\mathbf{H}_0 + \omega^2 \mathbf{H}_2 - \lambda \mathbf{I} \right] = \mathbf{0}$. Substitute equation (4.21) into (4.22) and re-arrange to get

$$\frac{\mathrm{d}^2\omega}{\mathrm{d}\lambda^2} = \frac{\mathbf{Y}^{\mathrm{T}} \left[2\omega \frac{\mathrm{d}\omega}{\mathrm{d}\lambda} \mathbf{H}_2 - \mathbf{I} \right] \left[\mathbf{H}_0 + \omega^2 \mathbf{H}_2 - \lambda \mathbf{I} \right]^{+} \left[2\omega \frac{\mathrm{d}\omega}{\mathrm{d}\lambda} \mathbf{H}_2 - \mathbf{I} \right] \mathbf{X}}{\omega \mathbf{Y}^{\mathrm{T}} \mathbf{H}_2 \mathbf{X}} - \frac{1}{\omega} \left(\frac{\mathrm{d}\omega}{\mathrm{d}\lambda} \right)^2 . \tag{4.23}$$

The maximum group velocity of a propagating wave with wavenumber φ must occur when $dc_g/d\varphi = 0$. Write

$$\frac{dc_g}{d\varphi} = \frac{dc_g}{d\lambda}\frac{d\lambda}{d\varphi},$$ (4.24)

but $\lambda = \exp(i\varphi)$ and $d\lambda/d\varphi = i\exp(i\varphi) = i\lambda$, therefore equation (4.24) can be written as

$$\frac{dc_g}{d\varphi} = i\lambda\frac{dc_g}{d\lambda}.$$ (4.25)

From Chapter 2, we know that $c_g = i\lambda(d\omega/d\lambda)$, therefore

$$\frac{dc_g}{d\lambda} = i\left(\frac{d\omega}{d\lambda} + \lambda\frac{d^2\omega}{d\lambda^2}\right).$$ (4.26)

Substitute equation (4.26) into (4.25) to give

$$\frac{dc_g}{d\varphi} = -\lambda\left(\frac{d\omega}{d\lambda} + \lambda\frac{d^2\omega}{d\lambda^2}\right),$$ (4.27)

which implies that $dc_g/d\varphi = 0$ when $\lambda = 0$ (this condition is never met) or

$$\frac{d\omega}{d\lambda} + \lambda\frac{d^2\omega}{d\lambda^2} = 0.$$ (4.28)

Substitute equation (4.23) into (4.28) and multiply with $\mathbf{Y}^T\mathbf{X}$; from Chapter 2, we know that we can substitute the term $(\mathbf{Y}^T\mathbf{X})/(\omega\mathbf{Y}^T\mathbf{H}_2\mathbf{X})$ with $2(d\omega/d\lambda)$, upon simplification, the resulting equation can be rearranged to get

$$\mathbf{Y}^T\left\{\left(1 - \frac{\lambda}{\omega}\frac{d\omega}{d\lambda}\right)\mathbf{I} + 2\lambda\left[2\omega\frac{d\omega}{d\lambda}\mathbf{H}_2 - \mathbf{I}\right]\left[\mathbf{H}_0 + \omega^2\mathbf{H}_2 - \lambda\mathbf{I}\right]^+\left[2\omega\frac{d\omega}{d\lambda}\mathbf{H}_2 - \mathbf{I}\right]\right\}\mathbf{X} = 0.$$ (4.29)

Equation (4.29) must be satisfied at the maximum group velocity. To identify the wavenumber at which the maximum group velocity occurs, one can plot $dc_g/d\varphi$ against φ and find the point where the curve intersects the line $dc_g/d\varphi = 0$. Figure 4.5 shows the plot of $dc_g/d\varphi$ against φ for the six modes associated with the model structure. It is noted that the wavenumbers associated with the maximum group velocities found in Figure 4.3 match with the wavenumbers where the curves in Figure 4.5 intersect with the line $dc_g/d\varphi = 0$.
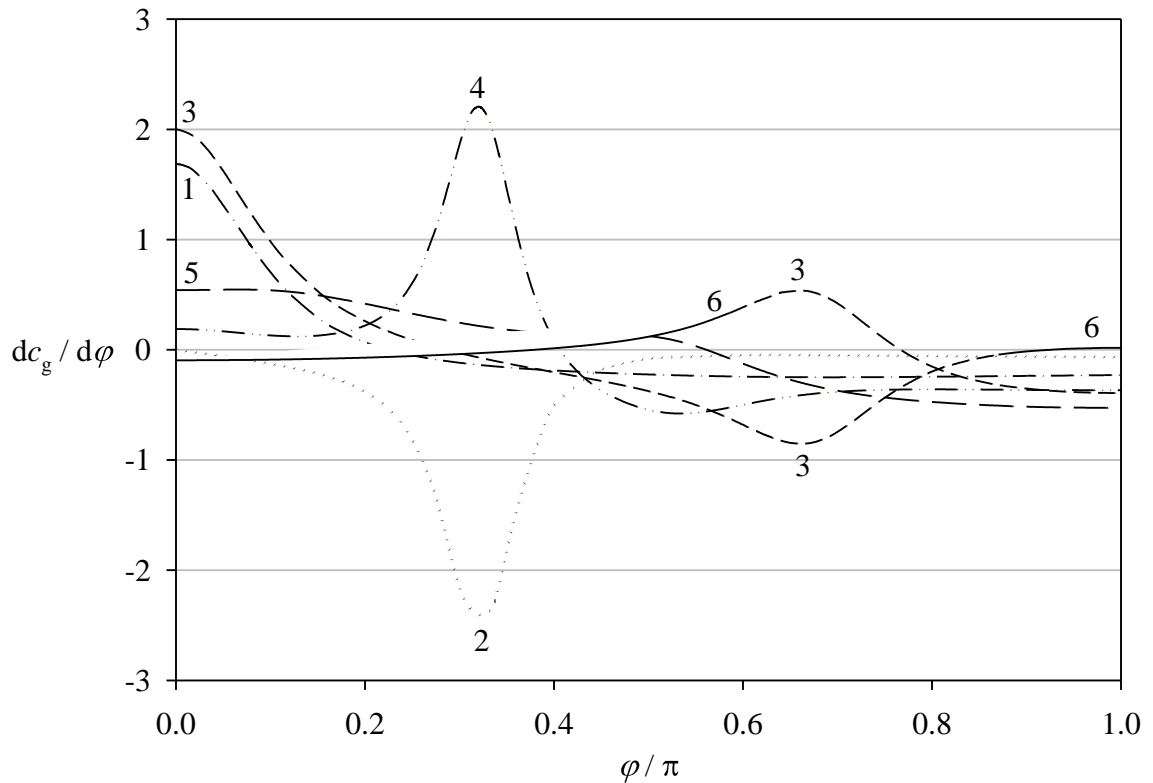
Figure 4.5 First derivative of the group velocity with respect to the wavenumber as a function of normalised wavenumber.

$-\cdot-\cdot-$	1 Bending,	$\cdots\cdots$	2 Extensional,
$-----$	3 First thickness shear,	$-\cdot\cdot-\cdot\cdot-$	4 Second thickness shear,
$-\ -\ -$	5 First breathing,	$\textemdash\textemdash$	6 Second breathing.

When two dispersion branches intersect, one can refer to the associated eigenvectors to determine which branch each of the identical eigenvalues is associated with. One can also find the gradients of the points associated with the eigenvalues to ascertain the branches. For example, when $\omega^2 = 1.3536$, the gradients of branches 3 and 4 are 0.6423 and 0.6183, respectively; when $\omega^2 \approx 1.6702$, the gradients of branches 3 and 4 are 0.7119 and 0.7501, respectively. The gradients are then compared with the gradients obtained at the frequencies before (or after) the intersection, and one would expect that the values change smoothly.

Now, from equation (4.19), substitute P with equation (4.15) and expand the force term, then substitute E_S and E_K with equations (4.4) and (4.5), respectively; the resulting equation is

$$\frac{1}{2}\text{Re}\left\{i\,\mathbf{D}_{L}^{*}\left[\mathbf{K}_{LL}\mathbf{D}_{L}+\mathbf{K}_{LR}\mathbf{D}_{R}-\frac{\omega^{2}}{2}\mathbf{m}\mathbf{D}_{L}\right]\right\}\omega=\frac{1}{2}\text{Re}\left\{\mathbf{D}_{L}^{*}\left[\mathbf{K}_{LL}\mathbf{D}_{L}+\mathbf{K}_{LR}\mathbf{D}_{R}-\frac{\omega^{2}}{2}\mathbf{m}\mathbf{D}_{L}\right]\right\}c_{g}.\quad(4.30)$$

The terms on left-hand side of equation (4.30) are associated with imaginary, or reactive, energy while the terms on the right-hand side are associated with real, or active, energy; the terms of equation (4.30) can then be re-written as

$$\left(\text{reactive energy}\right)\times\left(\text{reactive energy velocity}\right)=\left(\text{active energy}\right)\times\left(\text{active energy velocity}\right).$$

Equation (4.30) reveals the existence of reactive energy and its role in mediating the energy exchange across the cell boundary. Nonetheless, reactive energy is usually considered insignificant because it cycles within the boundary.

4.5   Energy flow in two attenuating waves

The attenuating waves are represented by loops 1,6 and 3,6 on the dispersion diagram (Figure 3.3 in Chapter 3). The waves are associated with complex non-unity eigenvalues which occur as a quartet of reciprocals and complex conjugates: $\lambda_{1},\lambda_{2},\lambda_{3}$ and λ_{4} where $\lambda_{1}=1/\lambda_{2}^{*}$, $\lambda_{3}=1/\lambda_{4}^{*}$, $\lambda_{1}=\lambda_{3}^{*}$ and $\lambda_{2}=\lambda_{4}^{*}$. Consider the following two pairs of eigenvalues from the quartet: the first pair is $[\lambda_{1},\lambda_{2}]=[\exp(+\delta_{1}+i\varphi_{1}),\exp(-\delta_{2}+i\varphi_{2})]$ where $\lambda_{1}=1/\lambda_{2}^{*}$ and the second pair is $[\lambda_{3},\lambda_{4}]=[\exp(+\delta_{3}-i\varphi_{3}),\exp(-\delta_{4}-i\varphi_{4})]$ where $\lambda_{3}=1/\lambda_{4}^{*}$. Note that, each pair consists of two waves that travel in the same direction, but decay in opposite directions; for attenuating waves, the direction of travel and decay are determined by the signs of φ and δ, respectively.

Employing equation (4.15) and by the principle of superposition, the time-averaged energy flow into the left boundary of a cell in two attenuating waves associated with the first eigenvalues pair is given by

$$P_{12}=\text{Re}\left\{-\frac{1}{2}i\,\omega\left[\mathbf{D}_{1}^{*}+\mathbf{D}_{2}^{*}\right]\cdot\left[\mathbf{F}_{1}+\mathbf{F}_{2}\right]\right\}=\text{Re}\left\{-\frac{1}{2}\omega\left[\mathbf{D}_{1}^{*}\mathbf{F}_{1}+\mathbf{D}_{2}^{*}\mathbf{F}_{2}+\mathbf{D}_{1}^{*}\mathbf{F}_{2}+\mathbf{D}_{2}^{*}\mathbf{F}_{1}\right]\right\},\quad(4.31)$$

where the subscripts 1 and 2 represent each of the two waves; strictly, all terms should have an additional subscript L for left-hand side, but this is omitted for brevity. From Section 4.2, we know that the first two terms are zero and the last two terms can be simplified numerically as,

$$P_{12}=\text{Re}\left\{-\frac{1}{2}i\,\omega\left[\mathbf{D}_{1}^{*}\mathbf{F}_{2}+\mathbf{D}_{2}^{*}\mathbf{F}_{1}\right]\right\}=\text{Re}\left\{-\frac{1}{2}i\,\omega\left[(a+bi)+(-a+bi)\right]\right\}=\omega b\quad(4.32)$$

where a and b are real numbers. Equation (4.32) can be expressed in terms of eigenvector $\mathbf{V}$ as $P_{12} = -\mathrm{i}\,\omega\left(\mathbf{V}_1\mathbf{J}\mathbf{V}_2 + \mathbf{V}_2\mathbf{J}\mathbf{V}_1\right)/4$; the derivation is given in Appendix C.2.

Following the same procedures for the second wave pair gives

$$P_{34} = \mathrm{Re}\left\{-\frac{1}{2}\mathrm{i}\,\omega\left[\mathbf{D}_3^*\mathbf{F}_4 + \mathbf{D}_4^*\mathbf{F}_3\right]\right\} = \mathrm{Re}\left\{-\frac{1}{2}\mathrm{i}\,\omega\left[(a-b\mathrm{i})+(-a-b\mathrm{i})\right]\right\} = -\omega b \quad (4.33)$$

where the subscripts 3 and 4 represent each of the two waves; the negative sign implies that the power associated with the second wave pair flows in opposite direction to the first wave pair.

For an arbitrary cell, time-averaged power that flows into the left- and out of the right-hand sides of a cell are found to be the same and this can be shown as

$$P_{\mathrm{R}} = \mathrm{Re}\left\{-\frac{1}{2}\mathrm{i}\,\omega\left[(\lambda_1\mathbf{D}_1)^*(\lambda_2\mathbf{F}_2)+(\lambda_2\mathbf{D}_2)^*(\lambda_1\mathbf{F}_1)\right]\right\} = \mathrm{Re}\left\{-\frac{1}{2}\mathrm{i}\,\omega\left[\mathbf{D}_1^*\mathbf{F}_2 + \mathbf{D}_2^*\mathbf{F}_1\right]\right\} = P_{\mathrm{L}} \quad (4.34)$$

since $\lambda_1^*\lambda_2 = \lambda_2^*\lambda_1 = 1$. Equations (4.32)-(4.34) imply that there is a uniform cross-flow of energy between two mutually interacting attenuating waves that decay in the opposite directions. The nodal displacement and nodal force are not in quadrature, so there is a component of work done by the force from wave 1 through the displacement of wave 2. However, the work is counteracted by the force of wave 2 through the displacement of wave 1 resulting in zero work done across the boundary. Energy flow across the boundary is due to the components of displacement and force that are in quadrature.

As the energy flow is uniform along the infinite structure, one should be able to evaluate the group velocity. Consider the left-hand side of a cell, the equations of motion associated with the first attenuating wave pair are

$$-\mathbf{F}_1 = \left[\mathbf{K}_{\mathrm{LL}} - \frac{\omega^2\mathbf{m}}{2}\right]\mathbf{D}_1 + \lambda_1\mathbf{K}_{\mathrm{LR}}\mathbf{D}_1, \quad (4.35)$$

$$-\mathbf{F}_2 = \left[\mathbf{K}_{\mathrm{LL}} - \frac{\omega^2\mathbf{m}}{2}\right]\mathbf{D}_2 + \lambda_2\mathbf{K}_{\mathrm{LR}}\mathbf{D}_2, \quad (4.36)$$

where the subscripts 1 and 2 represent each of the two attenuating waves decaying in opposite directions; again, the displacement and force terms have additional subscript L for left-hand side but omitted for brevity. Pre-multiply equation (4.35) by $\mathbf{D}_2^*/2$ and equation (4.36) by $\mathbf{D}_1^*/2$, take the real part of each term and the sum to give the time-averaged energy balance as

$$W_{21} + W_{12} = E_{S,21} + E_{S,12} - E_{K,21} - E_{K,12} \tag{4.37}$$

where

$$W_{21} = -\frac{1}{2}\text{Re}\left(\mathbf{D}_2^*\mathbf{F}_1\right), \; W_{12} = -\frac{1}{2}\text{Re}\left(\mathbf{D}_1^*\mathbf{F}_2\right),$$

$$E_{S,21} = \frac{1}{2}\text{Re}\left\{\mathbf{D}_2^*\left[\mathbf{K}_{LL}\mathbf{D}_1 + \lambda_1\mathbf{K}_{LR}\mathbf{D}_1\right]\right\}, \; E_{S,12} = \frac{1}{2}\text{Re}\left\{\mathbf{D}_1^*\left[\mathbf{K}_{LL}\mathbf{D}_2 + \lambda_2\mathbf{K}_{LR}\mathbf{D}_2\right]\right\},$$

$$E_{K,21} = \frac{1}{4}\omega^2\text{Re}\left(\mathbf{D}_2^*\mathbf{m}\mathbf{D}_1\right), \; E_{K,12} = \frac{1}{4}\omega^2\text{Re}\left(\mathbf{D}_1^*\mathbf{m}\mathbf{D}_2\right).$$

It is noted that $W_{21} + W_{12} = 0$ and $E_{S,21} + E_{S,12} = E_{K,21} + E_{K,12}$, so the time-averaged total energy is simply the sum of all the four energy terms. The group velocity associated with the two attenuating waves is then given by

$$c_{g,12} = \frac{P_{12}}{E_{S,21} + E_{S,12} + E_{K,21} + E_{K,12}} . \tag{4.38}$$

Figures 4.6 and 4.7 show the group velocity of energy flow pertaining to two oppositely decaying attenuating waves corresponding to loops 1,6 and 3,6, respectively. From Figure 4.6, the bottom segment of the loop 1,6 ($1.3536 < \omega^2 < 2.195$) is found to be anomalous, but the top segment ($2.195 < \omega^2 < 3.022$) is normal. The change from anomalous to normal occurs at $\omega^2 \approx 2.195$ where $\delta = \pm1.8066$ and $\varphi = 0.8119\pi$; this point does not coincide with the maximum decay rate point ($\delta = 1.8131$ at $\omega^2 \approx 2.022$) nor the minimum wavenumber point ($\varphi = 0.8112\pi$ at $\omega^2 \approx 2.3$) of the loop. Also, at $\omega^2 \approx 2.195$, the group velocity is apparently infinite; this could mean that the peak of the energy wave packet at the left- and right-hand boundaries of a cell occurs simultaneously [105].

In Figure 4.7, loop 3,6 is found to be anomalous as a function of frequency. The maximum group velocity occurs at $\omega^2 \approx 3.415$ where $\delta = \pm0.5113$ and $\varphi = 0.6701\pi$; this point does not coincide with the maximum decay rate point of the loop which occurs at $\omega^2 \approx 3.35$, $\delta = \pm0.5222$, $\varphi = 0.6958\pi$.
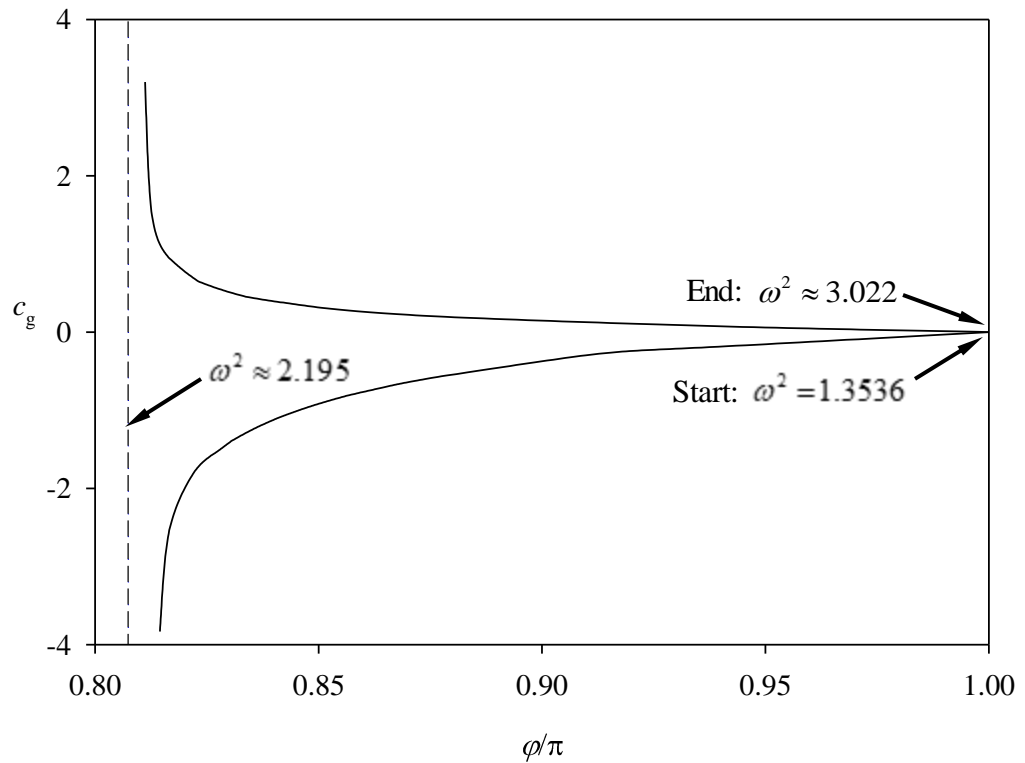
Figure 4.6 Group velocity of energy flow associated with two oppositely decaying attenuating waves pertaining to loop 1,6. The asymptotic line is at $\varphi/\pi \approx 0.8119$.
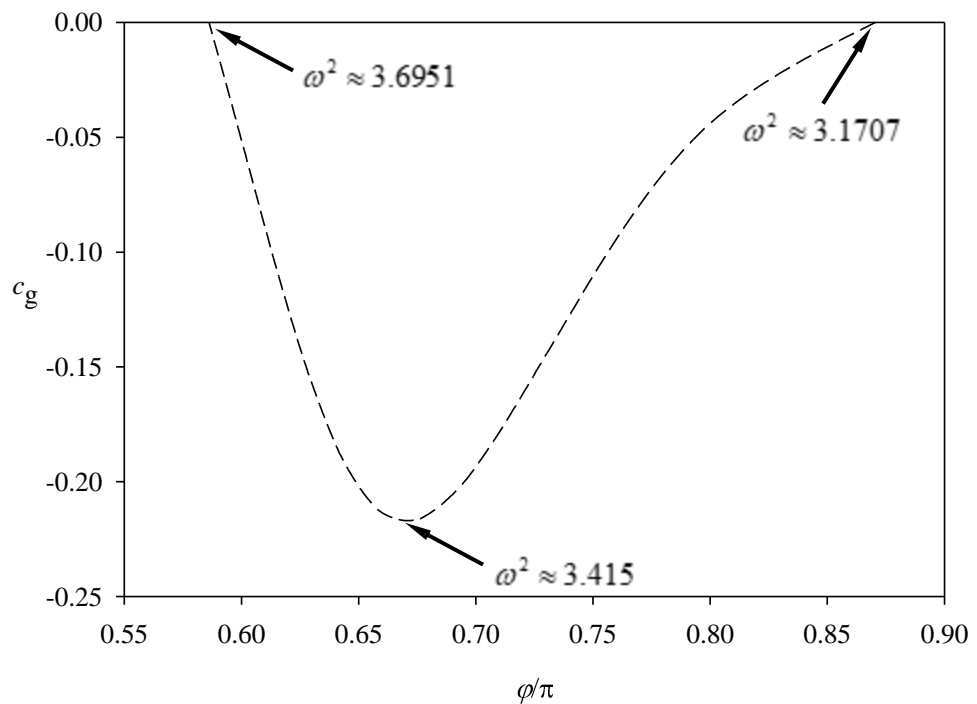

Figure 4.7 Group velocity of energy flow associated with two oppositely decaying attenuating waves pertaining to loop 3,6.

4.6   Anomalous dispersion

Dispersion refers to the phenomena where a wave propagates at different phase velocity at different wavenumber. If the phase velocity and the group velocity of the wave are in the same direction, the dispersion is termed normal and the wave's energy is regarded as flowing in the forward direction; otherwise, if the two velocities are in opposite directions, the dispersion is termed anomalous and the wave's energy is regarded as flowing in the backward direction. In terms of frequency derivative with respect to the wavenumber, a normal dispersion satisfies either one of the following conditions: $d\omega/d\varphi < 0$ for $\varphi < 0$ or $d\omega/d\varphi > 0$ for $\varphi > 0$; while anomalous dispersion satisfies either one of the following conditions: $d\omega/d\varphi < 0$ for $\varphi > 0$ or $d\omega/d\varphi > 0$ for $\varphi < 0$. Note that, positive wavenumber and positive group velocity implies that the phase velocity and energy transfer, respectively, are left-going.

For a one-dimensional beam-like system, anomalous dispersion occurs in multi-coupled structures with at least two degrees of freedom at the cross-section, so the minimum size of the transfer matrix is (4×4). However, as pointed out in Section 2.4, attenuating waves occurs in multi-coupled structures with at least four degrees of freedom at the coupling, so the minimum size of the transfer matrix is (8×8). One might expect that the minimum size is (4×4) because the complex non-unity eigenvalues occur as a quartet but this is not the case. Figure 4.8 shows the unit cells of four infinite frameworks with different number of cross-sectional degrees of freedom. The systems shown in Figures 4.8(a) and 4.8(b) which can be represented by a (4×4) and a (6×6) transfer matrices, respectively, do not exhibit anomalous dispersion. However, the systems in Figures 4.8(c) and 4.8(d) which can be represented by a (4×4) and an (8×8) transfer matrices, respectively, do exhibit an anomalous dispersion in form of a breathing mode; and only the latter allows attenuating waves to occur.

Seemingly, anomalous dispersion occurs as a result of opposing nodal displacements in the y-direction at the cross-section that inevitably leads to opposing displacements in the x-direction along the same tier of mass, as described in Section 3.11. To illustrate this once again, consider the system in Figure 4.8(d). The displacements associated with the four degrees of freedom on the left-hand side of the cell are $D_{L,1x}$, $D_{L,1y}$, $D_{L,2x}$ and $D_{L,2y}$; and the displacements on the right-hand side are $D_{R,1x}$, $D_{R,1y}$, $D_{R,2x}$ and $D_{R,2y}$. Under static pinching load, $D_{L,1y}$ and $D_{L,2y}$ are displaced downwards and upwards respectively, the

vertical member on the left shortens while both diagonal members lengthen. Therefore, it is inevitable that $D_{R,1y}$ and $D_{R,2y}$ will be displaced upwards and downwards, respectively, and that means $D_{L,1y}$ and $D_{R,1y}$ are displaced in opposing directions. The decay eigenvalue must be negative. Under dynamic condition, this mode will appear as symmetric breathing wave, and one can expect that the wave would interact with symmetric extensional wave to form attenuating waves.

For the example framework, there are three tiers (or layers) of point masses and anomalous dispersion manifests as second breathing mode which is characterized by predominantly opposing *y*-displacement in the transverse (or *y*-) direction. The wavenumber of an anomalous dispersion reduces from π to zero as frequency increases from the cut-on to the cut-off. Detailed account on the displacement vector of the second breathing mode is given in Section 3.6.


(a) 2 DOF (b) 3 DOF (c) 2 DOF (d) 4 DOF
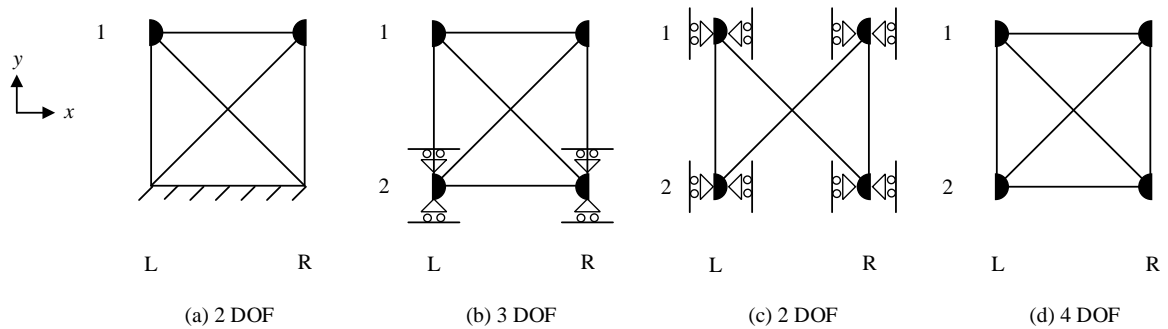
Figure 4.8 Unit cells of infinite frameworks with different numbers of cross-sectional degrees of freedom. Numbers 1 and 2 indicate tiers of the masses.

In order to understand the energy flow mechanism, recall that the time-averaged power equation is defined as the product of velocity and force. If velocity and force act in the same direction, then the power flow is in the forward direction, otherwise the power flow is in the backward direction. At each cross-section, it is possible for a particular mode to have both forward and backward components of the power flow, therefore, the resultant of all components will determine the actual direction of the power flow. For the example framework, it is found numerically that there is no backward power flow component for the bending and extensional modes. However, for the other modes, there are forward and backward power components.

4.7   Conclusions

Time-averaged work done, energy and power associated with evanescent, attenuating and propagating waves are studied numerically by considering the sectional nodal components contribution. Work is done by evanescent and attenuating waves at each cross-section over one period and no transfer of energy occurs across the cell boundaries. Work done, kinetic energy and potential energy are bounded within each cross-section. However, on time-average, no work is done by propagating wave at each cross-section and energy is transferred from one cell to the next at a speed given by the group velocity. At the cut-on and cut-off frequencies, there is no work done and no energy transfer occurs across the cell boundaries.

The normal and anomalous dispersions are studied by considering the cross-sectional nodal contribution. In a structure which has diagonal connections, backward power flow can occur as a result of opposing y-displacement at the nodal cross-section that leads to negative decay eigenvalue under static case. For both dispersions, it is possible that both forward and backward power components to appear at the cross-section and at the same time; in such situation, the forward power components are dominant in the case of normal dispersion while backward power components are dominant in the case of anomalous dispersion.

Two interacting attenuating waves that decay in opposite directions is found to transfer energy. The energy flow in two interacting attenuating waves that are formed by oscillatory evanescent waves can change from being backward to forward.

Chapter 5:   An Alternative to the Riccati Transfer Matrix Method for Repetitive Structures

5.1   Introduction

In 2010, Stephen [49] provided an exposition of the Riccati transfer matrix method applied to the static analysis of a repetitive structure subjected to point, and distributed loading; this approach resolves the numerical instability issues identified by the author in [39]. As noted in [49], when a complete structure is to be analysed, one typically has a two-point boundary value problem (TPBVP); thus for a tip-loaded cantilever beam of N repeating cells, the load vector at the tip, $\mathbf{F}(N)$, and the displacement vector at the fixed root, $\mathbf{d}(0)$, will be known; the displacement vector at the tip, $\mathbf{d}(N)$, and the reaction force vector at the root, $\mathbf{F}(0)$, are unknowns. The need to construct powers of the transfer matrix, up to $\mathbf{G}^N$, is the source of the ill-conditioning; this becomes more clear when the cross-sectional state-vector of displacement and force components is expressed in terms of the participation coefficients of the eigen- and principal vectors, and spatial evolution is expressed in terms of powers of the Jordan canonical form. In particular, the eigenvalues of $\mathbf{G}$ are unity with a multiplicity of six, 0.059596, -0.070207 and 0.28292, together with their reciprocals 16.780, -14.244 and 3.5346, respectively; for a 10 cell structure, the calculation of $\mathbf{G}^{10}$ leads to the term $16.780^{10} \approx 1.8 \times 10^{12}$ which magnifies any errors.

In contrast, the Riccati transfer matrix method [49,67,106] is based on a recursive Riccati matrix $\mathbf{R}$, which relates the force and displacement vectors, $\mathbf{F}$ and $\mathbf{d}$ respectively, at the n th cross-section; that is $\mathbf{F}(n) = \mathbf{R}(n)\mathbf{d}(n)$. The method is numerically stable because recursive factors which feature in both the "backward in space" and the "forward in space" solution process have eigenvalues which converge onto 0.059596, -0.070207 and 0.28292, together with unity with a multiplicity of three. While the approach can be applied to a wide range of transfer matrix analyses, see for example [107], it is not at all intuitive, and rather lacks elegance.

In this chapter, the issue of numerical stability is addressed in a much more direct and transparent manner. The approach is more aligned with that presented in [39], and avoids

multiplication by powers of eigenvalues greater than unity – the source of the instability – by constructing *mixed* column vectors of participation coefficients.

Some repetition of the content of [39,49] is necessary for completeness, but this has been kept to a minimum. A full description of the framework are already given in Chapter 2 (without the point masses) and with the following properties: Young's modulus $E = 200$ GPa, horizontal and vertical rods of length $l = 1$ m and cross-sectional area 1 cm^2, diagonal rods of length $\sqrt{2}$ m and cross-sectional area 1/2 cm^2. The eigen- and principal vectors are given in reference [12] and reproduced in Appendix D.1.

The transfer matrix method calculations were performed using MATLAB, including a symbolic computation toolkit, to double precision using format long command. The vpa command is used to convert large fractions into floating-points. FEA results reported in [39] which is obtained from ANSYS is taken as benchmark.

5.2   Theory

The stiffness matrix $\mathbf{K}$ of a single cell of a repetitive structure relates the force and displacement vectors on both sides as $\mathbf{F} = \mathbf{K}\mathbf{d}$, or in partitioned form

$$
\begin{bmatrix} \mathbf{F}_L \\ \mathbf{F}_R \end{bmatrix} = \begin{bmatrix} \mathbf{K}_{LL} & \mathbf{K}_{LR} \\ \mathbf{K}_{RL} & \mathbf{K}_{RR} \end{bmatrix} \begin{bmatrix} \mathbf{d}_L \\ \mathbf{d}_R \end{bmatrix},
\tag{5.1}
$$

where the subscripts L and R denote left and right, respectively. The transfer matrix $\mathbf{G}$ is determined from the stiffness matrix $\mathbf{K}$ according to

$$
\begin{bmatrix} \mathbf{d}_R \\ \mathbf{F}_R \end{bmatrix} = \begin{bmatrix} -\mathbf{K}_{LR}^{-1}\mathbf{K}_{LL} & -\mathbf{K}_{LR}^{-1} \\ \mathbf{K}_{RL} - \mathbf{K}_{RR}\mathbf{K}_{LR}^{-1}\mathbf{K}_{LL} & -\mathbf{K}_{RR}\mathbf{K}_{LR}^{-1} \end{bmatrix} \begin{bmatrix} \mathbf{d}_L \\ -\mathbf{F}_L \end{bmatrix} = \begin{bmatrix} \mathbf{G}_{dd} & \mathbf{G}_{dF} \\ \mathbf{G}_{Fd} & \mathbf{G}_{FF} \end{bmatrix} \begin{bmatrix} \mathbf{d}_L \\ -\mathbf{F}_L \end{bmatrix},
\tag{5.2}
$$

or more compactly $\mathbf{s}_R = \mathbf{G}\mathbf{s}_L$; the force sign convention of finite element analysis (FEA) is employed, hence the negative force vector on the right-hand side of equation (5.2). The transfer matrix thus describes how a state-vector evolves as one moves from the left-hand side of the cell to the right-hand side. For an extended structure, it is more convenient to write this as $\mathbf{s}(n+1) = \mathbf{G}\,\mathbf{s}(n)$, which relates the state-vector on the right-hand side of the $(n+1)$ th cell to the state-vector on the right-hand side of the n th cell.

An eigenvector of the transfer matrix $\mathbf{G}$ represents a pattern of nodal displacement and force components, which is unique to within a scalar multiplier, say λ. Translational symmetry demands that this pattern is preserved as one moves from cell-to-cell, implying that $\mathbf{s}(n+1) = \lambda \mathbf{s}(n)$; this leads directly to the standard eigenproblem

$$(\mathbf{G} - \lambda \mathbf{I})\mathbf{s}(n) = \mathbf{0}. \tag{5.3}$$

Non-unity eigenvalues of $\mathbf{G}$ are the rates of decay of self-equilibrated loading, as anticipated by Saint-Venant's principle. Multiple unity eigenvalues pertain to the transmission of load, e.g. tension, or bending moment, as well as the rigid body displacements and rotations.

5.3   Tip loading

The expansion of state-vectors into their constituent eigen- and principal vectors is first developed in the context of the 10-cell structure shown in Figure 5.1, but with the intermediate support removed and with load applied at the free-end only, for which one has

$$\mathbf{s}(10) = \mathbf{G}^{10}\mathbf{s}(0). \tag{5.4}$$
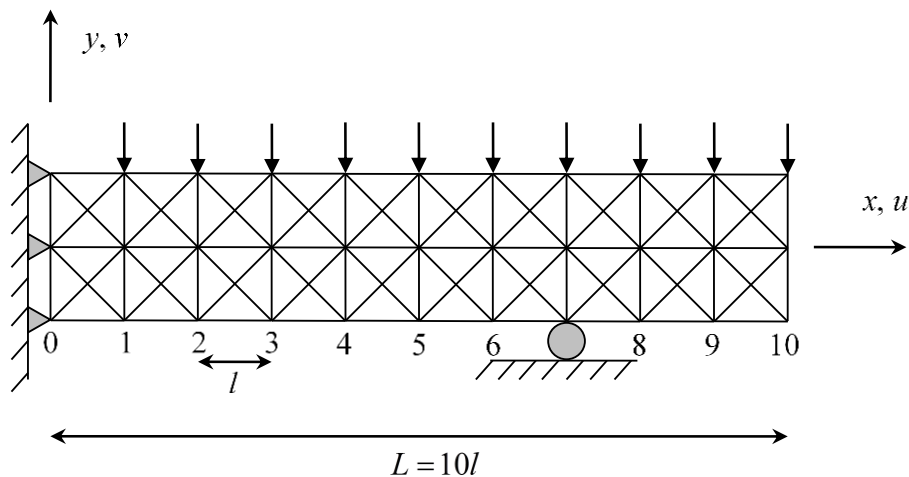
Figure 5.1 Ten-cell repetitive structure subject to distributed surface loading, with an intermediate support at the 7th nodal cross-section. Each downward arrow represents a force of $1\,\text{kN}$.

The state-vectors $\mathbf{s}(0)$ and $\mathbf{s}(10)$ can be expressed as the linear combinations

$$\mathbf{s}(0) = C_{1,0}\mathbf{X}_1 + C_{2,0}\mathbf{X}_2 + \cdots + C_{12,0}\mathbf{X}_{12} = \mathbf{T}\mathbf{C}_0 \tag{5.5}$$

$$\mathbf{s}(10) = C_{1,10}\mathbf{X}_1 + C_{2,10}\mathbf{X}_2 + \cdots + C_{12,10}\mathbf{X}_{12} = \mathbf{T}\mathbf{C}_{10} \tag{5.6}$$

where $\mathbf{T}$ is the transformation matrix of eigen- and principal vectors $\mathbf{X}_1, \mathbf{X}_2, \cdots \mathbf{X}_{12}$ and $\mathbf{C}$ is the column vector of participation coefficients C; the first subscript of C pertains to the vector, the second to the nodal cross-section. The matrix $\mathbf{T}$ transforms $\mathbf{G}$ to its Jordan canonical form $\mathbf{J}$ according to $\mathbf{T}^{-1}\mathbf{G}\mathbf{T} = \mathbf{J}$, or $\mathbf{G} = \mathbf{T}\mathbf{J}\mathbf{T}^{-1}$; powers of $\mathbf{G}$ are then $\mathbf{G}^n = \mathbf{T}\mathbf{J}^n\mathbf{T}^{-1}$. Substituting into equation (5.4) gives $\mathbf{T}\mathbf{C}_{10} = \mathbf{T}\mathbf{J}^{10}\mathbf{T}^{-1}\mathbf{T}\mathbf{C}_0$, and pre-multiplying by $\mathbf{T}^{-1}$ gives

$$\mathbf{C}_{10} = \mathbf{J}^{10}\mathbf{C}_0 ; \tag{5.7}$$

compared with equation (5.4), this represents the simplest possible description of spatial evolution as one moves from one end of the structure to the other. The matrix $\mathbf{J}$ is given explicitly in Appendix D.1.

The expression $\mathbf{s}(0) = \mathbf{T}\mathbf{C}_0$ may be written in partitioned form as

$$\begin{bmatrix} \mathbf{d}(0) \\ \mathbf{F}(0) \end{bmatrix} = \begin{bmatrix} \mathbf{T}_1 & \mathbf{T}_2 \\ \mathbf{T}_3 & \mathbf{T}_4 \end{bmatrix} \mathbf{C}_0 , \tag{5.8}$$

and $\mathbf{s}(10) = \mathbf{T}\mathbf{C}_{10}$ as

$$\begin{bmatrix} \mathbf{d}(10) \\ \mathbf{F}(10) \end{bmatrix} = \begin{bmatrix} \mathbf{T}_1 & \mathbf{T}_2 \\ \mathbf{T}_3 & \mathbf{T}_4 \end{bmatrix} \mathbf{C}_{10} . \tag{5.9}$$

In [39], matrices $\mathbf{T}_1, \mathbf{T}_2, \mathbf{T}_3$ and $\mathbf{T}_4$ were all (6×6) partitions of $\mathbf{T}$; however, this is no longer the case. Rather, $\mathbf{T}_1$ and $\mathbf{T}_2$ are respectively the (6×3) top-left and (6×9) top-right partitions of $\mathbf{T}$, while $\mathbf{T}_3$ and $\mathbf{T}_4$ are the (6×3) bottom-left and (6×9) bottom-right partitions.

The Jordan canonical form $\mathbf{J}$ has eigenvalues greater than unity (in particular $\lambda_1 = 16.780$, $\lambda_2 = 3.5346$ and $\lambda_3 = -14.244$). To eliminate these from the formulation, the

corresponding coefficients in $\mathbf{C}_{10}$ and $\mathbf{C}_0$ are exchanged, and their reciprocal eigenvalues employed instead.

Equation (5.7) now becomes

$$
\begin{bmatrix} C_{1,0} \\ C_{2,0} \\ C_{3,0} \\ C_{4,10} \\ \vdots \\ C_{12,10} \end{bmatrix} = \begin{bmatrix} \mathbf{J}_1^{-1} & \mathbf{0} \\ \mathbf{0} & \mathbf{J}_4 \end{bmatrix}^{10} \begin{bmatrix} C_{1,10} \\ C_{2,10} \\ C_{3,10} \\ C_{4,0} \\ \vdots \\ C_{12,0} \end{bmatrix} = \begin{bmatrix} \left(\mathbf{J}_1^{-1}\right)^{10} & \mathbf{0} \\ \mathbf{0} & \left(\mathbf{J}_4\right)^{10} \end{bmatrix} \begin{bmatrix} C_{1,10} \\ C_{2,10} \\ C_{3,10} \\ C_{4,0} \\ \vdots \\ C_{12,0} \end{bmatrix},
\tag{5.10}
$$

where the exchanged coefficients are shown in bold.

Now, consider the boundary conditions. The root of the cantilever is assumed fully fixed, so one has $\mathbf{d}(0) = \mathbf{0}$. From equation (5.8), $\mathbf{d}(0)$ can be written in partitioned form as $\mathbf{d}(0) = \begin{bmatrix} \mathbf{T}_1 & \mathbf{T}_2 \end{bmatrix} \mathbf{C}_0$. However, in order to apply equation (5.10), $C_{1,0}$, $C_{2,0}$ and $C_{3,0}$ in $\mathbf{C}_0$ must be expressed in terms of $C_{1,10}$, $C_{2,10}$ and $C_{3,10}$, respectively. Therefore, write

$$
\mathbf{d}(0) = \mathbf{T}_1 \begin{bmatrix} C_{1,0} \\ C_{2,0} \\ C_{3,0} \end{bmatrix} + \mathbf{T}_2 \begin{bmatrix} C_{4,0} \\ \vdots \\ C_{12,0} \end{bmatrix}.
\tag{5.11}
$$

Recall that $\begin{bmatrix} C_{1,0} \\ C_{2,0} \\ C_{3,0} \end{bmatrix} = \left(\mathbf{J}_1^{-1}\right)^{10} \begin{bmatrix} C_{1,10} \\ C_{2,10} \\ C_{3,10} \end{bmatrix}$. Upon substitution into equation (5.11), one obtains

$$
\begin{aligned}
\mathbf{d}(0) &= \mathbf{T}_1 \left(\mathbf{J}_1^{-1}\right)^{10} \begin{bmatrix} C_{1,10} \\ C_{2,10} \\ C_{3,10} \end{bmatrix} + \mathbf{T}_2 \begin{bmatrix} C_{4,0} \\ \vdots \\ C_{12,0} \end{bmatrix} \\
&= \begin{bmatrix} \mathbf{T}_1 \left(\mathbf{J}_1^{-1}\right)^{10} & \mathbf{T}_2 \end{bmatrix} \begin{bmatrix} C_{1,10} & C_{2,10} & C_{3,10} & C_{4,0} & \cdots & C_{12,0} \end{bmatrix}^{\mathrm{T}},
\end{aligned}
\tag{5.12}
$$

where $\mathbf{T}_1 \left(\mathbf{J}_1^{-1}\right)^{10}$ is a (6×3) matrix of vanishingly small numbers; the first, second and third columns of $\mathbf{T}_1 \left(\mathbf{J}_1^{-1}\right)^{10}$ are of order $O(-12)$, $O(-5)$ and $O(-11)$, respectively. This effectively eliminates the coefficients $C_{1,10}, C_{2,10}$ and $C_{3,10}$ from the displacement vector $\mathbf{d}(0)$. Physically, this implies that any displacement components associated with self-

equilibrated loads at the free end will have decayed to insignificant levels at the fixed end, as would be anticipated by Saint-Venant's principle; further, as the number of cells, say n, increases, so the components within $\mathbf{T}_1 \left(\mathbf{J}_1^{-1} \right)^n$ would become even smaller.

At the free end, we know that $\mathbf{F}(10) = \begin{bmatrix} 0 & -1000 & 0 & 0 & 0 & 0 \end{bmatrix}^{\mathrm{T}}$. From equation (5.9), one has $\mathbf{F}(10) = \begin{bmatrix} \mathbf{T}_3 & \mathbf{T}_4 \end{bmatrix} \mathbf{C}_{10}$. Again, in order to apply equation (5.10), we want to express $C_{4,10}$, $C_{5,10}$, $\cdots C_{12,10}$ in terms of $C_{4,0}$, $C_{5,0}$, $\cdots C_{12,0}$, respectively. Therefore, write

$$\mathbf{F}(10) = \mathbf{T}_3 \begin{bmatrix} C_{1,10} \\ C_{2,10} \\ C_{3,10} \end{bmatrix} + \mathbf{T}_4 \begin{bmatrix} C_{4,10} \\ \vdots \\ C_{12,10} \end{bmatrix}. \tag{5.13}$$

Recall that

$$\begin{bmatrix} C_{4,10} \\ \vdots \\ C_{12,10} \end{bmatrix} = \left(\mathbf{J}_4 \right)^{10} \begin{bmatrix} C_{4,0} \\ \vdots \\ C_{12,0} \end{bmatrix} \text{ where } \mathbf{J}_4 \text{ is the } (9 \times 9) \text{ bottom-right partition of } \mathbf{J}. \text{ Upon}$$

substitution into equation (5.13), one gets

$$\mathbf{F}(10) = \mathbf{T}_3 \begin{bmatrix} C_{1,10} \\ C_{2,10} \\ C_{3,10} \end{bmatrix} + \mathbf{T}_4 \left(\mathbf{J}_4 \right)^{10} \begin{bmatrix} C_{4,0} \\ \vdots \\ C_{12,0} \end{bmatrix} \tag{5.14}$$

$$= \begin{bmatrix} \mathbf{T}_3 & \mathbf{T}_4 \left(\mathbf{J}_4 \right)^{10} \end{bmatrix} \begin{bmatrix} C_{1,10} & C_{2,10} & C_{3,10} & C_{4,0} & \cdots & C_{12,0} \end{bmatrix}^{\mathrm{T}}.$$

Note that some columns of $\mathbf{T}_4 \left(\mathbf{J}_4 \right)^{10}$ appear as zero columns because the first three diagonal elements of $\left(\mathbf{J}_4 \right)^{10}$ are vanishingly small. Again, any force components associated with self-equilibrated loading at the fixed end – in particular, that required to negate the Poisson's ratio effect present within the shearing force and bending moment principal vectors – will have decayed to insignificant levels at the free end.

From equations (5.12) and (5.14), one may now construct

$$\begin{bmatrix} \mathbf{d}(0) \\ \mathbf{F}(10) \end{bmatrix} = \begin{bmatrix} \mathbf{T}_1 \left(\mathbf{J}_1^{-1} \right)^{10} & \mathbf{T}_2 \\ \mathbf{T}_3 & \mathbf{T}_4 \left(\mathbf{J}_4 \right)^{10} \end{bmatrix} \begin{bmatrix} C_{1,10} & C_{2,10} & C_{3,10} & C_{4,0} & \cdots & C_{12,0} \end{bmatrix}^{\mathrm{T}}, \tag{5.15}$$

and hence the unknown column vector of mixed participation coefficients is given by

$$\begin{bmatrix} C_{1,10} & C_{2,10} & C_{3,10} & C_{4,0} & \cdots & C_{12,0} \end{bmatrix}^{\mathrm{T}} = \begin{bmatrix} \mathbf{T}_1 \left(\mathbf{J}_1^{-1} \right)^{10} & \mathbf{T}_2 \\ \mathbf{T}_3 & \mathbf{T}_4 \left(\mathbf{J}_4 \right)^{10} \end{bmatrix}^{-1} \begin{bmatrix} \mathbf{d}(0) \\ \mathbf{F}(10) \end{bmatrix}. \tag{5.16}$$

Substituting into equation (5.10) allows one to determine the remaining unknowns. The participation coefficients at the fixed end is

$$\mathbf{C}_0 = \begin{bmatrix} 0 & 0 & 0 & 0 & 0 & -353 & 0 & 0 & 347 & 3803 & 4500 & -500 \end{bmatrix}^{\mathrm{T}}$$

which agrees perfectly with the result obtained in [39].

The displacements at the free-end, $\mathbf{d}(10)$, and the reactions at the fixed-end, $\mathbf{F}(0)$ are then calculated from the first row of equation (5.9) and the second row of equation (5.8), respectively. Agreement with the FEA predictions reported in [39] is perfect, as seen in the first and second columns of Table 5.1.

5.4   Distributed loading

The above formalism is now extended to include the distributed loading shown in Figure 5.1, but without the intermediate support; extending equation (5.4) one may write

$$\mathbf{s}(10) = \mathbf{G}^{10}\mathbf{s}(0) - \left(\mathbf{G} + \mathbf{G}^2 + \cdots + \mathbf{G}^9 \right) \begin{bmatrix} \mathbf{0} \\ \mathbf{F}_{\mathrm{ext}} \end{bmatrix} \tag{5.17}$$

where $\mathbf{F}_{\mathrm{ext}} = \begin{bmatrix} 0 & -1000 & 0 & 0 & 0 & 0 \end{bmatrix}^{\mathrm{T}}$. The derivation of equation (5.17) is given in [39] and reproduced in Appendix D.2. An external load state-vector can be written as $\mathbf{s}_{\mathrm{ext}} = \begin{bmatrix} 0 & 0 & 0 & 0 & 0 & 0 & \mathbf{F}_{\mathrm{ext}}^{\mathrm{T}} \end{bmatrix}^{\mathrm{T}}$, and expressed in terms of the eigen- and principal vectors as $\mathbf{s}_{\mathrm{ext}} = \mathbf{T}\mathbf{C}_{\mathrm{ext}}$, and hence $\mathbf{C}_{\mathrm{ext}} = \mathbf{T}^{-1}\mathbf{s}_{\mathrm{ext}}$. Following the development in Section 5.3, equation (5.17) can now be written as

$$\mathbf{C}_{10} = \mathbf{J}^{10}\mathbf{C}_0 - \left(\mathbf{J} + \mathbf{J}^2 + \cdots + \mathbf{J}^9 \right)\mathbf{C}_{\mathrm{ext}}. \tag{5.18}$$

Pre-multiply equation (5.18) with $\mathbf{J}^{-10}$ and re-arrange to give

$$\mathbf{C}_0 = \mathbf{J}^{-10}\mathbf{C}_{10} + \left(\mathbf{J}^{-9} + \mathbf{J}^{-8} + \cdots + \mathbf{J}^{-1} \right)\mathbf{C}_{\mathrm{ext}}. \tag{5.19}$$

Again, in order to eliminate the eigenvalues greater than unity, mixed column vectors of participation coefficients are constructed by taking the (9×9) bottom-right partition of

(powers of) $\mathbf{J}$ in equation (5.18) and the (3×3) top-left partition of (powers of) $\mathbf{J}^{-1}$ in equation (5.19), giving

$$
\begin{bmatrix} C_{1,0} \\ C_{2,0} \\ C_{3,0} \\ C_{4,10} \\ C_{5,10} \\ \vdots \\ C_{12,10} \end{bmatrix} = \begin{bmatrix} \left(\mathbf{J}_1^{-1}\right)^{10} & \mathbf{0} \\ \mathbf{0} & \left(\mathbf{J}_4\right)^{10} \end{bmatrix} \begin{bmatrix} C_{1,10} \\ C_{2,10} \\ C_{3,10} \\ C_{4,0} \\ C_{5,0} \\ \vdots \\ C_{12,0} \end{bmatrix} + \begin{bmatrix} \sum_{n=1}^{9}\left(\mathbf{J}_1^{-1}\right)^{n} & \mathbf{0} \\ \mathbf{0} & -\sum_{n=1}^{9}\left(\mathbf{J}_4\right)^{n} \end{bmatrix} \mathbf{C}_{\text{ext}} .
\tag{5.20}
$$

Then, consider the boundary conditions. The displacement vector at the fixed-end is $\mathbf{d}(0)=\mathbf{0}$ and can be expressed as

$$
\mathbf{d}(0) = \begin{bmatrix} \mathbf{T}_1 & \mathbf{T}_2 \end{bmatrix} \mathbf{C}_0 = \mathbf{T}_1 \begin{bmatrix} C_{1,0} & C_{2,0} & C_{3,0} \end{bmatrix}^{\mathrm{T}} + \mathbf{T}_2 \begin{bmatrix} C_{4,0} & \cdots & C_{12,0} \end{bmatrix}^{\mathrm{T}} .
\tag{5.21}
$$

But, from equation (5.20),

$$
\begin{bmatrix} C_{1,0} \\ C_{2,0} \\ C_{3,0} \end{bmatrix} = \left(\mathbf{J}_1^{-1}\right)^{10} \begin{bmatrix} C_{1,10} \\ C_{2,10} \\ C_{3,10} \end{bmatrix} + \sum_{n=1}^{9}\left(\mathbf{J}_1^{-1}\right)^{n} \begin{bmatrix} C_{1,\text{ext}} \\ C_{2,\text{ext}} \\ C_{3,\text{ext}} \end{bmatrix} ;
$$

upon substitution into equation (5.21) and re-arranging, one gets

$$
\mathbf{d}(0) - \mathbf{T}_1 \sum_{n=1}^{9}\left(\mathbf{J}_1^{-1}\right)^{n} \begin{bmatrix} C_{1,\text{ext}} \\ C_{2,\text{ext}} \\ C_{3,\text{ext}} \end{bmatrix} = \mathbf{T}_1 \left(\mathbf{J}_1^{-1}\right)^{10} \begin{bmatrix} C_{1,10} \\ C_{2,10} \\ C_{3,10} \end{bmatrix} + \mathbf{T}_2 \begin{bmatrix} C_{4,0} \\ \vdots \\ C_{12,0} \end{bmatrix} .
\tag{5.22}
$$

At the free-end, the force vector can be expressed as

$$
\mathbf{F}(10) = \begin{bmatrix} \mathbf{T}_3 & \mathbf{T}_4 \end{bmatrix} \mathbf{C}_{10} = \mathbf{T}_3 \begin{bmatrix} C_{1,10} & C_{2,10} & C_{3,10} \end{bmatrix}^{\mathrm{T}} + \mathbf{T}_4 \begin{bmatrix} C_{4,10} & \cdots & C_{12,10} \end{bmatrix}^{\mathrm{T}} .
\tag{5.23}
$$

But, from equation (5.20),

$$
\begin{bmatrix} C_{4,10} \\ \vdots \\ C_{12,10} \end{bmatrix} = \left(\mathbf{J}_4\right)^{10} \begin{bmatrix} C_{4,0} \\ \vdots \\ C_{12,0} \end{bmatrix} - \sum_{n=1}^{9}\left(\mathbf{J}_4\right)^{n} \begin{bmatrix} C_{4,\text{ext}} \\ \vdots \\ C_{12,\text{ext}} \end{bmatrix} ;
$$

upon substitution into equation (5.23) and re-arranging, one gets

$$\mathbf{F}(10)+\mathbf{T}_4\sum_{n=1}^{9}\left(\mathbf{J}_4\right)^{n}\begin{bmatrix}C_{4,\text{ext}}\\\vdots\\C_{12,\text{ext}}\end{bmatrix}=\mathbf{T}_3\begin{bmatrix}C_{1,10}\\C_{2,10}\\C_{3,10}\end{bmatrix}+\mathbf{T}_4\left(\mathbf{J}_4\right)^{10}\begin{bmatrix}C_{4,0}\\\vdots\\C_{12,0}\end{bmatrix}. \tag{5.24}$$

From equations (5.22) and (5.24), one may now construct

$$\begin{bmatrix}\mathbf{d}(0)-\mathbf{T}_1\sum_{n=1}^{9}\left(\mathbf{J}_1^{-1}\right)^{n}\begin{bmatrix}C_{1,\text{ext}}\\C_{2,\text{ext}}\\C_{3,\text{ext}}\end{bmatrix}\\\mathbf{F}(10)+\mathbf{T}_4\sum_{n=1}^{9}\left(\mathbf{J}_4\right)^{n}\begin{bmatrix}C_{4,\text{ext}}\\\vdots\\C_{12,\text{ext}}\end{bmatrix}\end{bmatrix}=\begin{bmatrix}\mathbf{T}_1\left(\mathbf{J}_1^{-1}\right)^{10} & \mathbf{T}_2\\\mathbf{T}_3 & \mathbf{T}_4\left(\mathbf{J}_4\right)^{10}\end{bmatrix}\begin{bmatrix}C_{1,10}\\C_{2,10}\\C_{3,10}\\C_{4,0}\\\vdots\\C_{12,0}\end{bmatrix}, \tag{5.25}$$

and hence the unknown column vector of mixed participation coefficients is given by

$$\begin{bmatrix}C_{1,10}\\C_{2,10}\\C_{3,10}\\C_{4,0}\\\vdots\\C_{12,0}\end{bmatrix}=\begin{bmatrix}\mathbf{T}_1\left(\mathbf{J}_1^{-1}\right)^{10} & \mathbf{T}_2\\\mathbf{T}_3 & \mathbf{T}_4\left(\mathbf{J}_4\right)^{10}\end{bmatrix}^{-1}\begin{bmatrix}\mathbf{d}(0)-\mathbf{T}_1\sum_{n=1}^{9}\left(\mathbf{J}_1^{-1}\right)^{n}\begin{bmatrix}C_{1,\text{ext}}\\C_{2,\text{ext}}\\C_{3,\text{ext}}\end{bmatrix}\\\mathbf{F}(10)+\mathbf{T}_4\sum_{n=1}^{9}\left(\mathbf{J}_4\right)^{n}\begin{bmatrix}C_{4,\text{ext}}\\\vdots\\C_{12,\text{ext}}\end{bmatrix}\end{bmatrix}. \tag{5.26}$$

Substituting into equation (5.20) allows one to determine the remaining unknowns. The participation coefficients at the fixed-end are found to be

$$\mathbf{C}_0=\begin{bmatrix}-8.41 & 37.08 & 8.70 & -8.40 & 37.06 & -1932\end{bmatrix}$$
$$\begin{bmatrix}-0.0067 & 0 & 1906 & 26988 & 22500 & -5000\end{bmatrix}^{\text{T}}.$$

The participation coefficients $C_{7,0}$ and $C_{8,0}$ are found to be close to zero and zero, respectively, indicating that there is no contribution from the x-direction rigid-body displacement and tensile force vectors. In comparison to the result obtained in [39], this also shows that the present method is less susceptible to accumulated errors from the sum of powers of the Jordan canonical form. The displacement at the free-end, $\mathbf{d}(10)$, and the reactions at the fixed end, $\mathbf{F}(0)$ are given by $\begin{bmatrix}\mathbf{T}_1 & \mathbf{T}_2\end{bmatrix}\mathbf{C}_{10}$ and $\begin{bmatrix}\mathbf{T}_3 & \mathbf{T}_4\end{bmatrix}\mathbf{C}_0$, respectively. Again, agreement with FEA is near perfect.

5.5   Additional simple-support

Last, consider the addition of a simple-support at the 7th nodal cross-section, as shown in Figure 5.1. First define $\mathbf{F}_{\text{ext}}(7) = \begin{bmatrix} 0 & -1000 & 0 & 0 & 0 & F \end{bmatrix}^{\text{T}}$, where F is the unknown support reaction. For the complete structure one may write

$$\mathbf{s}(10) = \mathbf{G}^{10}\mathbf{s}(0) - \left(\mathbf{G} + \mathbf{G}^2 + \mathbf{G}^4 + \cdots + \mathbf{G}^9\right)\begin{bmatrix} \mathbf{0} \\ \mathbf{F}_{\text{ext}} \end{bmatrix} - \mathbf{G}^3 \begin{bmatrix} \mathbf{0} \\ \mathbf{F}_{\text{ext}}(7) \end{bmatrix}, \tag{5.27}$$

(note the absence of the $\mathbf{G}^3$ term in the summation) or in terms of the participation coefficients

$$\mathbf{C}_{10} = \mathbf{J}^{10}\mathbf{C}_0 - \left(\mathbf{J} + \mathbf{J}^2 + \mathbf{J}^4 + \cdots + \mathbf{J}^9\right)\mathbf{C}_{\text{ext}} - \mathbf{J}^3\mathbf{C}_{\text{ext}\,7}, \tag{5.28}$$

where $\mathbf{C}_{\text{ext}\,7} = \mathbf{T}^{-1}\begin{bmatrix} \mathbf{0} \\ \mathbf{F}_{\text{ext}}(7) \end{bmatrix}$. Pre-multiply equation (5.28) with $\mathbf{J}^{-10}$ and re-arrange to give

$$\mathbf{C}_0 = \mathbf{J}^{-10}\mathbf{C}_{10} + \left(\mathbf{J}^{-9} + \mathbf{J}^{-8} + \mathbf{J}^{-6} + \cdots + \mathbf{J}^{-1}\right)\mathbf{C}_{\text{ext}} + \mathbf{J}^{-7}\mathbf{C}_{\text{ext}\,7}. \tag{5.29}$$

Construct a mixed column vector of participation coefficients by taking the (9×9) bottom-right partition of (powers of) $\mathbf{J}$ in equation (5.28) and the (3×3) top-left partition of (powers of) $\mathbf{J}^{-1}$ in equation (5.29), to give

$$\begin{bmatrix} C_{1,0} \\ C_{2,0} \\ C_{3,0} \\ C_{4,10} \\ \vdots \\ C_{12,10} \end{bmatrix} = \begin{bmatrix} \left(\mathbf{J}_1^{-1}\right)^{10} & \mathbf{0} \\ \mathbf{0} & \left(\mathbf{J}_4\right)^{10} \end{bmatrix} \begin{bmatrix} C_{1,10} \\ C_{2,10} \\ C_{3,10} \\ C_{4,0} \\ \vdots \\ C_{12,0} \end{bmatrix} + \begin{bmatrix} \left[\sum_{n=1}^{6}\left(\mathbf{J}_1^{-1}\right)^n + \sum_{n=8}^{9}\left(\mathbf{J}_1^{-1}\right)^n \right] & \mathbf{0} \\ \mathbf{0} & -\sum_{n=1,2,4,\cdots}^{9}\left(\mathbf{J}_4\right)^n \end{bmatrix}\mathbf{C}_{\text{ext}}$$

$$+ \begin{bmatrix} \left(\mathbf{J}_1^{-1}\right)^7 & \mathbf{0} \\ \mathbf{0} & -\left(\mathbf{J}_4\right)^3 \end{bmatrix}\mathbf{C}_{\text{ext}\,7} \tag{5.30}$$

Now consider the boundary conditions: the displacement vector at the fixed-end is $\mathbf{d}(0) = \mathbf{0}$ and can be expressed as

$$\mathbf{d}(0) = \begin{bmatrix} \mathbf{T}_1 & \mathbf{T}_2 \end{bmatrix}\mathbf{C}_0 = \mathbf{T}_1 \begin{bmatrix} C_{1,0} & C_{2,0} & C_{3,0} \end{bmatrix}^{\text{T}} + \mathbf{T}_2 \begin{bmatrix} C_{4,0} & \cdots & C_{12,0} \end{bmatrix}^{\text{T}}. \tag{5.31}$$

But, from equation (5.30),

$$\begin{bmatrix} C_{1,0} \\ C_{2,0} \\ C_{3,0} \end{bmatrix} = \left(\mathbf{J}_1^{-1}\right)^{10} \begin{bmatrix} C_{1,10} \\ C_{2,10} \\ C_{3,10} \end{bmatrix} + \left[\sum_{n=1}^{6} \left(\mathbf{J}_1^{-1}\right)^n + \sum_{n=8}^{9} \left(\mathbf{J}_1^{-1}\right)^n \right] \begin{bmatrix} C_{1,\text{ext}} \\ C_{2,\text{ext}} \\ C_{3,\text{ext}} \end{bmatrix} + \left(\mathbf{J}_1^{-1}\right)^7 \begin{bmatrix} C_{1,\text{ext 7}} \\ C_{2,\text{ext 7}} \\ C_{3,\text{ext 7}} \end{bmatrix};$$

substitute into equation (5.31) and re-arrange to obtain

$$\mathbf{d}(0) - \mathbf{T}_1 \left[\sum_{n=1}^{6} \left(\mathbf{J}_1^{-1}\right)^n + \sum_{n=8}^{9} \left(\mathbf{J}_1^{-1}\right)^n \right] \begin{bmatrix} C_{1,\text{ext}} \\ C_{2,\text{ext}} \\ C_{3,\text{ext}} \end{bmatrix} - \mathbf{T}_1 \left(\mathbf{J}_1^{-1}\right)^7 \begin{bmatrix} C_{1,\text{ext 7}} \\ C_{2,\text{ext 7}} \\ C_{3,\text{ext 7}} \end{bmatrix} = \mathbf{T}_1 \left(\mathbf{J}_1^{-1}\right)^{10} \begin{bmatrix} C_{1,10} \\ C_{2,10} \\ C_{3,10} \end{bmatrix} + \mathbf{T}_2 \begin{bmatrix} C_{4,0} \\ \vdots \\ C_{12,0} \end{bmatrix}.$$

$$(5.32)$$

At the free-end, the force vector can be expressed as

$$\mathbf{F}(10) = \begin{bmatrix} \mathbf{T}_3 & \mathbf{T}_4 \end{bmatrix} \mathbf{C}_{10} = \mathbf{T}_3 \begin{bmatrix} C_{1,10} & C_{2,10} & C_{3,10} \end{bmatrix}^{\mathrm{T}} + \mathbf{T}_4 \begin{bmatrix} C_{4,10} & \cdots & C_{12,10} \end{bmatrix}^{\mathrm{T}}. \tag{5.33}$$

But, from equation (5.30),

$$\begin{bmatrix} C_{4,10} \\ \vdots \\ C_{12,10} \end{bmatrix} = \left(\mathbf{J}_4\right)^{10} \begin{bmatrix} C_{4,0} \\ \vdots \\ C_{12,0} \end{bmatrix} - \sum_{n=1,2,4,\cdots}^{9} \left(\mathbf{J}_4\right)^n \begin{bmatrix} C_{4,\text{ext}} \\ \vdots \\ C_{12,\text{ext}} \end{bmatrix} - \left(\mathbf{J}_4\right)^3 \begin{bmatrix} C_{4,\text{ext 7}} \\ \vdots \\ C_{12,\text{ext 7}} \end{bmatrix};$$

substitute into equation (5.33) and re-arrange to get

$$\mathbf{F}(10) + \mathbf{T}_4 \sum_{n=1,2,4,\cdots}^{9} \left(\mathbf{J}_4\right)^n \begin{bmatrix} C_{4,\text{ext}} \\ \vdots \\ C_{12,\text{ext}} \end{bmatrix} + \mathbf{T}_4 \left(\mathbf{J}_4\right)^3 \begin{bmatrix} C_{4,\text{ext 7}} \\ \vdots \\ C_{12,\text{ext 7}} \end{bmatrix} = \mathbf{T}_3 \begin{bmatrix} C_{1,10} \\ C_{2,10} \\ C_{3,10} \end{bmatrix} + \mathbf{T}_4 \left(\mathbf{J}_4\right)^{10} \begin{bmatrix} C_{4,0} \\ \vdots \\ C_{12,0} \end{bmatrix}. \tag{5.34}$$

From equations (5.32) and (5.34), one may now construct

$$\begin{bmatrix} \mathbf{d}(0) - \mathbf{T}_1 \left[\sum_{n=1}^{6} \left(\mathbf{J}_1^{-1}\right)^n + \sum_{n=8}^{9} \left(\mathbf{J}_1^{-1}\right)^n \right] \begin{bmatrix} C_{1,\text{ext}} \\ C_{2,\text{ext}} \\ C_{3,\text{ext}} \end{bmatrix} - \mathbf{T}_1 \left(\mathbf{J}_1^{-1}\right)^7 \begin{bmatrix} C_{1,\text{ext 7}} \\ C_{2,\text{ext 7}} \\ C_{3,\text{ext 7}} \end{bmatrix} \\ \mathbf{F}(10) + \mathbf{T}_4 \sum_{n=1,2,4,\cdots}^{9} \left(\mathbf{J}_4\right)^n \begin{bmatrix} C_{4,\text{ext}} \\ \vdots \\ C_{12,\text{ext}} \end{bmatrix} + \mathbf{T}_4 \left(\mathbf{J}_4\right)^3 \begin{bmatrix} C_{4,\text{ext 7}} \\ \vdots \\ C_{12,\text{ext 7}} \end{bmatrix} \end{bmatrix} = \begin{bmatrix} \mathbf{T}_1 \left(\mathbf{J}_1^{-1}\right)^{10} & \mathbf{T}_2 \\ \mathbf{T}_3 & \mathbf{T}_4 \left(\mathbf{J}_4\right)^{10} \end{bmatrix} \begin{bmatrix} C_{1,10} \\ C_{2,10} \\ C_{3,10} \\ C_{4,0} \\ \vdots \\ C_{12,0} \end{bmatrix}$$

$$(5.35)$$

and hence the unknown column vector of mixed participation coefficients (in terms of F) is given by

$$\begin{bmatrix} C_{1,10} \\ C_{2,10} \\ C_{3,10} \\ C_{4,0} \\ \vdots \\ C_{12,0} \end{bmatrix} = \begin{bmatrix} \mathbf{T}_1\left(\mathbf{J}_1^{-1}\right)^{10} & \mathbf{T}_2 \\ \mathbf{T}_3 & \mathbf{T}_4\left(\mathbf{J}_4\right)^{10} \end{bmatrix}^{-1} \begin{bmatrix} \mathbf{d}(0) - \mathbf{T}_1\left[\sum_{n=1}^{6}\left(\mathbf{J}_1^{-1}\right)^n + \sum_{n=8}^{9}\left(\mathbf{J}_1^{-1}\right)^n\right]\begin{bmatrix} C_{1,\text{ext}} \\ C_{2,\text{ext}} \\ C_{3,\text{ext}} \end{bmatrix} - \mathbf{T}_1\left(\mathbf{J}_1^{-1}\right)^{7}\begin{bmatrix} C_{1,\text{ext}\,7} \\ C_{2,\text{ext}\,7} \\ C_{3,\text{ext}\,7} \end{bmatrix} \\ \mathbf{F}(10) + \mathbf{T}_4\sum_{n=1,2,4,\cdots}^{9}\left(\mathbf{J}_4\right)^n\begin{bmatrix} C_{4,\text{ext}} \\ \vdots \\ C_{12,\text{ext}} \end{bmatrix} + \mathbf{T}_4\left(\mathbf{J}_4\right)^{3}\begin{bmatrix} C_{4,\text{ext}\,7} \\ \vdots \\ C_{12,\text{ext}\,7} \end{bmatrix} \end{bmatrix}.$$

$$(5.36)$$

Substituting into equation (5.30) allows one to determine the remaining boundary participation coefficients, that is $C_{1,0}, C_{2,0}, C_{3,0}, C_{4,10}, C_{5,10}, \cdots, C_{12,10}$.

At the support, the participation coefficients can be expressed in terms of $\mathbf{C}_0$ or $\mathbf{C}_{10}$ as

$$\mathbf{C}_7 = \mathbf{J}^7\mathbf{C}_0 - \left(\mathbf{J} + \mathbf{J}^2 + \cdots + \mathbf{J}^6\right)\mathbf{C}_{\text{ext}},$$

$$(5.37)$$

$$\mathbf{C}_7 = \mathbf{J}^{-3}\mathbf{C}_{10} + \left(\mathbf{J}^{-1} + \mathbf{J}^{-2}\right)\mathbf{C}_{\text{ext}} + \mathbf{C}_{\text{ext}\,7},$$

$$(5.38)$$

respectively. From equations (5.37) and (5.38), one obtains

$$\begin{bmatrix} C_{4,7} \\ \vdots \\ C_{12,7} \end{bmatrix} = \mathbf{J}_4^7\begin{bmatrix} C_{4,0} \\ \vdots \\ C_{12,0} \end{bmatrix} - \left(\mathbf{J}_4 + \mathbf{J}_4^2 + \cdots + \mathbf{J}_4^6\right)\begin{bmatrix} C_{4,\text{ext}} \\ \vdots \\ C_{12,\text{ext}} \end{bmatrix},$$

$$(5.39)$$

$$\begin{bmatrix} C_{1,7} \\ C_{2,7} \\ C_{3,7} \end{bmatrix} = \mathbf{J}_1^{-3}\begin{bmatrix} C_{1,10} \\ C_{2,10} \\ C_{3,10} \end{bmatrix} + \left(\mathbf{J}_1^{-1} + \mathbf{J}_1^{-2}\right)\begin{bmatrix} C_{1,\text{ext}} \\ C_{2,\text{ext}} \\ C_{3,\text{ext}} \end{bmatrix}.$$

$$(5.40)$$

(Note that equation (5.40) is just the first three rows of equation (5.38), from which the $\mathbf{C}_{\text{ext}\,7}$ contribution is zero.) The displacement vector at the support is then

$$\mathbf{d}(7) = \begin{bmatrix} \mathbf{T}_1 & \mathbf{T}_2 \end{bmatrix}\mathbf{C}_7 = \mathbf{T}_1\begin{bmatrix} C_{1,7} & C_{2,7} & C_{3,7} \end{bmatrix}^{\mathrm{T}} + \mathbf{T}_2\begin{bmatrix} C_{4,7} & \cdots & C_{12,7} \end{bmatrix}^{\mathrm{T}};$$

$$(5.41)$$

upon substitution of equations (5.39) and (5.40) into (5.41), the y-component of the displacement at the support is calculated as $31.8F - 232527$, and for this to be equal to zero requires $F = 7312.1\,\text{N}$. With F now known, the displacement at the free-end $\mathbf{d}(10)$, and

the reactions at the fixed-end $\mathbf{F}(0)$, are calculated from $\mathbf{d}(10) = \begin{bmatrix} \mathbf{T}_1 & \mathbf{T}_2 \end{bmatrix} \mathbf{C}_{10}$ and $\mathbf{F}(0) = \begin{bmatrix} \mathbf{T}_3 & \mathbf{T}_4 \end{bmatrix} \mathbf{C}_0$, respectively. Once again agreement with FEA is near perfect.

	End loading only		Distributed loading		Distributed loading with intermediate support	
	TMM	FEA	TMM	FEA	TMM	FEA
$\mathbf{d}(10)$	1.1808	1.1808	4.5602	4.5602	0.3861	0.3862
	−8.5423	−8.5423	−37.136	−37.136	−1.4536	−1.4536
	−0.0039971	−0.0039971	**0.035064**	**0.035066**	0.065226	0.065229
	−8.4786	−8.4786	−37.075	−37.075	−1.39454	−1.3946
	−1.1648	−1.1648	−4.4838	−4.4838	−0.25340	−0.25340
	−8.4609	−8.4609	−37.05749	−37.0578	−1.3787	−1.3787
$\mathbf{F}(0)$	5000.002	5000.002	27557	27557	1965.1	1965.1
	−587.45	**−587.45**	−4269.7	−4269.7	−747.89	−747.89
	0.0036568	0.0036568	−114.68	−114.67	−115.05	−115.03
	174.90	174.90	−1460.8	−1460.8	−1192.0	−1192.0
	−4999.998	−4999.998	−27,443	−27,443	−1850.0	−1850.0
	−587.45	−587.45	−4269.6	−4269.6	−748.02	−748.02

Table 5.1 Free-end nodal displacement $\mathbf{d}(10)$, and fixed-end nodal force $\mathbf{F}(0)$ predictions under various loading conditions reproduced from reference [39]. TMM denotes transfer matrix, FEA denotes finite element analysis. Plus and minus sign errors in [39] are corrected and shown bold.

5.6   Conclusions

The Riccati transfer matrix method has previously been shown to provide a numerically stable solution to the two point boundary problem of a repetitive structure, fully fixed at one end and loaded at the other, and with distributed loading and intermediate support.   An alternative numerically stable approach has been developed, which is more direct and transparent, and is applied to the same examples.   Agreement with FEA predictions is near perfect.

Chapter 6:   Summary, Conclusions and Future Work

In this thesis, wave propagation in a one-dimensional (beam-like) repetitive pin-jointed structure with point masses located at nodal cross-sections is analysed with the aim of providing a simple physical explanation for the existence of frequency-propagation zones and decay zones. The thesis began by reviewing the literature on repetitive structures with the focus to identify different analytical techniques employed to analyse such structures. Transfer matrix method is found to be the best technique to be employed in this thesis due to its simple implementation and versatility in solving various static and dynamic problems. Detailed review of the transfer matrix method shows that different forms of transfer matrix have been introduced but relations between them have not been previously established. The transfer matrix method is also known for its numerical instability; solutions to most of the ill-conditioning problems have been proposed but a few issues remain to be addressed.

Transfer matrix eigenanalysis has been employed to quantify the effect of self-equilibrating load in the static case, as anticipated by the Saint-Venant's principle, however the method has not been extended to the dynamic case. We believe that extension of the method to the dynamic case could provide an answer to our research problem, and subsequently open a path towards quantifying the effect of dynamic Saint-Venant's principle. In general, the transfer matrix eigenanalysis involves two important steps: first, formulation of the transfer matrix, and second, employment of the Bloch's theorem which leads to frequency-dependent eigenvalue problem whose solution is a dispersion relation, i.e. frequency against decay rate and phase constant. Conventionally, the relation is plotted on a two-dimensional diagram, however we found that such plotting is disjointed as the decay rate and phase constant are plotted against frequency on separate axes. Instead, a three-dimensional plot offers a better graphical representation as it allows all branches to appear in a single graph, hence facilitate the analysis, particularly in identifying detailed evolution of the dispersion curve branches as frequency increases.

An important principle found to be useful is phase closure which states that for a standing wave, the total phase change for a complete circumnavigation of the structure is an integer multiple of 2π. The phase closure principle is first employed in the formulation of the determinantal equation to find the natural frequencies of finite structures. At first sight, the principle is seemingly relatable to the method of direct application of boundary conditions on the transfer matrix, the latter leads to two-point boundary value problems (TPBVP).

However, attempts to apply phase closure onto TPBVP have not been successful. Later in this work, phase closure appears again in the study of cut-on/off frequencies of wave modes, this time it seems to occur across and along the characteristic dimension of a unit cell.

Transfer matrix analysis of the energy and power flow associated with propagating and decaying waves have been presented by many but a few aspects remain to be explored such as the peculiar phenomena of anomalous dispersion, condition for maximum group velocity and the power flow associated with two interacting attenuating waves. An exposition of the basic energy equations are reviewed in order to understand the mathematical techniques involved and to find simpler techniques that could be use.

Finally, TPBVP under static case is reviewed with the objective to find a simpler numerically stable solution to the problem. This idea is pursued after an attempt to apply phase closure to the TPBVP failed because the force vectors associated with rigid body translations and rotation reduced to become columns of zero vector, hence the reflection matrix cannot be computed correctly through inversion of singular partitions of transmission matrix. Also, the diagonal matrix of eigenvalues under dynamic case becomes Jordan canonical block matrix under static case; the latter cannot be simply partitioned into blocks of 'eigenvalues' that represent rightward and leftward decay of self-equilibrating loads or transmission of the coupled principle vectors.

In Chapter 2, two forms of dynamic transfer matrix are derived for the model structure: the displacement-force transfer matrix $\mathbf{G}$, and the displacement-displacement transfer matrix, $\mathbf{H}$. Wave propagation through the structure is described by the eigenvalues of either transfer matrix, expressed as $\lambda = \exp(\delta + \mathrm{i}\varphi)$, where the real part δ is the decay constant, and φ is the phase constant as one moves from one cross-section to the next. The emphasis of this chapter has been the relationship between $\mathbf{G}$ and $\mathbf{H}$, and their respective properties, and also between their respective eigenvectors. Similarity matrices are introduced to relate $\mathbf{G}$ and $\mathbf{H}$, together with their respective metrics. Symplectic orthogonality relationships for the eigenvectors of both $\mathbf{G}$ and $\mathbf{H}$ are derived, together with relationships between their respective sets of eigenvectors; this allows an arbitrary disturbance to be resolved into propagating and decaying waves. Both $\mathbf{G}$ and $\mathbf{H}$ can be employed to determine new expressions for the group velocity, but that which employs $\mathbf{H}$ is the more succinct.

For structures of finite length, the determination of natural frequencies of standing waves requires the application of boundary conditions, normally in terms of zero force (free-end), and/or zero displacement (fixed-end); accordingly, the displacement-force transfer matrix $\mathbf{G}$

is the more natural choice. Direct application of boundary conditions leads to very succinct frequency determinants based on partitions of $\mathbf{G}^N$. This approach is suitable for short beam-like structures, where the number of cells N is small; however, since some of the eigenvalues are greater than unity, it becomes numerically unstable when N is large. The displacement-displacement transfer matrix $\mathbf{H}$ approach does not feature a force vector, so this needs to be introduced into the formulation, leading to less succinct frequency determinants; the exception is for the fixed-fixed beam. Again, this approach is numerically unstable when N is large. Instead, phase closure has been developed in terms of reflection matrices, and features only those eigenvalues less than, or equal to unity; this ensures numerical stability whatever the magnitude of N. Both these approaches require the search for zero-values of a determinant; this can be done by evaluating and plotting the determinant over a frequency range, and noting where the value changes sign. For the direct method, the determinant is real, whereas for phase closure, the determinant is complex, so both real and imaginary parts must be zero simultaneously.

The phase closure approach is not entirely free from numerical instability. Numerical studies on the model framework shows that partitions of the eigenvector matrix $\mathbf{V}_{R,F}$ and $\mathbf{V}_{L,F}$ can become singular when two branches cross and when a column is reduced to zero (at certain frequencies). As a result, the natural frequency determinantal equation yields large values. A real wave vector approach has been proposed by Luongo and Romeo [71] to overcome this ill-conditioning problem; the approach requires the eigenvectors and the eigenvalues matrices to be re-arranged, and the real and imaginary parts to be placed in separate columns, the resulting determinantal equation would give real values only. So far, the approach has not been demonstrated on multi-coupled structures. Attempts to implement this approach on the model framework have failed; the problem arises as one separate the complex number into its real and imaginary parts, the number of columns increases but the number of rows remain the same (the matrices are no longer square), so partitioning and inversion of rectangular matrices become an issue.

Chapter 3 describes an in-depth study of the dispersion diagram, in novel form, for the model repetitive structure, concentrating on wave propagation and decay characteristics. Propagation and decay characteristics of different modes are described in relation to the corresponding eigenvalues λ and their properties. The eigenvalues, expressed as $\exp(\delta + \mathrm{i}\varphi)$ where δ is decay rate and φ is phase constant, are plotted as a function of frequency (squared) in a three-dimensional dispersion diagram. The three axes are δ, φ

and ω^2. Such a representation has the advantage of clearly depicting the evolution of the dispersion branches, in particular where both the decay rate and phase constant change with frequency. The eigenvalues $\lambda = 1$ and $\lambda = -1$ are of particular significance and considered in detail as they are associated with the cut-on and cut-off frequencies. The need to be specific in the description of cut-on and cut-off frequencies, marking the start and finish of propagation zones with increasing frequency, is emphasised. The evolution of the different waves along each branch is described in detail. The existence of propagation zones is explained in terms of phase closure (implying a natural frequency) over the cross-section at the cut-on frequency, and phase closure over the smallest axial unit – the repeating cell – at the cut-off frequency; these zones can therefore be regarded as extended resonances. For example, a normal dispersion has a cut-on when one half-wavelength can be accommodated within some characteristic transverse dimension of the waveguide (that is a phase closure over the cross-section), while a cut-off occurs when one-half wavelength occupies the length of the repeating cell (that is a phase closure over a single cell in the axial direction). In the discrete model, the maximum number of wavelengths that can be accommodated over a unit cell is one half, which coincides with $\lambda = -1$; thus, the existence of a cut-off frequency is a consequence of the discrete nature of the model in the axial direction. On the other hand, an anomalous dispersion branch at cut-on displays phase closure over the cross-section and over the length of a single cell. The criterion for propagation, or attenuation, is not determined by the frequency *per se*, rather by the associated wavelength, so the present work goes some way towards answering Mead's question and the establishment of a dynamic SVP.

The propagating branches have an invariant property known as the Krein signature. Propagating normal and anomalous branches have opposite signatures; on a unit circle the two will collide and this is known as Krein collision. Wave interaction between branches displaying normal and anomalous dispersion is explained in terms of the Krein signature, and leads to attenuating waves. The Krein signature for propagating branches is found to be intimately related to the equation for the power flow. For evanescent branch, there is no power flow, therefore a new expression for the Krein signature is introduced. Three distinct types of decaying waves have been identified, namely, monotonic evanescent, oscillatory evanescent and attenuating. Monotonic evanescent and oscillatory evanescent generally occur at frequencies below cut-on and above cut-off, respectively; the exception is for the single anomalous branch, for which the situation is reversed. For the model structure, attenuating decay occurs as a result of interaction between asymmetric branches which display normal and anomalous dispersions, and results in the formation of loops on the

dispersion diagram. The latter can be explained in terms of a Krein collision. Some preliminary comments on the cause of anomalous dispersion are made. The very existence of a static decay mode having a negative eigenvalue appears to presage a propagation branch which exhibits anomalous dispersion.

In Chapter 4, energetics of the different wave types under the new wave type taxonomy is investigated. Equations for energy and power are derived in terms of eigenvectors of **G** and **H**. Numerical results for axial phase velocity and group velocity of the different modes show some familiar and some peculiar phenomena. Condition for maximum group velocity is shown, but physical interpretation is yet to be established. Numerical study on anomalous dispersion reveals that pin-jointed structure which allows negative eigenvalue to occur under static self-equilibrating load will presage anomalous dispersion under dynamic condition; the minimum size of the transfer matrix is (4×4). Nonetheless, for attenuating waves to occur the minimum size of the transfer matrix is (8×8).

Time-averaged work done, energy and power associated with evanescent, attenuating and propagating waves are studied numerically by considering the sectional nodal components contribution. Work is done by evanescent and attenuating waves at each cross-section over one period and no transfer of energy occurs across the cell boundaries. Work done, kinetic energy and potential energy are bounded within each cross-section. However, on time-average, no work is done by propagating wave at each cross-section and energy is transferred from one cell to the next at a speed given by the group velocity. At the cut-on and cut-off frequencies, there is no work done and no energy transfer occurs across the cell boundaries.

The normal and anomalous dispersions are studied by considering the cross-sectional nodal contribution. In a structure which has diagonal connections, backward power flow can occur as a result of opposing y-displacement at the nodal cross-section that leads to negative decay eigenvalue under static case. For both dispersions, it is possible that both forward and backward power components to appear at the cross-section and at the same time; in such situation, the forward power components are dominant in the case of normal dispersion while backward power components are dominant in the case of anomalous dispersion.

Two interacting attenuating waves that decay in opposite directions is found to transfer energy. The energy flow in two interacting attenuating waves that are formed by oscillatory evanescent waves can change from being backward to forward. This is different from a propagating wave as it could only remain to be normal, or anomalous, between its cut-on and cut-off frequencies.

Chapter 5 is concerned with elastostatic transfer matrix analysis of the model structure where a two point boundary value problem has been considered. It is known that the solution of the problem is numerically stable when one employs the Riccati transfer matrix method. However, an alternative numerically stable transfer matrix method, which is more direct and transparent, is developed for the model structure fixed at one end, and subject to point-wise distributed loading, with and without an intermediate support. This is achieved by constructing mixed column vectors of participation coefficients, so that spatial evolution involves multiplication by powers of the eigenvalues which are less than or equal to unity. Agreement with FEA predictions is near perfect.

This work has identified a number of areas that require further study. In Section 2.4, it is found numerically that the minimum size of the transfer matrix for complex non-unity eigenvalues to occur is (8×8). Theoretical proof to that finding is yet to be given. In Section 2.7, the phase closure (or complex wave vector) approach to determine natural frequencies is found to suffer from ill-conditioning at certain frequencies. Luongo and Romeo [71] have proposed real wave vector approach to solve this problem but early attempts to implement the approach on the model structure have failed because partitions of the resulting real rectangular eigenvector matrix cannot be inverted correctly as required by the proposed method. It is likely that additional steps to the proposed real wave vector approach are required for multi-coupled structure.

In Section 3.3, equation (3.3) is given; the equation relates the eigenvalue to the displacement vectors and partitions of the stiffness matrix. It is stated that for real and complex non-unity eigenvalues, the plus-minus sign corresponds to the reciprocal eigenvalue pair. However, for complex unity eigenvalues, the plus and the minus sign give the correct eigenvalues, but they are not reciprocal. An explanation for why this happen should be given.

In Section 3.7, we suspect that the QR algorithm employed by MATLAB is not able to compute the eigenvectors accurately at the point where the branches cross. In theoretical physics, such problem could be resolved through renormalisation, but such an approach has not been pursued. So, further study is required to find out how one can compute the eigenvectors accurately in the case of repeated eigenvalues.

In Section 3.9, detailed account of loops 1,6 and 3,6 is given but simple physical reasons that explain why the loops (and attenuating wave) appear as such has not been found.

In Section 3.11, it is found that branches associated with symmetric waves never cross each other while branches associated with asymmetric waves collide (leading to formation of

loops); also, branches associated with symmetric and asymmetric waves can cross each other, but without formation of loops. These observations are not true for all structures. Detailed study of the dispersion curves for the structure shown in Figure 4.8(d) reveals that the symmetric normal extensional mode collides with symmetric anomalous breathing mode (leading to formation of loops), and symmetric normal extensional mode never cross asymmetric normal shear mode. Therefore, symmetricity of mode is not the determining factor for mode crossing nor collision, rather its signature. Theoretical proof of this, as well as relation between mode symmetricity and signature, has not been established.

In Section 4.4, an equation that must be satisfied at maximum group velocity is given. However, physical (or graphical) interpretation to the equation that clearly explain the condition for maximum group velocity has not been given.

In Section 4.5, it is found that two attenuating waves emanating from the same cross-section can interact to transfer energy. A case where two decaying waves emanating from a distance apart has not been considered.

So far, the analysis is based on the model framework which has 6 cross-sectional degrees of freedom. More peculiar phenomena and wave types could be revealed if a framework with more degrees of freedom is analysed. For example, it would be interesting to find out whether a propagating branch can change from being normal to being anomalous, or *vice versa*, and whether two loops can occur simultaneously and interact to form more loops. The model framework can also be modified to have a tapering end of power-law profile. It is known that a wave that travel towards such an end could become trapped and never get reflected back—a phenomenon dubbed as acoustical 'black hole' in analogy to astrophysical black hole [108].

Appendix A

A.1 Matrices $\mathbf{K}_{LL}$, $\mathbf{K}_{LR}$, $\mathbf{K}_{RL}$ and $\mathbf{K}_{RR}$

In Section 2.2, the equations of motion for a unit cell of the example framework are given in the matrix form. The explicit expressions for the matrices $\mathbf{K}_{LL}$, $\mathbf{K}_{RR}$ and $\mathbf{K}_{LR}$ in the equations are as follows:

$$\mathbf{K}_{LL} = k \begin{bmatrix} 1+1/(4\sqrt{2}) & -1/(4\sqrt{2}) & 0 & 0 & 0 & 0 \\ -1/(4\sqrt{2}) & 1/2+1/(4\sqrt{2}) & 0 & -1/2 & 0 & 0 \\ 0 & 0 & 1+1/(2\sqrt{2}) & 0 & 0 & 0 \\ 0 & -1/2 & 0 & 1+1/(2\sqrt{2}) & 0 & -1/2 \\ 0 & 0 & 0 & 0 & 1+1/(4\sqrt{2}) & 1/(4\sqrt{2}) \\ 0 & 0 & 0 & -1/2 & 1/(4\sqrt{2}) & 1/2+1/(4\sqrt{2}) \end{bmatrix}$$

$$\mathbf{K}_{RR} = k \begin{bmatrix} 1+1/(4\sqrt{2}) & 1/(4\sqrt{2}) & 0 & 0 & 0 & 0 \\ 1/(4\sqrt{2}) & 1/2+1/(4\sqrt{2}) & 0 & -1/2 & 0 & 0 \\ 0 & 0 & 1+1/(2\sqrt{2}) & 0 & 0 & 0 \\ 0 & -1/2 & 0 & 1+1/(2\sqrt{2}) & 0 & -1/2 \\ 0 & 0 & 0 & 0 & 1+1/(4\sqrt{2}) & -1/(4\sqrt{2}) \\ 0 & 0 & 0 & -1/2 & -1/(4\sqrt{2}) & 1/2+1/(4\sqrt{2}) \end{bmatrix}$$

$$\mathbf{K}_{LR} = k \begin{bmatrix} -1 & 0 & -1/(4\sqrt{2}) & 1/(4\sqrt{2}) & 0 & 0 \\ 0 & 0 & 1/(4\sqrt{2}) & -1/(4\sqrt{2}) & 0 & 0 \\ -1/(4\sqrt{2}) & -1/(4\sqrt{2}) & -1 & 0 & -1/(4\sqrt{2}) & 1/(4\sqrt{2}) \\ -1/(4\sqrt{2}) & -1/(4\sqrt{2}) & 0 & 0 & 1/(4\sqrt{2}) & -1/(4\sqrt{2}) \\ 0 & 0 & -1/(4\sqrt{2}) & -1/(4\sqrt{2}) & -1 & 0 \\ 0 & 0 & -1/(4\sqrt{2}) & -1/(4\sqrt{2}) & 0 & 0 \end{bmatrix}$$

where $k = EA/L$ and $\mathbf{K}_{RL} = \mathbf{K}_{LR}^{T}$. Note that $\mathbf{K}_{LL}$ and $\mathbf{K}_{RR}$ are symmetric, but $\mathbf{K}_{LR}$ is not.

A.2   Formula for block matrix inversion

If $\mathbf{A}$, $\mathbf{B}$, $\mathbf{C}$ and $\mathbf{D}$ are an $(n \times n)$, an $(n \times m)$, an $(m \times n)$ and an $(m \times m)$ matrix, respectively, then

$$\begin{bmatrix} \mathbf{A} & \mathbf{B} \\ \mathbf{C} & \mathbf{D} \end{bmatrix}^{-1} = \begin{bmatrix} \left(\mathbf{A} - \mathbf{B}\mathbf{D}^{-1}\mathbf{C}\right)^{-1} & -\mathbf{A}^{-1}\mathbf{B}\left(\mathbf{D} - \mathbf{C}\mathbf{A}^{-1}\mathbf{B}\right)^{-1} \\ -\mathbf{D}^{-1}\mathbf{C}\left(\mathbf{A} - \mathbf{B}\mathbf{D}^{-1}\mathbf{C}\right)^{-1} & \left(\mathbf{D} - \mathbf{C}\mathbf{A}^{-1}\mathbf{B}\right)^{-1} \end{bmatrix}$$

provided $|\mathbf{A}| \neq 0$ and $|\mathbf{D} - \mathbf{C}\mathbf{A}^{-1}\mathbf{B}| \neq 0$ [109]. When $|\mathbf{A}| = 0$, as with similarity matrix $\mathbf{N}$, one may use the Schur complement to give

$$\begin{bmatrix} \mathbf{A} & \mathbf{B} \\ \mathbf{C} & \mathbf{D} \end{bmatrix}^{-1} = \begin{bmatrix} \left(\mathbf{A} - \mathbf{B}\mathbf{D}^{-1}\mathbf{C}\right)^{-1} & -\left(\mathbf{A} - \mathbf{B}\mathbf{D}^{-1}\mathbf{C}\right)^{-1}\mathbf{B}\mathbf{D}^{-1} \\ -\mathbf{D}^{-1}\mathbf{C}\left(\mathbf{A} - \mathbf{B}\mathbf{D}^{-1}\mathbf{C}\right)^{-1} & \mathbf{D}^{-1} + \mathbf{D}^{-1}\mathbf{C}\left(\mathbf{A} - \mathbf{B}\mathbf{D}^{-1}\mathbf{C}\right)^{-1}\mathbf{B}\mathbf{D}^{-1} \end{bmatrix}.$$

A.3   Physical interpretation of symplectic orthogonality relation

Consider a cell as shown in Figure 2.2(a). The cell is subjected to two different load systems denoted by subscripts 1 and 2. The Betti-Maxwell reciprocal theorem requires that the work done by forces $\mathbf{F}_1$ acting through displacements $\mathbf{D}_2$ is equal to the work done by forces $\mathbf{F}_2$ acting through displacements $\mathbf{D}_1$; however, we specialise load system 1 as the eigenvector $\mathbf{V}_i$ associated with eigenvalue λ_i, and load system 2 as the eigenvector $\mathbf{V}_j$ associated with eigenvalue λ_j, and the reciprocal theorem becomes

$$\mathbf{D}_i^{\mathrm{T}}(n-1)\mathbf{F}_j(n-1) + \mathbf{D}_i^{\mathrm{T}}(n)\mathbf{F}_j(n) = \mathbf{D}_j^{\mathrm{T}}(n-1)\mathbf{F}_i(n-1) + \mathbf{D}_j^{\mathrm{T}}(n)\mathbf{F}_i(n)$$

where $(n-1)$ and (n) are the LHS and RHS of the cell, respectively. Express the RHS vectors in terms of LHS vectors as follows

$$\mathbf{D}_i(n) = \lambda_i \mathbf{D}_i(n-1), \ \mathbf{D}_j(n) = \lambda_j \mathbf{D}_j(n-1), \ \mathbf{F}_i(n) = -\lambda_i \mathbf{F}_i(n-1) \text{ and } \mathbf{F}_j(n) = -\lambda_j \mathbf{F}_j(n-1)$$

and the above simplifies to

$$\left(1 - \lambda_i \lambda_j\right)\mathbf{D}_i^{\mathrm{T}}(n-1)\mathbf{F}_j(n-1) = \left(1 - \lambda_i \lambda_j\right)\mathbf{D}_j^{\mathrm{T}}(n-1)\mathbf{F}_i(n-1)$$

or

$$\left(1 - \lambda_i \lambda_j\right)\left[\mathbf{D}_i^{\mathrm{T}}(n-1)\mathbf{F}_j(n-1) - \mathbf{D}_j^{\mathrm{T}}(n-1)\mathbf{F}_i(n-1)\right] = 0.$$

But the term

$$\left[\mathbf{D}_i^{\mathrm{T}}\left(n-1\right)\mathbf{F}_j\left(n-1\right) - \mathbf{D}_j^{\mathrm{T}}\left(n-1\right)\mathbf{F}_i\left(n-1\right) \right] \equiv \mathbf{V}_i^{\mathrm{T}}\mathbf{J}\mathbf{V}_j,$$

which indicates that the symplectic orthogonality relation $\left(1 - \lambda_i \lambda_j\right)\mathbf{V}_i^{\mathrm{T}}\mathbf{J}\,\mathbf{V}_j = 0$ is a special case of the reciprocal theorem. Note that there is no equivalent direct link between the reciprocal theorem and the weighted symplectic orthogonality of the eigenvectors $\mathbf{X}$ of transfer matrix $\mathbf{H}$.

Appendix B

ω^2	Mode 3 First thickness shear
1.66	$\begin{bmatrix} 1 & \pm0.2640i & 0 & \mp0.0724i & -1 & \pm0.2640i \end{bmatrix}^T$
1.67	$\begin{bmatrix} 1 & \pm0.2642i & 0 & \mp0.0749i & -1 & \pm0.2642i \end{bmatrix}^T$
1.6702	$\begin{bmatrix} 1 & 0.0001\pm0.0157i & 0.1088 & \mp0.0370i & 0.0125\pm0.0004i & \pm0.2452i \end{bmatrix}^T$
1.68	$\begin{bmatrix} 1 & \pm0.2644i & 0 & \mp0.0775i & -1 & \pm0.2644i \end{bmatrix}^T$
1.69	$\begin{bmatrix} 1 & \pm0.2647i & 0 & \mp0.08i & -1 & \pm0.2647i \end{bmatrix}^T$

ω^2	Mode 4 Second thickness shear
1.66	$\begin{bmatrix} 1 & \mp0.2328i & 0.2141 & 0 & 1 & \pm0.2328i \end{bmatrix}^T$
1.67	$\begin{bmatrix} 1 & \mp0.2268i & 0.2150 & 0 & 1 & \pm0.2268i \end{bmatrix}^T$
1.6702	$\begin{bmatrix} 0.7938\mp0.1242i & 0.0023\mp0.2306i & 0.1928\mp0.0134i \\ -0.0047\pm0.0077i & 1 & 0.0305\pm0.1761i \end{bmatrix}^T$
1.68	$\begin{bmatrix} 1 & \mp0.2210i & 0.2157 & 0 & 1 & \pm0.2210i \end{bmatrix}^T$
1.69	$\begin{bmatrix} 1 & \mp0.2153i & 0.2162 & 0 & 1 & \pm0.2153i \end{bmatrix}^T$

Table B.1 Displacement vectors below, at and above crossing frequency $\omega^2 \approx 1.6702$ for modes 3 and 4. The imaginary part of the displacement components are shown with $\pm$ and $\mp$ conjugates: the lower sign pertains to left-going waves while the upper sign pertains to right-going.

ω^2	Mode 3 First thickness shear
3.70	$\begin{bmatrix} 1 & \mp 0.7375i & 0 & \pm 1.9718i & -1 & \mp 0.7375i \end{bmatrix}^{\mathrm{T}}$
3.71	$\begin{bmatrix} 1 & \mp 0.6264i & 0 & \pm 1.7189i & -1 & \mp 0.6264i \end{bmatrix}^{\mathrm{T}}$
3.7151	$\begin{bmatrix} 1 & 0.0077 \mp 0.5862i & 0.1012 \mp 0.2539i & -0.1170 \pm 1.5865i \\ -0.9429 \mp 0.1433i & 0.0767 \mp 0.5586i \end{bmatrix}^{\mathrm{T}}$
3.72	$\begin{bmatrix} 1 & \mp 0.5594i & 0 & \pm 1.5639i & -1 & \mp 0.5594i \end{bmatrix}^{\mathrm{T}}$
3.73	$\begin{bmatrix} 1 & \mp 0.5100i & 0 & \pm 1.4480i & -1 & \mp 0.5100i \end{bmatrix}^{\mathrm{T}}$

ω^2	Mode 5 First breathing
3.70	$\begin{bmatrix} \pm 2.0266i & 1 & \pm 7.2826i & 0 & \pm 2.0266i & -1 \end{bmatrix}^{\mathrm{T}}$
3.71	$\begin{bmatrix} \pm 2.0590i & 1 & \pm 7.3303i & 0 & \pm 2.0590i & -1 \end{bmatrix}^{\mathrm{T}}$
3.7151	$\begin{bmatrix} 0.0189 \pm 1.7646i & 1 & 0.3676 \pm 1.3118i \\ -2.2774 \mp 0.1385i & 0.1886 \mp 1.0243i & 0.6433 \pm 0.1000i \end{bmatrix}^{\mathrm{T}}$
3.72	$\begin{bmatrix} \pm 2.0916i & 1 & \pm 7.3784i & 0 & \pm 2.0916i & -1 \end{bmatrix}^{\mathrm{T}}$
3.73	$\begin{bmatrix} \pm 2.1244i & 1 & \pm 7.4269i & 0 & \pm 2.1244i & -1 \end{bmatrix}^{\mathrm{T}}$

Table B.2 Displacement vectors below, at and above the crossing frequency $\omega^2 \approx 3.7151$ for modes 3 and 5. The imaginary part of the displacement components are shown with $\pm$ and $\mp$ conjugates: the lower sign pertains to left-going waves while the upper sign pertains to right-going.

Appendix C

C.1 The derivations of time-averaged work done, strain energy and kinetic energy

For a given harmonic displacement $\mathbf{D}_\mathrm{L} \exp(\mathrm{i}\omega t)$ and harmonic force $-\mathbf{F}_\mathrm{L} \exp(\mathrm{i}\omega t)$, the instantaneous work done by the force is given by

$$W_{\mathrm{L,\,ins}} = -\mathrm{Re}\left[\mathbf{D}_\mathrm{L}^\mathrm{T} \exp(\mathrm{i}\omega t)\right] \cdot \mathrm{Re}\left[\mathbf{F}_\mathrm{L} \exp(\mathrm{i}\omega t)\right], \tag{C.1}$$

where the minus sign takes into account the fact that forces on the left side of the cell act in opposite direction to the forces on the right side. Re-writing equation (C.1) to include the complex conjugate terms, gives

$$
\begin{aligned}
W_{\mathrm{L,\,ins}} &= -\frac{1}{2}\left[\mathbf{D}_\mathrm{L}^\mathrm{T} \exp(\mathrm{i}\omega t) + \bar{\mathbf{D}}_\mathrm{L}^\mathrm{T} \exp(\bar{\mathrm{i}}\,\omega t)\right] \cdot \frac{1}{2}\left[\mathbf{F}_\mathrm{L} \exp(\mathrm{i}\omega t) + \bar{\mathbf{F}}_\mathrm{L} \exp(\bar{\mathrm{i}}\,\omega t)\right] \\
&= -\frac{1}{4}\left[\mathbf{D}_\mathrm{L}^\mathrm{T}\mathbf{F}_\mathrm{L} \exp(2\mathrm{i}\omega t) + \bar{\mathbf{D}}_\mathrm{L}^\mathrm{T}\bar{\mathbf{F}}_\mathrm{L} \exp(2\bar{\mathrm{i}}\,\omega t) + \bar{\mathbf{D}}_\mathrm{L}^\mathrm{T}\mathbf{F}_\mathrm{L} + \mathbf{D}_\mathrm{L}^\mathrm{T}\bar{\mathbf{F}}_\mathrm{L}\right] \\
&= -\frac{1}{4}\left[\mathbf{D}_\mathrm{L}^\mathrm{T}\mathbf{F}_\mathrm{L} \exp(2\mathrm{i}\omega t) + \bar{\mathbf{D}}_\mathrm{L}^\mathrm{T}\bar{\mathbf{F}}_\mathrm{L} \exp(2\bar{\mathrm{i}}\,\omega t) + \bar{\mathbf{D}}_\mathrm{L}^\mathrm{T}\mathbf{F}_\mathrm{L} + \overline{\bar{\mathbf{D}}_\mathrm{L}^\mathrm{T}\mathbf{F}_\mathrm{L}}\right] \\
&= -\frac{1}{2}\mathrm{Re}\left[\mathbf{D}_\mathrm{L}^\mathrm{T}\mathbf{F}_\mathrm{L} \exp(2\mathrm{i}\omega t)\right] + \frac{1}{2}\mathrm{Re}\left[\bar{\mathbf{D}}_\mathrm{L}^\mathrm{T}\mathbf{F}_\mathrm{L}\right]
\end{aligned}
$$

where the overbar indicates complex conjugate. Integrating W_{ins} over one period T gives

$$\int_0^T W_{\mathrm{L,\,ins}}\,\mathrm{d}t = -\frac{1}{2}\mathrm{Re}\left[\bar{\mathbf{D}}_\mathrm{L}^\mathrm{T}\mathbf{F}_\mathrm{L}\right] = -\frac{1}{2}\mathrm{Re}\left[\mathbf{D}_\mathrm{L}^*\mathbf{F}_\mathrm{L}\right] \tag{C.2}$$

since

$$\int_0^T \frac{1}{2}\mathrm{Re}\left[\mathbf{D}_\mathrm{L}^\mathrm{T}\mathbf{F}_\mathrm{L} \exp(2\mathrm{i}\omega t)\right]\,\mathrm{d}t = \int_0^T \frac{1}{2}\left[\mathbf{D}_\mathrm{L}^\mathrm{T}\mathbf{F}_\mathrm{L} \cos(2\mathrm{i}\omega t)\right]\,\mathrm{d}t = 0.$$

The instantaneous strain energy on the left-hand side of a cell is given by

$$E_{\mathrm{S,L,\,ins}} = \mathrm{Re}\left\{\mathbf{D}_\mathrm{L}^\mathrm{T} \exp(\mathrm{i}\omega t)\right\} \cdot \mathrm{Re}\left\{\mathbf{K}_\mathrm{LL}\mathbf{D}_\mathrm{L} \exp(\mathrm{i}\omega t) + \mathbf{K}_\mathrm{LR}\mathbf{D}_\mathrm{R} \exp(\mathrm{i}\omega t)\right\}. \tag{C.3}$$

Following the same procedure, expand and rearrange the terms to get

$$E_{\mathrm{S,L,\,ins}} = \frac{1}{2}\mathrm{Re}\left\{\mathbf{D}_\mathrm{L}^\mathrm{T}\left[\mathbf{K}_\mathrm{LL}\mathbf{D}_\mathrm{L} + \mathbf{K}_\mathrm{LR}\mathbf{D}_\mathrm{R}\right]\exp(2\mathrm{i}\omega t)\right\} + \frac{1}{2}\mathrm{Re}\left\{\bar{\mathbf{D}}_\mathrm{L}^\mathrm{T}\left[\mathbf{K}_\mathrm{LL}\mathbf{D}_\mathrm{L} + \mathbf{K}_\mathrm{LR}\mathbf{D}_\mathrm{R}\right]\right\}. \tag{C.4}$$

Therefore, the time-averaged strain energy over one time cycle is

$$E_{\mathrm{S,L}} = \frac{1}{2}\mathrm{Re}\left\{\bar{\mathbf{D}}_\mathrm{L}^\mathrm{T}\left[\mathbf{K}_\mathrm{LL}\mathbf{D}_\mathrm{L} + \mathbf{K}_\mathrm{LR}\mathbf{D}_\mathrm{R}\right]\right\} = \frac{1}{2}\mathrm{Re}\left\{\mathbf{D}_\mathrm{L}^*\left[\mathbf{K}_\mathrm{LL}\mathbf{D}_\mathrm{L} + \mathbf{K}_\mathrm{LR}\mathbf{D}_\mathrm{R}\right]\right\}. \tag{C.5}$$

The expression for harmonic velocity can be obtained by differentiating the harmonic displacement expression with respect to time, that is $(\mathrm{d}/\mathrm{d}t)\left[\mathbf{D}_{\mathrm{L}}\exp(\mathrm{i}\,\omega t)\right]$, which gives $\mathrm{i}\,\omega\mathbf{D}_{\mathrm{L}}\exp(\mathrm{i}\,\omega t)$. The instantaneous kinetic energy of the (one half) point masses on the left-hand side of a cell can then be written as

$$E_{\mathrm{K,L,ins}}=\frac{1}{2}\mathrm{Re}\left[\mathrm{i}\,\omega\mathbf{D}_{\mathrm{L}}^{\mathrm{T}}\exp(\mathrm{i}\,\omega t)\right]\frac{\mathbf{m}}{2}\mathrm{Re}\left[\mathrm{i}\,\omega\mathbf{D}_{\mathrm{L}}\exp(\mathrm{i}\,\omega t)\right]\qquad\text{(C.6)}$$

where $\mathbf{m}$ is the mass matrix. Again, following the same procedure, expand and rearrange the terms to get

$$E_{\mathrm{K,L,ins}}=-\frac{1}{4}\omega^{2}\mathrm{Re}\left[\mathbf{D}_{\mathrm{L}}^{\mathrm{T}}\mathbf{m}\mathbf{D}_{\mathrm{L}}\exp(2\mathrm{i}\,\omega t)\right]+\frac{1}{4}\omega^{2}\mathrm{Re}\left[\bar{\mathbf{D}}_{\mathrm{L}}^{\mathrm{T}}\mathbf{m}\mathbf{D}_{\mathrm{L}}\right].\qquad\text{(C.7)}$$

Integrating equation (C.7) over one time-cycle gives

$$E_{\mathrm{K,L}}=\frac{1}{4}\omega^{2}\mathrm{Re}\left[\bar{\mathbf{D}}_{\mathrm{L}}^{\mathrm{T}}\mathbf{m}\mathbf{D}_{\mathrm{L}}\right]=\frac{1}{4}\omega^{2}\mathrm{Re}\left[\mathbf{D}_{\mathrm{L}}^{*}\mathbf{m}\mathbf{D}_{\mathrm{L}}\right].\qquad\text{(C.8)}$$

C.2   The derivations of time-averaged power

Instantaneous power flow into the left-hand side of a cell is given by the product of velocity of the masses and the (traction) forces acting on them [83] (page 73), that is

$$P_{\mathrm{L,ins}}=\mathrm{Re}\left[\mathrm{i}\,\omega\mathbf{D}_{\mathrm{L}}^{\mathrm{T}}\exp(\mathrm{i}\,\omega t)\right]\cdot\mathrm{Re}\left[\mathbf{F}_{\mathrm{L}}\exp(\mathrm{i}\,\omega t)\right].\qquad\text{(C.9)}$$

There is no negative sign before the force term because the directions of forces on both sides of the cell are taken to be consistent with the frame of reference. Rewrite equation (C.9) to include the complex conjugate terms and expand as follows.

$$\begin{aligned}P_{\mathrm{L,ins}}&=\frac{1}{2}\mathrm{Re}\left[\mathrm{i}\,\omega\mathbf{D}_{\mathrm{L}}^{\mathrm{T}}\exp(\mathrm{i}\,\omega t)+\bar{\mathrm{i}}\,\omega\bar{\mathbf{D}}_{\mathrm{L}}^{\mathrm{T}}\exp(\bar{\mathrm{i}}\,\omega t)\right]\cdot\frac{1}{2}\mathrm{Re}\left[\mathbf{F}_{\mathrm{L}}\exp(\mathrm{i}\,\omega t)+\bar{\mathbf{F}}_{\mathrm{L}}\exp(\bar{\mathrm{i}}\,\omega t)\right]\\&=\frac{1}{4}\left[\mathrm{i}\,\omega\mathbf{D}_{\mathrm{L}}^{\mathrm{T}}\mathbf{F}_{\mathrm{L}}\exp(2\mathrm{i}\,\omega t)+\bar{\mathrm{i}}\,\omega\bar{\mathbf{D}}_{\mathrm{L}}^{\mathrm{T}}\bar{\mathbf{F}}_{\mathrm{L}}\exp(2\,\bar{\mathrm{i}}\,\omega t)+\bar{\mathrm{i}}\,\omega\bar{\mathbf{D}}_{\mathrm{L}}^{\mathrm{T}}\mathbf{F}_{\mathrm{L}}+\mathrm{i}\,\omega\mathbf{D}_{\mathrm{L}}^{\mathrm{T}}\bar{\mathbf{F}}_{\mathrm{L}}\right]\\&=\frac{1}{2}\mathrm{Re}\left[\mathrm{i}\,\omega\mathbf{D}_{\mathrm{L}}^{\mathrm{T}}\mathbf{F}_{\mathrm{L}}\exp(2\mathrm{i}\,\omega t)\right]+\frac{1}{2}\mathrm{Re}\left[\bar{\mathrm{i}}\,\omega\bar{\mathbf{D}}_{\mathrm{L}}^{\mathrm{T}}\mathbf{F}_{\mathrm{L}}\right]\end{aligned}$$

where the overbar denotes complex conjugate. The average power over one period is

$$P_{\mathrm{L}}=\frac{1}{2}\mathrm{Re}\left(\bar{\mathrm{i}}\,\omega\bar{\mathbf{D}}_{\mathrm{L}}^{\mathrm{T}}\mathbf{F}_{\mathrm{L}}\right)=-\frac{1}{2}\mathrm{Re}\left(\mathrm{i}\,\omega\mathbf{D}_{\mathrm{L}}^{*}\mathbf{F}_{\mathrm{L}}\right).\qquad\text{(C.10)}$$

Note that the minus sign appears because $\bar{\mathrm{i}}=-\mathrm{i}$.

To obtain equation (4.17), proceed as follows. Substitute equation (4.1) into equation (C.10) to give

$$P_L = \frac{1}{2} \text{Re}\left(i\omega \mathbf{D}_L^* \left[\mathbf{K}_{LL}\mathbf{D}_L + \mathbf{K}_{LR}\mathbf{D}_R - \frac{\omega^2 \mathbf{m}}{2}\mathbf{D}_L \right] \right). \tag{C.11}$$

The power that flows out of the right-hand side of a cell is

$$P_R = -\frac{1}{2}\text{Re}\left(i\omega \mathbf{D}_R^* \mathbf{F}_R \right). \tag{C.12}$$

Substitute equation (4.2) into equation (C.12) to give

$$P_R = -\frac{1}{2}\text{Re}\left(i\omega \mathbf{D}_R^* \left[\mathbf{K}_{RL}\mathbf{D}_L + \mathbf{K}_{RR}\mathbf{D}_R - \frac{\omega^2 \mathbf{m}}{2}\mathbf{D}_R \right] \right). \tag{C.13}$$

From equation (4.18), we know that $P_L = P_R$. Therefore, we can write

$$P_L = \frac{1}{2}\left(P_L + P_L \right) = \frac{1}{2}\left(P_L + P_R \right). \tag{C.14}$$

Substitute equations (C.11) and (C.13) into equation (C.14); noting that

$$\frac{1}{4}\text{Re}\left(i\omega^3 \mathbf{D}_L^* \frac{\mathbf{m}}{2}\mathbf{D}_L \right) = \frac{1}{4}\text{Re}\left(i\omega^3 \mathbf{D}_R^* \frac{\mathbf{m}}{2}\mathbf{D}_R \right) \text{ and}$$

$$\frac{1}{4}\text{Re}\left(i\omega \mathbf{D}_L^* \mathbf{K}_{LL}\mathbf{D}_L \right) = \frac{1}{4}\text{Re}\left(i\omega \mathbf{D}_R^* \mathbf{K}_{RR}\mathbf{D}_R \right), \text{ leads to}$$

$$\begin{aligned}
P_L &= \frac{1}{4}\text{Re}\left(i\omega \mathbf{D}_L^* \mathbf{K}_{LR}\mathbf{D}_R \right) - \frac{1}{4}\text{Re}\left(i\omega \mathbf{D}_R^* \mathbf{K}_{RL}\mathbf{D}_L \right) \\
&= \frac{1}{4}\left(\frac{i\omega \mathbf{D}_L^* \mathbf{K}_{LR}\mathbf{D}_R + \overline{i\omega \mathbf{D}_L^* \mathbf{K}_{LR}\mathbf{D}_R}}{2} \right) - \frac{1}{4}\left(\frac{i\omega \mathbf{D}_R^* \mathbf{K}_{RL}\mathbf{D}_L + \overline{i\omega \mathbf{D}_R^* \mathbf{K}_{RL}\mathbf{D}_L}}{2} \right) \\
&= \frac{1}{8}\left(i\omega \mathbf{D}_L^* \mathbf{K}_{LR}\mathbf{D}_R - i\omega \mathbf{D}_R^* \mathbf{K}_{RL}\mathbf{D}_L \right) - \frac{1}{8}\left(i\omega \mathbf{D}_R^* \mathbf{K}_{RL}\mathbf{D}_L - i\omega \mathbf{D}_L^* \mathbf{K}_{LR}\mathbf{D}_R \right) \\
&= \frac{1}{4}\left(i\omega \mathbf{D}_L^* \mathbf{K}_{LR}\mathbf{D}_R - i\omega \mathbf{D}_R^* \mathbf{K}_{RL}\mathbf{D}_L \right) \\
&= -\frac{1}{4}i\omega \begin{bmatrix} \mathbf{D}_L^* & \mathbf{D}_R^* \end{bmatrix} \begin{bmatrix} \mathbf{0} & -\mathbf{K}_{LR} \\ \mathbf{K}_{RL} & \mathbf{0} \end{bmatrix} \begin{bmatrix} \mathbf{D}_L \\ \mathbf{D}_R \end{bmatrix} \\
&= -\frac{1}{4}i\omega \mathbf{X}^* \tilde{\mathbf{J}} \mathbf{X}.
\end{aligned}$$

Using similar procedures as shown above allows one to write equation (4.32) in terms of eigenvector $\mathbf{V}$, so

$$P_{12} = -\frac{1}{2}\omega \operatorname{Re}\left(i\,\mathbf{D}_1^*\mathbf{F}_2 + i\,\mathbf{D}_2^*\mathbf{F}_1\right)$$

$$= -\frac{1}{2}\omega\left(\frac{i\,\mathbf{D}_1^*\mathbf{F}_2 + \overline{i\,\mathbf{D}_1^*\mathbf{F}_2}}{2} + \frac{i\,\mathbf{D}_2^*\mathbf{F}_1 + \overline{i\,\mathbf{D}_2^*\mathbf{F}_1}}{2}\right)$$

$$= -\frac{1}{4}\omega\left(i\,\mathbf{D}_1^*\mathbf{F}_2 - i\,\mathbf{F}_2^*\mathbf{D}_1 + i\,\mathbf{D}_2^*\mathbf{F}_1 - i\,\mathbf{F}_1^*\mathbf{D}_2\right)$$

where $\mathbf{D}$ and $\mathbf{F}$ are displacement and force vectors, respectively, and the subscripts 1 and 2 associate the vectors to the complex non-unity eigenvalues $\lambda_1 = +\delta + i\varphi$ and $\lambda_2 = -\delta + i\varphi$, respectively. Note that

$$\mathbf{D}_1^*\mathbf{F}_2 - \mathbf{F}_1^*\mathbf{D}_2 = \begin{bmatrix} \mathbf{D}_1^* & \mathbf{F}_1^* \end{bmatrix}\begin{bmatrix} \mathbf{0} & \mathbf{I} \\ -\mathbf{I} & \mathbf{0} \end{bmatrix}\begin{bmatrix} \mathbf{D}_2 \\ \mathbf{F}_2 \end{bmatrix} = \mathbf{V}_1\mathbf{J}\mathbf{V}_2,$$

$$\mathbf{D}_2^*\mathbf{F}_1 - \mathbf{F}_2^*\mathbf{D}_1 = \begin{bmatrix} \mathbf{D}_2^* & \mathbf{F}_2^* \end{bmatrix}\begin{bmatrix} \mathbf{0} & \mathbf{I} \\ -\mathbf{I} & \mathbf{0} \end{bmatrix}\begin{bmatrix} \mathbf{D}_1 \\ \mathbf{F}_1 \end{bmatrix} = \mathbf{V}_2\mathbf{J}\mathbf{V}_1.$$

Therefore, $P_{12} = -i\,\omega\left(\mathbf{V}_1\mathbf{J}\mathbf{V}_2 + \mathbf{V}_2\mathbf{J}\mathbf{V}_1\right)/4$ where $\mathbf{V}$ is the eigenvector of matrix $\mathbf{G}$ and subscripts 1 and 2 associate the eigenvectors to eigenvalues λ_1 and λ_2, respectively.

Appendix D

D.1 Transmission matrix and Jordan canonical form

The transmission matrix is

$$\mathbf{T} = \begin{bmatrix}
1.6410\times10^{-8} & 4.2911\times10^{-8} & -6.1298\times10^{-9} & -1.6410\times10^{-8} & -4.2911\times10^{-8} & -6.1298\times10^{-9} \\
1.7438\times10^{-7} & 3.9532\times10^{-8} & 4.6103\times10^{-8} & 1.7438\times10^{-7} & 3.9532\times10^{-8} & -4.6103\times10^{-8} \\
-7.9855\times10^{-8} & -9.3087\times10^{-8} & 0 & 7.9855\times10^{-8} & 9.3087\times10^{-8} & 0 \\
0 & 0 & -4.0777\times10^{-8} & 0 & 0 & 4.0777\times10^{-8} \\
1.6410\times10^{-8} & 4.2911\times10^{-8} & 6.1298\times10^{-9} & -1.6410\times10^{-8} & -4.2911\times10^{-8} & 6.1298\times10^{-9} \\
-1.7438\times10^{-7} & 3.9532\times10^{-8} & 4.6103\times10^{-8} & -1.7438\times10^{-7} & -3.9532\times10^{-8} & -4.6103\times10^{-8} \\
1 & 1 & 0 & 1 & 1 & 0 \\
2.4351 & 7.7990\times10^{-1} & 1 & -2.4351 & -7.7990\times10^{-1} & 1 \\
-2 & -2 & 0 & -2 & -2 & 0 \\
0 & 0 & -2 & 0 & 0 & -2 \\
1 & 1 & 0 & 1 & 1 & 0 \\
-2.4351 & -7.7990\times10^{-1} & 1 & 2.4351 & 7.7990\times10^{-1} & 1
\end{bmatrix}$$

$$\begin{bmatrix}
3.9645\times10^{-8} & 0 & 0 & 4.6935\times10^{-8} & -2.3468\times10^{-8} & 1.5009\times10^{-7} \\
0 & -1.0355\times10^{-8} & -4.6935\times10^{-8} & 0 & 0 & 0 \\
3.9645\times10^{-8} & 0 & 0 & 0 & 0 & 0 \\
0 & 0 & -4.6935\times10^{-8} & 0 & 6.1298\times10^{-9} & -6.1298\times10^{-9} \\
3.9645\times10^{-8} & 0 & 0 & -4.6935\times10^{-8} & 2.3468\times10^{-8} & -1.5009\times10^{-7} \\
0 & 1.0355\times10^{-8} & -4.6935\times10^{-8} & 0 & 0 & 0 \\
0 & 8.9645\times10^{-1} & 0 & 0 & 1 & -1 \\
0 & 0 & 0 & 0 & 0 & 4.6935\times10^{-1} \\
0 & 1 & 0 & 0 & 0 & 0 \\
0 & 0 & 0 & 0 & 0 & 1.0613 \\
0 & 8.9645\times10^{-1} & 0 & 0 & -1 & 1 \\
0 & 0 & 0 & 0 & 0 & 4.6935\times10^{-1}
\end{bmatrix}$$

The Jordan canonical form is

$$\mathbf{J} = \begin{bmatrix} 16.78 & 0 & 0 & 0 & 0 & 0 & 0 & 0 & 0 & 0 & 0 & 0 \\ 0 & 3.5346 & 0 & 0 & 0 & 0 & 0 & 0 & 0 & 0 & 0 & 0 \\ 0 & 0 & -14.24 & 0 & 0 & 0 & 0 & 0 & 0 & 0 & 0 & 0 \\ 0 & 0 & 0 & 0.0596 & 0 & 0 & 0 & 0 & 0 & 0 & 0 & 0 \\ 0 & 0 & 0 & 0 & 0.2829 & 0 & 0 & 0 & 0 & 0 & 0 & 0 \\ 0 & 0 & 0 & 0 & 0 & -0.0702 & 0 & 0 & 0 & 0 & 0 & 0 \\ 0 & 0 & 0 & 0 & 0 & 0 & 1 & 1 & 0 & 0 & 0 & 0 \\ 0 & 0 & 0 & 0 & 0 & 0 & 0 & 1 & 0 & 0 & 0 & 0 \\ 0 & 0 & 0 & 0 & 0 & 0 & 0 & 0 & 1 & 1 & 0 & 0 \\ 0 & 0 & 0 & 0 & 0 & 0 & 0 & 0 & 0 & 1 & 1 & 0 \\ 0 & 0 & 0 & 0 & 0 & 0 & 0 & 0 & 0 & 0 & 1 & 1 \\ 0 & 0 & 0 & 0 & 0 & 0 & 0 & 0 & 0 & 0 & 0 & 1 \end{bmatrix} = \begin{bmatrix} \mathbf{J}_1 & \mathbf{0} \\ \mathbf{0} & \mathbf{J}_4 \end{bmatrix} ;$$

note that these partition sizes differ from those of $\mathbf{T}$.

D.2 Derivation of end state vector for repetitive structure under distributed loading

Consider the n th and $(n+1)$ th cells, as shown in Figure D.2.1. For the n th cell one has

$$\begin{bmatrix} \mathbf{d}(n) \\ \mathbf{F}(n) \end{bmatrix}^n = \begin{bmatrix} \mathbf{G}_{dd} & \mathbf{G}_{dF} \\ \mathbf{G}_{Fd} & \mathbf{G}_{FF} \end{bmatrix} \begin{bmatrix} \mathbf{d}(n-1) \\ -\mathbf{F}(n-1) \end{bmatrix}^n , \tag{D.2.1}$$

while for the $(n+1)$ th, one has

$$\begin{bmatrix} \mathbf{d}(n+1) \\ \mathbf{F}(n+1) \end{bmatrix}^{n+1} = \begin{bmatrix} \mathbf{G}_{dd} & \mathbf{G}_{dF} \\ \mathbf{G}_{Fd} & \mathbf{G}_{FF} \end{bmatrix} \begin{bmatrix} \mathbf{d}(n) \\ -\mathbf{F}(n) \end{bmatrix}^{n+1} ; \tag{D.2.2}$$

in the above the superscripts pertains to the cell, the argument denotes the nodal cross-section, and the transfer matrix $\mathbf{G}$ is written in partitioned form.

Suppose that an external force vector $\mathbf{F}_{ext}(n)$ is applied at the n th nodal cross-section; displacement compatibility requires

$$\mathbf{d}(n)^n = \mathbf{d}(n)^{n+1} \tag{D.2.3}$$

while force equilibrium requires

$$\mathbf{F}(n)^n + \mathbf{F}(n)^{n+1} = \mathbf{F}_{ext}(n).$$ (D.2.4)

Substitution of equations (D.2.3) and (D.2.4) into equation (D.2.2) gives

$$\begin{bmatrix} \mathbf{d}(n+1) \\ \mathbf{F}(n+1) \end{bmatrix}^{n+1} = \begin{bmatrix} \mathbf{G}_{dd} & \mathbf{G}_{dF} \\ \mathbf{G}_{Fd} & \mathbf{G}_{FF} \end{bmatrix} \begin{bmatrix} \mathbf{d}(n) \\ \mathbf{F}(n) - \mathbf{F}_{ext}(n) \end{bmatrix}^n,$$ (D.2.5)

or more compactly

$$\mathbf{s}(n+1) = \mathbf{G}\mathbf{s}(n) - \mathbf{G} \begin{bmatrix} \mathbf{0} \\ \mathbf{F}_{ext}(n) \end{bmatrix}.$$ (D.2.6)
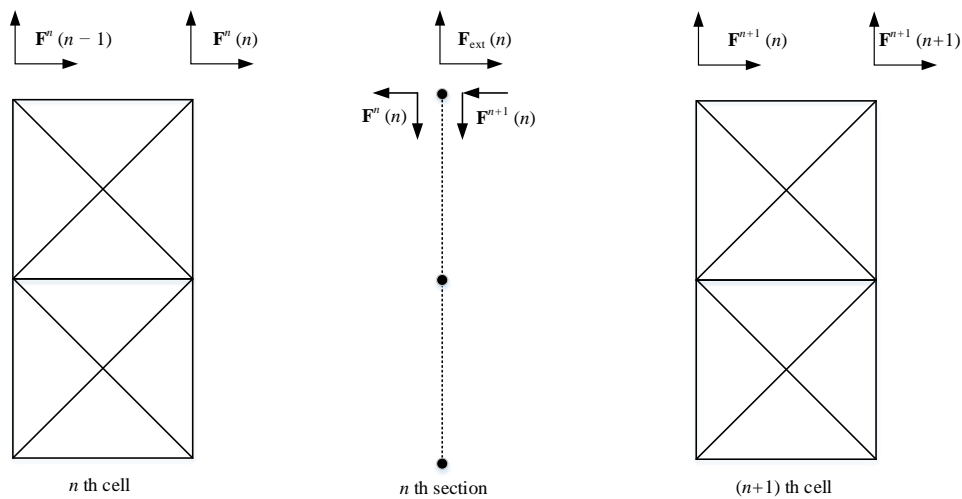
Figure D.2.1   The nth and $(n + 1)$th cells, together with force vectors applied to the nth cross-section; for clarity these are shown on the uppermost nodes only. The superscript and argument pertain to the cell and cross-section, respectively.

Suppose the external forces are applied at the 1st, 2nd, 3rd etc. until nth nodal cross-sections; the general expression is given by

$$\mathbf{s}(n) = \mathbf{G}^n \mathbf{s}(0) - \sum_{r=1}^{n-1} \mathbf{G}^{n-r} \begin{bmatrix} \mathbf{0} \\ \mathbf{F}_{ext}(r) \end{bmatrix};$$

note that the superscript now denotes powers of the transfer matrix.

List of References

[1]   N.G. Stephen, Transfer matrix analysis of the elastostatics of one-dimensional repetitive structures, *Proceedings of the Royal Society A: Mathematical, Physical and Engineering Sciences*, **462** (2006) 2245–2270.

[2]   E. Emaci, M.A.F. Azeez, F. Vakakis, Dynamics of trusses: numerical and experimental results, *Journal of Sound and Vibration*, **214** (1998) 953–964.

[3]   M. Ruzzene, F. Scarpa, F. Soranna, Wave beaming effects in two-dimensional cellular structures, *Smart Materials and Structures*, **12** (2003) 363–372.

[4]   A.K. Noor, M.M. Mikulas, Continuum Modeling of Large Lattice Structures: Status and Projections, in: S.N. Atluri, A.K. Amos (Eds.), *Large Space Structures: Dynamics and Control*, 1st edition, Springer, Berlin and Heidelberg, 1988: pp. 1–34.

[5]   S.S. Mester, H. Benaroya, Periodic and near-periodic structures, *Shock and Vibration*, **2** (1995) 69–95.

[6]   D.J. Mead, Wave propagation in continuous periodic structures: Research contributions from Southampton, 1964-1995, *Journal of Sound and Vibration*, **190** (1996) 495–524.

[7]   N.G. Stephen, S. Ghosh, Eigenanalysis and continuum modelling of a curved repetitive beam-like structure, *International Journal of Mechanical Sciences*, **47** (2005) 1854–1873.

[8]   N.G. Stephen, Y. Zhang, Coupled tension-torsion vibration of repetitive beam-like structures, *Journal of Sound and Vibration*, **293** (2006) 253–265.

[9]   E.G. Karpov, D.L. Dorofeev, N.G. Stephen, Characteristic solutions for the statics of repetitive beam-like trusses, *International Journal of Mechanical Sciences*, **44** (2002) 1363–1379.

[10]   R.C. Engels, L. Meirovitch, Response of periodic structures by modal analysis, *Journal of Sound and Vibration*, **56** (1978) 481–493.

[11]   H. Tollenaere, D. Caillerie, Continuous modeling of lattice structures by homogenization, *Advances in Engineering Software*, **29** (1998) 699–705.

[12]   N.G. Stephen, P.J. Wang, On Saint-Venant's principle in pin-jointed frameworks, *International Journal of Solids and Structures*, **33** (1996) 79–97.

[13]   N.G. Stephen, Y. Zhang, Eigenanalysis and continuum modelling of an asymmetric beam-like repetitive structure, *International Journal of Mechanical Sciences*, **46** (2004) 1213–1231.

[14]   N.G. Stephen, Y. Zhang, Eigenanalysis and continuum modelling of pre-twisted repetitive beam-like structures, *International Journal of Solids and Structures*, **43** (2006) 3832–3855.

[15]   Y. Waki, B.R. Mace, M.J. Brennan, Numerical issues concerning the wave and finite element method for free and forced vibrations of waveguides, *Journal of Sound and Vibration*, **327** (2009) 92–108.

[16]   D. Duhamel, B.R. Mace, M.J. Brennan, Finite element analysis of the vibrations of waveguides and periodic structures, *Journal of Sound and Vibration*, **294** (2006) 205–220.

[17]   N. Bhutani, R.G. Loewy, Combined finite element-transfer matrix method, *Journal of Sound and Vibration*, **226** (1999) 1048–1052.

[18]   D.J. Mead, A general theory of harmonic wave propagation in linear periodic systems with multiple coupling, *Journal of Sound and Vibration*, **27** (1973) 235–260.

[19]   D.J. Mead, Waves and modes in finite beams: Application of the phase-closure principle, *Journal of Sound and Vibration*, **171** (1994) 695–702.

[20]   M.I. Hussein, M.J. Leamy, M. Ruzzene, Dynamics of phononic materials and structures: historical origins, recent progress, and future outlook, *Applied Mechanics Reviews*, **66** (2014) 040802.

[21]   D. Beli, J.R.F. Arruda, M. Ruzzene, Wave propagation in elastic metamaterial beams and plates with interconnected resonators, *International Journal of Solids and Structures*, **139–140** (2018) 105–120.

[22]   D.J. Colquitt, V. V. Danishevskyy, J. Kaplunov, Composite dynamic models for periodically heterogeneous media, *Mathematics and Mechanics of Solids*, **24** (2019) 2663–2693.

[23]   A. Yariv, P. Yeh, *Photonics: Optical Electronics in Modern Communications*, 6th ed., Oxford University Press, New York, 2007.

[24]   I. V. Andrianov, V. V. Danishevskyy, G. Rogerson, Elastic waves in periodically heterogenous two-dimensional media: locally periodic and anti-periodic modes, *Proceedings of the Royal Society A: Mathematical, Physical and Engineering Sciences*, **474** (2018) 20170908.

[25]   C. Boutin, S. Hans, Homogenisation of periodic discrete medium: application to dynamics of framed structures, *Computers and Geotechnics*, **30** (2003) 303–320.

[26]   R. V. Craster, J. Kaplunov, A. V. Pichugin, High-frequency homogenization for periodic media, *Proceedings of the Royal Society A: Mathematical, Physical and Engineering Sciences*, **466** (2010) 2341–2362.

[27]   R. V. Craster, J. Kaplunov, J. Postnova, High-frequency asymptotics, homogenisation and localisation for lattices, *The Quarterly Journal of Mechanics and Applied Mathematics*, **63** (2010) 497–519.

[28]   E. Nolde, R. V. Craster, J. Kaplunov, High frequency homogenization for structural mechanics, *Journal of the Mechanics and Physics of Solids*, **59** (2011) 651–671.

[29]   R. V. Craster, J. Kaplunov, E. Nolde, S. Guenneau, Bloch dispersion and high frequency homogenization for separable doubly-periodic structures, *Wave Motion*, **49** (2012) 333–346.

[30]   P. Fossat, C. Boutin, M. Ichchou, Homogenized bending model of a periodic ribbed plate with inner resonance, *Procedia Engineering*, **199** (2017) 1435–1440.

[31]   A. Rallu, S. Hans, C. Boutin, High frequency reduced models for repetitive beams, *Procedia Engineering*, **199** (2017) 1501–1506.

[32]   A. Rallu, S. Hans, C. Boutin, Asymptotic analysis of high-frequency modulation in periodic systems. Analytical study of discrete and continuous structures, *Journal of the Mechanics and Physics of Solids*, **117** (2018) 123–156.

[33]   Z. Changwei, S. Xiangkun, M. Ichchou, A.-M. Zine, J.-P. Lainé, S. Hans, C. Boutin, Investigation of dynamics of discrete framed structures by a numerical wave-based method and an analytical homogenization approach, *Chinese Journal of Aeronautics*, **30** (2017) 66–74.

[34]   B.J. Olson, S.W. Shaw, C. Shi, C. Pierre, R.G. Parker, Circulant matrices and their application to vibration analysis, *Applied Mechanics Reviews*, **66** (2014) 040803.

[35]   L.Y. Banakh, M.L. Kempner, *Vibrations of mechanical systems with regular structure*, Springer, Berlin, 2010.

[36]   J.-M. Mencik, A wave finite element approach for the analysis of periodic structures with cyclic symmetry in dynamic substructuring, *Journal of Sound and Vibration*, **431** (2018) 441–457.

[37]   N.G. Stephen, Y. Zhang, On the continuum properties of repetitive beam-like pin-jointed structures, *Journal of Strain Analysis*, **37** (2002) 459–464.

[38]   N.G. Stephen, P.J. Wang, On transfer matrix eigenanalysis of pin-jointed frameworks, *Computers and Structures*, **78** (2000) 603–615.

[39]   N.G. Stephen, Repetitive beam-like structures: Distributed loading and intermediate support, *International Journal of Solids and Structures*, **46** (2009) 3664–3668.

[40]   W.X. Zhong, F.W. Williams, On the direct solution of wave propagation for repetitive structures, *Journal of Sound and Vibration*, **181** (1995) 485–501.

[41]   F. Farzbod, M.J. Leamy, The treatment of forces in Bloch analysis, *Journal of Sound and Vibration*, **325** (2009) 545–551.

[42]   F. Farzbod, M.J. Leamy, Analysis of Bloch's method and the propagation technique in periodic structures, *Journal of Vibration and Acoustics*, **133** (2011) 031010.

[43]   J.A. Kulpe, K.G. Sabra, M.J. Leamy, Bloch-wave expansion technique for predicting wave reflection and transmission in two-dimensional phononic crystals, *The Journal of the Acoustical Society of America*, **135** (2018) 1808–1819.

[44]   J.A. Kulpe, M.J. Leamy, K.G. Sabra, Determination of acoustic scattering from a two-dimensional finite phononic crystal using Bloch wave expansion, in: *ASME International Design Engineering Technical Conferences*, Buffalo, NY, 2014.

[45]   J.A. Kulpe, K.G. Sabra, M.J. Leamy, A three-dimensional Bloch wave expansion to determine external scattering from finite phononic crystals, *The Journal of the Acoustical Society of America*, **137** (2015) 3299–3313.

[46]   J.A. Kulpe, K.G. Sabra, M.J. Leamy, Acoustic scattering from phononic crystals

with complex geometry, *The Journal of the Acoustical Society of America*, **139** (2016) 3009–3020.

[47]   J. Signorelli, A.H. von Flotow, Wave propagation, power flow, and resonance in a truss beam, *Journal of Sound and Vibration*, **126** (1988) 127–144.

[48]   Y. Yong, Y.K. Lin, Propagation of decaying waves in periodic and piecewise periodic structures of finite length, *Journal of Sound and Vibration*, **129** (1989) 99–118.

[49]   N.G. Stephen, On the Riccati transfer matrix method for repetitive structures, *Mechanics Research Communications*, **37** (2010) 663–665.

[50]   B. Karp, D. Durban, Saint-Venant's principle in dynamics of structures, *Applied Mechanics Reviews*, **64** (2011) 020801.

[51]   V. Berdichevsky, D.J. Foster, On Saint-Venant's principle in the dynamics of elastic beams, *International Journal of Solids and Structures*, **40** (2003) 3293–3310.

[52]   B. Karp, Dynamic equivalence, self-equilibrated excitation and Saint-Venant's principle for an elastic strip, *International Journal of Solids and Structures*, **46** (2009) 3068–3077.

[53]   E. Babenkova, J. Kaplunov, Low-frequency decay conditions for a semi-infinite elastic strip, *Proceedings of the Royal Society A: Mathematical, Physical and Engineering Sciences*, **460** (2004) 2153–2169.

[54]   E. Babenkova, J. Kaplunov, Radiation conditions for a semi-infinite elastic strip, *Proceedings of the Royal Society A: Mathematical, Physical and Engineering Sciences*, **461** (2005) 1163–1179.

[55]   E. Babenkova, J. Kaplunov, The two-term interior asymptotic expansion in the case of low-frequency longitudinal vibrations of an elongated elastic rectangle, in: A. Movchan (Ed.), *Proceedings of the IUTAM Symposium on Asymptotics, Singularities and Homogenisation in Problems of Mechanics*, Kluwer, Dordrecht, 2003: pp. 137–145.

[56]   J. Kaplunov, L.Y. Kossovich, E. V. Nolde, *Dynamics of thin walled elastic bodies*, Academic Press, New York, 1998.

[57]   W.X. Zhong, F.W. Williams, Wave problems for repetitive structures and

symplectic mathematics, *Proceedings of the Institution of Mechanical Engineers Part C: Journal of Mechanical Engineering Science*, **206** (1992) 371–379.

[58] W.X. Zhong, F.W. Williams, Physical interpretation of the symplectic orthogonality of the eigensolutions of a Hamiltonian or symplectic matrix, *Computers and Structures*, **49** (1993) 749–750.

[59] R.S. Langley, On the modal density and energy flow characteristics of periodic structures, *Journal of Sound and Vibration*, **172** (1994) 491–511.

[60] E. El Masri, N.S. Ferguson, T. Waters, Application of the wave finite element method to reinforced concrete, *Journal of Physics: Conference Series*, **744** (2016) 012053.

[61] D.J. Mead, Wave propagation and natural modes in periodic systems: I. mono-coupled systems, *Journal of Sound and Vibration*, **40** (1975) 1–18.

[62] D.J. Mead, Wave propagation and natural modes in periodic systems: II. multi-coupled systems, with and without damping, *Journal of Sound and Vibration*, **40** (1975) 19–39.

[63] O.N. Kirillov, *Nonconservative Stability Problems of Modern Physics*, De Gruyter, Berlin, 2013.

[64] J. Miklowitz, *The Theory of Elastic Waves and Waveguides*, 2nd edition, North-Holland, Netherlands, 1980.

[65] F.S. Crawford, *Waves. Berkeley Physics Course, Volume 3*, McGraw-Hill, New York, 1968.

[66] J.M. Mencik, New advances in the forced response computation of periodic structures using the wave finite element (WFE) method, *Computational Mechanics*, **54** (2014) 789–801.

[67] I.H. Mufti, C.K. Chow, F.T. Stock, Solution of ill-conditioned linear two-point boundary value problems by the Riccati transformation, *SIAM Review*, **11** (1969) 616–619.

[68] H. Xue, A combined finite element-Riccati transfer matrix method in frequency domain for transient structural response, *Computers and Structures*, **62** (1997) 215–220.

[69] H. Xue, A stiffness equation transfer method for transient dynamic response analysis of structures, *Journal of Sound and Vibration*, **273** (2004) 1063–1078.

[70] H. Xue, A stiffness equation transfer method for natural frequencies of structures, *Journal of Sound and Vibration*, **268** (2003) 881–895.

[71] A. Luongo, F. Romeo, Real wave vectors for dynamic analysis of periodic structures, *Journal of Sound and Vibration*, **279** (2005) 309–325.

[72] R.S. Langley, A transfer matrix analysis of the energetics of structural wave motion and harmonic vibration, *Proceedings of the Royal Society A: Mathematical, Physical and Engineering Sciences*, **452** (1996) 1631–1648.

[73] Y.I. Bobrovnitskii, On the energy flow in evanescent waves, *Journal of Sound and Vibration*, **152** (1992) 175–176.

[74] M.J. Lighthill, Group Velocity, *IMA Journal of Applied Mathematics*, **1** (1965) 1–28.

[75] S. Finnveden, Evaluation of modal density and group velocity by a finite element method, *Journal of Sound and Vibration*, **273** (2004) 51–75.

[76] Y. Waki, B.R. Mace, M.J. Brennan, On Numerical Issues for the Wave/Finite Element Method, in: *ISVR Technical Memorandum No 964*, 2006.

[77] J.D. Meiss, *Differential Dynamical Systems*, Society for Industrial and Applied Mathematics, Philadelphia, 2017.

[78] M. Ibanescu, S.G. Johnson, D. Roundy, C. Luo, Y. Fink, J.D. Joannopoulos, Anomalous dispersion relations by symmetry breaking in axially uniform waveguides, *Physical Review Letters*, **92** (2004) 1–4.

[79] F.W. Williams, Natural frequencies of repetitive structures, *The Quarterly Journal of Mechanics and Applied Mathematics*, **24** (1971) 285–310.

[80] W.H. Wittrick, F.W. Williams, A general algorithm for computing natural frequencies of elastic structures, *The Quarterly Journal of Mechanics and Applied Mathematics*, **24** (1971) 263–284.

[81] C.A. Mercer, C. Seavey, Prediction of natural frequencies and normal modes of skin-stringer panel rows, *Journal of Sound and Vibration*, **6** (1967) 149–162.

[82] C.W. Cai, J.K. Liu, F.T.K. Au, L.G. Tham, Dynamic analysis of continuous plane trusses with equidistant supports, *Journal of Sound and Vibration*, **246** (2001) 157–174.

[83] L. Brillouin, *Wave Propagation in Periodic Structures: Electric Filters and Crystal Lattices*, 1st edition, McGraw-Hill Book Company Inc, New York, 1946.

[84] F. Leckie, E. Pestel, Transfer-matrix fundamentals, *International Journal of Mechanical Sciences*, **2** (1960) 137–167.

[85] W.T. Thomson, Transfer matrix relationships for repeated structures, *International Journal of Mechanical Sciences*, **13** (1971) 737–738.

[86] R.C. Engels, Response of infinite periodic structures, *Journal of Sound and Vibration*, **69** (1980) 181–197.

[87] N. Wicks, S.D. Guest, Single member actuation in large repetitive truss structures, *International Journal of Solids and Structures*, **41** (2004) 965–978.

[88] Z. You, S. Pellegrino, Foldable bar structures, *International Journal of Solids and Structures*, **34** (1997) 1825–1847.

[89] W.X. Zhong, F.W. Williams, On the localization of the vibration mode of a sub-structural chain-type structure, *Proceedings of the Institution of Mechanical Engineers Part C: Journal of Mechanical Engineering Science*, **205** (1991) 281–288.

[90] M. Zhou, W.X. Zhong, F.W. Williams, Wave propagation in substructural chain-type structures excited by harmonic forces, *International Journal of Mechanical Sciences*, **35** (1993) 953–964.

[91] B.R. Mace, D. Duhamel, M.J. Brennan, L. Hinker, Finite element prediction of wave motion in structural waveguides, *The Journal of the Acoustical Society of America*, **117** (2005) 2835–2843.

[92] L. Gry, C. Gontier, Dynamic modelling of railway track: a periodic model based on a generalized beam formulation, *Journal of Sound and Vibration*, **199** (1997) 531–558.

[93] M.N. Ichchou, S. Akrout, J.-M. Mencik, Guided waves group and energy velocities via finite elements, *Journal of Sound and Vibration*, **305** (2017) 931–944.

[94] H.M. Saeed, F. Vestroni, Simulation of combined systems by periodic structures: the wave transfer matrix approach, *Journal of Sound and Vibration*, **213** (1998) 55–73.

[95] L. Hinke, B.R. Mace, M.J. Brennan, Finite Element Analysis of Waveguides, in: *ISVR Technical Memorandum No 932*, 2004.

[96] Y. Waki, B.R. Mace, M.J. Brennan, Free and forced vibrations of a tyre using a wave/finite element approach, *Journal of Sound and Vibration*, **323** (2009) 737–756.

[97] W.X. Zhong, *Duality System in Applied Mechanics and Optimal Control*, Kluwer Academic Publishers, Boston, 2004.

[98] F. Lalonde, D. McDuff, Positive paths in the linear symplectic group, in: *The Arnold-Gelfand Mathematical Seminars*, Birkhäuser, Boston, 1997: pp. 361–387.

[99] R. V. Craster, Near cut-off behaviour in waveguides, in: J.G. Harris (Ed.), *Elastic Waves at High Frequencies: Techniques for Radiation and Diffraction of Elastic and Surface Waves*, Cambridge University Press, 2012: pp. 133–146.

[100] R. V. Craster, L.M. Joseph, J. Kaplunov, Long-wave asymptotic theories: The connection between functionally graded waveguides and periodic media, *Wave Motion*, **51** (2014) 581–588.

[101] S. Hans, C. Boutin, Dynamics of discrete framed structures: a unified homogenized description, *Journal of Mechanics of Materials and Structures*, **3** (2008) 1709–1739.

[102] C. Chesnais, S. Hans, C. Boutin, Dynamics of reticulated structures: evidence of atypical gyration modes, *International Journal for Multiscale Computational Engineering*, **9** (2011) 515–528.

[103] A.H. Meitzler, Backward-wave transmission of stress pulses in elastic cylinders and plates, *The Journal of the Acoustical Society of America*, **38** (1965) 835–842.

[104] E.E. Zayac, Propagation of elastic waves, in: W. Flügge (Ed.), *Handbook of Engineering Mechanics*, McGraw-Hill, New York, 1962.

[105] P.W. Milonni, *Fast Light, Slow Light and Left-Handed Light*, 1st edition, Institute of Physics Publishing, Bristol and Philadelphia, 2005.

[106] G.C. Horner, W.D. Pilkey, The Riccati transfer matrix method, *Journal of Mechanical Design*, **100** (1978) 297–302.

[107] J. Gu, X. Rui, J. Zhang, G. Chen, Q. Zhou, Riccati transfer matrix method for linear tree multibody systems, *ASME Journal of Applied Mechanics*, **84** (2017) 011008-011008-7.

[108] V. V. Krylov, F.J.B.S. Tilman, Acoustic "black holes" for flexural waves as effective vibration dampers, *Journal of Sound and Vibration*, **274** (2004) 605–619.

[109] K. Ogata, *Modern Control Engineering*, 2nd edition, Prentice Hall, USA, 1990.